Buckling of Laminated Composite Conical Shells; Theory and Experiment

Farjad Shadmehri

A thesis
In the Department
Of
Mechanical and Industrial Engineering

Presented in Partial Fulfillment of the Requirements
For the Degree of
Doctor of Philosophy (Mechanical Engineering) at
Concordia University
Montreal, Quebec, Canada

September 2012

CONCORDIA UNIVERSITY
SCHOOL OF GRADUATE STUDIES

This is to certify that the thesis prepared

By: Farjad Shadmehri

Entitled: Buckling of Laminated Composite Conical Shells; Theory and Experiment

and submitted in partial fulfillment of the requirements for the degree of

complies with the regulations of the University and meets the accepted standards with respect to originality and quality.

Signed by the final examining committee:

_____ Chair

Dr. Michael W. Hyer External Examiner

Dr. Khaled. Galal External to Program

Dr. Martin. Pugh Examiner

Dr. Ramin Sedaghati Examiner

Dr. Suong V. Hoa , Dr. Mehdi Hojjati Thesis Supervisor

Approved by

_____
Chair of Department or Graduate Program Director

_____ _____
Dean of Faculty

Abstract

Buckling of Laminated Composite Conical Shells; Theory and Experiment

Farjad Shadmehri, Ph.D.
Concordia University, 2012

Composite conical and cylindrical shells are gaining more application in aerospace industry (e.g., helicopter tailboom, airplane fuselage) due to their high specific strength and stiffness properties coming from material (composite) and geometry advantages. Stability is always a concern for these types of structures under different loading conditions. One of the major loading scenarios is the bending load in which composite conical shells can buckle under bending. Although there have been extensive studies on the buckling of conical and cylindrical shells under axial load, buckling under bending receives less attention in the literature from theoretical and experimental points of view. In this study, the bucking behavior of composite conical shells has been studied experimentally and theoretically.

In the theoretical approach, a first order shear deformation shell theory has been proposed to study buckling and bending behavior of composite conical shells. A semi-analytical approach (Ritz method) has been applied to study buckling under axial load and buckling under bending of composite conical shells. An analytical solution (Levy type solution) has been applied to study the bending response of cross-ply conical shells under sinusoidal bending load. Also, a new formulation has been proposed to study bending, buckling and vibration of cross-ply cylindrical shells using an analytical solution (Levy type solution). A different displacement field from what

was assumed in the literature has been proposed and consequently a new formulation has been obtained for the problem.

In the experimental approach, a composite tube-bending setup has been designed and developed to study bending, and buckling under bending load, behavior of composite shells. The setup has been designed to apply equal bending moments at the both ends of the structure, simulating pure bending test conditions. Experimental result has been obtained for buckling under pure bending of composite conical shells.

Regarding the manufacturing technique, Automated Fiber Placement (AFP) has attracted the aerospace industry due to its fast production rate, repeatability, and minimum material waste. Advanced thermoplastic composites obtain special attention in the aerospace industry as well, considering their superior properties (e.g., fracture toughness) and their capability to make aero-structures without requiring autoclave treatment with respect to thermoset ones. Considerable challenges remained unresolved regarding optimum process parameters for manufacturing of thermoplastic composites made by AFP and their quality. This thesis also addresses the effect of autoclave treatment on the stiffness quality of the thermoplastic composite cones made by AFP. The determination of optimum process parameters for AFP in the manufacturing of thermoplastic composite (AS4/PEEK) has been performed from both stiffness and strength point of view.

Acknowledgements

My first, foremost and most sincere thanks go to Dr. Suong V. Hoa, not only as my thesis supervisor, but also as a teacher with whom I am always impressed by his moral and ethical attitude toward the people in general and students specially. Dr. Hoa has an exceptional industrial view point while at the same time he is not compromising the scientific aspect of his research. I learned from him to look at research as a tool that should or possibly could have application in our real lives and can resolve industrial issues. I would like to thank him for his strong belief and trust in his students' abilities. I should say that during this research, there was no barrier in terms of facilities and tools and the project was financially well supported by him for which I am really grateful. Dr. Hoa is stunningly passionate about composites and his hard work always inspires me during my Ph.D. One of the most amazing things about Dr. Hoa is his availability to students. Although he is supervising a large research group and dealing with different companies, he has always time for questions and concerns. This is a great endowment that I had during this period, thanks to Dr. Hoa's dedication to students and research. Besides learning about research and composites from Dr. Hoa, I have learned much more from him about a good work ethic. While he has vast knowledge on the field, he is very humble and has sense of humor which makes the students feel comfortable with him. I am truly honored to have had this opportunity to work under his supervision and have had the privilege to work with such an outstanding scholar as Dr. Hoa. I would like to say "thank you Dr. Hoa for everything!".

I would also like to express my sincere appreciation to my co-supervisor, Dr. Mehdi Hojjati, whose friendly advice and supervision were always incredible guides toward my degree completion. Furthermore, his great industrial view point and connections were of great

importance to this research. His contribution in manufacturing aspects of this thesis is very much appreciated as well.

I would also like to acknowledge and thank my examination committee members, Dr. Michael W. Hyer, Dr. Martin Pugh, Dr. Ramin Sedaghati and Dr. Khaled E. Galal for their support and insightful comments.

Special thanks to Mr. Dan Juras (Technical Officer) and Mr. Henry Szczawinski (Technician), from research and technical staffs, Mechanical and Industrial Engineering Department at Concordia University. Their help and support for this project was essential and very much appreciated.

I would like to thank all my colleagues and members of Concordia Center for Composite (CONCOM) for their support. Specially, I would like to express my appreciations of the following persons:

1- Mr. Jeffery Simpson: he joined CONCOM group as his summer internship and continued as member of Consortium for Research and Innovation in Aerospace in Quebec (CRIAQ) COMP 5 project. His contribution in design and analysis of the composite tube bending setup is very much appreciated.
2- Mr. Xiao Cai: I collaborated with him as part of CRIAQ COMP 5 project. His contribution in manufacturing of thermoplastic composite samples, testing and analysis of results is very much appreciated.
3- Mr. Mohammad Geuchy: he helped me in preparation and in performing the bending test on the thermoplastic composite cone. His help is appreciated.

I would like to thank Dr. J. Chen from Aerospace Manufacturing Technology Centre (AMTC) of National Research Council Canada (NRC) in Montreal for his contribution in manufacturing of the thermoplastic composite cones and his helpful comments during this project. Also, insightful comments and design hints received from Mr. Robert S. Rutledge and Mr. John Rogers from Institute for Aerospace Research of NRC in Ottawa is appreciated.

Technical support and comments from Mr. Michel Dion, Mr. Kevin Morris, and Mr. Peter Beaulieu from Bell Helicopter Textron Canada Ltd., Mr. Simon Legault from Bombardier Aerospace, and Mr. Giuseppe Ombra from Dema Aeronautics during CRIAQ meetings are appreciated.

I would like to thank Mr. René Côté from Bosch-Rexroth Canada for his support and consultation regarding the hydraulic system of the composite tube bending setup.

Likewise, the help and support from Mr. Alain Nadeau and Mr. Marc-André Salois (from local machine shop in Montreal, SE Technology) is appreciated.

Furthermore, I would like to acknowledge the support of this research by CRIAQ (Consortium for Research and Innovation in Aerospace in Quebec), NSERC (Natural Sciences and Engineering Research Council of Canada), Bell Helicopter Textron Canada Ltd., Bombardier Aerospace, and Dema Aeronautics.

To end with, I would like to express my heartfelt gratitude to my father and my mother for their unconditional and unlimited love and support through my whole life. Finally, I would like to thank my spouse, Motahareh, words cannot express how thankful I am to have her in my life and how much her love and support has meant to me.

Dedication

This thesis is dedicated to:

my beloved mother and my beloved father

my dear sister,

and my beautiful beloved spouse, Motahareh.

Table of Contents

List of Figures

List of Tables

Nomenclature

α	Semi-cone angle
α_1, α_2	Shell coordinate system which coincides with orthogonal lines of principal curvature
ζ	Through thickness coordinate of shell element
x, θ, z	Conical shell coordinate system
β_1, β_2	Rotations of a normal to the mid-surface about α_2 and α_1 (shell element)
β_x, β_θ	Rotations of a normal to the mid-surface about θ and x axis (conical shell)
$\sigma_1, \sigma_2, \tau_{12}, \tau_{13}, \tau_{21}, \tau_{23}$	Stress components for shell element
$\bar{\sigma}_1, \bar{\sigma}_2, \bar{\tau}_{12}, \bar{\tau}_{13}, \bar{\tau}_{21}, \bar{\tau}_{23}$	Edge stresses for shell element
V	Total potential energy
$\Phi_{ij}^{u}, \Phi_{ij.}^{v}, \Phi_{ij}^{w}, \Phi_{ij}^{\beta_x}, \Phi_{ij}^{\beta_\theta}$	Approximation functions in Ritz method
A_1, A_2	Lame coefficients
A_{ij}, B_{ij}, D_{ij}	Laminate stiffness coefficints
$H(f)$	Frequency response function
H	Total laminate thickness
$I_i, i = 1,2,3$	Inertias
K_s	Shear correction factor
L	Length of the conical or cylindrical shell
$N_{11}, N_{12}, N_{22}, N_{21}$	In-plane force resultants for shell element
$M_{11}, M_{12}, M_{22}, M_{21}$	Moment resultants for shell element
Q_1, Q_2	Transverse force resultants for shell element
$N_{xx}, N_{\theta\theta}, N_{x\theta}$	In-plane force resultants for conical shell
$M_{xx}, M_{\theta\theta}, M_{x\theta}$	Moment resultants for conical shell
Q_x, Q_θ	Transverse force resultants for conical shell
$\widehat{N}_{xx}(x)$	In-plane compressive force
P_{cr}	Axial buckling load
$\bar{P}_{cr}$	Dimensionless critical axial buckling load
M_{cr}	Critical buckling moment
$\bar{M}_{cr}$	Dimensionless critical buckling moment
R_1, R_2	Principal radii of curvature
R	Radius of cylindrical shell

r	Radius of conical shell
U	Strain energy
W_s	Work of the body and surface forces
W_{e1}, W_{e2}	Work of the edge stresses
u_1, u_2, u_3	Displacements of mid-surface of shell element
u, v, w	Displacements of mid-surface of conical shell
x_t, x_b	Top and bottom coordinates of conical shell
q_x, q_θ, q_z	Static equivalents of the surface and body loads for conical shell

Chapter 1

Literature review and objectives

1.1 Introduction

Conical and cylindrical composite shells have wide applications in aerospace/aeronautical, naval and civil structures. There is an increasing interest in understanding the mechanical behavior of conical and cylindrical composite shells due to increased application of advanced composite materials in industry, which in turn, calls for developing efficient theoretical and experimental tools to analyze the mechanical behavior of these structures. In many applications, e.g., helicopter tailboom, the dominant loading is bending and the primarily concern is the stability of the structure under bending load. Due to the nature of the bending load, one side of the structure would be subjected to compression stress which can lead to buckling. Although there have been extensive studies on the buckling of conical and cylindrical shells under axial load, buckling under bending receives less attention in the literature from theoretical and experimental point of view. Even, to the best of author's knowledge, experimental result for buckling under bending of composite conical shells is nonexistent. In view of this lack of information on the topic, both theoretical and experimental investigation is necessary to predict the critical buckling load of composite conical shells under bending.

Advanced thermoplastic composites materials have attracted the attention of many aerospace companies due to their superior mechanical properties (e.g., fracture toughness, solvent resistance, and fire/smoke/toxicity performance) and being recyclable (green technology) in comparison with thermoset composites [1]. Furthermore, automated fiber placement technique as

a manufacturing solution for in-situ consolidation of advanced thermoplastic composite material opens a new window to aerospace/aeronautical companies.

In this research, a theoretical formulation is proposed and an experimental setup is developed to investigate buckling and bending characteristics of composite conical shells under pure bending. Automated fiber placement technique is used for manufacturing of advanced thermoplastic composite conical shell which then is tested using the developed composite tube bending setup. Comparison between theory and experiment is performed and the validity of the theory is substantiated by experiment.

1.2 Literature review

Cylindrical and conical shells are well known to buckle under axial compression. Since under the bending condition one side of the shell is under compression and the other side is under tension, it is expected that shells experience buckling at a certain applied moment. Therefore, one can say that a clear insight into the axial buckling phenomenon could help to understand the buckling under bending condition.

1.2.1 Buckling of cylindrical and conical shells under axial compression

In some cases, axial compression is the primary loading condition. Because of wide application, many investigations have been done on the buckling of cylinders under axial load. There are a number of studies dealing with three-dimensional analysis of cylindrical shells [2-12]. Soldatos [2] has presented a comprehensive review paper. Kardomateas et al., [3],[4] and[5], proposed an elasticity-based bucking analysis of orthotropic cylindrical shells under different loading conditions. Vardan and Bhaskar [6] presented three-dimensional solutions for bending of

orthotropic cylindrical shells. The buckling analysis of cross-ply laminated composite cylindrical shells subjected to axial compression was presented by Ye and Soldatos [7].

A number of studies exist on basis of two-dimensional theories for cylindrical shells [13-23]. A review on this type of theories has been made by Noor and Burton [12]. Jones [14] proposed formulation and design criteria for buckling of both isotropic and orthotropic circular cylinder under different type of loading. He assumed special orthotropy for laminate and considered a correlation factor to relate the calculation to the available experimental data. Messina and Soldatos [15] applied Ritz-type procedure to analyze dynamic behavior of cross-ply laminated circular cylinders. They presented the effect of different edge boundary conditions on natural frequencies of these structures. Vibration and buckling of cross-ply laminated composite cylindrical shells according to higher-order theory was investigated by Matsunaga [16] using the method of power series. In 1989, Khdeir et al. [17] proposed an analytical solution for bending, buckling under axial load and vibration of cross-ply cylindrical shells under various boundary conditions using classical and first order shell theory. Later, in 1992, Nosier and Reddy [18] developed an improved and computationally more efficient analytical procedure for the same type of problems solved by Khdeir et al. [17].

There have been extensive studies on the buckling of isotropic conical shells under axial load and external pressure [24-30]. Seide [24] proposed a formula for buckling of isotropic conical shell which is independent of boundary conditions and best fits the behavior of long shells. Baruch [25] investigated the stability of simply supported isotropic conical shells under axial load for four different sets of in-plane boundary conditions using Donnell-type theory.

However, although laminated composite materials have found extensive industrial applications during the last decades, only few studies have been published targeting the buckling behavior of conical composite shells. Using Donnell-type shell theory, Tong and Wang [31-32] proposed a power series based solution for buckling analysis of laminated conical shells under axial compressive load and external pressure. Li [33] considered the stability of composite stiffened shell under axial compression load. He assumed classical lamination theory and used Rayleigh-Ritz approximation to solve the governing equations. Sofiyev [34] studied the buckling of orthotropic composite conical shell incorporating the effect of thickness variation and time dependent external pressure. Donnell-type shell theory was assumed in his work and Galerkin's method and variational technique were applied to obtain the solution. Static, free vibration and buckling analysis of laminated conical shell using finite element method based on higher order shear deformation theory was carried out by Pinto Correia et al. [35]. The effect of variations of the stiffness coefficients on the buckling of laminated conical shells was studied by Goldfeld and Arbocs [36] using classical shell theory and computer code STAGS-A. Patel et al. and Singh et al. studied the buckling, postbuckling and thermoelastic stability characteristics of laminated conical shells using nonlinear theory and finite element approach [37-43].

Experimental data for composite cylinder in axial compression are widely reported. But generally, there is a large discrepancy between the test data and analytically predicted value. This attribute has usually been related to the sensitivity of cylindrical shells to imperfection such as variation in shape, thickness and loading conditions. These imperfections are usually caused by manufacturing techniques which are traditionally non-automated and relatively imprecise. The

full explanation of these issues is currently an active flied of research. References [44] and [45] summarized the subject until the mid 1980's.

Regarding the manufacturing point of view, composite cylinders are conventionally manufactured by either filament winding or prepreg layup and autoclave process. The test data that are available for both methods will be discussed in the following paragraphs. Automated fiber placement (AFP) technique is relatively a new technique for manufacturing of cylindrical and conical composite shells and no experimental results are available regarding the buckling of AFP made conical shells.

Filament-wound cylinders: Card and his co-worker have carried out test and investigation on the instability of orthotropic filament wound cylinders at NASA Langley Research Center [46-47]. Similar research has been done by Tsai et al. [48], Jensen and Hipp [49] and Hahn et al. [50], all sponsored by NASA. Card et al. [46] investigated relatively thick glass-epoxy cylinders loaded in compression at both room and elevated temperature. The test results were assessed by analytical predictions obtained from Donnell-type laminated theory.

Another early investigation on the buckling of filament-wound composite cylinders including both experimental and analytical approach was reported by Tsai and his co-workers [48]. The experimental results were reported to be between 65-85 percent of buckling loads obtained from classical linear theory [51].

More recently, Jensen and Hipp [49] considered the effect of material defects on the axial strength of composite cylinder in axial compression. They also reported on details of manufacturing process of six cylinders which were used in the tests. As a result of their

investigation, they found that the failure stresses are about 58-75 percent of the ones predicted by finite element analysis [51].

Prepreg-laid cylinder: At the Institute for Aerospace Studies, University of Toronto (UTIAS), a comprehensive experimental and analytical investigation were performed on buckling of composite cylinder under axial compression (see [52-54]). The main concept followed in these studies was the effect of initial imperfections of cylinder on the buckling behaviour. Tennyson and Muggeridge [52], studied experimentally and analytically the buckling of glass-epoxy cylinders fabricated from unidirectional prepreg. The purpose of this study was whether or not the buckling strength could be estimated based on the measurement of the imperfections present in the shell structures. Consequently, based on the analytical modeling of the buckling strength of imperfect shells, they found that the initial shape imperfections significantly reduce the compressive strength of the cylinders in comparison with the perfect ones. In addition, the experimental data are reported to be in a good agreement of the one predicted by analytical modeling and the discrepancy did not exceed 20 percent [51].

Giavotto, Poggi and their co-workers [55-56], at the Department of Aerospace Engineering and Structural Engineering, Milan Polytechnic, carried out an extensive experimental and analytical study on the buckling behaviour of composite cylinders. The goal was to provide a database for the development of Eurocodes for composite shells subjected to combined loading (axial compression and torsion). This was done based on test results complemented by numerical analysis [51].

1.2.2 Buckling of cylindrical and conical shells under bending

Bending load is the dominant load in many applications and thin structural components may buckle under bending in some applications including aircraft fuselage, helicopter tailboom, launch vehicles and transportation containers. Nevertheless, experimental results are rare especially for composite cylindrical shells and nonexistent for composite conical shells.

Published as a NASA technical note, Block [57] studied the buckling of eccentrically stiffened orthotropic cylinders under pure bending. Simply support boundary condition was considered for numerical results and Galerkin's method was used to obtain solutions. Holston [58] proposed a theoretical analysis for buckling of inhomogeneous anisotropic cylindrical shells under bending combined with pressure, axial load, and torsion. The through-thickness transverse shear strain was not considered in his study. Ugural and Cheng [59] presented an analysis for the buckling of laminated, long, cylindrical shells under pure bending. The coupling between in-plane stretching and bending was investigated and shear deformation was not considered in the formulation. Shell theory based on Euler-Bernoulli hypothesis was considered in their study and because of long cylinder assumption, boundary conditions was not considered. Lou and Yaniv [60] studied the buckling behavior of cylindrical composite shells under axial compression, bending and combined load. The displacement field was assumed based on the classical shell theory and as a result of this assumption, shear deformation was neglected. Galerkin's method was used in their study to solve the governing equation and the effect of length-to-thickness and radius-to-thickness ratios was studied. Fuchs and Hyer [61] studied the linear response of thin, symmetrically laminated circular cylinders subject to bending by end rotations. The effect of geometry and ply orientation on the overall prebuckling response of cylinders was evaluated. They also compute

the inertlaminar stresses by integration of the three-dimensional equilibrium equations of elasticity. The boundary layer near the ends of the cylinder was also studied. The nonlinear prebuckling response of laminated cylinders was also solved by Fuchs and Hyer [62] using separation of variable technique and finite-difference procedure.

A numerical and experimental investigation sponsored by NASA Langley-Virginia Polytechnic Institute was carried out by Fuchs, Hyer and Starnes [63] on bending response and buckling of thin-walled composite cylinders. A nonlinear analysis based on the Donnell's shell equations developed to study the prebuckling of composite full cylinder under bending caused by known end-rotation applied to each end of the cylinder. The initial shape imperfections were also considered in analytical modelling for comparison of test data with theory. The prebuckling, buckling and post-buckling problem was solved using geometrically nonlinear finite element analysis and the prebuckling results were compared by nonlinear developed theory. Extensive experimental data are obtained from test of six eight-ply graphite-epoxy circular cylinders. The cylinders were tested in bending test setup developed by authors. It was shown that the buckling moments obtained from test correlated well with predictions considering geometrical imperfections.

More recently, Blom et al. [64] developed a bending test fixture to perform bending test on a carbon fiber-reinforced cylinder in the Netherlands. The bending fixture was installed on a MTS test bench which provides the loading power. Experimental data (strains) were compared with finite element model obtained using commercial software package ABAQUS. The maximum load that could be applied to their composite cylinder was limited by the strength of the bolts in the fixture and the composite cylinder was too stiff to be buckled in the gage area.

1.3 Thesis approach

With reference to aforementioned discussions in this chapter and bearing in mind the lack of analytical investigation and non-existing experimental data on the bending and buckling behavior of composite conical shells under pure bending as well as considering the importance of application of conical composite shells in aerospace industry, this research is devoted to developing both experimental setup and analytical formulation to study bending and buckling behavior of conical composite shells under bending. To the best of author's knowledge, this is the first time experimental work has been conducted on the composite conical shells under pure bending load. The following theoretical and experimental approaches are accomplished in the current study:

1.3.1 Theoretical approach

Since classical laminated shell theories based on Love-Kirchhoff hypothesis were shown to overpredict the stability threshold of shells, a first order shear deformation theory which considers the effect of transverse shear deformation in analysis is considered in this research. General first order shell formulation is presented in Chapter 2 (section 2.1) followed by solving the buckling problem for composite conical shells under both axial load (section 2.1.3) and pure bending (section 2.3) using semi-analytical approach. The governing equations are obtained using principle of minimum (stationary) potential energy and solved using Ritz's method. An analytical solution is proposed for bending of cross-ply conical shells using Levy-type solution in section 2.4.

Chapter 3 is devoted to study the effect of displacement field on buckling, bending, and vibration of cross-ply circular cylindrical shells. A different displacement field than that proposed by Khdeir et al. [17] is assumed and numerical results are obtained using analytical solution proposed by Nosier and Reddy [18]. It is shown that assumed displacement field has a significant effect on numerical results in some cases and consequently an appropriate displacement field should be assumed.

1.3.2 Experimental approach

A composite tube bending setup is developed to study bending and buckling behavior of conical shells under bending. The setup consists of three units, namely, structural components, loading unit, and instrumentation and is explained in detail in Chapter 4. The goal of this experimental setup is to apply bending moment to both ends of the test specimen until failure happens.

Manufacturing of the thermoplastic composite tailboom, which has conical geometry and serves as a test specimen, and the experimental results obtained from bending test are presented in Chapter 5. The thermoplastic composite tailboom was manufactured using automated fiber placement (AFP) machine at the National Research Council of Canada as part of collaborations in CRIAQ COMP 5 project. Effect of autoclave treatment on the quality of the AFP-made thermoplastic composite cones is discussed in section 5.2. Optimum process parameters for manufacturing thermoplastic composite material using AFP are determined from stiffness and strength point of view in sections 5.3 and 5.4, respectively. Experimental bending and buckling under bending results are presented in section 5.6. Comparison between experimental critical buckling moment and theoretical one developed in Chapter 2 is performed in section 5.7.

Chapter 2

Buckling and bending of composite conical shells

2.1 Basic assumptions and shell formulation

In theoretical modeling of laminated shell, a first-order shear deformation theory is considered. In this theory the Kirchhoff hypothesis denoting that the transverse normal to the reference surface remains perpendicular to it after deformation, is relaxed (but the normal still remain straight). As a result of this relaxation, the transverse shear strains and consequently shear stresses are no more zero. The effect of transverse shear deformation is taken into account since the classical theory of shells was shown not to be accurate enough for moderately thick laminated shells and where the material anisotropy is severe [35] and [65]. However, the transverse normal is inextensible and consequently the transverse normal stress is zero. Furthermore, it is assumed that the shell is thin which means the ratio of thickness to the radius of curvature of the reference surface is negligible. Another assumption that comes from the linear relation between strain-displacement is that the deflections of the shell are small.

2.1.1 Shell coordinates

A curvilinear coordinate system which coincides with the orthogonal lines of principal curvature of the middle surface of the general shell is established (Figure 2.1). The length of the shell element can be written as [66],

$$ds_1 = A_1\left(1+\frac{\zeta}{R_1}\right)d\alpha_1 \tag{2.1}$$

$$ds_2 = A_2\left(1 + \frac{\zeta}{R_2}\right)d\alpha_2$$

where A_1 and A_2 are Lame coefficients and R_1 and R_2 are principal radii of curvature.

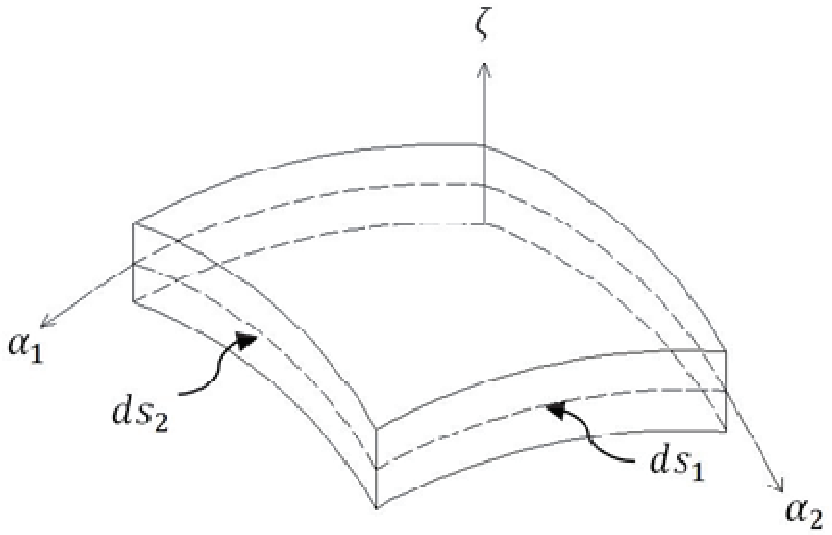

Figure 2.1: Shell element

Consistent with the assumptions made in preceding section, the displacements are distributed linearly across the thickness of shell and consequently the position of each point in the shell could be obtained based on the position of the corresponding point on the middle surface of the shell. Therefore, the displacement field can be written as

$$U_1(\alpha_1, \alpha_2, \zeta) = u_1(\alpha_1, \alpha_2) + \zeta\beta_1(\alpha_1, \alpha_2) \tag{2.2}$$

$$U_2(\alpha_1, \alpha_2, \zeta) = u_2(\alpha_1, \alpha_2) + \zeta\beta_2(\alpha_1, \alpha_2)$$

$$U_3(\alpha_1, \alpha_2, \zeta) = u_3(\alpha_1, \alpha_2)$$

in which (u_1, u_2, u_3) are the displacements of middle surface and (β_1, β_2) are the rotations of a normal to the middle surface about α_2 and α_1, respectively.

2.1.2 Strain-displacement relations

The linear strain-displacement relations for general shell element associated with the assumed displacement field are [66]

$$\varepsilon_1 = \frac{1}{A_1\left(1+\frac{\zeta}{R_1}\right)}\left(\frac{\partial U_1}{\partial \alpha_1}+\frac{U_2}{A_2}\frac{\partial A_1}{\partial \alpha_2}+\frac{A_1 U_3}{R_1}\right) \tag{2.3}$$

$$\varepsilon_2 = \frac{1}{A_2\left(1+\frac{\zeta}{R_2}\right)}\left(\frac{\partial U_2}{\partial \alpha_2}+\frac{U_1}{A_1}\frac{\partial A_2}{\partial \alpha_1}+\frac{A_2 U_3}{R_2}\right)$$

$$\varepsilon_n = \frac{\partial U_3}{\partial \zeta}$$

$$\gamma_{1n} = \frac{1}{A_1\left(1+\frac{\zeta}{R_1}\right)}\frac{\partial U_3}{\partial \alpha_1}+A_1\left(1+\frac{\zeta}{R_1}\right)\frac{\partial}{\partial \zeta}\left[\frac{U_1}{A_1\left(1+\frac{\zeta}{R_1}\right)}\right]$$

$$\gamma_{2n} = \frac{1}{A_2\left(1+\frac{\zeta}{R_2}\right)}\frac{\partial U_3}{\partial \alpha_2}+A_2\left(1+\frac{\zeta}{R_2}\right)\frac{\partial}{\partial \zeta}\left[\frac{U_2}{A_2\left(1+\frac{\zeta}{R_2}\right)}\right]$$

$$\gamma_{12} = \frac{A_2\left(1+\frac{\zeta}{R_2}\right)}{A_1\left(1+\frac{\zeta}{R_1}\right)}\frac{\partial}{\partial \alpha_1}\left[\frac{U_2}{A_2\left(1+\frac{\zeta}{R_2}\right)}\right]+\frac{A_1\left(1+\frac{\zeta}{R_1}\right)}{A_2\left(1+\frac{\zeta}{R_2}\right)}\frac{\partial}{\partial \alpha_2}\left[\frac{U_1}{A_1\left(1+\frac{\zeta}{R_1}\right)}\right]$$

2.1.3 Equations of motion

The governing equations of general shell are derived using principle of minimum (stationary) potential energy on account of its simplicity and due to the fact that it gives the natural boundary conditions of the problem as well. It can be written as [66]

$$\delta(U - W_s - W_{e1} - W_{e2}) = 0 \tag{2.4}$$

in which U represents the strain energy, while W_s is the work of the body and surface forces and W_{e1} and W_{e2} are the work done by the edge stresses. These parameters can be defined as

$$\delta U = \int_{\alpha_1} \int_{\alpha_2} \int_{\zeta} (\sigma_1 \delta\varepsilon_1 + \sigma_2 \delta\varepsilon_2 + \tau_{12}\delta\gamma_{12} + \tau_{13}\delta\gamma_{13} + \tau_{23}\delta\gamma_{23})\, d\alpha_1 d\alpha_2 d\zeta \tag{2.5}$$

$$\delta W_s = \int_{\alpha_1} \int_{\alpha_2} (q_1 \delta u_1 + q_2 \delta u_2 - q_3 \delta u_3)\, A_1 A_2 d\alpha_1 d\alpha_2$$

$$\delta W_{e1} = \int_{\alpha_2} \int_{\zeta} (\bar{\sigma}_1 \delta u_1 + \bar{\tau}_{12} \delta u_2 + \bar{\tau}_{13} \delta u_3)\, A_2 \left(1 + \frac{\zeta}{R_2}\right) d\alpha_2 d\zeta$$

$$\delta W_{e2} = \int_{\alpha_1} \int_{\zeta} (\bar{\sigma}_2 \delta u_2 + \bar{\tau}_{21} \delta u_1 + \bar{\tau}_{23} \delta u_3)\, A_1 \left(1 + \frac{\zeta}{R_1}\right) d\alpha_1 d\zeta$$

here q_i are the static equivalents of the surface and body loads which are applied to the upper and lower surfaces of the shell and considered to be applied on the middle surface of the shell. $\bar{\sigma}_1$, $\bar{\sigma}_2$, $\bar{\tau}_{12}$, $\bar{\tau}_{13}$, $\bar{\tau}_{21}$and $\bar{\tau}_{23}$ are the edge stresses.

Substituting the displacement field, equations (2.2), into equations (2.5) and equations (2.5) into principle of minimum potential energy, equation (2.4), and integrating over the thickness of the shell, one can get

$$\begin{aligned}
\iint_{\alpha_1\alpha_2} \Bigg\{ & \left[\frac{\partial(N_{11}A_2)}{\partial\alpha_1} + \frac{\partial(N_{12}A_1)}{\partial\alpha_2} + N_{12}\frac{\partial A_1}{\partial\alpha_2} - N_{22}\frac{\partial A_2}{\partial\alpha_1} + Q_1\frac{A_1A_2}{R_1} + q_1A_1A_2\right]\delta u_1 \\
& + \left[\frac{\partial(N_{12}A_2)}{\partial\alpha_1} + \frac{\partial(N_{22}A_1)}{\partial\alpha_2} + N_{21}\frac{\partial A_2}{\partial\alpha_1} - N_{11}\frac{\partial A_1}{\partial\alpha_2} + Q_2\frac{A_1A_2}{R_2}\right. \\
& \left. + q_2A_1A_2\right]\delta u_2 \\
& + \left[\frac{\partial(Q_1A_2)}{\partial\alpha_1} + \frac{\partial(Q_2A_1)}{\partial\alpha_2} - \left(\frac{N_1}{R_1} + \frac{N_2}{R_2}\right)A_1A_2 - q_3A_1A_2\right]\delta u_3 \\
& + \left[\frac{\partial(M_{11}A_2)}{\partial\alpha_1} + \frac{\partial(M_{21}A_1)}{\partial\alpha_2} + M_{12}\frac{\partial A_1}{\partial\alpha_2} - M_{22}\frac{\partial A_2}{\partial\alpha_1} - Q_1A_1A_2\right]\delta\beta_1 \\
& + \left[\frac{\partial(M_{12}A_2)}{\partial\alpha_1} + \frac{\partial(M_{22}A_1)}{\partial\alpha_2} + M_{21}\frac{\partial A_2}{\partial\alpha_1} - M_{11}\frac{\partial A_1}{\partial\alpha_2}\right. \\
& \left. - Q_2A_1A_2\right]\delta\beta_2\Bigg\} d\alpha_1 d\alpha_2 \\
& + \oint_{\alpha_1} [(\bar{N}_{21} - N_{21})\delta u_1 + (\bar{N}_{22} - N_{22})\delta u_2 + (\bar{Q}_2 - Q_2)\delta u_3 \\
& + (\bar{M}_{21} - M_{21})\delta\beta_1 + (\bar{M}_{22} - M_{22})\delta\beta_2]\, A_1 d\alpha_1 \\
& + \oint_{\alpha_2} [(\bar{N}_{11} - N_{11})\delta u_1 + (\bar{N}_{12} - N_{12})\delta u_2 + (\bar{Q}_1 - Q_1)\delta u_3 \\
& + (\bar{M}_{11} - M_{11})\delta\beta_1 + (\bar{M}_{12} - M_{12})\delta\beta_2]\, A_2 d\alpha_2 = 0
\end{aligned} \tag{2.6}$$

where

$$\begin{Bmatrix} N_{11} \\ N_{12} \\ Q_1 \end{Bmatrix} = \int_\zeta \begin{Bmatrix} \sigma_{11} \\ \tau_{12} \\ \tau_{13} \end{Bmatrix}\left(1 + \frac{\zeta}{R_2}\right)d\zeta \qquad \begin{Bmatrix} N_{22} \\ N_{21} \\ Q_2 \end{Bmatrix} = \int_\zeta \begin{Bmatrix} \sigma_{22} \\ \tau_{21} \\ \tau_{23} \end{Bmatrix}\left(1 + \frac{\zeta}{R_1}\right)d\zeta \tag{2.7}$$

$$\begin{Bmatrix} \bar{N}_{11} \\ \bar{N}_{12} \\ \bar{Q}_1 \end{Bmatrix} = \int_\zeta \begin{Bmatrix} \bar{\sigma}_{11} \\ \bar{\tau}_{12} \\ \bar{\tau}_{13} \end{Bmatrix}\left(1 + \frac{\zeta}{R_2}\right)d\zeta \qquad \begin{Bmatrix} \bar{N}_{22} \\ \bar{N}_{21} \\ \bar{Q}_2 \end{Bmatrix} = \int_\zeta \begin{Bmatrix} \bar{\sigma}_{22} \\ \bar{\tau}_{21} \\ \bar{\tau}_{23} \end{Bmatrix}\left(1 + \frac{\zeta}{R_1}\right)d\zeta$$

$$\begin{Bmatrix} M_{11} \\ M_{12} \end{Bmatrix} = \int_{\zeta} \begin{Bmatrix} \sigma_{11} \\ \tau_{12} \end{Bmatrix} \left(1 + \frac{\zeta}{R_2}\right) \zeta d\zeta \qquad \begin{Bmatrix} M_{22} \\ M_{21} \end{Bmatrix} = \int_{\zeta} \begin{Bmatrix} \sigma_{22} \\ \tau_{21} \end{Bmatrix} \left(1 + \frac{\zeta}{R_1}\right) \zeta d\zeta$$

$$\begin{Bmatrix} \bar{M}_{11} \\ \bar{M}_{12} \end{Bmatrix} = \int_{\zeta} \begin{Bmatrix} \bar{\sigma}_{11} \\ \bar{\tau}_{12} \end{Bmatrix} \left(1 + \frac{\zeta}{R_2}\right) \zeta d\zeta \qquad \begin{Bmatrix} \bar{M}_{22} \\ \bar{M}_{21} \end{Bmatrix} = \int_{\zeta} \begin{Bmatrix} \bar{\sigma}_{22} \\ \bar{\tau}_{21} \end{Bmatrix} \left(1 + \frac{\zeta}{R_1}\right) \zeta d\zeta$$

Since the variations δu_1, δu_2, δu_3, $\delta \beta_1$, and $\delta \beta_2$ could have any arbitrary values, equation (2.6) could vanish, as required, only if the coefficients of the variations each vanish. Applying this fact, five equations of motions are obtained as:

$$\delta u_1: \quad \frac{\partial (N_{11} A_2)}{\partial \alpha_1} + \frac{\partial (N_{21} A_1)}{\partial \alpha_2} + N_{12} \frac{\partial A_1}{\partial \alpha_2} - N_{22} \frac{\partial A_2}{\partial \alpha_1} + Q_1 \frac{A_1 A_2}{R_1} + q_1 A_1 A_2 = 0 \tag{2.8}$$

$$\delta u_2: \quad \frac{\partial (N_{12} A_2)}{\partial \alpha_1} + \frac{\partial (N_{22} A_1)}{\partial \alpha_2} + N_{21} \frac{\partial A_2}{\partial \alpha_1} - N_{11} \frac{\partial A_1}{\partial \alpha_2} + Q_2 \frac{A_1 A_2}{R_2} + q_2 A_1 A_2 = 0 \tag{2.9}$$

$$\delta u_3: \quad \frac{\partial (Q_1 A_2)}{\partial \alpha_1} + \frac{\partial (Q_2 A_1)}{\partial \alpha_2} - \left(\frac{N_1}{R_1} + \frac{N_2}{R_2}\right) A_1 A_2 - q_3 A_1 A_2 = 0 \tag{2.10}$$

$$\delta \beta_1: \quad \frac{\partial (M_{11} A_2)}{\partial \alpha_1} + \frac{\partial (M_{21} A_1)}{\partial \alpha_2} + M_{12} \frac{\partial A_1}{\partial \alpha_2} - M_{22} \frac{\partial A_2}{\partial \alpha_1} - Q_1 A_1 A_2 = 0 \tag{2.11}$$

$$\delta \beta_2: \quad \frac{\partial (M_{12} A_2)}{\partial \alpha_1} + \frac{\partial (M_{22} A_1)}{\partial \alpha_2} + M_{21} \frac{\partial A_2}{\partial \alpha_1} - M_{11} \frac{\partial A_1}{\partial \alpha_2} - Q_2 A_1 A_2 = 0 \tag{2.12}$$

Also four essential and natural boundary conditions on an edge of constant α_1 are obtained as

$$\begin{aligned} \bar{N}_{21} &= N_{21} \ or \ \delta u_1 \\ \bar{N}_{22} &= N_{22} \ or \ \delta u_2 \\ \bar{Q}_2 &= Q_2 \ or \ \delta u_3 \\ \bar{M}_{21} &= M_{21} \ or \ \delta \beta_1 \\ \bar{M}_{22} &= M_{22} \ or \ \delta \beta_2 \end{aligned} \tag{2.13}$$

whereas on an edge of constant α_2 are

$$\begin{aligned} \bar{N}_{11} &= N_{11} \ or \ \delta u_1 \\ \bar{N}_{12} &= N_{12} \ or \ \delta u_2 \\ \bar{Q}_1 &= Q_1 \ or \ \delta u_3 \\ \bar{M}_{11} &= M_{11} \ or \ \delta \beta_1 \\ \bar{M}_{12} &= M_{12} \ or \ \delta \beta_2 \end{aligned} \tag{2.14}$$

2.2 Buckling of conical composite shells under axial load[1]

In this section, axisymmetric and non-axisymmetric formulations for buckling analysis of conical composite shells subjected to axial compression load are developed and semi-analytical solution using Ritz method is obtained. Parametric study is carried out to reveal the influence of the semi-cone angle and the fiber orientation on critical buckling load.

2.2.1 Formulation

The total potential energy of a mechanical system (V) consists of two parts; strain energy (U) and potential energy of external forces (W)

$$V = U + W \tag{2.15}$$

[1] The content of section 2.1.3 has been published in [96] and [98].

The principle of minimum potential energy states that a mechanical system is in a stable equilibrium state if, and only if, the potential energy is a relative minimum for that equilibrium state. That is, a mechanical system in equilibrium is stable if a change in potential energy is positive ($\Delta V > 0$). A change in potential energy, ΔV, can be written in a Taylor series as [67]

$$\Delta V = \delta V + \frac{1}{2!}\delta^2 V + \frac{1}{3!}\delta^3 V + \cdots \tag{2.16}$$

For a system in equilibrium, the first variation of the potential energy is zero, i.e. $\delta V = 0$. A mechanical system become unstable when $\Delta V < 0$. So as a boundary between stable ($\Delta V > 0$) and unstable ($\Delta V < 0$) system, the equilibrium configuration which has $\Delta V = 0$ is called buckling criterion. However, because of the infinite number of terms in equation (2.16), the condition $\Delta V = 0$ does not give a practical criterion. Two practical buckling criteria are introduced in [67]; the first one is called "neutral equilibrium method" and is denoted by the condition in which $\bar{\delta}^2 V = \delta^2 V|_{\delta V = 0} = 0$. A bar over the variation symbol is to specify that the second variation should be evaluated at an equilibrium configuration.

The second buckling criterion is based on the concept of two very close equilibrium states and is known as the "adjacent equilibrium method". This criterion can be stated in mathematical notation as

$$\delta\left(\bar{\delta}^2 V\right) = 0 \tag{2.17}$$

and is known as Trefftz buckling criterion. As mentioned in[67], both criteria are equally valid and lead to the same buckling equations.

In the following sections, Trefftz criterion is used to derive the buckling equations for general laminated thin-walled conical shells.

Furthermore, classical shell buckling theory assumption is employed. That is, the shell expands and contracts in axial and circumferential directions as a membrane under load prior to buckling. As a result, the prebuckling rotations are neglected in the buckling analysis. Using first-order shear deformation shell theory, Kirchhoff hypothesis denoting that the transverse normal to the mid-surface remains perpendicular to it after deformation, is relaxed.

2.2.1.1 Kinematics

Conical shells are special case of the general shells. The coordinate system associated with these kinds of shells is shown in Figure 2.2. Considering this coordinate system, one can cast the variation of the displacement field given in equation (2.2) into following form which is appropriate for the conical shells

$$\begin{gathered}\delta U(x,\theta,z) = \delta u(x,\theta) + z\delta\beta_x(x,\theta) \\ \delta V(x,\theta,z) = \delta v(x,\theta) + z\delta\beta_\theta(x,\theta) \\ \delta W(x,\theta,z) = \delta w(x,\theta)\end{gathered} \tag{2.18}$$

In these equations $\delta u(x,\theta)$, $\delta v(x,\theta)$ and $\delta w(x,\theta)$ are variations in the displacements u, v and w (from the prebuckling equilibrium state) and $\delta\beta_x(x,\theta)$ and $\delta\beta_\theta(x,\theta)$ are variations in the rotations β_x and β_θ from the prebuckling equilibrium state. It should be mentioned that, in fact, $\delta u, \delta v, \delta w, \delta\beta_x$ and $\delta\beta_\theta$ are the increments in displacements as opposed to the displacements themselves.

The Lame coefficients (A_1, A_2) and principal radii of curvature (R_1, R_2) for conical shell are

$$A_1 = R_1 = r_\phi, A_2 = r = xsin(\alpha), R_2 = r_\theta = xtan(\alpha) \tag{2.19}$$

where r is the radius of the cone which varies with the cone length. r_ϕ represents the radius of curvature along the meridian and since conical shell has straight generator, the curvature along the meridian is zero and $1/r_\phi$ is vanished (i.e. r_ϕ is infinity). The linear strain-displacement relations for general shell element, equation (2.3), can be adapted for conical shell using equation (2.19) and considering thin-walled shell assumption. After some mathematical manipulations and making the change of variables $\alpha_1 = \phi$, $\alpha_2 = \theta$ and $r_\phi \partial\phi = \partial x$, one can write the strain-displacement relations for conical shell as

$$\begin{gathered} \varepsilon_x = \varepsilon_x^0 + z\acute{\varepsilon_x} \\ \varepsilon_\theta = \varepsilon_\theta^0 + z\acute{\varepsilon_\theta} \\ \gamma_{x\theta} = \gamma_{x\theta}^0 + z\acute{\gamma_{x\theta}} \\ \gamma_{xz} = \gamma_{xz}^0 \\ \gamma_{\theta z} = \gamma_{\theta z}^0 \end{gathered} \tag{2.20}$$

where

$$\varepsilon_x^0 = \frac{\partial u}{\partial x} \qquad \varepsilon_\theta^0 = \frac{1}{x\sin(\alpha)}\left(\frac{\partial v}{\partial \theta} + usin(\alpha) + wcos(\alpha)\right) \tag{2.21}$$

$$\acute{\varepsilon_x} = \frac{\partial \beta_x}{\partial x} \qquad \acute{\varepsilon_\theta} = \frac{1}{x\sin(\alpha)}\left(\frac{\partial \beta_\theta}{\partial \theta} + \beta_x sin(\alpha)\right)$$

$$\gamma_{x\theta}^0 = \frac{\partial v}{\partial x} - \frac{1}{x\sin(\alpha)}\left(vsin(\alpha) - \frac{\partial u}{\partial \theta}\right)$$

$$\gamma_{xz}^0 = \frac{\partial w}{\partial x} + \beta_x \qquad \acute{\gamma_{x\theta}} = \frac{\partial \beta_\theta}{\partial x} + \frac{1}{x\sin(\alpha)}\frac{\partial \beta_x}{\partial \theta} - \frac{\beta_\theta}{x}$$

$$\gamma_{\theta z}^0 = \frac{1}{x\sin(\alpha)}\frac{\partial w}{\partial \theta} - \frac{v}{x\sin(\alpha)}\cos(\alpha) + \beta_\theta$$

α in above equations is semi-cone angle (Figure 2.2).

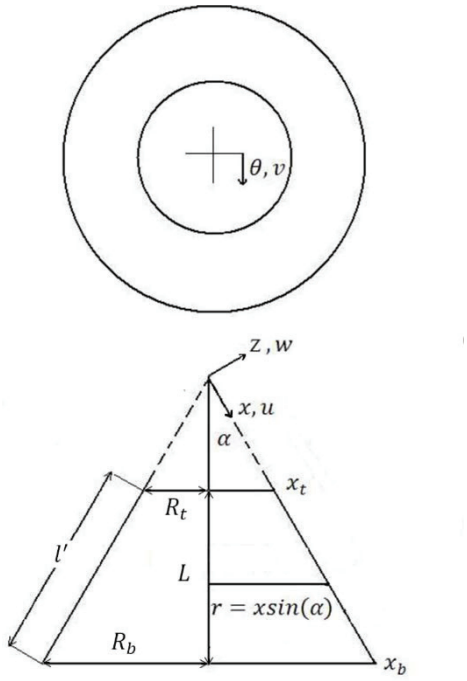

Figure 2.2: Conical shell coordinate system

2.2.1.2 Constitutive law

Assuming orthotropic properties for each layer and neglecting the transverse normal stress, force and moment resultants are related to strains by laminated stiffness coefficients as follows [68]

$$\begin{Bmatrix} N_{xx} \\ N_{\theta\theta} \\ N_{x\theta} \\ M_{xx} \\ M_{\theta\theta} \\ M_{x\theta} \end{Bmatrix} = \begin{bmatrix} A_{11} & A_{12} & A_{16} & B_{11} & B_{12} & B_{16} \\ A_{12} & A_{22} & A_{26} & B_{12} & B_{22} & B_{26} \\ A_{16} & A_{26} & A_{66} & B_{16} & B_{26} & B_{66} \\ B_{11} & B_{12} & B_{16} & D_{11} & D_{12} & D_{16} \\ B_{12} & B_{22} & B_{26} & D_{12} & D_{22} & D_{26} \\ B_{16} & B_{26} & B_{66} & D_{16} & D_{26} & D_{66} \end{bmatrix} \begin{Bmatrix} \varepsilon_x^0 \\ \varepsilon_\theta^0 \\ \gamma_{x\theta}^0 \\ \acute{\varepsilon}_x \\ \acute{\varepsilon}_\theta \\ \acute{\gamma}_{x\theta} \end{Bmatrix} \tag{2.22}$$

$$\begin{Bmatrix} Q_\theta \\ Q_x \end{Bmatrix} = K_s \begin{bmatrix} A_{44} & A_{45} \\ A_{45} & A_{55} \end{bmatrix} \begin{Bmatrix} \gamma_{\theta z}^0 \\ \gamma_{xz}^0 \end{Bmatrix}$$

In equation (2.22), K_s is shear correction factor and taken to be 5/6 for numerical results [17].

2.2.1.3 Buckling criterion

The critical load of the conical shell subjected to an axial compressive in-plane load can be obtained using Trefftz criterion as indicated in equation (2.17). The second variation of total potential energy of the conical shell ($\delta^2 V$) can be written as

$$\delta^2 V = \delta^2 U_1 + \delta^2 U_2 \tag{2.23}$$

$$\delta^2 U_1 = \iint_{x\theta} \left(\delta N_{xx}\delta\varepsilon_x^0 + \delta N_{\theta\theta}\delta\varepsilon_\theta^0 + \delta N_{x\theta}\delta\gamma_{x\theta}^0 + \delta M_{xx}\delta\acute{\varepsilon}_x + \delta M_{\theta\theta}\delta\acute{\varepsilon}_\theta + \delta M_{x\theta}\delta\acute{\gamma}_{x\theta} + \delta Q_\theta\delta\gamma_{xz}^0 + \delta Q_x\delta\gamma_{\theta z}^0\right) r d\theta dx$$

$$\delta^2 U_2 = -\iint_{x\theta} \left[\widehat{N}_{xx}\left(\delta\frac{\partial w}{\partial x}\right)^2 + \widehat{N}_{\theta\theta}\left(\frac{1}{\mathrm{r}}\delta\frac{\partial w}{\partial \theta}\right)^2 + \widehat{N}_{x\theta}\left(\frac{2}{r}\delta\left(\frac{\partial w}{\partial \theta}\right)\delta\left(\frac{\partial w}{\partial x}\right)\right)\right] r d\theta dx$$

The derivation of equation (2.23) is presented in Appendix A. As previously mentioned, in obtaining the second variation of total potential energy of the conical shell ($\delta^2 V$), a membrane prebuckling equilibrium state is assumed, i.e., the prebuckling rotations are neglected. The part

$\delta^2 U_2$ of the second variation of total potential energy is the contribution of external forces into internal energy that enters the buckling problem through the prebuckling equilibrium state, but do not appear explicitly in the expression for $\delta^2 V$ since $\delta^2 W = 0$. Timoshenko [69] refers to this part as ΔT and called it "the work done by external forces during buckling", while Jones [67] clearly disagrees with this interpretation because the second variation of the potential energy of external forces is zero ($\delta^2 W = 0$) (See Appendix A).

For the buckling of conical shells under axial load, $\widehat{N}_{\theta\theta}$ and $\widehat{N}_{x\theta}$ are zero in equation (2.25) and $\widehat{N}_{xx}$ is the in-plane compressive buckling force resultant that is defined as positive in compression for convenience. By integrating around the circumference of the cone, one can get the relation between the axial buckling load (P_{cr}) and in-plane compressive buckling force resultant ($\widehat{N}(x)$) as

$$\widehat{N}_{xx}(x) = \frac{P_{cr}}{2\pi\, cos(\alpha)\, r} \tag{2.24}$$

where α is the semi-cone angle and $r = xsin(\theta)$ is the radius of the cone that varies with length.

Recalling Trefftz criterion (equation (2.17)), the equations governing loss of stability of the conical shell subjected to compressive axial load can be written

$$\delta\left(\bar{\delta}^2 V\right) = \delta(\bar{\delta}^2 U_1 + \bar{\delta}^2 U_2) = 0 \tag{2.25}$$

in which the bars denote variations that are from prebuckled equilibrium state.

2.2.1.4 Ritz method

Ritz method is a powerful tool to determine approximate solutions of the stability equations (equation (2.25)). This method has an advantage of giving directly the solution from variational statement by bypassing the equilibrium equations [70].

The approximate solutions for the variation of the displacements are assumed in series form as

$$[\delta u(x,\theta), \delta v(x,\theta), \delta w(x,\theta), \delta\beta_x(x,\theta), \delta\beta_\theta(x,\theta)] = \sum_{i=1}^{m}\sum_{j=1}^{n}\left[\mathrm{C}_{ij}^{u}\Phi_{ij}^{u}, \mathrm{C}_{ij}^{v}\Phi_{ij}^{v}, \mathrm{C}_{ij}^{w}\Phi_{ij}^{w}, \mathrm{C}_{ij}^{\beta_x}\Phi_{ij}^{\beta_x}, \mathrm{C}_{ij}^{\beta_\theta}\Phi_{ij}^{\beta_\theta}\right] \tag{2.26}$$

where Φ_{ij}^{u}, Φ_{ij}^{v}, Φ_{ij}^{w}, $\Phi_{ij}^{\beta_x}$ and $\Phi_{ij}^{\beta_\theta}$ are approximation functions and they need to satisfy convergence and completeness requirements [70].

Considering equation (2.26) and using equations (2.20)-(2.24) and rewriting them in a matrix form, one can derive the first variation of the strain energy and work of the applied force by performing repeated integration by part as

$$\delta(\bar{\delta}^2 U_1) = 2\iint_{x\theta} \delta[C]^T[\Phi]^T[B]^T[F][B][\Phi][C] r d\theta dx \tag{2.27}$$

$$\delta(\bar{\delta}^2 U_2) = 2\iint_{x\theta} \delta[C]^T[\Phi]^T\left[\hat{B}\right][\Phi][C] r d\theta dx$$

in equation (2.27), $\delta[C]^T = [\delta c_{11}^u\ \delta c_{11}^v\ \delta c_{11}^w\ \delta c_{11}^{\beta_x}\ \delta c_{11}^{\beta_\theta}\ \ldots\ \delta c_{mn}^u\ \delta c_{mn}^v\ \delta c_{mn}^w\ \delta c_{mn}^{\beta_x}\ \delta c_{mn}^{\beta_\theta}]$, and $[\Phi]$, $[B]$, $[F]$and $\left[\hat{B}\right]$ matrices are defined in Appendix A. Substituting equation (2.27) into equation (2.25) and rearranging the matrices, one can get

$$2\delta[C]^T \left\{ \iint_{x\theta} \left([\Phi]^T \langle [B]^T [F] [B] + \left[\hat{B}\right] \rangle [\Phi] \right) r d\theta dx \right\} [C] = 0 \tag{2.28}$$

Since equation (2.28) is required to be satisfied for all possible values of the coefficient vector [C], it implies that the coefficient of variation of $\delta[C]^T$ must vanish as

$$[Z][C] = 0 \tag{2.29}$$

where

$$[Z] = \left\{ \iint_{x\theta} \left([\Phi]^T \langle [B]^T [F] [B] + \left[\hat{B}\right] \rangle [\Phi] \right) r d\theta dx \right\} \tag{2.30}$$

Equation (2.29) is an eigenvalue problem and the corresponding lowest eigenvalue is the critical axial buckling load. The buckling load is the existence of a nontrivial solution of equation (2.29) which means the determinant of matrix $[Z]$ must be vanished, that is

$$det|Z| = 0 \tag{2.31}$$

2.2.1.5 Axisymmetric problem

Up to this point, it was assumed that the buckling mode is not axisymmetric. In this section we will consider the axisymmteric mode in which δv, the variation of the displacements of mid-

surface in circumferential direction and $\delta\beta_\theta$, the variation of the rotations of a normal to the mid-surface about x axis are equated to zero. Also there is no dependence on θ. Consequently, the displacement field, equation (2.18), reduces to

$$\begin{aligned} \delta U(x,z) &= \delta u(x) + z\delta\beta_x(x) \\ \delta W(x,z) &= \delta w(x) \end{aligned} \tag{2.32}$$

and the strain-displacement relations, equation (2.20), get simplified accordingly as

$$\begin{aligned} \varepsilon_x &= \varepsilon_x^0 + z\acute{\varepsilon}_x \\ \varepsilon_\theta &= \varepsilon_\theta^0 + z\acute{\varepsilon}_\theta \\ \gamma_{xz} &= \gamma_{xz}^0 \end{aligned} \tag{2.33}$$

where

$$\begin{aligned} &\varepsilon_x^0 = \frac{du}{dx} && \varepsilon_\theta^0 = \frac{1}{x\sin(\alpha)}\big(usin(\alpha) + wcos(\alpha)\big) \\ &\acute{\varepsilon}_x = \frac{d\beta_x}{dx} && \acute{\varepsilon}_\theta = \frac{1}{x}(\theta_x) \qquad \gamma_{xz}^0 = \frac{dw}{dx} + \beta_x \end{aligned} \tag{2.34}$$

The force and moment resultants, equation (2.22), reduce to

$$\begin{Bmatrix} N_{xx} \\ N_{\theta\theta} \\ M_{xx} \\ M_{\theta\theta} \\ Q_x \end{Bmatrix} = \begin{bmatrix} A_{11} & A_{12} & B_{11} & B_{12} & 0 \\ A_{12} & A_{22} & B_{12} & B_{22} & 0 \\ B_{11} & B_{12} & D_{11} & D_{12} & 0 \\ B_{12} & B_{22} & D_{12} & D_{22} & 0 \\ 0 & 0 & 0 & 0 & K_s A_{55} \end{bmatrix} \begin{Bmatrix} \varepsilon_x^0 \\ \varepsilon_\theta^0 \\ \acute{\varepsilon}_x \\ \acute{\varepsilon}_\theta \\ \gamma_{xz}^0 \end{Bmatrix} \tag{2.35}$$

By applying the Trefftz criterion (equation (2.25)), equation similar to equation (2.28) will be obtained, which is not presented here for the sake of saving space. The definitions of the involved matrices are different from equation (2.28) and are presented for axisymmetric problem in Appendix A.

2.2.2 Solution

Following the Ritz method, the boundary conditions can be applied through the assumed displacement functions. These approximation functions must satisfy the essential boundary conditions and must be linearly independent and complete. In this study, it is assumed that the conical composite shells subjected to S2-type simply supported boundary condition ($\delta w = \delta M_{xx} = \delta \beta_\theta = \delta u = \delta N_{x\theta} = 0$) by seeking solutions of the form

$$\Phi_{ij}^{u} = \sin\left(i\pi \frac{x - x_t}{x_b - x_t}\right) cos(j\theta) \tag{2.36}$$

$$\Phi_{ij}^{v} = cos\left(i\pi \frac{x - x_t}{x_b - x_t}\right) sin(j\theta)$$

$$\Phi_{ij}^{w} = \sin\left(i\pi \frac{x - x_t}{x_b - x_t}\right) sin(j\theta)$$

$$\Phi_{ij}^{\beta_x} = cos\left(i\pi \frac{x - x_t}{x_b - x_t}\right) sin(j\theta)$$

$$\Phi_{ij}^{\beta_\theta} = \sin\left(i\pi \frac{x - x_t}{x_b - x_t}\right) cos(j\theta)$$

where x_t and x_b are the top and bottom coordinates of the cone shown in Figure 2.2.

For axisymmetric buckling problem the approximation functions are only function of axial coordinate x and therefore get the form of

$$\Phi_i^u = \sin\left(i\pi \frac{x - x_t}{x_b - x_t}\right) \tag{2.37}$$

$$\Phi_i^w = \sin\left(i\pi \frac{x - x_t}{x_b - x_t}\right)$$

$$\Phi_i^{\beta_x} = cos\left(i\pi \frac{x - x_t}{x_b - x_t}\right)$$

The buckling load for each conical shell configuration (different geometry or layup sequence) is obtained by solving equation (2.31) to find the minimum value of P_{cr}. This procedure should be repeated based on the axisymmetric assumption as well and finally whichever value of P_{cr} that is the lowest would be selected as the critical axial buckling load.

2.2.3 Validation

Analytical solution for buckling loads of cross-ply circular cylindrical shells under axial load was presented by Khdeir et al. [17] and Shadmehri et al. [71]. Since exact solution is available for cross-ply cylindrical shells, it is selected for validation purposes. In order to verify with a composite cylindrical shell, the cone angle is set to zero. The approximation functions are selected to satisfy the simply-supported and clamped boundary conditions defined in [17] and [71] and material properties and geometric specifications are set accordingly (see [17] and [71] for details). The critical buckling loads for two different cases are compared with references [17] and [71] and shown in Table 2.1. It is assumed that the total thickness (H) of the shell is the same for different laminations, which implies that the thickness of a ply is different in laminates with different number of layers.

Table 2.1: Validation of dimensionless critical buckling load of cross-ply cylindrical shell($\bar{N} = \frac{\hat{N}_{xx}L^2}{100h^3E_{22}}, \frac{R}{H} = 10, \frac{R}{L} = 1$)*

Lamination	SS			CC		
	Present work	**Ref.** [71]	**Ref.** [17]	**Present work**	**Ref.** [71]	**Ref.** [17]
0/90/0	0.2765	0.2765	0.2813	0.4168	0.4168	0.4197
0/90	0.1525	0.1525	0.1670	0.2406	0.2406	0.2508

*** R: cylinder radius, L: cylinder length, H: total thickness of the cylinder**

2.2.4 Numerical results

In order to evaluate the effect of semi-cone angle, fiber orientation, length-to-radius ratio, and radius-to-thickness ratio on the critical buckling load of the conical composite shells, typical properties of graphite-epoxy material are assumed as shown in Table 2.2.

Table 2.2: Material properties of conical shell for buckling analysis

Material properties
$E_{11} = 3.05 \times 10^7\ psi = 210.29\ GPa$
$E_{22} = E_{33} = E_1/40$
$G_{12} = G_{13} = 0.6E_{22}$
$G_{23} = 0.5E_{22}$
$\nu_{12} = 0.25$

2.2.4.1 Effect of fiber orientation on critical buckling load

A set of conical shells with the radius-to-thickness ratio of 100 ($R_b/H = 100$) and radius-to-length ratio of 10 ($R_b/L = 10$) are assumed. The dimensionless critical axial buckling load is defined as

$$\bar{P}_{cr} = \frac{P_{cr} L^2}{H^3 E_{22} 2\pi \cos(\alpha)\, R_b} \tag{2.38}$$

where P_{cr} is the critical axial buckling load, E_{22} is elastic modulus perpendicular to fiber direction, H is the total thickness of the laminate, α is semi-cone angle, R_b is the base radius and L is the length of the conical shell shown in Figure 2.2.

The critical axial buckling load is obtained by calculating non-axisymmetric and axisymmetric buckling loads and selecting the lowest value.

Effect of fiber orientation on critical buckling load of conical shells for four different semi-cone angles are shown in Figure 2.3 and Figure 2.4. The angle-ply laminated conical shells with $[+\theta/-\theta]$ layup are considered for analysis. Fiber orientation θ is defined with respect to x axis (Figure 2.2) and alternates between 0 and 90 degree.

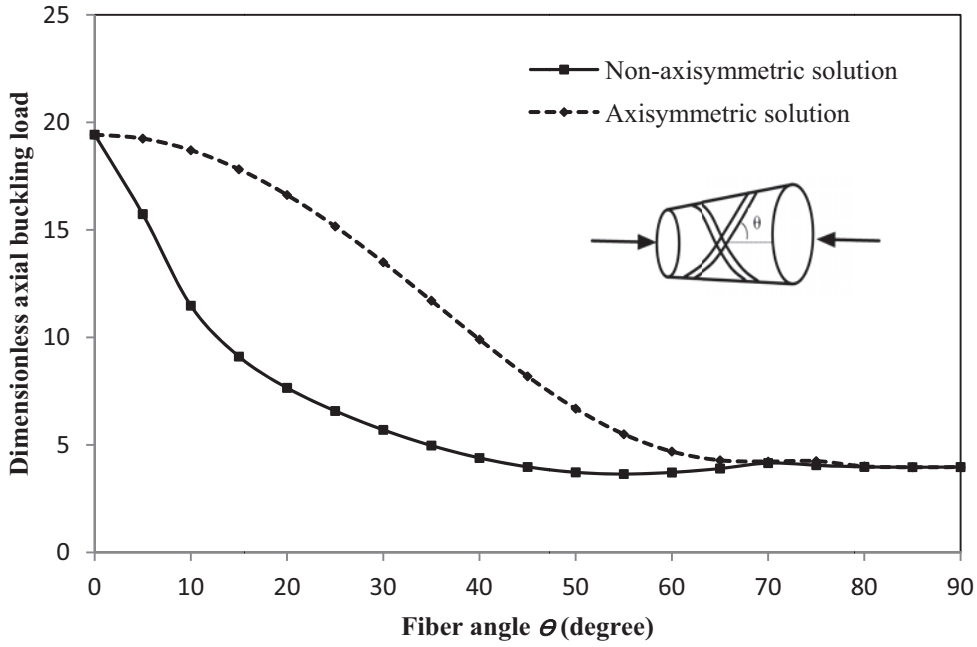

Figure 2.3: Axisymmetric and non-axisymmetric dimensionless axial buckling load versus fiber angle (θ) for α=10°, R_b/H=100 and R_b/L=10

For comparison purposes, the axisymmetric and non-axisymmetric buckling loads are plotted in Figure 2.3 for semi-cone angle $\alpha=10^{\circ}$. It can be seen that non-axisymmteric buckling load is less than the axisymmteric one for all fiber angles except at 0 and from 85 to 90 degrees where both axisymmetric and non-axisymmetric buckling loads are almost the same. So one can say that non-axisymetric buckling load is representative of critical buckling load in this case. This trend is the same for other angle-ply cones with the same $R_b/H=100$ and $R_b/L=10$ ratios and different semi-cone angle and the results are shown in Figure 2.4.

The curves shown in Figure 2.4 indicate a rapid drop in the buckling load of angle-ply conical shells as the fiber angle (θ) varies from 0 degree up to 45 degree (about 77% reduction). Then one can observe a relatively constant region where θ alternates between 45 and 90 degree with a

minimum around 55 and maximum around 70 degrees. Also, as can be expected from the results of previous section, it is clear from Figure 2.4 that increasing the semi-cone angle α has detrimental effect on critical buckling load.

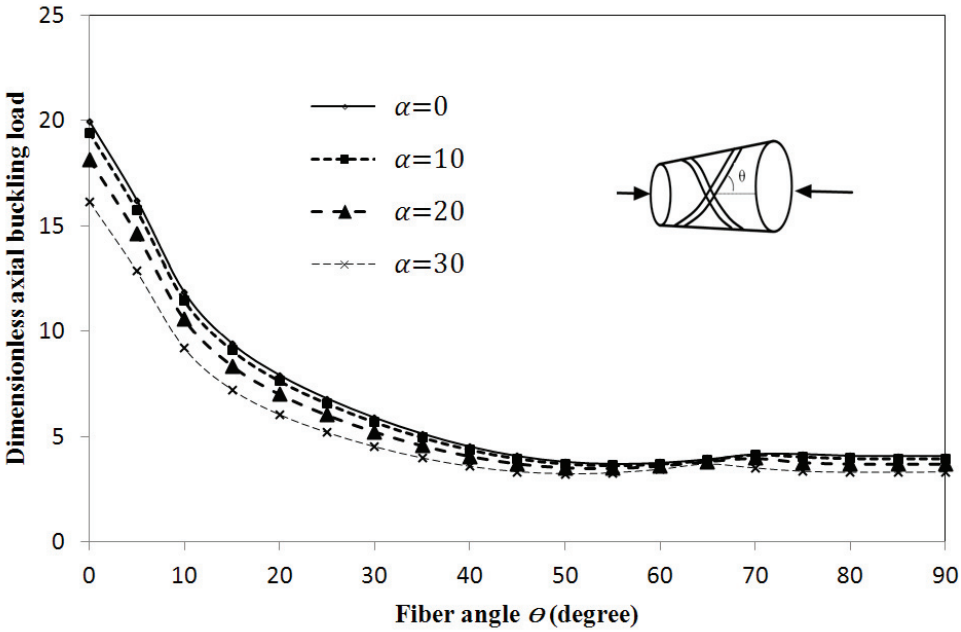

Figure 2.4: Dimensionless axial buckling load versus fiber angle (θ), R_b/H=100 and R_b/L=10

2.2.4.2 Effect of semi-cone angle on critical buckling load

Effect of semi-cone angle α on critical buckling load of conical shells with geometrical specification of R_b/H=100, R_b/L=10 is shown in Figure 2.5. The base radius (R_b) is kept constant while the semi-cone angle (α) varies from 0 to 44 deg to evaluate the effect of α on dimensionless critical axial buckling load. Three layups (two cross-ply layups and one quasi-isotropic layup) are studied and results are shown in Figure 2.5. It was found that for all three layups the axisymmetric buckling loads are always lower than the non-axisymmetric ones. For

[0/90] the difference is about 17% while for [0/90/0] and $[0/+45/-45/90]_s$ the difference is about 0.5%.

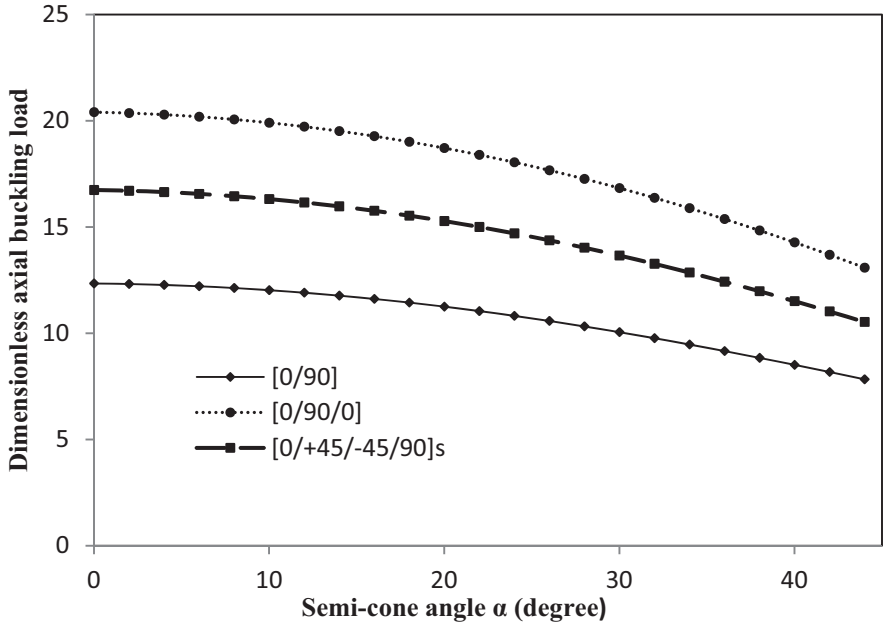

Figure 2.5: Dimensionless axial buckling load ($\bar{P}_{cr}$) versus semi-cone angle (α)

As can be seen from Figure 2.5 the critical buckling load decreases as the semi-cone angle (α) increases for all three layups. This decrease is not at constant rate. While in the range of α between 0 and 20 degree the reduction in critical buckling load is not considerable (about 7%), after α exceeds 20 degree the reduction in critical buckling load is considerable (about 33% from initial value at $\alpha = 0$). The reduction in buckling strength can be attributed to the change in the geometry of the conical shells. As α increases the radius of the small end of the conical shell gets smaller and consequently the critical buckling load decreases. From layup sequence point of

view, [0/90/0] layup has the highest critical buckling load for all α values, offering that 0 degree layers laid at the outer skin of the conical shells provide more stiffness than other two layups.

2.2.5 Conclusions

Buckling analysis of laminated conical shells under axial compression load has been performed through a shear deformation shell theory. The principle of minimum potential energy along with the Ritz method has been used to obtain the governing equation and to find the solution for buckling problem. Both non-axisymmetric and axisymmetric formulations have been derived and solved for each laminated conical shell and the lowest buckling load has been nominated as critical buckling load. The following conclusion can be drawn from parametric studies presented in the numerical results:

For thin and short conical shells considered in this study the critical buckling load decreases with increasing semi-cone angle. The reduction in critical buckling load becomes more pronounced as the semi-cone angle exceeds 20 degree. This can be important from design point of view. The critical buckling load decreases with increasing fiber orientation of angle-ply thin and short conical shells.

2.3 Buckling under bending

2.3.1 Formulation

In order to obtain the critical buckling load under bending, the distribution of in-plane axial force resultant within the cross section of the cone prior to the buckling is assumed as

$$N_b(x,\theta) = \widehat{N}_{xx}(x)\sin(\theta) \tag{2.39}$$

By integrating around the circumference of the cone, one can get the relation between the critical buckling moment ($\mathrm{M_{cr}}$) and in-plane compressive force resultant ($\widehat{N}_{xx}(x)$) as

$$\widehat{N}_{xx}(x) = \frac{\mathrm{M_{cr}}}{\pi\cos(\alpha)\,r^2} \tag{2.40}$$

where α is the semi-cone angle and $r = xsin(\theta)$ is the radius of the cone that varies by length. Considering equations (2.39) and (2.40), the term $\delta^2 U_2$ in expression for second variation of total potential energy (equation (2.23)) can be written as

$$\delta^2 U_2 = -\iint_{x\theta} \frac{\mathrm{M_{cr}}}{\pi\cos(\alpha)\,r^2}\sin(\theta)\left(\delta\frac{\partial w}{\partial x}\right)^2 r\,d\theta\,dx \tag{2.41}$$

Using the Trefftz buckling criterion, equation (2.25) can be used to derive the stability equations of the conical shell subjected to critical buckling moment. The Ritz method as explained in section 2.2.1.4 is used to obtain the critical buckling moment. The approximation solutions for the variation of the displacements are assumed in series from, equation (2.26), and the same procedure mentioned in section 2.2.1.4 is followed to obtain the stability equation as

$$[Z][C] = 0 \tag{2.42}$$

where

$$[Z] = \left\{ \iint_{x\theta} \left([\Phi]^T \langle [B]^T [F][B] + \left[\hat{B}_{bend}\right] \rangle [\Phi] \right) r d\theta dx \right\} \tag{2.43}$$

where $[\Phi], [B], [F]$ and $[\hat{B}_{bend}]$ are defined in Appendix A. The critical buckling moment is the lowest eigenvalue of equation (2.42) and can be determined by setting the determinant of $[Z]$ equal to zero.

2.3.2 Solution

According to the Ritz method, the assumed displacement functions must satisfy the essential boundary conditions and must be linearly independent and complete as well. Here, simply supported ($\delta w = \delta M_{xx} = \delta \beta_\theta = \delta N_{xx} = \delta v = 0$, S3-type) conical shells are considered for study which the displacement functions are given by the following equation

$$\Phi_{ij}^{u} = cos\left(i\pi \frac{x - x_t}{x_b - x_t} \right) cos(j\theta) \tag{2.44}$$

$$\Phi_{ij}^{v} = sin\left(i\pi \frac{x - x_t}{x_b - x_t} \right) sin(j\theta)$$

$$\Phi_{ij}^{w} = \sin\left(i\pi \frac{x - x_t}{x_b - x_t} \right) cos(j\theta)$$

$$\Phi_{ij}^{\beta_x} = cos\left(i\pi \frac{x - x_t}{x_b - x_t} \right) cos(j\theta)$$

$$\Phi_{ij}^{\beta_\theta} = \sin\left(i\pi \frac{x - x_t}{x_b - x_t} \right) sin(j\theta)$$

Since the loading is not axisymmetric, there is no need to consider the axisymmetric problem for buckling under bending of composite conical shells.

2.3.3 Numerical results

In order to evaluate the effect of semi-cone angle, fiber orientation and length-to-radius ratio on the critical buckling moment of the conical composite shells, typical properties of graphite-epoxy material are assumed and tabulated in Table 2.2. It is assumed that the total thickness (H) of the shell is the same for different laminations, which implies that the thickness of a ply is different in laminates with different number of layers.

In order to present the numerical results, the following dimensionless critical buckling moment is presented

$$\bar{M}_{cr} = \frac{M_{cr} L^2}{H^3 E_{22} \pi R_b^2 cos(\alpha)} \tag{2.45}$$

where M_{cr} is the critical buckling moment.

2.3.3.1 Effect of semi-cone angle on critical buckling moment

A set of conical shells with the radius-to-thickness ratio of 100 ($R_b/H = 100$) are assumed to study the effect of semi-cone angle varying from 5 to 40 degree on the dimensionless critical buckling moment. The base radius (R_b) is kept constant. Figure 2.6 shows the results for three layup sequences including two cross-ply laminates (one symmetric and one non-symmetric) and one quasi-isotropic laminate. As can be seen, the dimensionless critical buckling moment decreases as the semi-cone angle (α) increases. Since the R_b and L are kept constant, as the α

increases, the top radius (R_t) of the cone decreases which consequently means less stiffness at the small end of the cone. This is the reason for the decrease in buckling strength as illustrated by Figure 2.6.

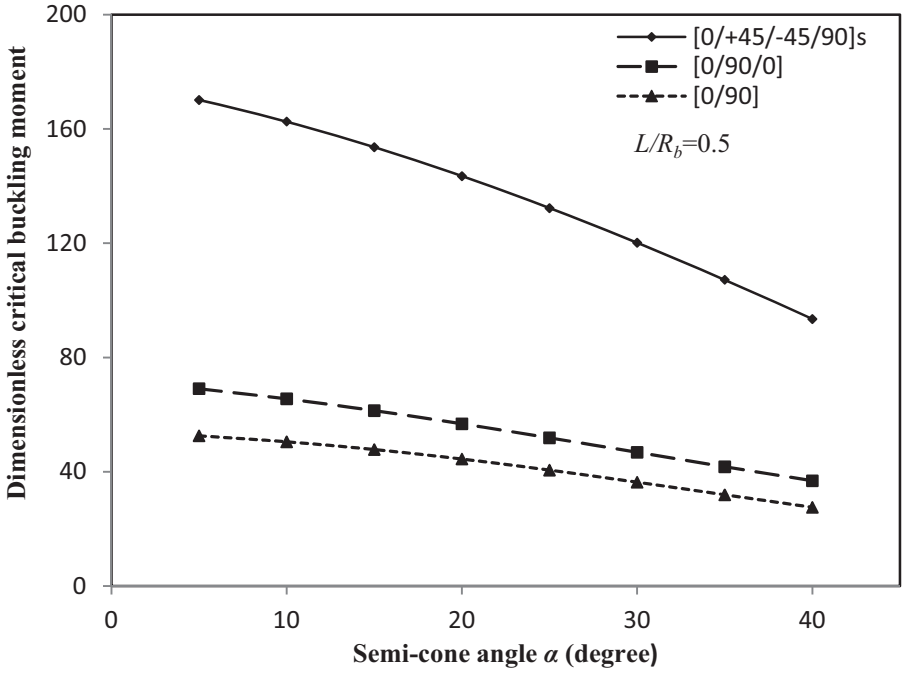

Figure 2.6: Dimensionless buckling moment vs. semi-cone angle for different layups

Also, one can see form Figure 2.6 that the cones with $[0/+45/-45/90]_s$ layup have critical buckling moment about three times more than cones with cross-ply layups which can be associated with 45 degree layers that provide both axial and circumferential strength to the cone.

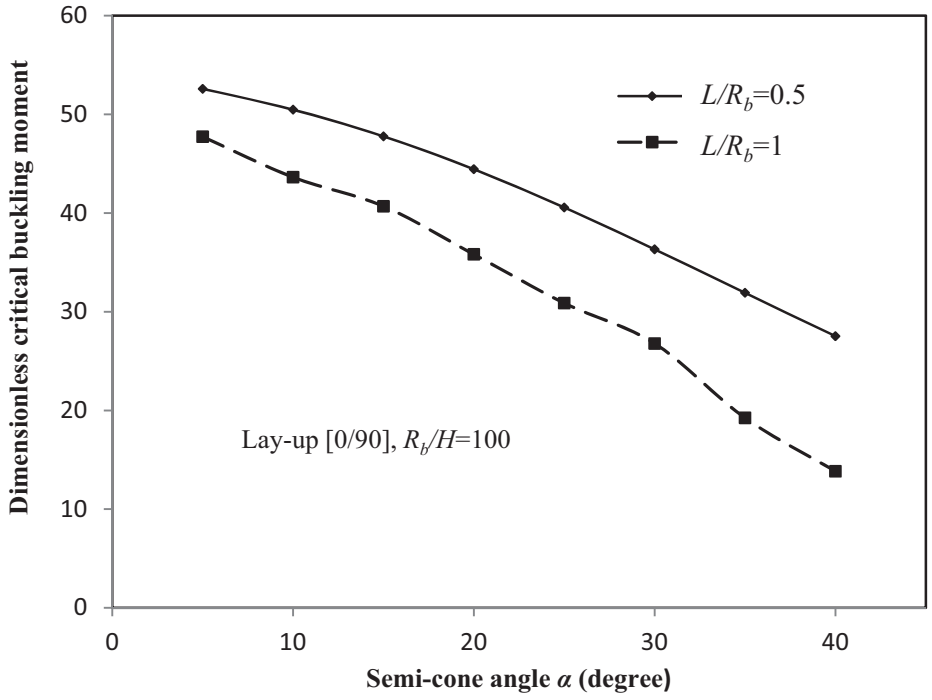

Figure 2.7: Dimensionless buckling moment vs. semi-cone angle for different length-to-radius ratios

Figure 2.7 shows the effect of length-to-radius ratio and semi-cone angle on the dimensionless critical buckling moment. As one could expect, the critical buckling moment for all semi-cone angles (from 5 to 40 degrees) for L/R_b=0.5 is more than for L/R_b=1. As the semi-cone angle increases, the difference between two curves gets pronounced.

2.3.3.2 Effect of fiber orientation on critical buckling moment

The effect of fiber orientation on the dimensionless critical buckling moment of composite cones with two different semi-cone angles and two length-to-radius ratios are presented in Figure 2.8 and Figure 2.9, respectively. It is assumed that all cones have antisymmetric angle-ply layup of $[+\theta/-\theta]$ and the radius-to-thickness ratio of 100 ($R_b/H = 100$). As can be seen from Figure 2.8, the dimensionless critical buckling moment increases steeply where the fiber angle varies

from 0 to 15 degrees. From 15 to 75 degrees, the dimensionless critical buckling moment has a very moderate decreasing trend by about 7% and 8.5% for cones with semi-cone angle of 10 and 20 degree, respectively. When fiber angle exceeds 75 degrees, there can be seen a steep decrease in the buckling moment until fiber angle reaches 90 degree. The results came from Figure 2.8 is quite interesting because, although the layup with all the fiber oriented at 0 degree (along the axial direction) has the maximum axial stiffness, it is not the best from buckling under bending point of view. For example for cones with $\alpha = 10^{o}$, the maximum critical buckling moment is achieved when the fibers are oriented at 15 degree (for $[+15/-15]$ layup). The possible explanation for this behavior could be the circumferential support that is created as the fiber angles varies from 0 degree. In other words, when fibers are placed at 15 degree, for example, they provide circumferential stiffness to some extent that can reduce the effective buckling length, the concept which is popular in buckling of beams.

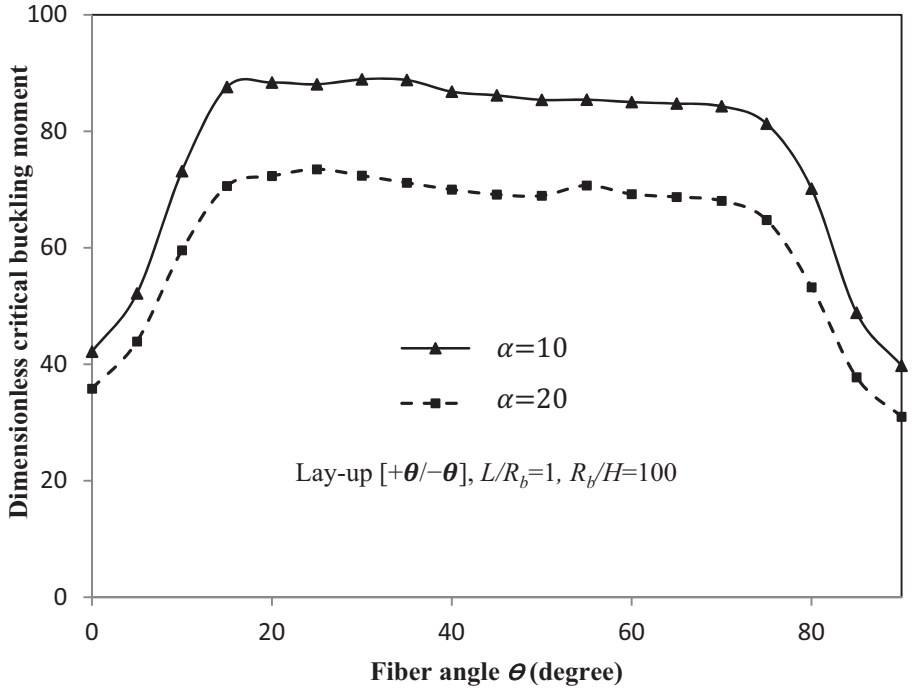

Figure 2.8: Dimensionless buckling moment vs. fiber angle for different semi-cone angle

Figure 2.9 shows the dimensionless critical buckling moment for two different length-to-radius ratios. Similar behavior seen in Figure 2.8 can be seen here too except that for $L/R_b = 0.5$, the maximum buckling moment happens at $\theta = 25^{\circ}$. At this point a distinctive peak can be seen while there is not such a peak for the curve of $L/R_b = 1$. The general trend is predictable that as the length-to-radius ratio decreases, the buckling load increases.

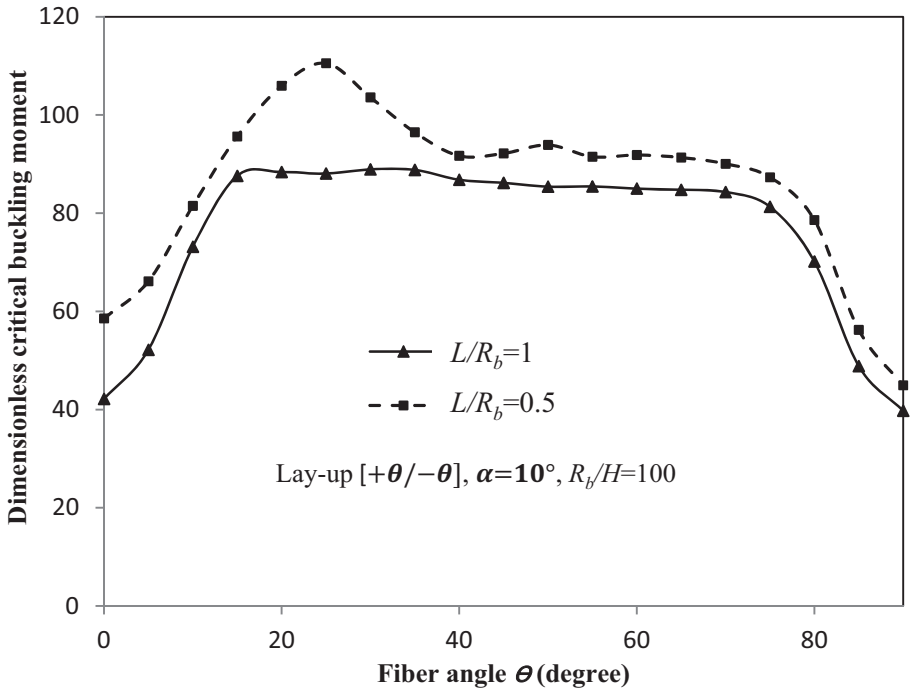

Figure 2.9: Dimensionless buckling moment vs. fiber angle for different length-to-radius ratios

2.3.4 Conclusions

A first order shear deformation shell theory has been employed to find the buckling of laminated conical shells under pure bending. The Ritz method has been used to obtain the solution for simply supported composite conical shells. The following conclusion can be drawn from parametric studies presented in the numerical results:

For thin and short conical shells considered in this study, the critical buckling moment decreases as the semi-cone angle increases. Both layup and the length-to-radius ratio have significant effect on the dimension less buckling moment.

For antisymmetric angle-ply cones, the dimensionless critical buckling moment depends significantly on the fiber angle in two intervals, namely $0^o < \theta < 15^o$ and $75^o < \theta < 90^o$ while

it changes moderately when $15^{o} < \theta < 75^{o}$. Both semi-cone angle and the length-to-radius ratio have considerable effect on the dimensionless buckling moment.

2.4 Bending analysis of cross-ply laminated conical shells[2]

An analytical solution is considered in this section to investigate the bending behavior of cross-ply laminated conical shells. The governing equations are derived from principle of minimum (stationary) potential energy. Assuming Levy-type solution, the governing equations are then converted to ordinary differential equations and changed to state-space form introducing ten unknown variables. The new first-order ordinary differential equation system is solved for displacements using numeric technique. As a loading case, a distributed sinusoidal transverse load is applied. Different lamination sequences including symmetric and asymmetric laminate are studied and compared. The effect of cone angle, various boundary conditions (i.e. clamped, simply supported and free edge), radius-to-thickness and length-to-thickness ratio on the displacement of mid surface is investigated.

2.4.1 Formulation

2.4.1.1 Kinematics

The coordinate system associated with conical shell is shown in Figure 2.2. Based on the shear deformation shell theory assumption, the displacement field is assumed as stated in equation (2.18). The linear strain-displacement relations for conical shell are assumed as shown in equation (2.20).

[2] The content of section 2.4 has been published in [101].

2.4.1.2 Equilibrium equations

The governing equations of the motion of conical shell are derived using principle of minimum (stationary) potential energy on account of its simplicity and due to the fact that it gives the natural boundary conditions of the problem as well. Principle of minimum (stationary) potential energy, as stated in equation (2.4) as well, can be written as [66]

$$\delta(U - W_s - W_{e1} - W_{e2}) = 0 \tag{2.46}$$

in which U represents the strain energy, while W_s is the work of the body and surface forces and W_{e1} and W_{e2} are the work done by the edge stresses. These parameters are defined as [66]

$$\delta U = \int_\theta \int_x \int_z (\sigma_{xx}\delta\varepsilon_x + \sigma_{\theta\theta}\delta\varepsilon_\theta + \tau_{x\theta}\delta\gamma_{x\theta} + \tau_{xz}\delta\gamma_{xz} + \tau_{\theta z}\delta\gamma_{\theta z})\, r d\theta dx dz \tag{2.47}$$

$$\delta W_s = \int_\theta \int_x (q_x\delta u + q_\theta\delta v - q_z\delta w)\, r d\theta dx$$

$$\delta W_{e1} = \int_\theta \int_z (\bar{\sigma}_{xx}\delta u + \bar{\tau}_{x\theta}\delta v + \bar{\tau}_{xz}\delta w)\, r d\theta dz$$

$$\delta W_{e2} = \int_x \int_z (\bar{\sigma}_{\theta\theta}\delta v + \bar{\tau}_{\theta x}\delta u + \bar{\tau}_{\theta z}\delta w)\, dx dz$$

here (q_x, q_θ, q_z) are the static equivalents of the surface and body loads which are applied to the upper and lower surface of the shell and considered to be applied on the mid-surface of the shell. $\bar{\sigma}_{xx}$, $\bar{\sigma}_{\theta\theta}$, $\bar{\tau}_{x\theta}$, $\bar{\tau}_{xz}$, and $\bar{\tau}_{\theta z}$ are the edge stresses.

Substituting the displacement field, equation (2.18), into equations (2.47) and equations (2.47) into equation (2.46), and integrating over the thickness of the shell and vanishing the coefficient of variations, one can get the five equations of motion for conical shell as

$$\frac{\partial N_{xx}}{\partial x}+\frac{1}{x}N_{xx}+\frac{1}{xsin(\alpha)}\frac{\partial N_{x\theta}}{\partial \theta}-\frac{1}{x}N_{\theta\theta}+q_x=0 \tag{2.48}$$

$$\frac{\partial N_{x\theta}}{\partial x}+2\frac{1}{x}N_{x\theta}+\frac{1}{xsin(\alpha)}\frac{\partial N_{\theta\theta}}{\partial \theta}+\frac{1}{xtan(\alpha)}Q_{\theta\theta}+q_\theta=0$$

$$\frac{\partial Q_{xx}}{\partial x}+\frac{1}{xsin(\alpha)}\frac{\partial Q_{\theta\theta}}{\partial \theta}-\frac{1}{xtan(\alpha)}N_{\theta\theta}-q_z=0$$

$$\frac{\partial M_{xx}}{\partial x}+\frac{1}{x}M_{xx}+\frac{1}{xsin(\alpha)}\frac{\partial M_{x\theta}}{\partial \theta}-\frac{1}{x}M_{\theta\theta}-Q_{xx}=0$$

$$\frac{1}{xsin(\alpha)}\frac{\partial M_{\theta\theta}}{\partial \theta}+\frac{\partial M_{x\theta}}{\partial x}+\frac{2}{x}M_{x\theta}-Q_{\theta\theta}=0$$

where

$$\begin{Bmatrix}N_{xx}\\N_{x\theta}\\Q_{xx}\end{Bmatrix}=\int_z\begin{Bmatrix}\sigma_{xx}\\\tau_{x\theta}\\\tau_{xz}\end{Bmatrix}dz \qquad \begin{Bmatrix}N_{\theta\theta}\\N_{\theta x}\\Q_{\theta\theta}\end{Bmatrix}=\int_z\begin{Bmatrix}\sigma_{\theta\theta}\\\tau_{\theta x}\\\tau_{\theta z}\end{Bmatrix}dz \tag{2.49}$$

$$\begin{Bmatrix}M_{xx}\\M_{x\theta}\end{Bmatrix}=\int_z\begin{Bmatrix}\sigma_{xx}\\\tau_{x\theta}\end{Bmatrix}zdz \qquad \begin{Bmatrix}M_{\theta\theta}\\M_{\theta x}\end{Bmatrix}=\int_z\begin{Bmatrix}\sigma_{\theta\theta}\\\tau_{\theta x}\end{Bmatrix}zdz$$

2.4.1.3 Governing equations for cross-ply laminated conical shells

In order to find a Levy type solution for cross-ply laminated conical shell, the governing equations, equations (2.48), may be written in terms of displacement variables. For cross-ply laminate, the constitutive relations have the form of [68]

$$\begin{Bmatrix} N_{xx} \\ N_{\theta\theta} \\ N_{x\theta} \\ M_{xx} \\ M_{\theta\theta} \\ M_{x\theta} \end{Bmatrix} = \begin{bmatrix} A_{11} & A_{12} & 0 & B_{11} & B_{12} & 0 \\ A_{12} & A_{22} & 0 & B_{12} & B_{22} & 0 \\ 0 & 0 & A_{66} & 0 & 0 & B_{66} \\ B_{11} & B_{12} & 0 & D_{11} & D_{12} & 0 \\ B_{12} & B_{22} & 0 & D_{12} & D_{22} & 0 \\ 0 & 0 & B_{66} & 0 & 0 & D_{66} \end{bmatrix} \begin{Bmatrix} \varepsilon_x^0 \\ \varepsilon_\theta^0 \\ \gamma_{x\theta}^0 \\ \varepsilon_x^{'} \\ \varepsilon_\theta^{'} \\ \gamma_{x\theta}^{'} \end{Bmatrix} \tag{2.50}$$

$$\begin{Bmatrix} Q_{\theta\theta} \\ Q_{xx} \end{Bmatrix} = K_s \begin{bmatrix} A_{44} & 0 \\ 0 & A_{55} \end{bmatrix} \begin{Bmatrix} \gamma_{\theta z}^0 \\ \gamma_{xz}^0 \end{Bmatrix}$$

K_s is shear correction factor and taken to be 5/6 for numerical results [17]. Substituting equation (2.20) into equations (2.50), the force and moment resultant can be written in terms of displacement variable, namely $u(x,\theta), v(x,\theta), w(x,\theta), \beta_x(x,\theta)$ and $\beta_\theta(x,\theta)$. Now if one substitutes these relations into equations (2.48), the governing equations for cross-ply laminated conical shell obtained in terms of displacement variables as

$$\begin{aligned} & A_{11}\left(\frac{\sin(\alpha)}{r}\frac{\partial u}{\partial x}+\frac{\partial^2 u}{\partial x^2}\right)+A_{12}\left(\frac{1}{r}\frac{\partial^2 v}{\partial x\,\partial\theta}+\frac{\cos(\alpha)}{r}\frac{\partial w}{\partial x}\right)+A_{16}\left(\frac{\partial^2 v}{\partial x^2}+\frac{2}{r}\frac{\partial^2 u}{\partial x\,\partial\theta}+\frac{\cos(\alpha)}{r}\frac{\partial w}{\partial x}\right) \\ & +A_{22}\left(-\frac{\sin(\alpha)}{r^2}\frac{\partial v}{\partial\theta}\frac{\partial^2 v}{\partial x^2}-\left(\frac{\sin(\alpha)}{r}\right)^2 u-\frac{\sin(\alpha)\cos(\alpha)}{r^2}w\right) \\ & +A_{26}\left(-\frac{\sin(\alpha)}{r}\frac{\partial v}{\partial x}+\left(\frac{\sin(\alpha)}{r}\right)^2 v+\frac{1}{r^2}\frac{\partial^2 v}{\partial\theta^2}\right) \\ & +A_{66}\left(\frac{1}{r}\frac{\partial^2 v}{\partial x\,\partial\theta}-\frac{\sin(\alpha)}{r^2}\frac{\partial v}{\partial\theta}+\frac{1}{r^2}\frac{\partial^2 u}{\partial\theta^2}\right)+B_{11}\left(\frac{\sin(\alpha)}{r}\frac{\partial\beta_x}{\partial x}+\frac{\partial^2\beta_x}{\partial x^2}\right) \\ & +B_{12}\left(\frac{1}{r}\frac{\partial^2\beta_\theta}{\partial x\,\partial\theta}\right)+B_{16}\left(\frac{2}{r}\frac{\partial^2\beta_x}{\partial x\,\partial\theta}+\frac{\partial^2\beta_\theta}{\partial x^2}\right) \\ & +B_{22}\left(-\frac{\sin(\alpha)}{r^2}\frac{\partial\beta_\theta}{\partial\theta}-\left(\frac{\sin(\alpha)}{r}\right)^2\beta_x\right) \\ & +B_{26}\left(\frac{1}{r^2}\frac{\partial^2\beta_\theta}{\partial\theta^2}-\frac{\sin(\alpha)}{r}\frac{\partial\beta_\theta}{\partial x}+\left(\frac{\sin(\alpha)}{r}\right)^2\beta_\theta\right) \\ & +B_{66}\left(\frac{1}{r}\frac{\partial^2\beta_\theta}{\partial x\,\partial\theta}+\frac{1}{r^2}\frac{\partial^2\beta_x}{\partial\theta^2}-\frac{\sin(\alpha)}{r^2}\frac{\partial\beta_\theta}{\partial\theta}\right)+q_x=0 \end{aligned} \tag{2.51}$$

$$A_{12}\left(\frac{1}{r}\frac{\partial^2 u}{\partial x\,\partial\theta}\right)+A_{16}\left(\frac{\partial^2 u}{\partial x^2}+\frac{2\sin(\alpha)}{r}\frac{\partial u}{\partial x}\right)+A_{22}\left(\frac{1}{r^2}\frac{\partial^2 v}{\partial\theta^2}+\frac{\sin(\alpha)}{r^2}\frac{\partial u}{\partial\theta}+\frac{\cos(\alpha)}{r^2}\frac{\partial w}{\partial\theta}\right)$$
$$+A_{26}\left(\left(\frac{\sin(\alpha)}{r}\right)^2 u+\frac{\sin(\alpha)\cos(\alpha)}{r^2}w+\frac{2}{r}\frac{\partial^2 v}{\partial x\,\partial\theta}+\frac{\sin(\alpha)}{r}\frac{\partial u}{\partial x}+\frac{\cos(\alpha)}{r}\frac{\partial w}{\partial x}\right.$$
$$\left.+\frac{1}{r^2}\frac{\partial^2 u}{\partial\theta^2}\right)+A_{66}\left(\frac{\sin(\alpha)}{r}\frac{\partial v}{\partial x}-\left(\frac{\sin(\alpha)}{r}\right)^2 v+\frac{\sin(\alpha)}{r^2}\frac{\partial u}{\partial\theta}+\frac{\partial^2 v}{\partial x^2}+\frac{1}{r}\frac{\partial^2 u}{\partial x\,\partial\theta}\right)$$
$$+A_{44}\left(\frac{\cos(\alpha)}{r^2}\frac{\partial w}{\partial\theta}-\left(\frac{\cos(\alpha)}{r}\right)^2 v+\frac{\cos(\alpha)}{r}\beta_\theta\right)$$
$$+A_{45}\left(\frac{\cos(\alpha)}{r}\frac{\partial w}{\partial x}+\frac{\cos(\alpha)}{r}\beta_x\right)+B_{12}\left(\frac{1}{r}\frac{\partial^2\beta_x}{\partial x\,\partial\theta}\right)$$
$$+B_{16}\left(\frac{\partial^2\beta_x}{\partial x^2}+\frac{2\sin(\alpha)}{r}\frac{\partial\beta_\theta}{\partial x}\right)+B_{22}\left(\frac{1}{r^2}\frac{\partial^2\beta_\theta}{\partial\theta^2}+\frac{\sin(\alpha)}{r^2}\frac{\partial\beta_x}{\partial\theta}\right)$$
$$+B_{26}\left(\left(\frac{\sin(\alpha)}{r}\right)^2\beta_x+\frac{2}{r}\frac{\partial^2\beta_\theta}{\partial x\,\partial\theta}+\frac{\sin(\alpha)}{r}\frac{\partial\beta_\theta}{\partial x}+\frac{1}{r^2}\frac{\partial^2\beta_x}{\partial\theta^2}\right)$$
$$+B_{66}\left(\frac{\sin(\alpha)}{r}\frac{\partial\beta_\theta}{\partial x}+\frac{\sin(\alpha)}{r^2}\frac{\partial\beta_x}{\partial\theta}-\left(\frac{\sin(\alpha)}{r}\right)^2\beta_\theta+\frac{\partial^2\beta_\theta}{\partial x^2}+\frac{1}{r}\frac{\partial^2\beta_x}{\partial x\,\partial\theta}\right)+q_\theta$$
$$=0 \tag{2.52}$$

$$A_{12}\left(-\frac{\cos(\alpha)}{r}\frac{\partial u}{\partial x}\right)+A_{26}\left(-\frac{\cos(\alpha)}{r}\frac{\partial v}{\partial x}+\frac{\sin(\alpha)\cos(\alpha)}{r^2}v-\frac{\cos(\alpha)}{r^2}\frac{\partial u}{\partial\theta}\right)$$
$$+A_{22}\left(-\frac{\cos(\alpha)}{r^2}\frac{\partial v}{\partial\theta}-\frac{\sin(\alpha)\cos(\alpha)}{r^2}u-\left(\frac{\cos(\alpha)}{r}\right)^2 w\right)$$
$$+A_{44}\left(\frac{1}{r^2}\frac{\partial^2 w}{\partial\theta^2}-\frac{\cos(\alpha)}{r^2}\frac{\partial v}{\partial\theta}+\frac{1}{r}\frac{\partial\beta_\theta}{\partial\theta}\right)$$
$$+A_{45}\left(\frac{2}{r}\frac{\partial^2 w}{\partial x\,\partial\theta}+\frac{1}{r}\frac{\partial\beta_x}{\partial\theta}-\frac{\sin(\alpha)}{r^2}\frac{\partial w}{\partial\theta}-\frac{\cos(\alpha)}{r}\frac{\partial v}{\partial x}+\frac{\sin(\alpha)\cos(\alpha)}{r^2}v\right.$$
$$\left.+\frac{\partial\beta_\theta}{\partial x}\right)+A_{55}\left(\frac{\partial^2 w}{\partial x^2}+\frac{\partial\beta_x}{\partial x}\right)+B_{12}\left(-\frac{\cos(\alpha)}{r}\frac{\partial\beta_x}{\partial x}\right)$$
$$+B_{22}\left(-\frac{\cos(\alpha)}{r^2}\frac{\partial\beta_\theta}{\partial\theta}-\frac{\sin(\alpha)\cos(\alpha)}{r^2}\beta_x\right)$$
$$-B_{26}\left(-\frac{\cos(\alpha)}{r}\frac{\partial\beta_\theta}{\partial x}-\frac{\cos(\alpha)}{r^2}\frac{\partial\beta_x}{\partial\theta}+\frac{\sin(\alpha)\cos(\alpha)}{r^2}\beta_\theta\right)-q_z=0 \tag{2.53}$$

$$A_{45}\left(-\frac{1}{r}\frac{\partial w}{\partial \theta}+\frac{\cos(\alpha)}{r}v-\beta_\theta\right)+A_{55}\left(-\frac{\partial w}{\partial \theta}-\beta_x\right)+D_{11}\left(\frac{\sin(\alpha)}{r}\frac{\partial \beta_x}{\partial x}+\frac{\partial^2\beta_x}{\partial x^2}\right) \tag{2.54}$$
$$+D_{12}\left(\frac{1}{r}\frac{\partial^2\beta_\theta}{\partial x\,\partial\theta}\right)+D_{16}\left(\frac{2}{r}\frac{\partial^2\beta_x}{\partial x\,\partial\theta}+\frac{\partial^2\beta_\theta}{\partial x^2}\right)$$
$$+D_{22}\left(-\frac{\sin(\alpha)}{r^2}\frac{\partial\beta_\theta}{\partial\theta}-\left(\frac{\sin(\alpha)}{r}\right)^2\beta_x\right)$$
$$+D_{26}\left(\frac{1}{r^2}\frac{\partial^2\beta_\theta}{\partial\theta^2}-\frac{\sin(\alpha)}{r}\frac{\partial\beta_\theta}{\partial x}+\left(\frac{\sin(\alpha)}{r}\right)^2\beta_\theta\right)$$
$$+D_{66}\left(\frac{1}{r}\frac{\partial^2\beta_\theta}{\partial x\,\partial\theta}+\frac{1}{r^2}\frac{\partial^2\beta_x}{\partial\theta^2}-\frac{\sin(\alpha)}{r^2}\frac{\partial\beta_\theta}{\partial\theta}\right)+B_{11}\left(\frac{\sin(\alpha)}{r}\frac{\partial u}{\partial x}+\frac{\partial^2 u}{\partial x^2}\right)$$
$$+B_{12}\left(\frac{1}{r}\frac{\partial^2 v}{\partial x\,\partial\theta}+\frac{\cos(\alpha)}{r}\frac{\partial w}{\partial x}\right)+B_{16}\left(\frac{\partial^2 v}{\partial x^2}+\frac{2}{r}\frac{\partial^2 u}{\partial x\,\partial\theta}\right)$$
$$+B_{22}\left(-\frac{\sin(\alpha)}{r^2}\frac{\partial v}{\partial\theta}-\left(\frac{\sin(\alpha)}{r}\right)^2u-\frac{\sin(\alpha)\cos(\alpha)}{r^2}w\right)$$
$$+B_{26}\left(-\frac{\sin(\alpha)}{r}\frac{\partial v}{\partial x}+\left(\frac{\sin(\alpha)}{r}\right)^2v+\frac{1}{r^2}\frac{\partial^2 v}{\partial\theta^2}+\frac{\cos(\alpha)}{r^2}\frac{\partial w}{\partial\theta}\right)$$
$$+B_{66}\left(\frac{1}{r}\frac{\partial^2 v}{\partial x\,\partial\theta}-\frac{\sin(\alpha)}{r^2}\frac{\partial v}{\partial\theta}+\frac{1}{r^2}\frac{\partial^2 u}{\partial\theta^2}\right)=0$$

$$A_{44}\left(-\frac{1}{r}\frac{\partial w}{\partial\theta}+\frac{\cos(\alpha)}{r}v-\beta_\theta\right)+A_{45}\left(-\frac{\partial w}{\partial\theta}-\beta_x\right)+D_{12}\left(\frac{1}{r}\frac{\partial^2\beta_x}{\partial x\,\partial\theta}\right) \tag{2.55}$$
$$+D_{16}\left(\frac{2\sin(\alpha)}{r}\frac{\partial\beta_x}{\partial x}+\frac{\partial^2\beta_x}{\partial x^2}\right)+D_{22}\left(\frac{1}{r^2}\frac{\partial^2\beta_\theta}{\partial\theta^2}+\frac{\sin(\alpha)}{r^2}\frac{\partial\beta_x}{\partial\theta}\right)$$
$$+D_{26}\left(\frac{2}{r}\frac{\partial^2\beta_\theta}{\partial x\,\partial\theta}+\frac{1}{r^2}\frac{\partial^2\beta_x}{\partial\theta^2}+\left(\frac{\sin(\alpha)}{r}\right)^2\beta_x+\frac{\sin(\alpha)}{r}\frac{\partial\beta_x}{\partial x}\right)$$
$$+D_{66}\left(\frac{\sin(\alpha)}{r}\frac{\partial\beta_\theta}{\partial x}+\frac{\sin(\alpha)}{r^2}\frac{\partial\beta_x}{\partial\theta}-\left(\frac{\sin(\alpha)}{r}\right)^2\beta_\theta+\frac{\partial^2\beta_\theta}{\partial x^2}+\frac{1}{r}\frac{\partial^2\beta_x}{\partial x\,\partial\theta}\right)$$
$$+B_{12}\left(\frac{1}{r}\frac{\partial^2 u}{\partial x\,\partial\theta}\right)+B_{16}\left(\frac{\partial^2 u}{\partial x^2}+\frac{2\sin(\alpha)}{r}\frac{\partial u}{\partial x}\right)$$
$$+B_{22}\left(\frac{1}{r^2}\frac{\partial^2 v}{\partial\theta^2}+\frac{\sin(\alpha)}{r^2}\frac{\partial u}{\partial\theta}+\frac{\cos(\alpha)}{r^2}\frac{\partial w}{\partial\theta}\right)$$
$$+B_{26}\left(\left(\frac{\sin(\alpha)}{r}\right)^2u+\frac{\sin(\alpha)\cos(\alpha)}{r^2}w+\frac{2}{r}\frac{\partial^2 v}{\partial x\,\partial\theta}+\frac{\sin(\alpha)}{r}\frac{\partial u}{\partial x}+\frac{\cos(\alpha)}{r}\frac{\partial w}{\partial x}\right.$$
$$\left.+\frac{1}{r^2}\frac{\partial^2 u}{\partial\theta^2}\right)+B_{66}\left(\frac{\sin(\alpha)}{r}\frac{\partial v}{\partial x}-\left(\frac{\sin(\alpha)}{r}\right)^2v+\frac{\sin(\alpha)}{r^2}\frac{\partial u}{\partial\theta}+\frac{\partial^2 v}{\partial x^2}+\frac{1}{r}\frac{\partial^2 u}{\partial x\,\partial\theta}\right)$$
$$=0$$

2.4.2 Solution of governing equations under bending

For bending analysis, a distributed transverse load is applied as

$$q_z(x,\theta) = q_0 \sin\left(\frac{\pi\left(x - \frac{x_b + x_t}{2}\right)}{x_b - x_t} + \frac{\pi}{2}\right)\cos(\theta) \tag{2.56}$$

in which x_b and x_t are shown in Figure 2.2.

Seeking for the Levy-type solution of the equations, the following representation was taken for displacement quantities [18]

$$\begin{Bmatrix} u(x,\theta) \\ v(x,\theta) \\ w(x,\theta) \\ \beta_x(x,\theta) \\ \beta_\theta(x,\theta) \end{Bmatrix} = \begin{Bmatrix} \bar{u}(x)\cos(\theta) \\ \bar{v}(x)\sin(\theta) \\ \bar{w}(x)\cos(\theta) \\ \bar{\beta}_x(x)\cos(\theta) \\ \bar{\beta}_\theta(x)\sin(\theta) \end{Bmatrix} \tag{2.57}$$

The above displacement quantities can be used for conical shell with arbitrary boundary conditions at both ends. One can get five coupled ordinary differential equation by substituting equations (2.57) into equations (2.51)-(2.55). Rewriting these equations, the equations of motion can be written as

$$\bar{u}'' = C_1\bar{u} + C_2\bar{u}' + C_3\bar{v} + C_4\bar{v}' + C_5\bar{w} + C_6\bar{w}' + C_7\bar{\beta}_x + C_8\bar{\beta}_x' + C_9\bar{\beta}_\theta + C_{10}\bar{\beta}_\theta' \tag{2.58}$$

$$\bar{v}'' = C_{11}\bar{u} + C_{12}\bar{u}' + C_{13}\bar{v} + C_{14}\bar{v}' + C_{15}\bar{w} + C_{16}\bar{w}' + C_{17}\bar{\beta}_x + C_{18}\bar{\beta}_x' + C_{19}\bar{\beta}_\theta + C_{20}\bar{\beta}_\theta'$$

$$\bar{w}'' = C_{21}\bar{u} + C_{22}\bar{u}' + C_{23}\bar{v} + C_{24}\bar{v}' + C_{25}\bar{w} + C_{26}\bar{w}' + C_{27}\bar{\beta}_x + C_{28}\bar{\beta}_x' + C_{29}\bar{\beta}_\theta + C_{30}\bar{\beta}_\theta' + F$$

$$\bar{\beta}_x'' = C_{31}\bar{u} + C_{32}\bar{u}' + C_{33}\bar{v} + C_{34}\bar{v}' + C_{35}\bar{w} + C_{36}\bar{w}' + C_{37}\bar{\beta}_x + C_{38}\bar{\beta}_x' + C_{39}\bar{\beta}_\theta + C_{40}\bar{\beta}_\theta'$$

$$\bar{\beta}_\theta'' = C_{41}\bar{u} + C_{42}\bar{u}' + C_{43}\bar{v} + C_{44}\bar{v}' + C_{45}\bar{w} + C_{46}\bar{w}' + C_{47}\bar{\beta}_x + C_{48}\bar{\beta}_x' + C_{49}\bar{\beta}_\theta + C_{50}\bar{\beta}_\theta'$$

where prime denotes the derivative with respect to x and the coefficients C_i $(i = 1..50)$ and F are defined in Appendix B.

It is more practical and convenient to deal with the first order system of differential equations. So to convert the above system of equations to a state-space form, the following new variables can be introduced

$$Z_1 = \bar{u};\ Z_2 = \bar{u}'\ = Z_1';\ Z_3 = \bar{v};\ Z_4 = \bar{v}'\ = Z_3'\ ;\ Z_5 = \bar{w}; \tag{2.59}$$

$$Z_6 = \bar{w}'\ = Z_5';\ Z_7 = \bar{\beta}_x;\ Z_8 = \bar{\beta}_x' = Z_7';\ Z_9 = \bar{\beta}_\theta;\ Z_{10} = \bar{\beta}_\theta' = Z_9'$$

Considering the new variable defined above, the system of equations stated in equations (2.58) can be written in the form of

$$\{\acute{Z}\} = [C]\{Z\} + \{l\} \tag{2.60}$$

where $Z = \{Z_{1m}, Z_{2m}, \dots, Z_{10m}\}^T$ and $[C]$ and $\{l\}$ are defined in the Appendix B.

Boundary conditions can be defined at both ends of the conical shell for simply supported, clamped and free edges as

$$Simply\ support\ (S):\ v = w = \beta_\theta = N_{xx} = M_{xx} = 0 \tag{2.61}$$

$$Clamped\ (C):\ u = v = w = \beta_x = \beta_\theta = 0$$

$$Free\ (F): N_{xx} = M_{xx} = Q_{xx} = N_{x\theta} = M_{x\theta} = 0$$

Equation (2.60) including a set of ten first order differential equations can be solved in conjunction with boundary conditions sated in equation (2.61) using a numerical method.

2.4.3 Validation

A computer code was developed to solve ten first-order differential equations (2.60) and numerical results are obtained for geometrical specifications and material properties stated in Table 2.3. It is also assumed that $q_0 = -1000\ lbf/in^2$ in all calculations.

Table 2.3: Geometrical specifications and material properties of conical shell

Material properties	Geometric specifications
$E_{11} = 3.05 \times 10^7\ psi = 210.29\ MPa$ $E_{22} = E_{33} = E_1/25$ $G_{12} = G_{13} = 0.5E_{22}$ $G_{23} = 0.2E_{22}$ $\nu_{12} = 0.25$	Length along the generator , $l' = 10\ in = 254\ mm$ Bottom radius, $r_b = 10\ in = 254\ mm$ Total thickness, $H = 0.5\ in = 12.7\ mm$

For validation purposes the cone angle (α) is set to zero and as a result, a complete composite cylinder obtained. The bending results for two different cases are compared with references [7] and shown in Table 2.4.

Table 2.4: Validation of bending results ($\breve{w} = \frac{w\left(\frac{l}{2},0\right)H^3E_{22}10^2}{q_0R^4}, \frac{r}{H} = 10$)

	SS			CC			FC		
Lamination	Present work	Ref. [71]	Ref. [17]	Present work	Ref. [71]	Ref. [17]	Present work	Ref. [71]	Ref. [17]
0/90	0.2621	0.2621	0.2535	0.2191	0.2191	0.2132	0.5188	0.5188	0.4988
0/90/0	0.2262	0.2262	0.2257	0.1797	0.1797	0.1795	0.4313	0.4313	0.4303

2.4.4 Numerical results

2.4.4.1 Effect of semi-cone angle on normalized transverse displacement

Mid-span transverse displacement, $w(\frac{x_b+x_t}{2}, 0)$, for symmetric and non-symmetric cross-ply laminated cone is plotted as a function of semi-cone angle in Figure 2.10-Figure 2.12.

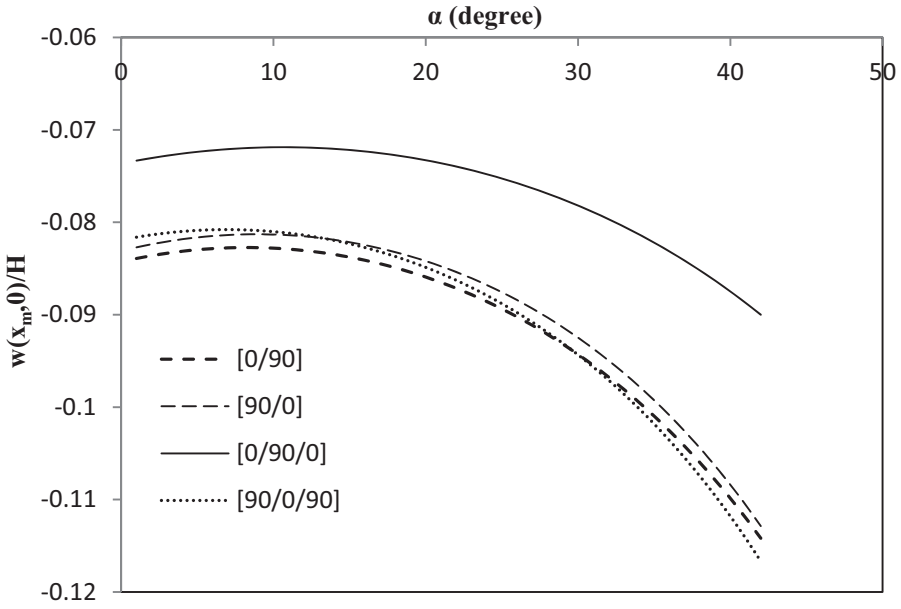

Figure 2.10: Normalized mid-span deflection for CC boundary condition($x_m = \frac{x_b+x_t}{2}, \frac{r_b}{l'} = 1, \frac{r_b}{H} = 20$)

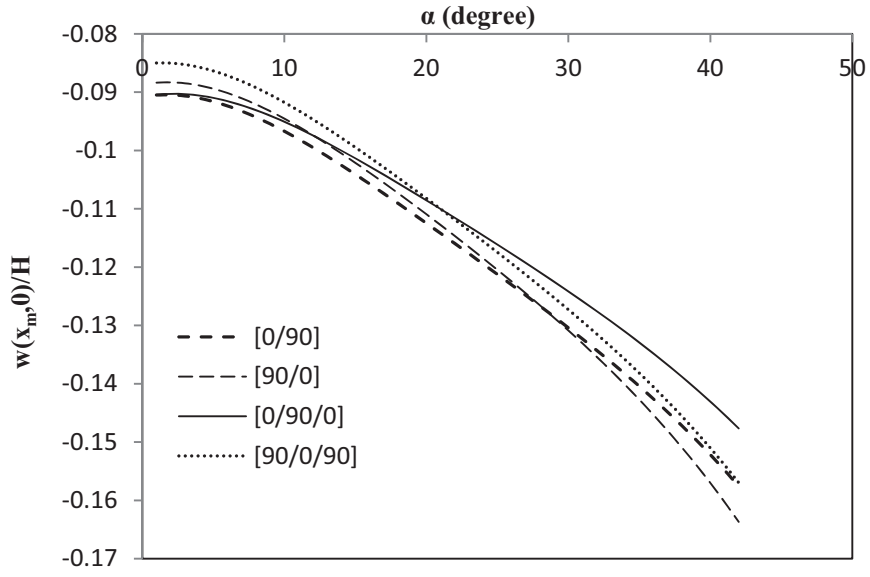

Figure 2.11: Normalized mid-span deflection for SS boundary condition($x_m = \frac{x_b+x_t}{2}, \frac{r_b}{l'} = 1, \frac{r_b}{H} = 20$)

For both ends clamped boundary condition (Figure 2.10), mid-span deflection decreases a little by increasing in semi-cone angle (α) until around $\alpha = 10^{\circ}$ and then increases as α increases. The rate of this increase is more while α exceeds 25°. Furthermore, one can see that [0/90/0] lamination has less deflection in comparison with the other configurations.

Figure 2.11 shows similar results for simply supported boundary condition. All four lamination schemes have the same trend and mid-span transverse displacement increases as α increases.

Unlike the clamped and simply supported boundary conditions, mid-span transverse displacement of conical shells with one end clamped and the other end free boundary condition has different trend. It decreases as α increases until around 30° to 35°. All graphs have a peak around these angles and then start decreasing with increasing α (Figure 2.12).

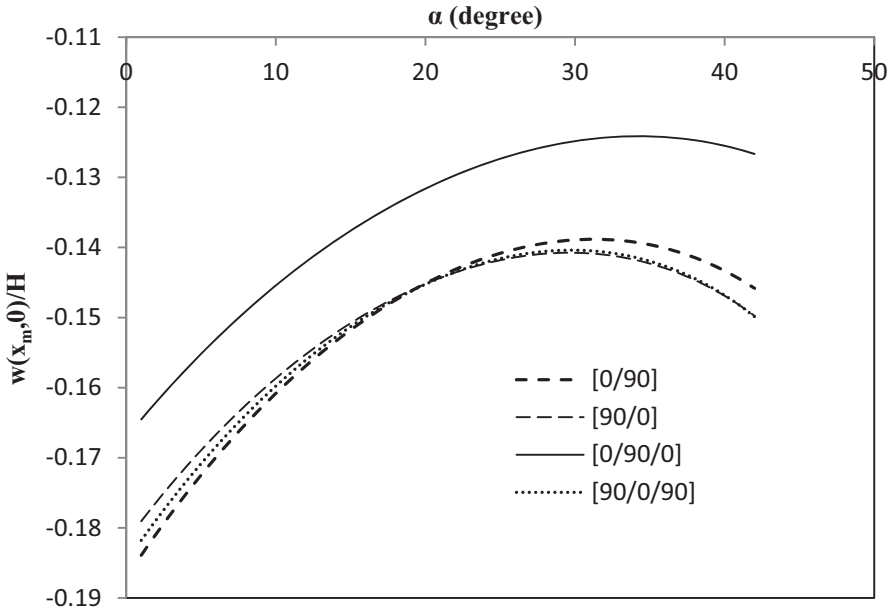

Figure 2.12: Normalized mid-span deflection for FC boundary condition($x_m = \frac{x_b + x_t}{2}, \frac{r_b}{l'} = 1, \frac{r_b}{H} = 20$)

2.4.4.2 Effect of radius-to-thickness ratio on normalized transverse displacement

Effect of radius-to-thickness ratio on normalized mid-span deflection is shown in Figure 2.13-Figure 2.16 by keeping the bottom radius of the cone, r_b, constant and continuously decreasing the total thickness of the cone. Likewise, the effects of three boundary conditions and different laminations are shown in Figure 2.13-Figure 2.16.

Figure 2.13 contains plots of normalized mid-span deflection as a function of radius-to-thickness ratio r_b/H for [0/90/0] lamination. As can be seen, for all three types of boundary conditions normalized mid-span deflection increases as the radius to thickness ration increases. However these increases are not at the same rate. Conical shells with one end clamped and the other end free have the steepest curve.

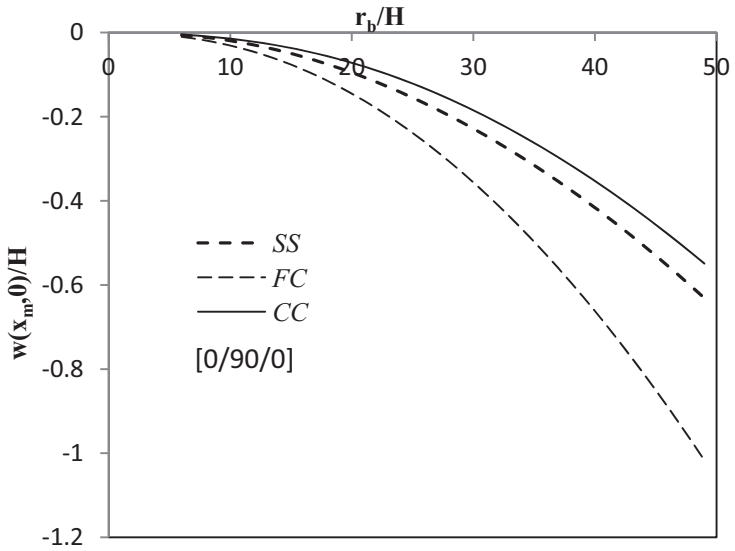

Figure 2.13: Normalized mid-span deflection versus radius to thickness ratio for [0/90/0] ($x_m = \frac{x_b+x_t}{2}, \frac{r_b}{l'} = 1, \alpha = 10^\circ$)

The results of normalized mid-span deflection versus radius-to-thickness ratio for [90/0/90], [0/90] and [90/0] lamination with different boundary conditions are plotted in Figure 2.14-Figure 2.16. One can see that in all situations normalized mid-span deflection increases as radius-to-thickness ratio increases.

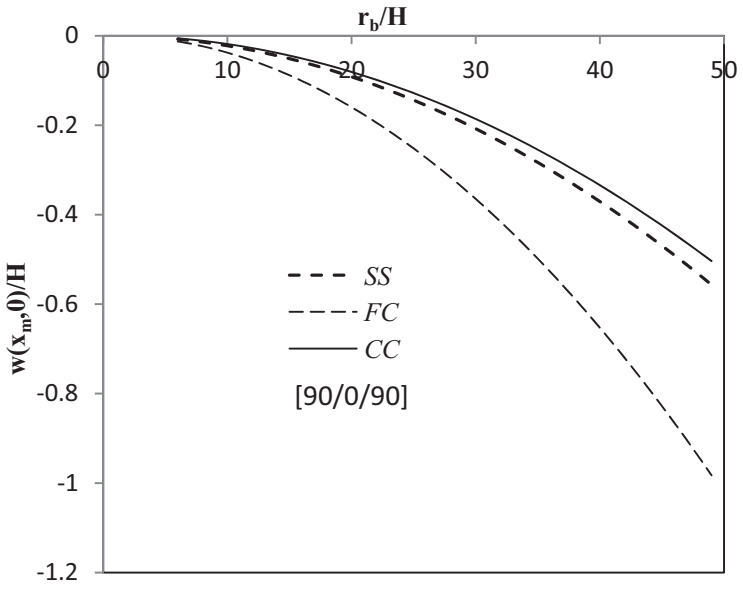

Figure 2.14: Normalized mid-span deflection versus radius to thickness ratio for [90/0/90] ($\boldsymbol{x_m = \frac{x_b+x_t}{2}, \frac{r_b}{L} = 1, \alpha = 10^\circ}$)

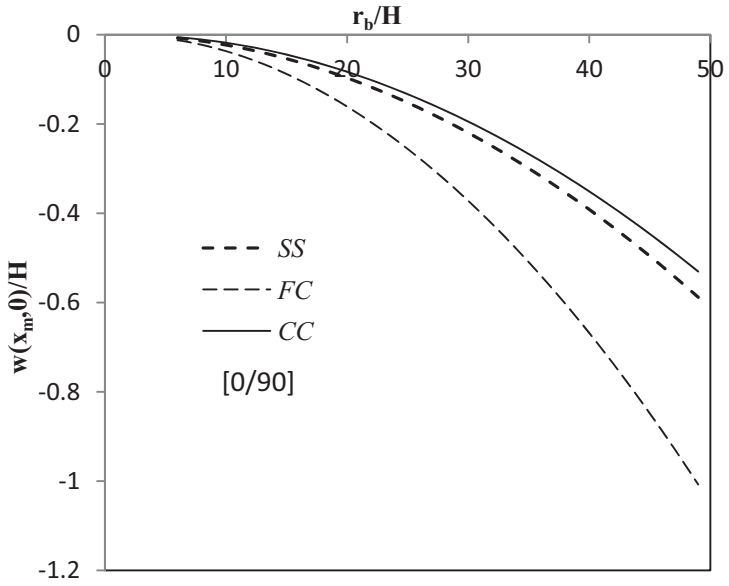

Figure 2.15: Normalized mid-span deflection versus radius to thickness ratio for [0/90] ($x_m = \frac{x_b+x_t}{2}, \frac{r_b}{L} = 1, \alpha = 10^\circ$)

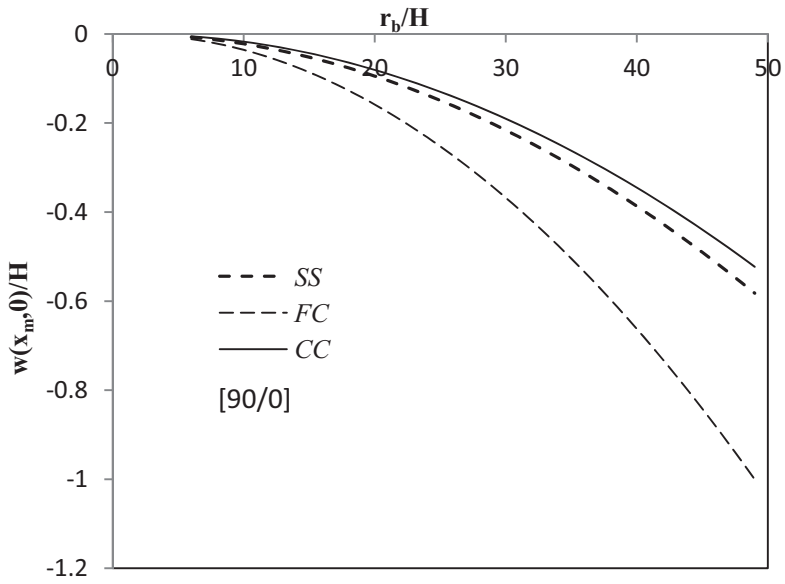

Figure 2.16: Normalized mid-span deflection versus radius to thickness ratio for [90/0] ($x_m = \frac{x_b+x_t}{2}, \frac{r_b}{l'} = 1, \alpha = 10^\circ$)

2.4.4.3 Effect of length-to-thickness ratio on normalized transverse displacement

Effect of length (along the cone generator) to thickness ratio is studied in Figure 2.17 for [90/0/90] configuration. Length to thickness ratio is changed from about 150 to 270 and consequently normalized mid-span transverse displacement is recorded for different boundary conditions. One can see that these graphs have similar trend to those obtained by varying the radius-to-thickness ratio and normalized mid-span deflection decreases as length-to-thickness ratio increases.

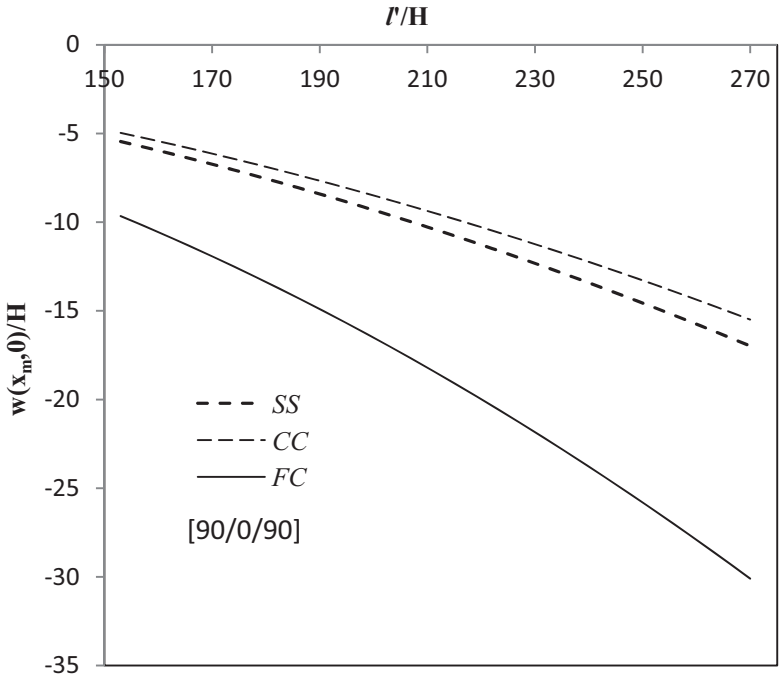

Figure 2.17: Normalized mid-span deflection versus length to thickness ratio for [90/0/90] ($x_m = \frac{x_b+x_t}{2}, \frac{r_b}{l'} = 1, \alpha = 10^\circ$)

2.4.5 Conclusions

It was shown that linear first-order shear deformation shell theory could be used to determine the bending response of cross-ply laminated conical shells. Governing equations are derived using principle of minimum (stationary) potential energy and solved using state-space approach. The effects of semi-cone angle, radius-to-thickness ratio, length-to-thickness ratio, lamination scheme, and boundary condition on normalized mid-span transverse displacement are studied. It is shown that the dependency of the cone deflection on semi-cone angle is very different for different boundary conditions.

Chapter 3

Bending, buckling, and vibration of cross-ply circular cylindrical shells[3]

In this chapter, the effect of assumed displacement field on the bending, bucking, and natural frequencies of cross-ply circular cylindrical shells is investigated using first-order shear deformation theory through an analytical solution. Linear strain displacement relation is assumed. The governing equations are derived from Hamilton's principle. Assuming Levy-type solution, the governing equations are then converted to ordinary differential equations and changed to state-space form introducing ten unknown variables and solved for displacements. Different lamination sequences including symmetric and asymmetric laminate are studied and compared. The effect of various boundary conditions (i.e., clamped, simply supported and free edge), radius-to-thickness and radius-to-length ratio on the displacement of mid surface is investigated.

3.1 Introduction

As it mentioned in literature review (section 1.2.1), Khdeir et al. [17] introduced an analytical solution for natural frequencies and buckling load of cross-ply cylindrical shells. This study proposes a different displacement field from what was assumed in the references [17] and [18] and investigates consequent changes in formulation and discusses the changes in numerical results. Furthermore, in order to facilitate comparison with the formulation proposed in reference [17] and [18], the same notation used in reference [17] is adapted in this chapter.

[3] The content of Chapter 3 has been published in [71] and [102].

3.2 Formulation

The governing equations for laminated cylindrical shells are derived using Hamilton's principle and variational techniques. It is assumed that the deformations are small and consequently linear strain-displacement relations are used.

3.2.1 Kinematics

Based on the shear deformation shell theory assumption explained in section 2.1, the displacement field assumed in this study is

$$\begin{aligned} \bar{u}(x_1, x_2, \zeta, t) &= u(x_1, x_2, t) + \zeta\phi_1(x_1, x_2, t) \\ \bar{v}(x_1, x_2, \zeta, t) &= v(x_1, x_2, t) + \zeta\phi_2(x_1, x_2, t) \\ \bar{w}(x_1, x_2, \zeta, t) &= w(x_1, x_2, t) \end{aligned} \tag{3.1}$$

in which (u, v, w) are the displacements of mid-surface and (ϕ_1, ϕ_2) are the rotations of a normal to the mid-surface about x_2 and x_1 axis respectively. t represents the time variable and ζ is the axis through the thickness of the layers (see Figure 3.1).

The Lame coefficients (A_1, A_2) and principal radii of curvature (R_1, R_2) for circular cylindrical shells are

$$A_1 = R_1 = r_\phi, A_2 = R_2 = R \tag{3.2}$$

where R is the radius of cylinder. r_ϕ represents the radius of curvature along the meridian and since cylindrical shell has straight generator, the curvature along the meridian is zero and $1/r_\phi$ is vanished (i.e. r_ϕ is infinity). The linear strain-displacement relations corresponding to the above displacement field for cylindrical shell can be obtained by substituting equation (3.1) and

equation (3.2) into strain-displacement relations for general shell element, equation (2.3) ([66], p. 30 and [68], p. 455). After some mathematical manipulations and making the change of variables $\alpha_1 = \phi,\ \alpha_2 = \theta,\ r_\phi \partial\phi = \partial x_1$ and $R\partial\theta = \partial x_2$, one can get the following strain-displacement relations

$$\begin{aligned} \varepsilon_1 &= \varepsilon_1^0 + \zeta\kappa_1^0 \\ \varepsilon_2 &= \varepsilon_2^0 + \zeta\kappa_2^0 \\ \varepsilon_4 &= \varepsilon_4^0 \\ \varepsilon_5 &= \varepsilon_5^0 \\ \varepsilon_6 &= \varepsilon_6^0 + \zeta\kappa_6^0 \end{aligned} \tag{3.3}$$

where

$$\begin{aligned} \varepsilon_1^0 &= \frac{\partial u}{\partial x_1} & \kappa_1^0 &= \frac{\partial \phi_1}{\partial x_1} \\ \varepsilon_2^0 &= \frac{\partial v}{\partial x_2} + \frac{w}{R} & \kappa_2^0 &= \frac{\partial \phi_2}{\partial x_2} \\ \varepsilon_4^0 &= \frac{\partial w}{\partial x_2} + \phi_2 - \frac{v}{R} & \kappa_6^0 &= \frac{\partial \phi_2}{\partial x_1} + \frac{\partial \phi_1}{\partial x_2} \\ \varepsilon_5^0 &= \frac{\partial w}{\partial x_1} + \phi_1 \\ \varepsilon_6^0 &= \frac{\partial v}{\partial x_1} + \frac{\partial u}{\partial x_2} \end{aligned} \tag{3.4}$$

In contrast with equation (3.1), the displacement field assumed in references [17] and [18] is

$$\bar{u}(x_1, x_2, \zeta, t) = u(x_1, x_2, t) + \zeta\phi_1(x_1, x_2, t) \tag{3.5}$$

$$\bar{v}(x_1, x_2, \zeta, t) = \left(1 + \frac{\zeta}{R}\right) v(x_1, x_2, t) + \zeta\phi_2(x_1, x_2, t)$$

$$\bar{w}(x_1, x_2, \zeta, t) = w(x_1, x_2, t)$$

The difference between the displacement field assumed in this chapter and the one in references [17] and [18] is in definition of $\bar{v}(x_1, x_2, \zeta, t)$, where the term $\frac{\zeta}{R} v(x_1, x_2, t)$ is added in references [17] and [18] to the displacement field. This added term comes from the classical shell assumption (Love hypothesis), when the transverse shear strain is assumed to be equal to zero ([66], p. 31). Consequently, keeping this term in first-order shear deformation theory will eliminate some other terms in formulation. This will be addressed in later paragraphs.

As a consequence of adding $\frac{\zeta}{R} v(x_1, x_2, t)$ to the displacement field, the strain-displacement relations will be affected in ε_4^0 as (see [18])

$$\varepsilon_4^0 = \frac{\partial w}{\partial x_2} + \phi_2 \tag{3.6}$$

Comparing equation (3.6) with the ε_4^0 definition from equations (3.4), one can see that the term "$-\frac{v}{R}$" is omitted (and this is because of including $\frac{\zeta}{R} v(x_1, x_2, t)$ in the displacement field). Looking at the strain-displacement relations for general shell element ([68], p. 456), one can see that term "$-\frac{v}{R}$" exists in definition of ε_4^0 and consequently should exist for cylindrical shell as well. The other strain-displacement relations remain unchanged as stated in equations (3.4).

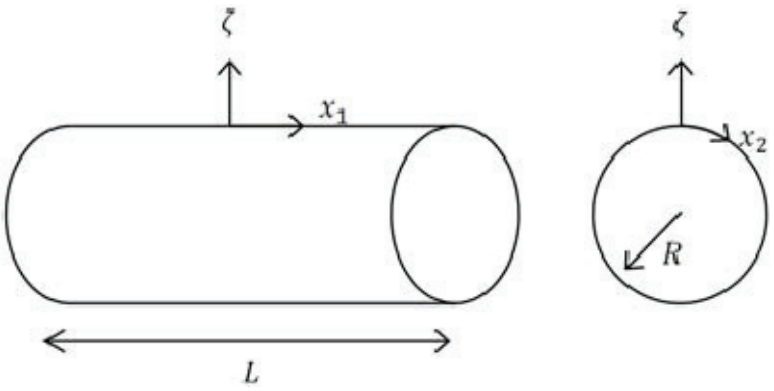

Figure 3.1: Shell coordinate system

3.2.2 Equilibrium equations

The governing equations of motion of cylindrical shell are derived using Hamilton's principle on account of its simplicity and due to the fact that it gives the natural boundary conditions of the problem as well. Hamilton's principle can be written as [66]

$$\delta \int_{t_1}^{t_2} (U - W_s - W_{e1} - W_{e2} - K) dt = 0 \tag{3.7}$$

in which U represents the strain energy, while W_s is the work of the body and surface forces, W_{e1} and W_{e2} are the work done by the edge stresses and K is kinetic energy. Considering the notation adapted in this chapter, the parameters used in Hamilton's principle can be defined as [66]:

$$\delta U = \int_{x_2} \int_{x_1} \int_{\zeta} (\sigma_1 \delta\varepsilon_1 + \sigma_2 \delta\varepsilon_2 + \sigma_6 \delta\varepsilon_6 + \sigma_5 \delta\varepsilon_5 + \sigma_4 \delta\varepsilon_4)\, d\zeta dx_1 dx_2 \tag{3.8}$$

$$\delta W_s = \int_{x_2} \int_{x_1} (q_1 \delta u + q_2 \delta v + q_3 \delta w)\, dx_1 dx_2$$

$$\delta W_{e1} = \int_{x_2} \int_{\zeta} (\bar{\sigma}_1 \delta u + \bar{\sigma}_6 \delta v + \bar{\sigma}_5 \delta w)\, dx_2 d\zeta$$

$$\delta W_{e2} = \int_{x_1} \int_{\zeta} (\bar{\sigma}_2 \delta v + \bar{\sigma}_6 \delta u + \bar{\sigma}_4 \delta w)\, dx_1 d\zeta$$

$$\delta K = \int_{x_2} \int_{x_1} \int_{\zeta} \rho(\ddot{u}\delta\dot{u} + \ddot{v}\delta\dot{v} + \ddot{w}\delta\dot{w})\, d\zeta dx_1 dx_2$$

Substituting the displacement field, equations (3.1), into Hamilton's principle, equation (3.7), and integrating over the thickness of the shell and vanishing the coefficient of variations, one can get the five equations of motion for cylindrical shell as

$$\frac{\partial N_1}{\partial x_1} + \frac{\partial N_6}{\partial x_2} + q_1 = I_1 \ddot{u} + I_2 \ddot{\phi}_1 \tag{3.9}$$

$$\frac{\partial N_6}{\partial x_1} + \frac{\partial N_2}{\partial x_2} + \frac{Q_2}{R} + q_2 = I_1 \ddot{v} + I_2 \ddot{\phi}_2$$

$$\frac{\partial Q_1}{\partial x_1} + \frac{\partial Q_2}{\partial x_2} - \frac{N_2}{R} - \bar{N}\frac{\partial^2 w}{\partial x_1^2} + q_3 = I_1 \ddot{w}$$

$$\frac{\partial M_1}{\partial x_1} + \frac{\partial M_6}{\partial x_2} - Q_1 = I_2 \ddot{u} + I_3 \ddot{\phi}_1$$

$$\frac{\partial M_2}{\partial x_2} + \frac{\partial M_6}{\partial x_1} - Q_2 = I_2 \ddot{v} + I_3 \ddot{\phi}_2$$

where $\bar{N}$ is a compressive axial load and (q_1, q_2, q_ζ) are distributed body forces acting on the mid-surface. Force resultants, moment resultants and inertias in equations (3.9) are defined as

$$\begin{Bmatrix} N_1 \\ N_2 \\ N_6 \\ Q_1 \\ Q_2 \end{Bmatrix} = \int_\zeta \begin{Bmatrix} \sigma_1 \\ \sigma_2 \\ \sigma_6 \\ \sigma_5 \\ \sigma_4 \end{Bmatrix} d\zeta \qquad \begin{Bmatrix} M_1 \\ M_2 \\ M_6 \end{Bmatrix} = \int_\zeta \begin{Bmatrix} \sigma_1 \\ \sigma_2 \\ \sigma_6 \end{Bmatrix} \zeta d\zeta \tag{3.10}$$

$$I_i = \sum_{k=1}^{N} \int_{\zeta_{k-1}}^{\zeta_k} \rho^k \zeta^{(i-1)} d\zeta \qquad (1 = 1,2,3)$$

Comparing governing equations (3.9) with the governing equations in references [17][18], one can see that the term "$\frac{Q_2}{R}$" is added to the second equation. Existence of this term, $\frac{Q_2}{R}$, is because of considering "$-\frac{v}{R}$" in ε_4 which itself is a consequence of not including "$\frac{\zeta}{R}v$" in definition of $\bar{v}$ in the displacement field in this study. Looking at second equilibrium equation of doubly-curved shells ([68], p. 463), one can see that the term "$\frac{Q_2}{R}$" exists and therefore should exist for cylindrical shell too.

For cross-ply shells, force and moment resultants are related to strains by laminated stiffness coefficients as shown in equation (2.50). The shear correction factor (K_s) in equation (2.50) is taken to be 5/6 for numerical results [17].

Substituting equations (3.4) into equation (2.50), the force and moment resultant can be written in terms of displacement variable, namely $(u, v, w, \phi_1, \phi_2)$. Now if one substitutes these relations into equations (3.9), the governing equations for cross-ply circular cylindrical shell obtained in terms of displacement variables as

$$A_{11}\left(\frac{\partial^2 u}{\partial x_1^2}\right)+A_{12}\left(\frac{\partial^2 v}{\partial x_1\,\partial x_2}+\frac{1}{R}\frac{\partial w}{\partial x_1}\right)+A_{16}\left(\frac{\partial^2 v}{\partial x_1^2}+2\frac{\partial^2 u}{\partial x_1\,\partial x_2}\right)+A_{26}\left(\frac{\partial^2 v}{\partial x_2^2}+\frac{1}{R}\frac{\partial w}{\partial x_2}\right)$$
$$+A_{66}\left(\frac{\partial^2 v}{\partial x_1\,\partial x_2}+\frac{\partial^2 u}{\partial x_2^2}\right)+B_{11}\left(\frac{\partial^2 \phi_1}{\partial x_1^2}\right)+B_{12}\left(\frac{\partial^2 \phi_2}{\partial x_1\,\partial x_2}\right)$$
$$+B_{16}\left(2\frac{\partial^2 \phi_1}{\partial x_1\,\partial x_2}+\frac{\partial^2 \phi_2}{\partial x_1^2}\right)+B_{26}\left(\frac{\partial^2 \phi_2}{\partial x_2^2}\right)+B_{66}\left(\frac{\partial^2 \phi_2}{\partial x_1\,\partial x_2}+\frac{\partial^2 \phi_1}{\partial x_2^2}\right)+q_1$$
$$=I_1\left(\frac{\partial^2 u}{\partial t^2}\right)+I_2\left(\frac{\partial^2 \phi_1}{\partial t^2}\right) \tag{3.11}$$

$$A_{12}\left(\frac{\partial^2 u}{\partial x_1\,\partial x_2}\right)+A_{16}\left(\frac{\partial^2 u}{\partial x_1^2}\right)+A_{22}\left(\frac{\partial^2 v}{\partial x_2^2}+\frac{1}{R}\frac{\partial w}{\partial x_2}\right)+A_{26}\left(2\frac{\partial^2 v}{\partial x_1\,\partial x_2}+\frac{1}{R}\frac{\partial w}{\partial x_1}+\frac{\partial^2 u}{\partial x_2^2}\right)$$
$$+A_{66}\left(\frac{\partial^2 v}{\partial x_1^2}+\frac{\partial^2 u}{\partial x_1\,\partial x_2}\right)+A_{44}\left(\frac{1}{R}\frac{\partial w}{\partial x_2}-\frac{1}{R^2}v+\frac{1}{R}\phi_2\right)+A_{45}\left(\frac{1}{R}\frac{\partial w}{\partial x_1}+\frac{1}{R}\phi_1\right)$$
$$+B_{12}\left(\frac{\partial^2 \phi_1}{\partial x_1\,\partial x_2}\right)+B_{16}\left(\frac{\partial^2 \phi_1}{\partial x_1^2}\right)+B_{22}\left(\frac{\partial^2 \phi_2}{\partial x_2^2}\right)+B_{26}\left(2\frac{\partial^2 \phi_2}{\partial x_1\,\partial x_2}+\frac{\partial^2 \phi_1}{\partial x_2^2}\right)$$
$$+B_{66}\left(\frac{\partial^2 \phi_2}{\partial x_1^2}+\frac{\partial^2 \phi_1}{\partial x_1\,\partial x_2}\right)+q_2=I_1\left(\frac{\partial^2 v}{\partial t^2}\right)+I_2\left(\frac{\partial^2 \phi_2}{\partial t^2}\right) \tag{3.12}$$

$$A_{12}\left(-\frac{1}{R}\frac{\partial u}{\partial x_1}\right)+A_{26}\left(-\frac{1}{R}\frac{\partial v}{\partial x_1}-\frac{1}{R}\frac{\partial u}{\partial x_2}\right)+A_{22}\left(-\frac{1}{R}\frac{\partial v}{\partial x_2}-\frac{1}{R^2}w\right)$$
$$+A_{44}\left(\frac{\partial^2 w}{\partial x_2^2}-\frac{1}{R}\frac{\partial v}{\partial x_2}+\frac{\partial \phi_2}{\partial x_2}\right)+A_{45}\left(2\frac{\partial^2 w}{\partial x_1\,\partial x_2}+\frac{\partial \phi_1}{\partial x_2}-\frac{1}{R}\frac{\partial v}{\partial x_1}+\frac{\partial \phi_2}{\partial x_1}\right)$$
$$+A_{55}\left(\frac{\partial^2 w}{\partial x_1^2}+\frac{\partial \phi_1}{\partial x_1}\right)+B_{12}\left(-\frac{1}{R}\frac{\partial \phi_1}{\partial x_1}\right)+B_{22}\left(-\frac{1}{R}\frac{\partial \phi_2}{\partial x_2}\right)$$
$$+B_{26}\left(-\frac{1}{R}\frac{\partial \phi_2}{\partial x_1}-\frac{1}{R}\frac{\partial \phi_1}{\partial x_2}\right)-\bar{N}\frac{\partial^2 w}{\partial x_1^2}+q_3=I_1\left(\frac{\partial^2 w}{\partial t^2}\right) \tag{3.13}$$

$$A_{45}\left(-\frac{\partial w}{\partial x_2}+\frac{1}{R}v-\phi_2\right)+A_{55}\left(-\frac{\partial w}{\partial x_1}-\phi_1\right)+D_{11}\left(\frac{\partial^2 \phi_1}{\partial x_1^2}\right)+D_{12}\left(\frac{\partial^2 \phi_2}{\partial x_1\,\partial x_2}\right)$$
$$+D_{16}\left(2\frac{\partial^2 \phi_1}{\partial x_1\,\partial x_2}+\frac{\partial^2 \phi_2}{\partial x_1^2}\right)+D_{26}\left(\frac{\partial^2 \phi_2}{\partial x_2^2}\right)+D_{66}\left(\frac{\partial^2 \phi_2}{\partial x_1\,\partial x_2}+\frac{\partial^2 \phi_1}{\partial x_2^2}\right)$$
$$+B_{11}\left(\frac{\partial^2 u}{\partial x_1^2}\right)+B_{12}\left(\frac{\partial^2 v}{\partial x_1\,\partial x_2}+\frac{1}{R}\frac{\partial w}{\partial x_1}\right)+B_{16}\left(\frac{\partial^2 v}{\partial x_1^2}+2\frac{\partial^2 u}{\partial x_1\,\partial x_2}\right)$$
$$+B_{26}\left(\frac{\partial^2 v}{\partial x_2^2}+\frac{1}{R}\frac{\partial w}{\partial x_2}\right)+B_{66}\left(\frac{\partial^2 v}{\partial x_1\,\partial x_2}+\frac{\partial^2 u}{\partial x_2^2}\right)$$
$$=I_2\left(\frac{\partial^2 u}{\partial t^2}\right)+I_3\left(\frac{\partial^2 \phi_1}{\partial t^2}\right) \tag{3.14}$$

$$A_{44}\left(-\frac{\partial w}{\partial x_2}+\frac{1}{R}v-\phi_2\right)+A_{45}\left(-\frac{\partial w}{\partial x_1}-\phi_1\right)+D_{12}\left(\frac{\partial^2\phi_1}{\partial x_1\,\partial x_2}\right)+D_{16}\left(\frac{\partial^2\phi_1}{\partial x_1^2}\right)$$
$$+D_{22}\left(\frac{\partial^2\phi_2}{\partial x_2^2}\right)+D_{26}\left(2\frac{\partial^2\phi_2}{\partial x_1\,\partial x_2}+\frac{\partial^2\phi_1}{\partial x_2^2}\right)+D_{66}\left(\frac{\partial^2\phi_2}{\partial x_1^2}+\frac{\partial^2\phi_1}{\partial x_1\,\partial x_2}\right)$$
$$+B_{12}\left(\frac{\partial^2 u}{\partial x_1\,\partial x_2}\right)+B_{16}\left(\frac{\partial^2 u}{\partial x_1^2}\right)+B_{22}\left(\frac{\partial^2 v}{\partial x_2^2}+\frac{1}{R}\frac{\partial w}{\partial x_2}\right)$$
$$+B_{26}\left(2\frac{\partial^2 v}{\partial x_1\,\partial x_2}+\frac{1}{R}\frac{\partial w}{\partial x_1}+\frac{\partial^2 u}{\partial x_2^2}\right)+B_{66}\left(\frac{\partial^2 v}{\partial x_1^2}+\frac{\partial^2 u}{\partial x_1\,\partial x_2}\right)$$
$$=I_2\left(\frac{\partial^2 v}{\partial t^2}\right)+I_3\left(\frac{\partial^2\phi_2}{\partial t^2}\right) \tag{3.15}$$

3.3 Solution of the governing equations

Seeking for the Levy-type solution for the equations (3.11)-(3.15), the following representation was taken for displacement quantities (see [17])

$$\begin{Bmatrix} u(x_1,x_2,t)\\ v(x_1,x_2,t)\\ w(x_1,x_2,t)\\ \phi_1(x_1,x_2,t)\\ \phi_2(x_1,x_2,t)\end{Bmatrix}=\begin{Bmatrix} U_m(x_1)\cos(\beta_m x_2)\\ V_m(x_1)\sin(\beta_m x_2)\\ W_m(x_1)\cos(\beta_m x_2)\\ X_m(x_1)\cos(\beta_m x_2)\\ Y_m(x_1)\sin(\beta_m x_2)\end{Bmatrix}e^{i\omega_m t}, \tag{3.16}$$

where $\beta_m = m/R$ and ω_m denotes the natural frequency corresponding to the m[th] mode. The above displacement quantities can be used for circular cylindrical shell with arbitrary boundary conditions at both ends. One can get five coupled ordinary differential equation by substituting equations (3.16) into equations (3.12)-(3.15). Rewriting these equations, the equations of motion can be written as

$$U_m'' = C_1 U_m + C_2 V_m' + C_3 W_m' + C_4 X_m + C_5 Y_m' \tag{3.17}$$

$$V_m'' = C_6 U_m' + C_7 V_m + C_8 W_m + C_9 X_m' + C_{10} Y_m$$

$$W_m'' = C_{11} U_m' + C_{12} V_m + C_{13} W_m + C_{14} X_m' + C_{15} Y_m$$

$$X_m'' = C_{16} U_m + C_{17} V_m' + C_{18} W_m' + C_{19} X_m + C_{20} Y_m'$$

$$Y_m'' = C_{21} U_m' + C_{22} V_m + C_{23} W_m + C_{24} X_m' + C_{25} Y_m$$

where prime denotes the derivative with respect to x_1 and the coefficients $c(i = 1..25)$ are defined in Appendix C. Comparing these C_i coefficients with reference [17], one can see that some C_i coefficients will have additional terms in comparison with their counterpart in reference [17]. The existence of these extra terms listed in Table 3.1 is because of considering the term "$\frac{Q_2}{R}$" in second equation of motion.

Table 3.1: Modified coefficients C_i for first-order shear deformation theory (FSDT)

C_i	Ref. [17]	Added terms in this thesis
C_7	$\frac{e_{11}e_{27} - e_{10}e_{28}}{c_0} = \frac{(-\beta^2 A_{22} + I_1\omega_m^2)D_{66} - B_{66}(-\beta^2 B_{22} + I_2\omega_m^2)}{B_{66}^2 - A_{66}D_{66}}$	$-\frac{K_s A_{44}(D_{66}/R^2 + B_{66}/R)}{B_{66}^2 - A_{66}D_{66}}$
C_8	$\frac{e_{27}e_{32} - e_{10}e_{30}}{c_0} = \frac{-D_{66}A_{22}\beta/R - B_{66}\beta(K_s A_{44} - B_{22}/R)}{B_{66}^2 - A_{66}D_{66}}$	$-\frac{(K_s A_{44}D_{66}\beta)/R}{B_{66}^2 - A_{66}D_{66}}$
C_{10}	$\frac{e_{12}e_{27} - e_{10}e_{29}}{c_0} = \frac{(-B_{22}\beta^2 + I_2\omega_m^2)D_{66} - B_{66}(-D_{22}\beta^2 - K_s A_{44} + I_3\omega_m^2)}{B_{66}^2 - A_{66}D_{66}}$	$\frac{(K_s A_{44}D_{66})/R}{B_{66}^2 - A_{66}D_{66}}$
C_{12}	$-\frac{e_{34}}{e_{13}} = \frac{\beta A_{22}/R}{K_s A_{55} - N}$	$\frac{(K_s A_{44}\beta)/R}{K_s A_{55} - N}$
C_{22}	$\frac{e_7 e_{28} - e_{11}e_{24}}{c_0} = \frac{A_{66}(-B_{22}\beta^2 + I_2\omega_m^2) - (-A_{22}\beta^2 + I_1\omega_m^2)B_{66}}{B_{66}^2 - A_{66}D_{66}}$	$\frac{K_s A_{44}(A_{66}/R + B_{66}/R^2)}{B_{66}^2 - A_{66}D_{66}}$
C_{23}	$\frac{e_7 e_{30} - e_{24}e_{32}}{c_0} = \frac{A_{66}\beta(K_s A_{44} - B_{22}/R) + B_{66}(A_{22}\beta)/R}{B_{66}^2 - A_{66}D_{66}}$	$\frac{(B_{66}K_s A_{44}\beta)/R}{B_{66}^2 - A_{66}D_{66}}$
C_{25}	$\frac{e_7 e_{29} - e_{12}e_{24}}{c_0} = \frac{A_{66}(-D_{22}\beta^2 - K_s A_{44} + I_3\omega_m^2) - (I_2\omega_m^2 - B_{22}\beta^2)B_{66}}{B_{66}^2 - A_{66}D_{66}}$	$-\frac{(K_s A_{44}B_{66})/R}{B_{66}^2 - A_{66}D_{66}}$

It is more practical and convenient to deal with the first order system of differential equations. So to convert the above system of equations to a state-space form, the following new variables can be introduced

$$Z_{1m} = U_m;\ \ Z_{2m} = U'_m = Z'_{1m};\ \ Z_{3m} = V_m;\ \ Z_{4m} = V'_m = Z'_{3m};\ \ Z_{5m} = W_m; \tag{3.18}$$

$$Z_{6m} = W'_m = Z'_{5m};\ \ Z_{7m} = X_m;\ \ Z_{8m} = X'_m = Z'_{7m};\ \ Z_{9m} = Y_m;\ \ Z_{10m} = Y'_m = Z'_{9m}$$

Considering the new variables defined above, the system of equations stated in equations (3.17) can be written in the form

$$\{\acute{Z}\} = [C]\,\{Z\} \tag{3.19}$$

where $Z = \{Z_{1m}, Z_{2m}, \dots, Z_{10m}\}^T$ and $[C]$ is defined in Appendix C.

Boundary conditions can be defined at both ends of the circular cylindrical shell for simply supported, clamped and free edges as

$$\begin{aligned} &Simply\ support\ (S):\ v = w = \phi_2 = N_1 = M_1 = 0, \\ &Clamped\ (C):\ u = v = w = \phi_1 = \phi_2 = 0, \\ &Free\ (F): N_1 = M_1 = Q_1 = N_6 = M_6 = 0 \end{aligned} \tag{3.20}$$

Equation (3.19) including a set of ten first order differential equations can be solved for natural frequencies or buckling load in conjunction with boundary conditions sated in equation (3.20) using the method proposed in [18].

For bending analysis, a sinusoidal distributed transverse load is assumed as

$$q_\zeta(x_1, x_2) = q_0 \sin\left(\frac{\pi x_1}{L} + \frac{\pi}{2}\right)\cos(\beta x_2) \tag{3.21}$$

Consequently, the governing equations can be written as

$$\{\acute{Z}\} = [C]\,\{Z\} + \{l\} \tag{3.22}$$

where $\{l\}$ is defined in Appendix C. Equation (3.22) consists of ten first order non homogenous differential equations and can be solved along with different combination of boundary condition sated in equation (3.20). A solution of such a system is available in many references (e.g., [17]).

3.4 Numerical results and discussion

3.4.1 Validation

In order to compare the present formulation's results with those appeared in the literature using different methods, the fundamental natural frequency of two simply supported cross-ply laminated cylindrical shells are presented in Table 3.2 (See [15] and [16] for material properties). It is assumed that the total thickness (H) of the shell is the same for different laminations, which implies that the thickness of a ply is different in laminates with different number of layers.

Table 3.2: Comparison of dimensionless fundamental frequency $\bar{\Omega} = \omega L^2\sqrt{\rho/E22}/H$ for two simply supported cross-ply cylindrical shells ($L/R = 5, R/H = 20$)

	Present solution	Matsunaga [16]	Messina and Soldatos [15]
[0/90]	92.38	92.32	92.42
[0/90/0]	92.58	92.55	92.57

The results agreed well with references [15] and [16] and show the efficiency of the present analytical solution.

3.4.2 Buckling and natural frequency

Numerical results are obtained for material properties stated in Table 2.2. The effect of two different lamination schemes along with various boundary conditions on dimensionless critical buckling is studied for assorted geometrical specification in Table 3.3. For all cases, results with

and without considering additional terms mentioned in Table 3.1 are presented for comparison purposes (for $L/R = 1$, the results without considering additional terms are also presented in [17]).

As a general trend, the larger the number of degrees of freedom at the boundaries, the lower the critical buckling loads (e.g., buckling load for SS boundary condition is lower than SC boundary condition and CC boundary condition has the highest buckling load). As an important observation, one can see that upon adding the terms mentioned in Table 3.1, the dimensionless critical buckling load decreases up to about 14.5 percent for some cases. The effect of these terms in decreasing the dimensionless critical buckling load is getting more evident as the length-to-radius ratio (L/R) increases.

Table 3.3: Comparison of dimensionless critical buckling load ($\breve{N} = \frac{NL^2}{100h^3E_2}, \frac{R}{H} = 10$)

		SS			SC			CC		
L/R	**Lamination**	**Without**	**With**	**Difference%**	**Without**	**With**	**Difference%**	**Without**	**With**	**Difference%**
1	0/90	0.1670*	0.1525	9.51	0.1969*	0.1851	6.37	0.2508*	0.2406	4.24
	0/90/0	0.2813*	0.2765	1.73	0.3452*	0.3411	1.20	0.4197*	0.4168	0.69
5	0/90	4.1739	3.8124	9.48	4.2108	3.8195	10.24	4.3197	3.9212	10.16
	0/90/0	5.3648	4.6818	14.59	5.4668	4.9161	11.20	5.8977	5.5092	7.04
10	0/90	16.6953	15.1163	10.44	16.7283	15.1557	10.38	16.8366	15.7176	7.12
	0/90/0	20.7243	18.7271	10.66	20.9740	18.8686	11.16	21.6520	19.6643	10.11

*** These results were presented in** [17]

The effect of two different lamination schemes along with various boundary conditions on dimensionless fundamental frequency is studied for two length-to-radius ratios (L/R) and shown in Table 3.4. For all cases, results with and without considering additional terms mentioned in Table 3.1 are presented for comparison purposes.

Table 3.4: Dimensionless fundamental frequency ($\breve{\omega} = \frac{\omega L^2}{100h}\sqrt{\frac{\rho}{E_2}}, \frac{R}{H} = 5$)

		SC			CC			FC		
L/R	**Lamination**	**Without**	**With**	**Difference %**	**Without**	**With**	**Difference %**	**Without**	**With**	**Difference %**
2	0/90	0.1697*	0.1543	10.04	0.1876*	0.1740	7.82	0.0914*	0.0873	4.81
	0/90/0	0.1945*	0.1895	2.64	0.2129*	0.2085	2.11	0.0988*	0.0913	8.21
10	0/90	0.9238	0.7588	21.74	0.9801	0.8219	19.25	0.6065	0.3321	82.62
	0/90/0	0.8949	0.8327	7.47	0.9616	0.9042	6.35	0.4981	0.3708	34.33

*** These results were presented in** [17]

For all cases regardless of which lamination and what kind of boundary condition, dimensionless fundamental frequency for $L/R = 2$ is less than that of $L/R = 10$ for the same lamination and boundary condition.

Looking at the three boundary conditions, one can see that both end clamped (CC) shells have the highest dimensionless fundamental frequency. One end simply-supported and one end clamped (SC) shells have lower frequency than CC. Shells with one end free and the other end clamped (FC) have the lowest dimensionless fundamental frequency when comparing same lamination and L/R ratio.

An important observation can be seen on the effect of the additional terms mentioned in Table 3.1 on fundamental frequency. The difference in results reaches to 82 percent discrepancy in some cases although in some cases it is as small as 2 percent. Another explanation for why these additional terms should be considered in the analysis can be drawn by comparing the fundamental frequency of [0/90] and [0/90/0] lamination for all shells with $L/R = 10$. As a rule of thumb, one can expect higher fundamental frequency for [0/90/0] lamination than [0/90] lamination because the former is stiffer than the later. This is due to the existence of two 0 layers at the top and bottom side of the [0/90/0] lamination. But as can be seen from Table 3.4, this expectation is not

met without considering the additional terms (for shells with $L/R = 10$) while if one added the additional terms to analysis, this expectation would be met.

3.4.3 Bending analysis

The material properties used for bending analysis are listed in Table 2.3 (these properties are selected the same as [17] for comparison purposes).

The effect of various length-to-radius ratios (L/R), boundary conditions, and two laminations on dimensionless center deflection is presented in Table 3.5. All results are obtained with and without considering additional terms mentioned in Table 3.1 for comparison purposes. As could be expected, the dimensionless center deflection ($\breve{w}$) increases as L/R increases. The effect of the additional terms mentioned in Table 3.1 on dimensionless deflection, as can be seen, is considerable. Including these terms increases the deflection up to 35% in some cases. This effect gets more obvious as the length-to-radius ratio increases.

Table 3.5: Comparison of dimensionless center deflection ($\breve{w} = \frac{w\left(\frac{l}{2},0\right)h^3E_2 10^2}{q_0R^4}, \frac{R}{H} = 10$)

		SS			CC			FC		
L/R	Lamination	Without	With	Difference %	Without	With	Difference %	Without	With	Difference %
1	0/90	0.2535*	0.2621	3.28	0.2132*	0.2191	2.69	0.4988*	0.5188	3.85
	0/90/0	0.2257*	0.2262	0.22	0.1795*	0.1797	0.11	0.4303*	0.4313	0.23
5	0/90	5.4858	5.8696	6.54	4.9559	5.2905	6.32	12.9240	14.7059	12.12
	0/90/0	5.3832	5.4477	1.18	4.7366	4.7848	1.01	12.8086	13.2581	3.39
10	0/90	25.5089	29.4821	13.48	19.9934	22.6742	11.82	48.8775	75.7760	35.50
	0/90/0	25.0687	26.2051	4.34	20.0414	20.7499	3.41	56.2918	66.4053	15.23

*** These results were presented in** [17]

Figure 3.2 and Figure 3.3 show the effect of radius-to-thickness ratio on dimensionless center deflection for two laminations and two boundary conditions. One can see that, as a general trend, the dimensionless deflection decreases as the radius-to-thickness ratio increases for both

laminations. Furthermore, the dimensionless center deflection is always more for Free-Clamped boundary condition (FC) than for both end simply supported (SS) as expected.

The effect of the additional terms mentioned in Table 3.1 on dimensionless center deflection is also shown in Figure 3.2 and Figure 3.3 (the curve including "with" in the legend). Including these terms always increases the deflection regardless of boundary condition and lamination. However, one can notice that for FC boundary condition this effect is more obvious that for SS boundary condition.

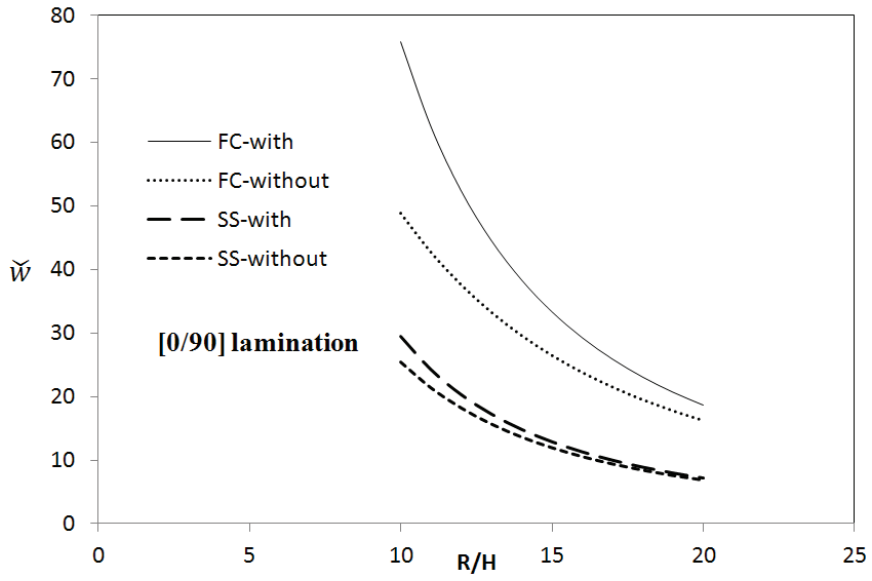

Figure 3.2: Dimensionless center deflection ($\breve{w} = \frac{w\left(\frac{l}{2},0\right)h^3E_2 10^2}{q_0R^4}$) versus R/H ratio for [0/90] (*L/R*=10)

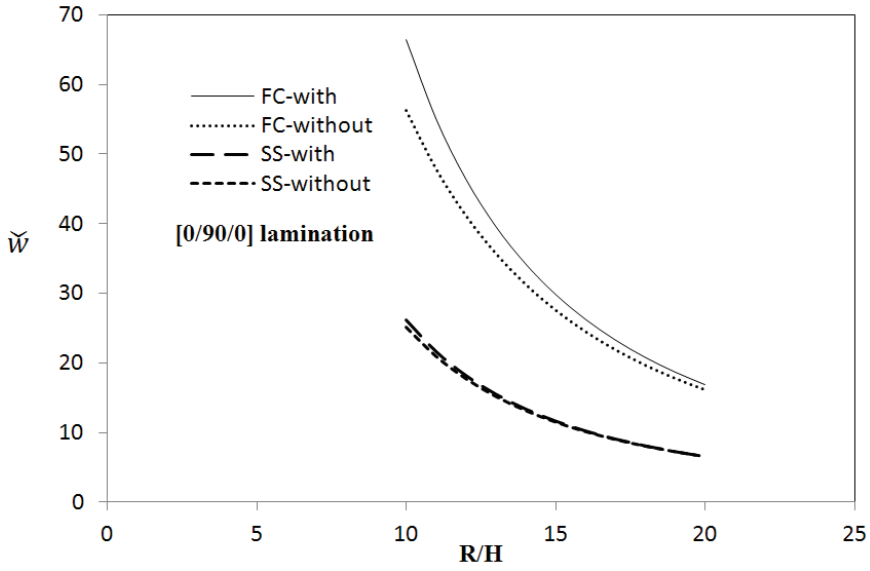

Figure 3.3: Dimensionless center deflection ($\breve{w} = \frac{w\left(\frac{l}{2},0\right)h^3E_2 10^2}{q_0R^4}$) versus R/H ratio for [0/90/0] (*L/R*=10)

3.5 Conclusions

First-order shear deformation shell theory is used to study bending, buckling and fundamental frequency of cross-ply circular cylindrical shells. The effects of lamination scheme, length-to-radius ratio, radius-to-thickness ratio, and boundary condition on shell behavior are studied.

The effect of assumed displacement field on both formulation and results is determined. It is shown that assumed displacement field has a significant effect on numerical results in some cases. Consequently, it is of substantial importance to choose an appropriate displacement field.

Chapter 4

Experimental approach

4.1 Introduction

As it mentioned earlier, bending is the dominant load on cylindrical and conical shells in many applications (e.g., helicopter tail boom) and buckling due to bending is the main failure concern for these structures. However, experimental setups to study bending and buckling behavior of cylindrical and conical shells under pure bending load are rare. Moreover, experimental results for buckling of composite conical shells under bending are non-existent to the best of author's knowledge. Only two experimental setups to study cylindrical shells under pure bending have been found in the literature. The first one was developed by Fuchs, Hyer and Starnes [63] and sponsored by NASA Langley-Virginia Polytechnic Institute in 1992. Their investigation was limited to cylindrical shells. The second setup developed, more recently, in 2009 by Blom et al. [64]. They made a bending fixture installed on a MTS test bench which provides the loading power. The study was limited to a composite cylinder and the composite cylinder was too stiff to be buckled in the gage area in that study.

In order to study bending and buckling due to bending behavior of conical shells, a setup has been designed, manufactured and installed at CONCOM laboratory. The work of Fuchs, Hyer and Starnes [63] served as the benchmark for the design of most of the setup. Due to load increases and in order to accommodate different sample geometries in the setup, several iterations were made on all parts. The setup shown in Figure 4.1 is composed of three sections including

structural components, loading unit, and instrumentation which will be discussed in details in upcoming sections.

The load is created by two hydraulic cylinders and converted to bending moment through the arms connecting the hydraulic cylinders to the main assembly. This bending moment, then, is transferred to the test specimen using a set of Back-plate Adaptor Plate, and inner and outer ring (see section 4.2). There are two mechanisms which transferred the load to the specimen: first, a series of radial bolts is inserted between the inner and outer ring and passes through the test specimen on the tension side. These bolts help to prevent the sample from slipping out of the rings during the test. Second, the specimen is potted with Low Melting Point Alloy (LMPA) which keeps the sample firm between the inner and outer ring and transfer the load smoothly to the specimen skin (see section 4.2.8).

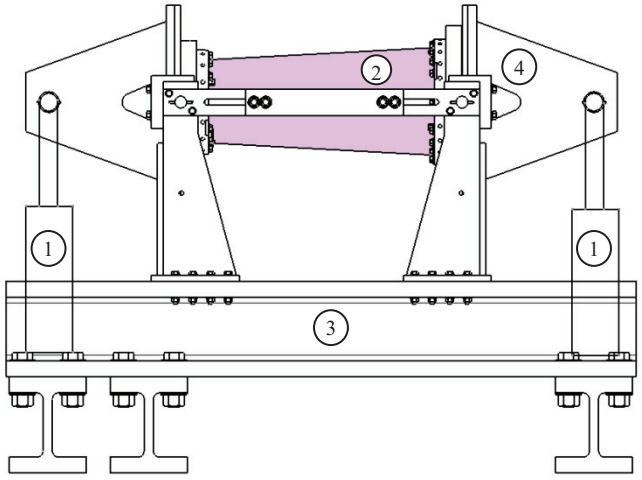

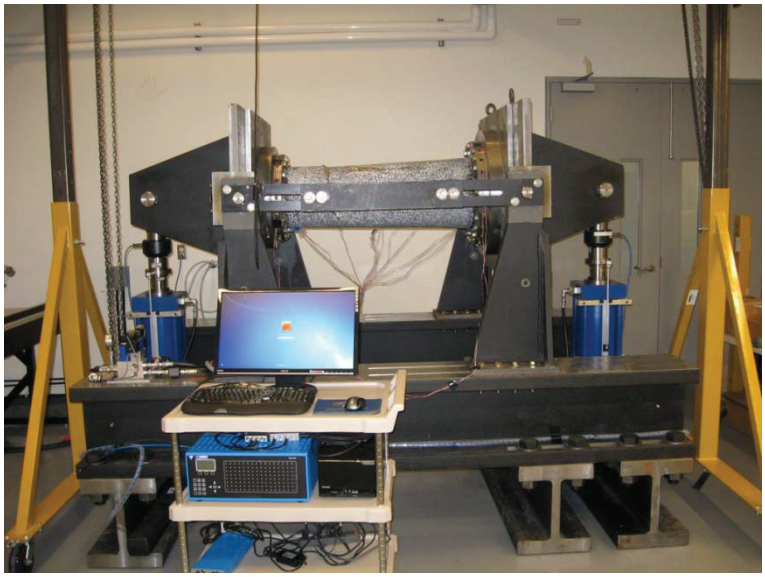

Figure 4.1: Composite tube bending test setup: 1- Hydraulic cylinders, 2- Test specimen, 3- Reaction frame, 4- Moment Arm assembly

The loading unit has been designed in such a way to assure applying equal bending moment on both sides of the sample, even when the sample is not symmetric (i.e., conical shells). The characteristics and functioning of the loading unit is explained in section 4.3.

Regarding the instrumentation, different methods used in the literature for detecting the buckling of shells are introduced in the following section and methods incorporated in our setup would be discussed in detail in section 4.4.

4.1.1 Detecting the onset of buckling

Buckling is usually a very quick phenomenon, meaning the onset of the buckling and its transition to postbucking usually happen within a fraction of a second. This time differs for various types of loading, but the shortest time could be seen in buckling under axial compression and bending load. This nature of buckling incident makes its recording difficult.

Having a large drop-off of applied load, overall buckling could be recognized easier than the exact initiation of buckling. Many experimenters considered the “puck” sound and the load drop at buckling as a sign of the onset of buckling. Usually more than one method is used to detect the onset of buckling. For example, Tenerelli and Horton [72] used three different methods to investigate local buckling of cylindrical shells. First, a concentric mandrel was fitted inside the samples to report the buckling through a buzzer when the contact between the shell and mandrel was conducted. Second method was a ring-type load cell which detected the buckling by the drop-off in applied load. The last device used for this test was a photonic sensor which could report the sudden lateral displacement at buckling using light rays. Any variation in the shell surface led to the variation in the reflected light collected by the probe and could be analyzed for detecting of the buckling [51].

4.1.1.1 High-speed photography

High-speed photography is an approach to study the initial buckling behavior of shells. However, triggering the camera could be a problem due to rapid occurrence of the buckling, especially in axial compression and bending. This means sometimes the bucking happened before the camera could get started for catching adequate photos of the shell. But if the time and the location of the buckling could be anticipated properly, very good records could be obtained. Modern high-speed cameras can take pictures up to 10,000 frames per second or more (even 100,000 frames per second). These speeds are usually more than enough for recording the onset of buckling, but then the total time span could be very short. Recording of the postbuckling behavior is less problematic due to slower nature of the phenomenon [51].

4.1.1.2 Strain gages and displacement transducers

Strain gages are usually implemented in pairs in a circumferential row to detect the onset of buckling. Measuring the strains, this circumferential row could be used to assess the symmetry and uniformity of load. If the load is uniform and the sample is without serious imperfection, consequently the buckling pattern would be more or less unique and the location of buckling could be predicted properly and even one circumferential row of strain gages would be sufficient for detecting the beginning of buckling. But if this is not the case and the buckling nature is more local and the location of buckling strongly depends on imperfections, many strain gages need to be applied to detecting the onset of buckling and even this cannot guarantee the correct detection. When the postbuckling behavior is milder, strain gages could be employed for recording of postbuckling behavior. As an example, Singer [73] studied the influence of stiffeners on the buckling of axially compressed cylinders and cones, using 6-12 gages around the circumference at each vertical position and total number of 38-48 strain gages per sample.

Nowadays, data acquisition system becomes more advanced and automatic, making the use of extensive strain gages convenient while it was not popular in the past because the lack of such data recording system. As a result, using a very large number of strain gages is a worthwhile option considering its advantages (e.g., using Southwell method).

Displacement transducers are also widely used by researchers to record the postbuckling behavior and obtain the buckling pattern. Contact or noncontact sensors could be employed for measurement of deformed shapes of the buckled shells as well as recording the initial geometrical imperfections. For example, Yamaki et al. [74] successfully applied a deflection transducer that

worked in conjunction with a strain gage to obtain postbuckling contours of cylindrical shells [51].

4.1.1.3 Shadow Moiré method

The word “Moiré”, a French name for a wavy pattern fabric, is used to describe the fringe interferences that happen whenever two geometrical similar patterns, usually parallel lines, are superimposed. The result is Moiré patterns used to measure displacements of surface and consequently strains. The principles of this technique could be explained as follows: there are two gratings used to obtain the Moiré patterns; the first is called model grating which may be engraved on the surface of the sample and shows the changes from the initial or reference state of the surface into the deformed shape. Second grating called master grating is used to characterize the changes in the model grating. The superposition of these two gratings would result in the Moiré patterns.

Moiré techniques could be categorized into four methods; intrinsic Moiré, reflection Moiré, shadow Moiré, and projection Moiré. The first two methods are used for determination of in-plane strains and measurement of slopes of the surface with respect to the reference sate, respectively, and therefore are not usually considered in buckling and postbuckling studies. Shadow Moiré and projection Moiré, which is an extension of the shadow Moiré, are used to measure out-of-plane displacements. In shadow Moiré method, the sample’s surface is covered by a matte white paint. A reference grating made up of black equidistance line placed on a glass plate is located in the front of the surface. Then a parallel light beam is directed at an oblique angle through the grating onto the sample’s surface. The Moiré patterns would happen as a result of interference between the reference grating and its shadow [51].

The main interest in buckling and postbuckling studies is to measure out-of-plane displacements and therefore shadow Moiré and projection Moiré methods are considered in that case. As an example, Kim [75] investigated the biaxial buckling of laminated composite plate in CONCOM laboratory at Concordia University using shadow Moire method.

4.1.1.4 Southwell's method

Southwell [76] introduced a method to obtain the critical buckling load for a column from experimental results. He suggested that the load-deflection curve could be curve fitted with a hyperbola and transformed to a line in which the slope of the line is the measure of critical buckling load.

For shells, Southwell's method was considered for parametric studies and nondestructive method for determination of buckling load. Application of this method for shells was first considered by Donnell [77] as he applied it to cylindrical shell under axial compression. According to Donnell, the conditions of applicability of Southwell's method for shells was either the amplitude of the radial deflection and initial imperfection are small as compared to about five times the thickness of the shell, or the initial imperfection is negligible compared to radial deflection. Southwell prediction results were a bit higher than the experimental data [51].

4.1.1.5 Optical 3D deformation and strain measurement technique

Optical 3D deformation measuring system is a non-destructive optical tool for shape, deformation and strain analysis of solid materials. This system works based on the combination of photogrammetry and Digital Image Correlation (DIC) techniques for materials analysis.

Due to rapid new developments in high resolution digital cameras and computer technology, the applications of the DIC system has been broadened, in both static and dynamic applications, and it has shown to be a flexible and useful tool for deformation analysis.

Considering that this technique is quite new and its application in composite material is not well known, in order to evaluate and verify its capability and to justify its application particularly in composite material field, an experiment was designed at CONCOM laboratory which is explained in section 4.4.1.3.

Following the successful results obtained from the above mentioned experiment, the DIC system is incorporated in the composite tube bending test setup. The working principles of DIC system are discussed in section 4.4.1.

4.2 Structural components

4.2.1 Design requirements

The structural parts of the setup are designed with the following criteria in mind:

- From stress point of view, it should be able to withstand up to 1,500,000 lbf-in (169.48 kN.m) moment
- Under maximum load, the deflection should stay less than 0.01 inch (0.254 mm) (this is necessary as the fixture is assumed to be non-deformable solid part)
- It should be able to handle samples with different lengths between 30 to 48 inches (762 to 1219 mm, adjustable length)
- It should be able to handle samples with different cross section shapes and dimensions (from 1 to 33 inches (2.54 to 838.2 mm))

The structural parts of the set up are shown in Figure 4.2 and the description of its components comes after.

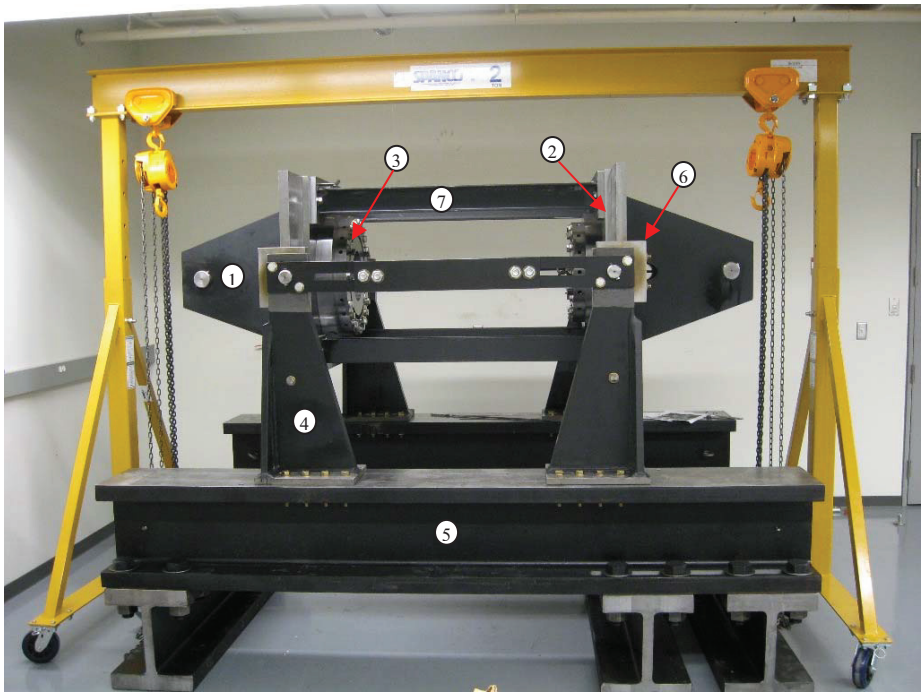

Figure 4.2: Structural parts of the bending test setup: 1- Moment Arm assembly, 2- Adaptor Plate, 3- inner and outer ring, 4- Vertical Support, 5- Reaction Frame, 6- Pivot Bracket, 7- Installation Spacer Beam

4.2.2 Moment Arm and Back-plate

The Moment Arm is the component that converts the vertical force generated in hydraulic cylinder to the moment, which is then transferred to the sample. After several iterations and considering different possible shapes (for minimizing the deflection and being simple from manufacturing point of view), eventually the moment arm has the shape shown in Figure 4.3. It is composed of two plates held together with brackets to better distribute the load across the Back-

plate. In order to display the connecting plates, one of the plates is shown as transparent in Figure 4.3. The Moment Arm is pinned from one side to the clevis joint of the hydraulic cylinder and bolted to the Back-plate on the other side using tapped holes in the Moment Arm, seen in Figure 4.3, and counter bored holes in the corresponding locations on the Back-plate, seen in Figure 4.4. The selection of bolts to fasten the Moment Arm to the Back-plate rather than welding was because welds would cause warping of the Back-plate. This warping could prevent the Adapter Plate (see section 4.2.3) from resting flush against the Back-plate surface.

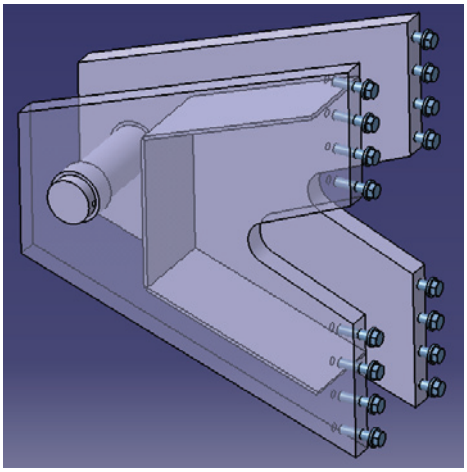

Figure 4.3: Moment Arm

The Back-plate is a 1.5-in thick plate (see Figure 4.4) which transfers the load from the Moment Arm to the Adaptor plate uniformly. It has 33 inches height and 51 inches length which determines the cross section size limitation of the sample that can be tested by the setup.

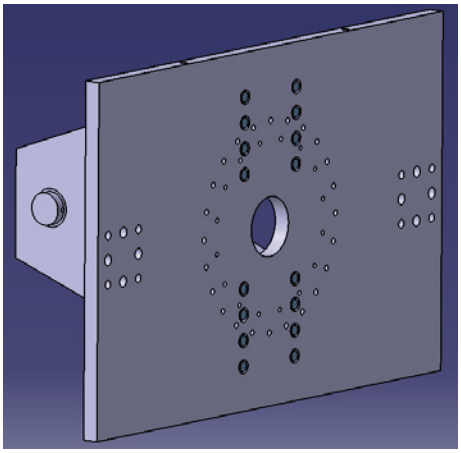

Figure 4.4: Back-plate

4.2.3 Adaptor Plate

The concept of adding an Adaptor Plate enables the setup to accommodate different sample geometrical shapes by using an appropriate set of Adaptor Plates. Another purpose of having the Adapter Plate is to ease installation and removal of the specimen once it has been fixed to the rings. Since the Back-plates are heavy and large, the use of smaller Adapter Plates allows easier manipulation of the sample once mounted between inner and outer rings. It also prevents the Low Melting Point Alloy (LMPA), see section 4.2.8, from flowing out from between the rings. Using the Adapter Plate, the Back-plate has less bolt holes and consequently has more structural rigidity. Because the Adapter Plate and Back-plate have different number of bolt holes, some of them (which connect the rings to the Adapter Plate) had to be counter bored, as shown in Figure 4.5.

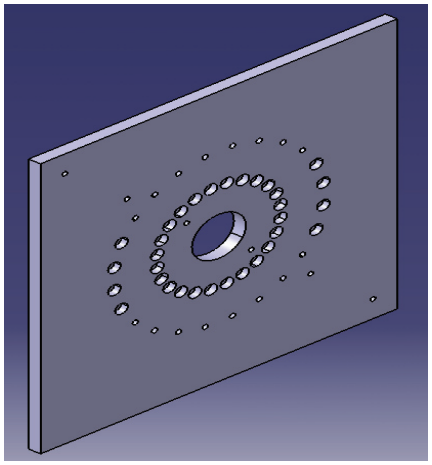

Figure 4.5: Adaptor Plate

4.2.4 Vertical Support and Pivot Bracket

The Vertical Support is the component which supports the axis of rotation of the Back-plate. It is bolted from the bottom to the Reaction Frame (section 4.2.7) and pinned from the top to the Pivot Bracket. The Vertical Supports are the links which transfer the load to the Reaction Frame and they are under high tension load during the test. The setup has four Vertical Supports of which two of them are affixed on the one side and the other two are movable and can be adjusted for different sample lengths. The final design of Vertical Support is shown in Figure 4.6.

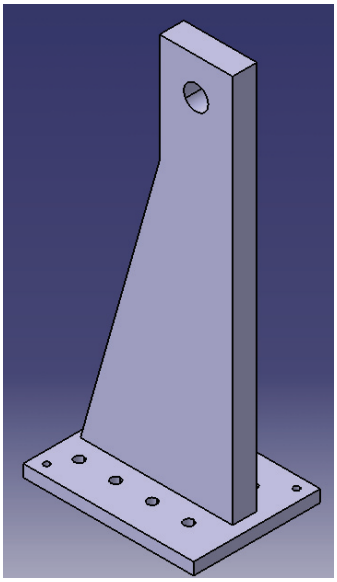

Figure 4.6: Vertical Support

The Pivot Bracket (Figure 4.7) is the connecting part between the Back-plate and the Vertical Support. It is designed in such a way that the axis of rotation of the setup is where the test specimen comes into contact with the Adaptor Plate. This way the entire test specimen (including the clamped ends) would be under bending load.

Due to high shear load (combination of torsion and transverse shear) on the Pivot Bracket, it is connected by four ¾-inch diameter shear pins to the Back-plate. Since it is also under bending, four 0.5-inch bolts are used to connect it to the Back-plate and to withstand this bending load. Welding is avoided because of possible warping that can occur on the Back-plate.

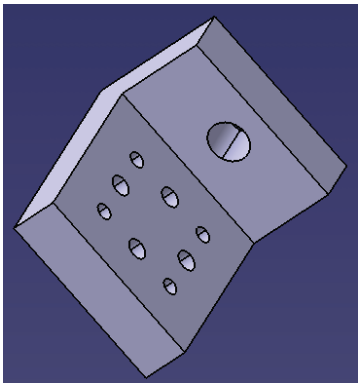

Figure 4.7: Pivot Bracket

4.2.5 Inner and outer ring

The test specimen seats between two rings, called inner and outer ring. The bending load is transferred to the Low Melting Point Alloy (LMPA) through these two rings and then applied to the specimen. A cross section view of the rings and specimen is shown in Figure 4.8. The outer ring has one step toward the inside and the inner ring also has one step toward the outside (see Figure 4.8). These two steps provide a self-locking mechanism and prevent the test specimen from sliding out of the rings during the test by getting benefit of the LMPA shear strength.

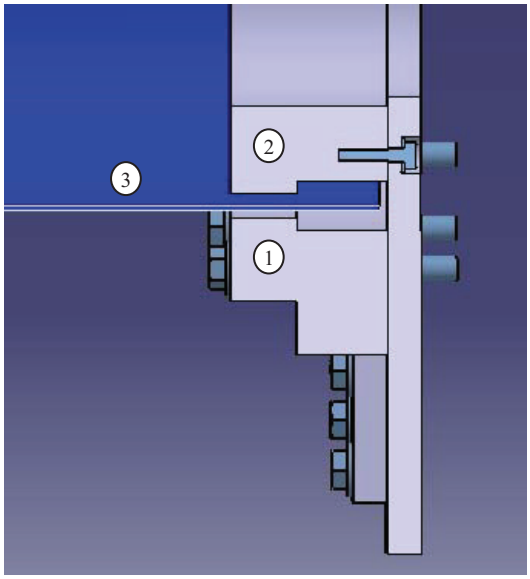

Figure 4.8: Cross-section of the rings: 1- outer ring, 2- inner ring, 3- specimen

The inner ring is bolted to the Adapter Plate while the outer ring is bolted to both the Adapter Plate and the Back-plate. The outer ring has radial holes which allow for cross bolts to pass through the specimen and to be tightened to the radial bolt holes in the inner ring (see Figure 4.9).

There is also a mechanism for centering the test specimen between two rings during installation which is basically three set screws mounted at 120 degree intervals (Figure 4.9).

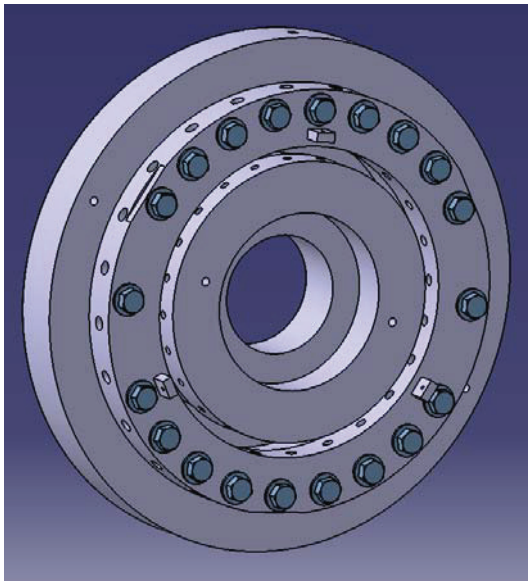

Figure 4.9: Inner and outer rings showing radial bolt holes

4.2.6 Installation Spacer Beams

The test specimen would be installed on the rings and Adaptor Plates on floor and then the assembly would be installed on the setup. In order to make sure that the two Adaptor Plates attached to two ends of the specimen are parallel, Installation Spacer Beams have been designed to give the assembly structural integrity on the floor. Another important function of the Spacer Beams is to prevent the specimen from any unwanted pre-loading that may occur during installation and manipulation on floor.

Installation Spacer Beams are basically four I-beams, two of which are installed on the top of the assembly and are connected by two plates. The other two I-beams are installed on the bottom of the assembly (Figure 4.10).

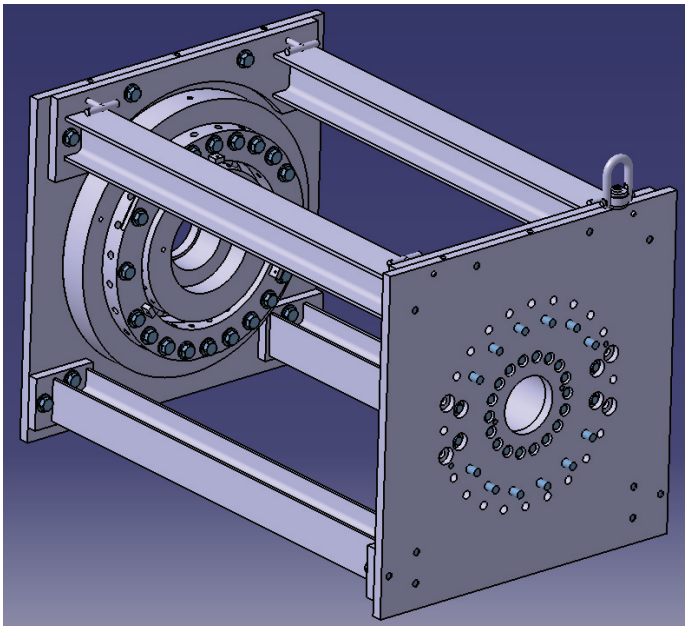

Figure 4.10: 4.2.6 Installation Spacer Beams inside the assembly

4.2.7 Reaction Frame

Due to the high magnitude of the load and weakness of the concrete floor in tension, a Reaction Frame composed of five I-beam has been designed. The closed shape of the Reaction Frame (see Figure 4.11) makes all the reaction forces stay on the frame and not to be transferred to the floor. So the only load acted on the concrete floor would be the weight of the setup which would be in compression and easily withstood by the floor.

Furthermore, the use of I-beams allows the frame to withstand the large moments and forces created by the application of the load. There are two longitudinal and three cross I-beams in the Reaction Frame. The longitudinal I-beams have been designed with slots on one end to allow the adjustment of cross I-beams when tests are being done on specimens of different lengths. The reason for having three cross I-beams rather than two is to keep the structural integrity of the

frame (perpendicularity and parallelism) while moving one of the cross I-beams to adjust the setup length.

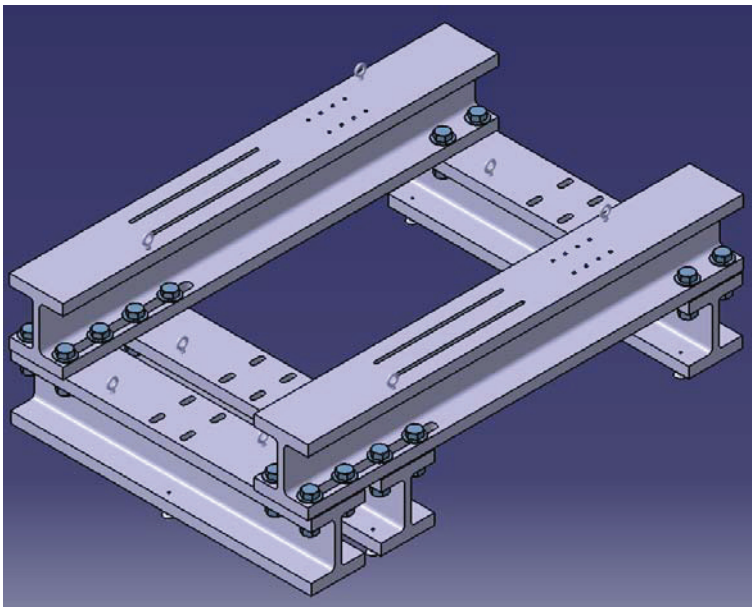

Figure 4.11: Reaction Frame

4.2.8 Low-temperature Melting Point Alloy technique

In order to provide the most uniform load transfer around the circumference of the specimen and also to keep the specimen in between the inner and outer ring, the specimen would be potted by Low Melting Point Alloy (LMPA). LMPA is a Bismuth alloy which has a melting point of 75 degree of Celsius and can be melted easily and potted around the specimen. The use of a LMPA to restrain the specimen and to transfer the load to the test specimen was an idea taken from the reference [63].

In order to examine the bonding strength between the LMPA and the specimen and to find out the best possible configuration, a series of simple axial tests have been performed. A composite plate

with dimensions of 6 inch by 12 inch was selected for the test. The top of the composite plate was fastened to a top bracket, and the bottom was submerged to a depth of 3 inches in the LMPA held inside a bottom bracket. The top and bottom brackets were then placed in an MTS machine (see Figure 4.12) and the force required to remove the specimen from the LMPA was then measured to find the best configuration to maximize the force.

Figure 4.12: LMPA test setup

It was found that when the stepped tabs were added to the bottom of the composite plate (which is submerged in the LMPA), the required load to remove the specimen increases dramatically. This is due to the fact that shear strength of the LMPA resists the slippage of the specimen rather than the bonding strength between the composite plate and the LMPA.

Consequently, this technique was adopted as a self-locking technique to be used in the bending setup by designing the steps for the inner and outer ring (as mentioned in section 4.2.5) on one hand and by implementing tabs on the test specimen on the other hand.

4.3 Loading unit

4.3.1 Design requirements

The loading unit is the section which generates the required load to be applied to the specimen. It should meet the following requirements:

- It should be powerful enough to exert at least 75,000 lbf (334 KN), which provides 1,500,000 lbf-in (169.48 kN.m) in term of bending moment)
- The loading rate should be adjustable
- It should exert exactly the same amount of force (and consequently moment) on both side of the test specimen even if the sample is not symmetric (e.g., conical shape)
- Loading rate should be independent from the resistance load created by the test specimen
- It should be able to handle the back pressure during unloading phase

In order to satisfy the above mentioned requirements, a custom-made control unit is designed which is explained in the following section.

The required forces are generated by two hydraulic cylinders which each have 8in diameter and 10in stroke each. At the pressure of 1500 psi, the generated force would be 80,110 lbf, which exceeds the requirement.

4.3.2 Control unit

Considering the above mentioned design requirements, a control unit, shown schematically in Figure 4.13, has been designed to regulate the hydraulic oil flow. The hydraulic power is supplied by the Hydraulic Power Unit which includes a tank, a vane pump, filters, a heat exchanger and a relief valve. The flow of the supplied hydraulic oil, then, would be adjusted by a flow control valve which is pressure-compensated valve. That means the flow rate (which could be translated to loading rate) would be independent of the upstream resistance. In other word, if any failure happens during the test and the specimen resistance is suddenly changed, the loading rate should not be influenced by that. This was one of the design requirements mentioned above.

A directional control valve with three positions was used to control the oil flow direction. It is a solenoid-activated valve and can be operated in loading, unloading, and stop mode. If the stop mode is activated during the test, all the ports from the hydraulic cylinders would be closed and the movement of the setup would be stopped while the specimen is under load. There is a counterbalance valve after the directional control valve which assures a smooth unloading stage and damps the back pressure produced by the specimen during unloading. It also has a pilot check valve inside its construction which acts a locker. That means this locker would prevent any flow to pass to the tank until the directional control valve is in unloading position. This is important specially if one wants to keep the test specimen under a constant bending load (in the stop mode) without losing the load due to leak inside the directional control valve.

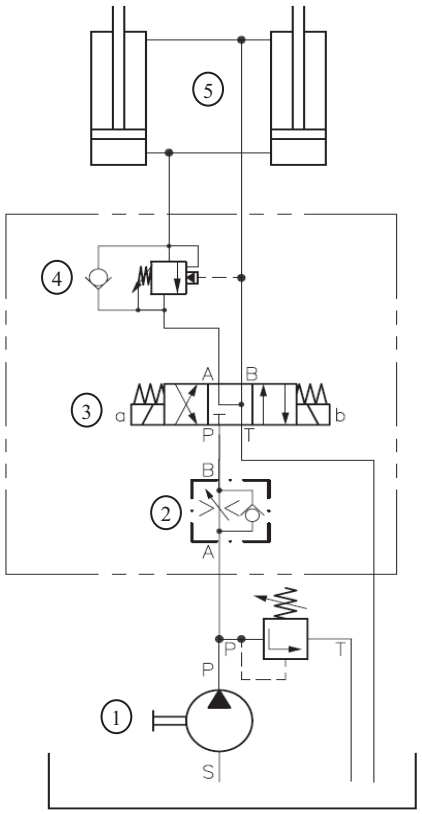

Figure 4.13: Hydraulic circuit: 1- Hydraulic Power Unit, 2- flow control valve, 3- directional control valve, 4- counterbalance vale, 5- hydraulic cylinders

Two hydraulic cylinders were connected to one another by hoses to make sure the same pressure (load) would be applied on both sides of the setup.

4.4 Instrumentation

The composite tube bending setup has been equipped to measure the following parameters:

- Deformation and strain using Digital Image Correlation (DIC) system
- Strain using strain gages
- Load using load cells

- Displacement of the hydraulic cylinders using non-contact position transducer

Details of the instrumentation used in the setup are explained in the following sections.

4.4.1 Deformation and strain measurement

The setup is equipped with a 3D Digital Image Correlation (DIC) system which is capable of measuring deformation and strain of the specimen during the test. The DIC system is equipped with four cameras (instead of two) working simultaneously which allows one to be able to measure a large area of interest on the test specimen. The measuring principle, system advantages, and the evaluation of the DIC system to be used on the composite specimen are explained in the upcoming sections.

4.4.1.1 Measuring Principle

Using a stereoscopic sensor setup, each object point is focused on a specific pixel in the image plane of the respective sensor. Knowing the imaging parameter for each sensor (intrinsic parameter) and the orientation of the sensors with respect to each other (extrinsic parameter), the position of each object point in three dimensions can be calculated. Using a stochastic intensity pattern on the object surface, the position of each object point in the two images can be identified by applying an image correlation algorithm.

In classical image correlation the deformation of an object is determined by observation with a CCD camera. Then a digital image correlation process determines the shift and/or rotation and distortion of little facet elements determined in the reference image. Such correlation algorithms can determine the maximum of the displacement with an accuracy of up to 1/100 pixel. This

procedure allows the determination of the object deformation in a plane parallel to the image plane of the camera.

For 3D measurement, two cameras are used. If the object is observed by two cameras from different directions, the position of each object point is focused on a specific pixel in the camera plane. If the positions of the two cameras relative to each other and the magnifications of the lenses and all imaging parameters are known, the absolute 3-dimensional coordinates of any surface point in space can be calculated, (Figure 4.14). If this calculation is done for every point of the object surface, the 3D surface contour of the object can be determined in all areas, which are observed by both cameras. However, it is important that the object surface shows enough structure to allow the algorithms to correlate identical points from both cameras.

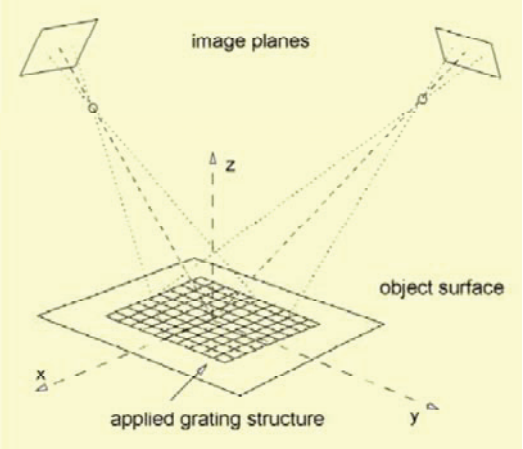

Figure 4.14: Principle of 3D image correlation with 2 cameras (Ref. [78])

Once the 3D contour has been determined, the second step in digital 3D correlation is the measurement and determination of the three-dimensional deformation of the object surface. This process is carried out by correlation of the images, taken by both cameras with their original reference images.

In Figure 4.15, the displacement vector of a surface element is shown. The center point P has been displaced from the reference state *u* to the deformed state *v*. Additionally, the surface element has been rotated, tilted, and distorted. With the known displacement vectors of each surface point and the reference contour, the strains can be calculated. They can be derived either directly by the differentiation of the displacements of adjacent surface points, or by the analysis of the distortion of each local facet, which has been used for correlation [78].

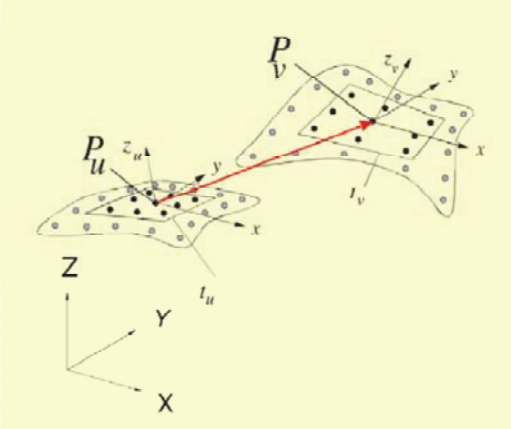

Figure 4.15: Deformation of 3D displacement vector (Ref. [78])

4.4.1.2 System Advantages

The DIC system has the following advantages in comparison with traditional strain measuring methods [79]:

- Full-Field Measurements: it allows one to see deformations (including strains and out-of-plane displacement) over an entire area. So measurements are not limited to single points,

which helps one to easily identify critical points, even in complicated structures or under complex loading conditions.

- Non-Contact Measurements: using this system eliminates strain gages, lacquers, gratings, and wiring. There is no mechanical interaction with the sample, no need for precise placement in order to get the results and no influence upon vibrating specimens. Samples can be prepared relatively fast and measured without undesirable influence from clips and gages.
- Safe and simple: this system uses white-light illumination and no optical isolation table is needed for accurate measurements.

4.4.1.3 Evaluation of the DIC system

As was pointed out, 3D DIC system has the ability to measure full field deformation and calculate the strains over the whole region. To evaluate the ability of the DIC system in detecting buckling and measuring the strain and justify its application, particularly in the field of composite materials, a buckling test under compression axial load on a composite tube was performed at CONCOM laboratory with DIC system from LaVision Company (called “StrainMaster”). The composite tube was made of graphite-epoxy pre-preg, using hand lay-up and autoclave process. Additional layers of pre-preg were wrapped at both ends of the cylinder to strengthen cylinder at the ends to prevent it from failure in this region.

Regarding the nature of the techniques used in measuring the surface deformation, the specimen needed some preparation before the test. The sample preparation included painting the sample surface with a white background and applying some random black spots using spray paint technique. After this step, the sample was ready for the test. Test setup is shown in Figure 4.16.

At the beginning of the test, two cameras of the system were calibrated by moving a calibration plate in front of the cameras using standard calibration panels.

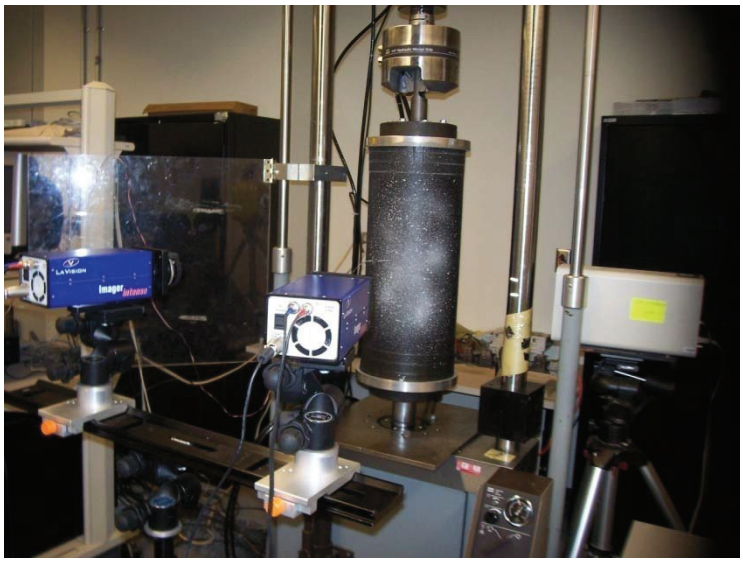

Figure 4.16: Test setup for evaluating the ability of DIC system to detect buckling and to measure strains

Axial load was exerted through the aluminum end plates by the rate of 1 mm/min. After two minutes, buckling occurred with a loud sound and visually recognizable deformation on the tube surface (Figure 4.17).

Figure 4.17: Buckling pattern on the axially loaded composite tube

In order to evaluate the DIC system, two strain gages were applied near the middle of the composite tube axis. The axial strain measured by strain gage and DIC system before and after buckling is plotted in Figure 4.18 and Figure 4.19, respectively.

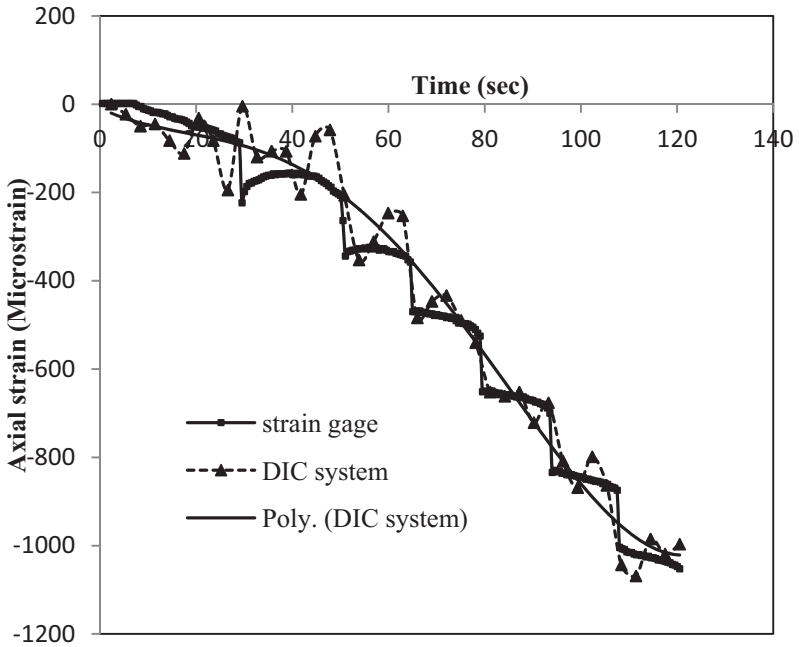

Figure 4.18: Comparison between strain gage and DIC system result before buckling

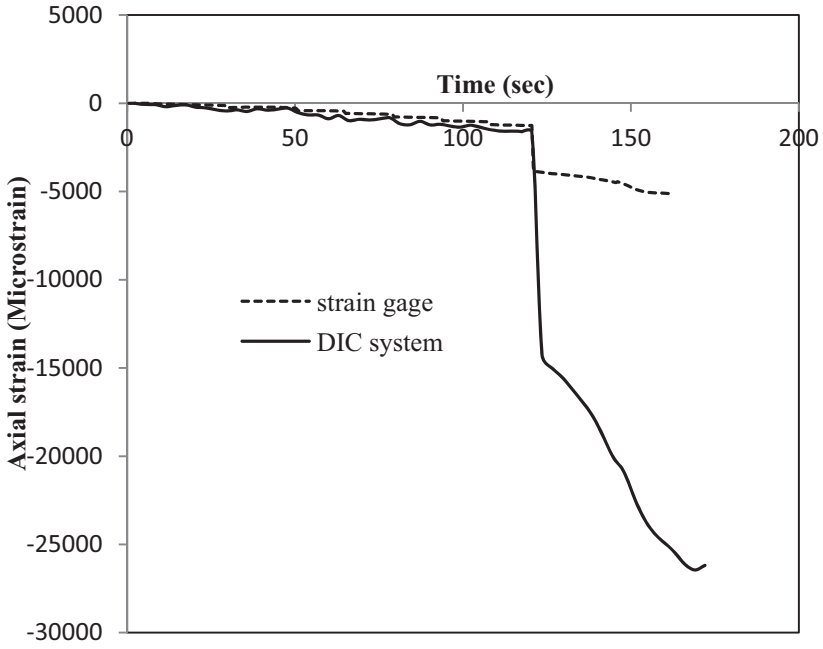

Figure 4.19: Comparison between strain gage and DIC system result after buckling

As one can see from Figure 4.19, buckling occurred at t=120 second with large change in the value of axial strain. Before buckling, the result of strain gage and the DIC system are relatively in a good agreement. After occurrence of the buckling, the results are not in agreement quantitatively, but they have a similar trend.

Considering the obtained results, one can conclude that the DIC system is an appropriate tool for detecting the buckling, thanks to full field measurement of strain. However, the DIC system is not accurate in measuring low strains (less than 300 microstrain). The accuracy for measuring the local strain could be expected to be around 250 microstrain.

4.4.2 Load and displacement measurement

The composite bending test setup is equipped with two load cells measuring independently the applied forces on both sides of the setup. Each load cell is mounted between the hydraulic cylinder and the Moment Arm (Figure 4.20) and has the capacity of 50,000 lbf with 0.1% precision. The output signals from the load cells are recorded by a data acquisition system during the test time.

The displacement of each hydraulic cylinder is measured by a non-contact magnetostrictive linear position transducer independently. It is mounted on the outside of the hydraulic cylinder (Figure 4.20). The output signals are recorded by a data acquisition system synchronized with the DIC system.

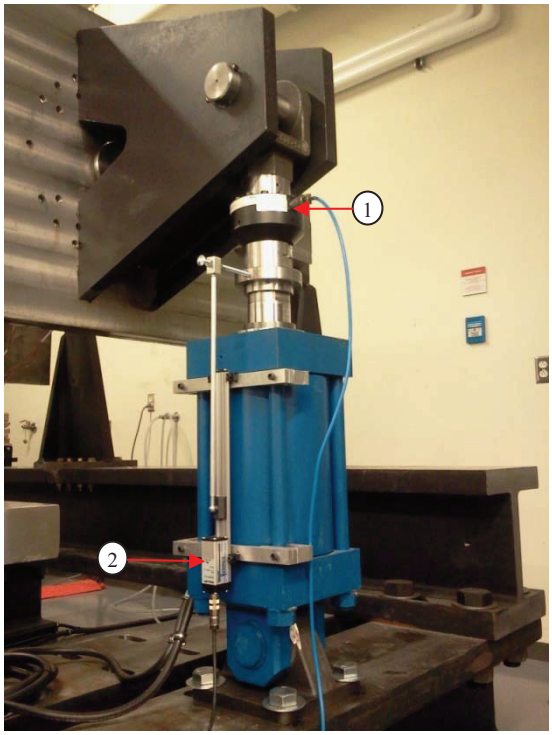

Figure 4.20: Load cell and position transducer in assembly: 1- load cell, 2- position transducer

Chapter 5

Manufacturing of the thermoplastic composite cone and test results

5.1 Introduction

In this chapter manufacturing of the thermoplastic composite cone, which is a section of the helicopter tail boom and used as a test specimen, and related topics (e.g., optimum manufacturing processing parameters) are to be discussed first. This is followed by the bending-buckling test results of the thermoplastic composite cone. Lastly, comparison between theoretical and experimental results is presented.

In the past 25 years, technical advances in the automated manufacturing of thermoplastic composite materials have increasingly attracted the interests of the aerospace industry, since the flexibility of the process allows the fabrication of highly contoured geometry with minimum machine setup. Regarding the manufacturing of the specimen, Automated Fiber Placement technique (AFP) has been employed to make the thermoplastic composite cone. Automated Fiber Placement (AFP) can be utilized for manufacturing both thermoset composites and thermoplastic composites. It is an automated process of laying up the impregnated fiber reinforced tapes onto a mold while heating it at the proper temperature with a heating system and applying pressure by means of a compaction roller simultaneously (Figure 5.1). Pressure application consolidates the fibers as they are being placed onto the surface of the mold and heat application makes the resin flow between the fibers. Combination of heat and pressure causes flow and consolidation [80].

In manufacturing of thermoplastic part, for manufacturing cost reasons, it is highly desirable to reach good consolidation by fiber placement alone and avoid having to use an autoclave process. By avoiding post consolidation of the laminates in a high-temperature autoclave, the manufacturing costs of thermoplastic composites could be reduced dramatically. However, it is a great challenge to achieve in-situ consolidation of thermoplastic composite in the manufacturing of thermoplastic composites. Many studies point out that the resulting laminate quality of fiber placed thermoplastic composites strongly depends on the processing parameters, such as heat flux, lay-down speed, and consolidation pressure [80-84]. The parameters play a significant role in determination of the quality of the final part, both from a stiffness and a strength point of view. These manufacturing parameters include, but are not limited to, nozzle temperature, nozzle location, process rate, and compaction force. Thus, a comprehensive study on the influence of processing parameters on the part quality is certainly necessary in the process optimization.

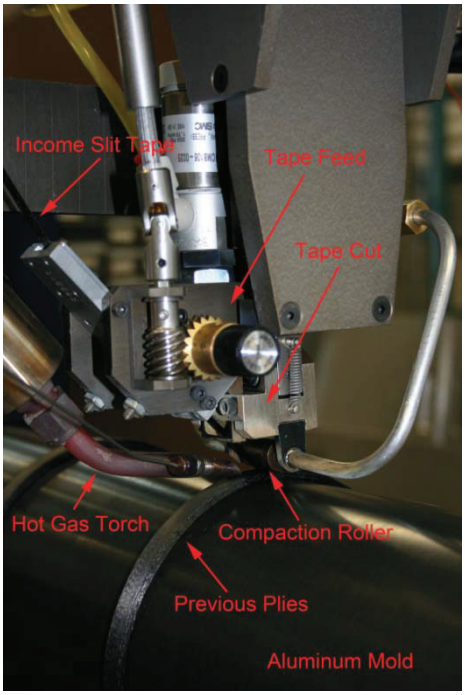

Figure 5.1: Illustration of Automated Fiber Placement (Coutesy of National Research Council Canada)

In order to determine whether the autoclave post-treatment could be avoided in manufacturing of thermoplastic composite, the effect of the autoclave treatment on the quality of the thermoplastic composite (from stiffness point of view) made by AFP is investigated in section 5.2.

In order to find the optimum AFP process parameters in the manufacturing of the thermoplastic composite cone (which is used as test specimen), two studies have been done on thermoplastic composite rings; the former considered the stiffness properties of the AFP made thermoplastic rings (section 5.3) and the latter investigated the strength aspect of the rings (section 5.4).

Once the optimum parameters were determined, the full scale thermoplastic composite cone (which is a section of helicopter tail boom) was manufactured and was tested on the bending test

setup described in Chapter 4. Manufacturing and preparation of the thermoplastic composite cone for the test is covered in section 5.5. Bending-buckling test results are presented in section 5.6 and comparison of the experimental buckling moment with the theoretical one is discussed in section 5.7.

5.2 Effect of autoclave process on the quality of the AFP-made thermoplastic composite cones[4]

5.2.1 Introduction

The quality of composite part, i.e. degree of cure, solidification, and void content, has direct effect on the resonant frequencies of the part. Therefore, this characteristic can be used for the purpose of quality control and acceptance of the sample. In order to see the effect of autoclave process on the stiffness properties of samples made by fiber placement technique, two short cones were made out of advanced thermoplastic material (AS4/PEEK) by AFP technique and then tested by impulse excitation of vibration to get experimental natural frequencies (modal test). On the other hand, tensile and compression coupons were made out of advanced thermoplastic material (AS4/PEEK) using hand lay-up and autoclave process and stiffness properties were obtained. Finite element analysis was performed using material properties obtained from testing coupons. Theoretical natural frequencies were extracted. Comparison between the natural frequencies obtained using finite element method and experimental modal analysis was performed. Furthermore, the two cones were treated inside the autoclave and theoretical and experimental natural frequencies were obtained. Comparison was made afterward.

---

[4] The content of section 5.2 has been published in [100].

5.2.2 Material properties

The material used in this study was AS4/PEEK (APC-2/AS4, 12K Unsized fiber) unidirectional tape supplied by Cytec Engineered Materials (CEM), USA. The matrix of tests used to determine basic mechanical properties of individual AS4/PEEK lamina is shown in Table 5.1. These tests are selected to examine the tensile, compression, and shear stiffness properties at room temperature and ambient humidity. The unidirectional tape consists of a 68:32 wt% mixture of carbon fiber (AS4) and PEEK (APC-2) [85]. The typical value of volume fraction of fibers is 61% [85]. The melting temperature (Tm) determined by DSC analysis was at 346.1°C.

Table 5.1: Test matrix [86-88]

Test Method	Measured Property	Panel ID	Number of Coupons	Dimensions of Coupons (Length/Width) [mm]	Stacking Sequence
D 3039-07	Tensile Modulus	PN-1	5	254/12.7	$[0]_8$
D 3410-03	Compressive Modulus	PN-2	5	139.7/12.7	$[0]_{24}$
D 5379-05	Shear Modulus	PN-3	5	76.2/19.05	$[0/90]_{6S}$

Three test panels were fabricated individually in a laboratory-size autoclave by following a processing cycle shown in Figure 5.2. A cross-section of the vacuum bag assembly and its use is shown schematically in Figure 5.3. Plies were carefully aligned to within 0.5° and tack welded in the trim area by temperature-controlled welding station to prevent movement during assembly. In addition, a thermocouple was placed in the middle plane of the laminates to read the part temperature. Stacking sequences and dimensions of the panels are shown in Table 5.2.

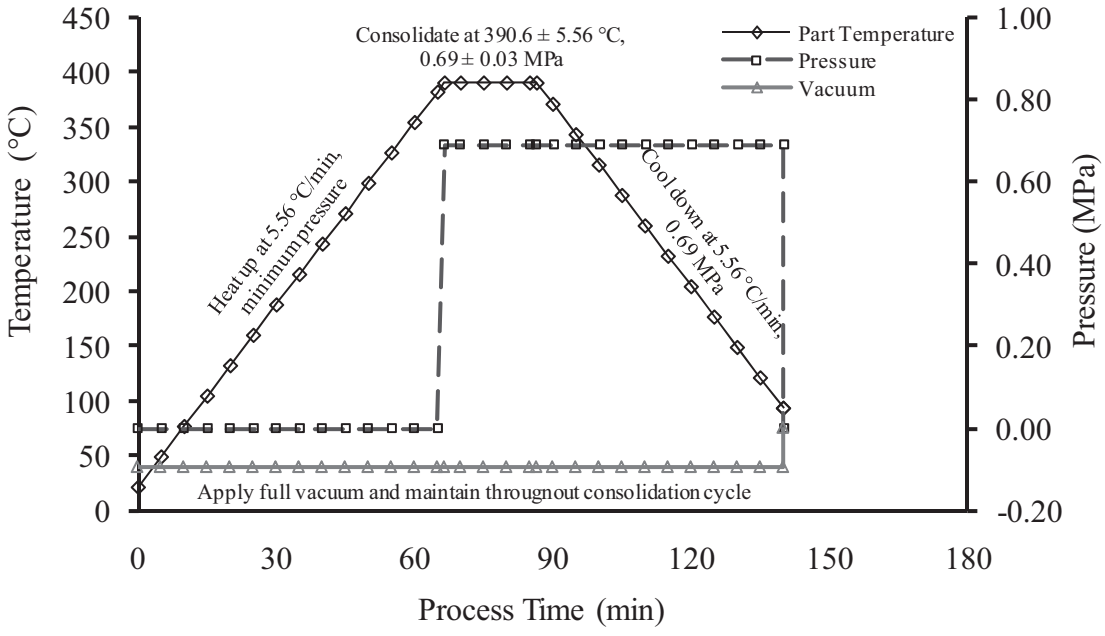

Figure 5.2: Processing cycle of AS4/PEEK

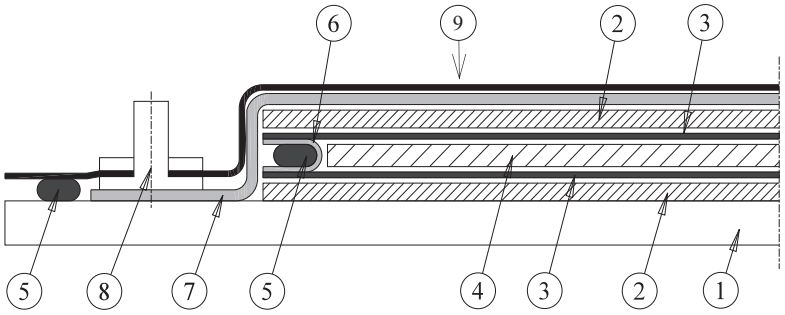

Figure 5.3: Cross-section of vacuum-bagged laminate: 1. Steel tool plate(12.7 mm) 2. Stainless steel plate (0.744 mm) 3. Bagging film (Thermalimide, Airtech) coated with release agent (Frekote® 44-NC™, Henkel) 4. Tack welded laminate 5. High-temperature sealant tape (SM-5160 TACKY-TAPE®, Schnee-Morehead) 6. 6 oz. plain woven fiberglass cloth 7. Breather (Airweave®UHT 800, Airtech), 8. Vacuum valve (VAC VALVE SSHTR and AHTC 1000 QTD, Aritech), 9. Bagging film

Table 5.2: Test Panel Configurations

Panel ID	Number of Panels	Dimensions of Panels (Length/Width) [mm]	Stacking Sequence
PN-1	1	304.8/152.4	$[0]_8$
PN-2	1	190.5/152.4	$[0]_{24}$
PN-3	1	127/177.8	$[0/90]_{6S}$

In order to meet the dimensional requirements specified in ASTM standards, test coupons, listed in Table 5.1, were cut from the panels using a 1/8 4FL REG EXCOARB®-Diamond end mill on a numerically controlled vertical milling machine equipped with dust collection system. The spindle speed and feed rate were set to 3056 RPM and 310 mm/min respectively.

All tests were conducted on a calibrated MTS axial test system located at CONCOM. The load frame is capable of delivering 100 KN of force, and the attached force transducer is available to measure tension and compression force of 100 KN. When determining tensile modulus, specimens were instrumented with strain-indication transducers which are centered about the loading axis in the gage section and mounted at 0° to the loading axis [86]. Static loads were introduced progressively into the specimens by hydraulic grips at a standard head displacement rate of 2 mm/min until the load dropped significantly [86]. The tensile modulus was calculated from stress-strain curves within the strain range between 1000 με and 3000 με [86].

When determining compressive modulus, specimens were instrumented with back-to-back strain indication transducers which are centered about the loading axis in the gage section and mounted at 0° to the loading axis [87]. An Illinois Institute of Technology Research Institute (IITRI) compression test fixture in accordance with ASTM standard D 3410-03 was used to provide

stability in unnotched compression testing [87]. Static loads were introduced progressively into the specimens via the fixture at a standard head displacement rate of 1.5 mm/min until the load dropped significantly [87]. The compressive modulus was calculated from stress-strain curves within the average strain range between 1000 με and 3000 με [87].

When determining shear modulus, specimens were instrumented with strain-indication transducers which are centered about the loading axis in the gage section and mounted at +45° and -45° to the loading axis [88]. A V-notched beam test fixture in accordance with ASTM standard D 5379M-05 was used to provide asymmetric flexure [88]. Static loads were introduced progressively into the specimens via the fixture at a standard head displacement rate of 2 mm/min until the specimens failed [88]. The compressive modulus was calculated from stress-strain curves within the average strain range between 1500 με and 2500 με [88]. A summary of stiffness properties of AS4/PEEK are presented in Table 5.3.

Table 5.3: Stiffness properties of AS4/PEEK

Material Type	APC-2/AS4
Tensile Modulus,Gpa (psi)	135.73 (19.69×10^6)
Compressive Modulus,Gpa (psi)	124.1 (18×10^6)
Shear Modulus,Gpa (psi)	4.7 (0.68×10^6)

5.2.3 Experimental modal analysis

5.2.3.1 Theory

One of the most useful techniques (and probably the simplest and fastest one) to obtain the dynamic properties of the structure is based on the excitation of the structure using impact

hammer. Basically the natural frequencies can be extracted directly from the peaks of the frequency response function (FRF) obtained by impulse technique. The frequency response function ($H(f)$) is the ratio of the Fourier transforms of the system output to the system input

$$H(f) = \frac{V(f)}{U(f)} \tag{5.1}$$

where $V(f)$ and $U(f)$ are Fourier transforms of system output and input respectively. However, in practice and in order to minimize the effect of noise at the output signal, the frequency response function is calculated as the ratio of the cross-spectrum between the input and output to the auto-spectrum of the input and usually indentified as $H_1(f)$

$$H_1(f) = \frac{G_{uv}(f)}{G_{uu}(f)} \tag{5.2}$$

where $G_{uv}(f) = U^*(f)V(f)$, $G_{uu}(f) = U^*(f)U(f)$ and $U^*(f)$ is complex conjugate of $U(f)$.

It is worth mentioning that in calculation of cross-spectrum, there is an intrinsic error which has a magnitude inversely proportional to the number of averages used in computation. As such, the greater the number of averages (hammer hits per FRF), the less bias the error associated with cross-spectrum calculation would be [89-91].

5.2.3.2 Samples specification and setup configuration

Two cones with geometric specifications and layup sequence listed in Table 5.4 were tested. In order to get the natural frequencies under free-free boundary condition, the cones were hanged by a very flexible rubber band in a horizontal position (See Figure 5.4). Since the rubber band has a very low spring constant, it is expected that it will not affect the natural frequencies of the cones.

The impact hammer with plastic cap was used to excite the cones (input) and output signals were captured using two small accelerometers attached to the small end of the cone 90 degrees apart (See Figure 5.4). A 4-channel data acquisition Bruel & Kjaer system was employed and frequency response functions (FRFs) and natural frequencies were obtained using PULSE 13 software provided by Bruel & Kjaer. The experimental setup is shown in Figure 5.4.

Table 5.4: Cone sections geometric and lay-up specifications

Lay-up	Cone # 1 $[90/45/0/-45]_S$	Cone # 2 [90/0/45/-45/0/45/0/-45/0/-45/45/0/90]
Small Diameter, mm (in)	335 (13.19)	337 (13.27)
Large Diameter, mm (in)	350 (13.78)	351 (13.82)
Length, mm (in)	319 (12.56)	271 (10.67)
Average thickness, mm (in)	0.93 (0.037)	1.61 (0.063)

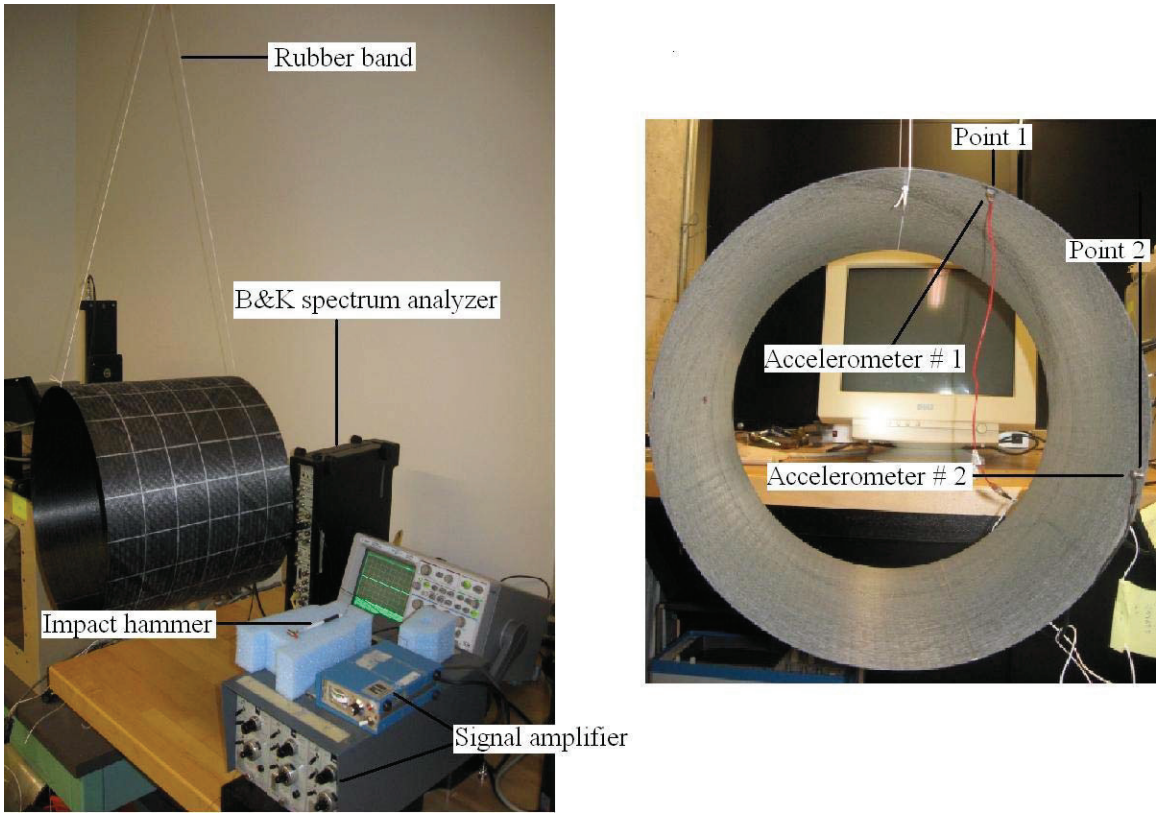

Figure 5.4: (a) experimental setup (b) accelerometers positions

5.2.4 Finite element method

In order to see the effect of material properties obtained from autoclave process on the natural frequencies, the cones were modeled using finite element technique. NASTRAN, commercial finite element software from MSC Corporation, was employed and "normal modes" analysis was performed to get natural frequencies and mode shapes. The cones were modeled with quadrilateral element topology containing 4 nodes, one at each corner. Material properties obtained from test coupons made by autoclave process were used in finite element analysis and are listed in Table 5.5. First cone having 8-layer symmetric lamination (See Table 5.4) was

modeled with 3240 elements and the second one having 13-layer lamination was modeled with 2916 elements.

Table 5.5: Material properties for AS4/PEEK used in finite element analysis

E_{11},GPa (psi)	129.9* (18.84×10^6)
E_{22},GPa (psi)	9.03 (1.31×10^6)
$G_{12} = G_{13,}$ GPa (psi)	4.7 (0.68×10^6)
G_{23}, ,GPa (psi)	2.21 (0.32×10^6)
ρ, kg/m^3 (ib/in^3)	1650** (0.0596)
ν_{12}	0.248

* This value is the average of tensile and compression modulus obtained from experiment
** The suggested number from Cytec is about 1600 (kg/m^3)

5.2.5 Autoclave treatment of the cones

In order to reach full consolidation and to release the residual stresses accumulated in the manufacturing process using AFP, the cone sections were treated in the high temperature autoclave. The autoclave process included the following steps:

- Preparation of the tool surface (cleaning and applying sealant)
- Appling a layer of high temperature release film on the tool surface
- Installing and fixing the sample on the tool surface
- Installing the thermocouples
- Appling a layer of high temperature release film on the sample surface
- Applying a layer of high temperature breather
- Making the vacuum bagging film around the assembly using the high temperature sealant tape

The final assembly is shown in Figure 5.5. After autoclave treatment, it was observed that the surface finish of both thermoplastic composite cones were smoother than before (Figure 5.6). Also measuring the thickness of the two specimens revealed that the thickness of the cone number 1 was reduced by 6.7% and cone number 2 by 8%. Experimental modal analysis was repeated on the autoclave-treated cones again and the finite element model was also updated to take into account the thickness reduction.

Figure 5.5: Autoclave treatment of the thermoplastic composite cone made by AFP

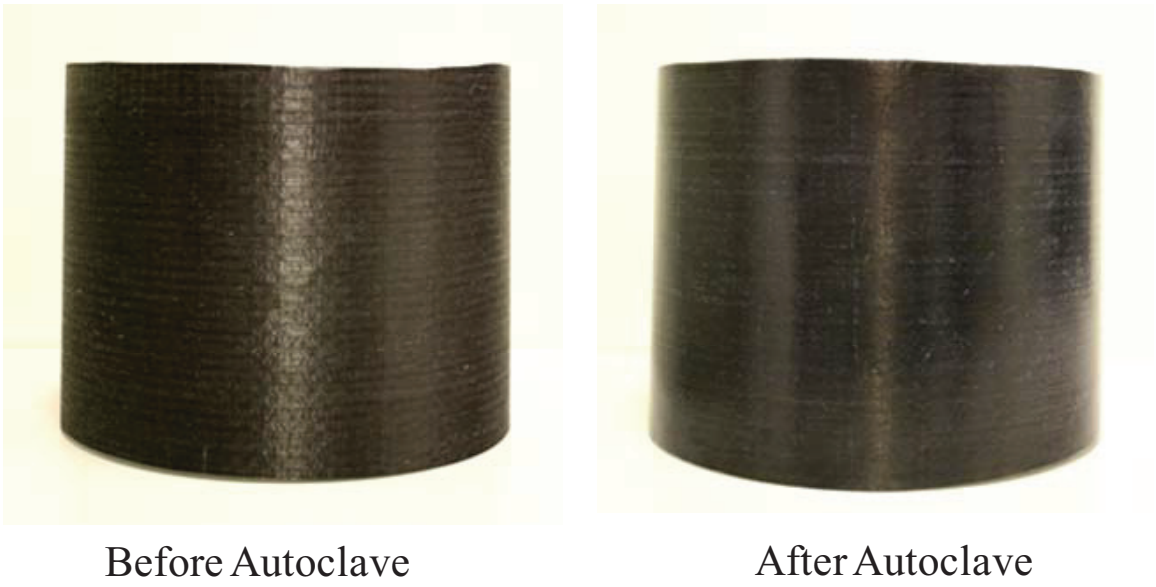

Figure 5.6: Surface finish of the thermoplastic composite cone before and after autoclave treatment

5.2.6 Results

5.2.6.1 Finite element modal analysis results before autoclave

Natural frequencies and mode shapes of two cone sections obtained using finite element method are shown in Table 5.6. The normal mode analysis was done for the first twenty modes excluding rigid body motion frequencies. Because of axisymmetric shape of the cone section, there are two mode shapes at each natural frequency which are the same in shape but shifted circumferentially.

Table 5.6: Theoretical natural frequencies and mode shape of two cones (before autoclave)

Mode No.	Cone#1 (Hz)	Cone#2 (Hz)	Mode shape	Mode No.	Cone#1 (Hz)	Cone#2 (Hz)	Mode shape
$f_1=f_2$	27.7	40.7	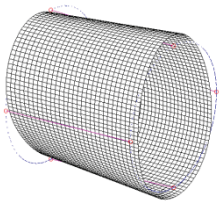	$f_9=f_{10}$	151.3	219.8	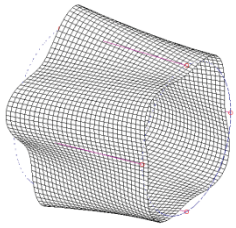
$f_3=f_4$	33.9	51.5	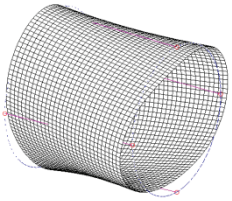	$f_{11}=f_{12}$	169.5	245.8	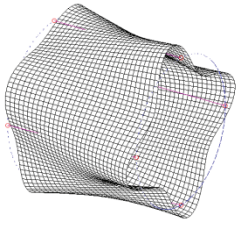
$f_5=f_6$	78.8	114.9	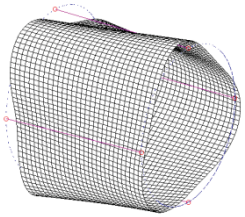	$f_{13}=f_{14}$	244.8	354.6	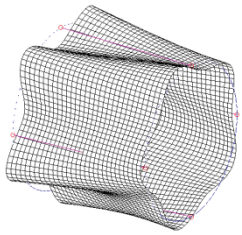
$f_7=f_8$	91.2	135.0	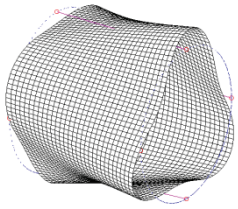	$f_{15}=f_{16}$	269.0	385.8	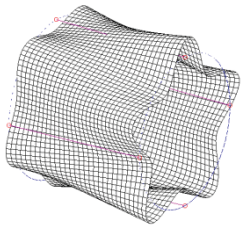

5.2.6.2 Experimental modal analysis results before autoclave treatment

In order to get frequency response functions (FRFs), two set of excitations were performed at the points where accelerometers were attached to the samples. First, the sample was hit at point 1 where accelerometer number 1 (See Figure 5.4) was attached (underneath the shell surface) and the responses were collected from two accelerometers (point 1 and 2). In the second set of excitation, the sample was hit at point 2 (the location of accelerometer number 2) and corresponding responses were captured by both accelerometers. As expected and because of the linear behavior of the cone sections, these two sets of excitation led to similar types of FRF graphs and consequently the same natural frequencies. Each set of excitation included 10 hits and the corresponded FRFs were the average of these 10 hits to reduce the bias error associated with cross-spectrum calculation.

The magnitude of FRFs for cone number 1 in which the excitation is performed at point 1 and the responses were collected from the point 1 (H11) and the point 2 (H21) are shown in Figure 5.7 and Figure 5.8 respectively.

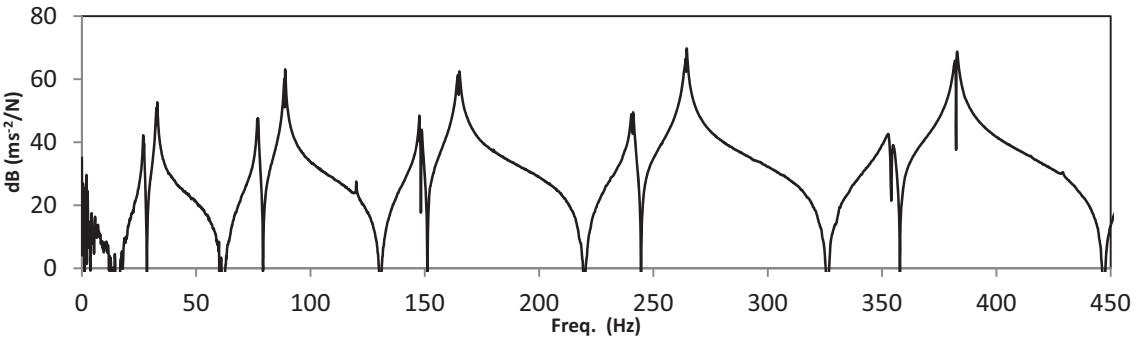

Figure 5.7: Magnitude of FRF corresponding to H11 for cone # 1

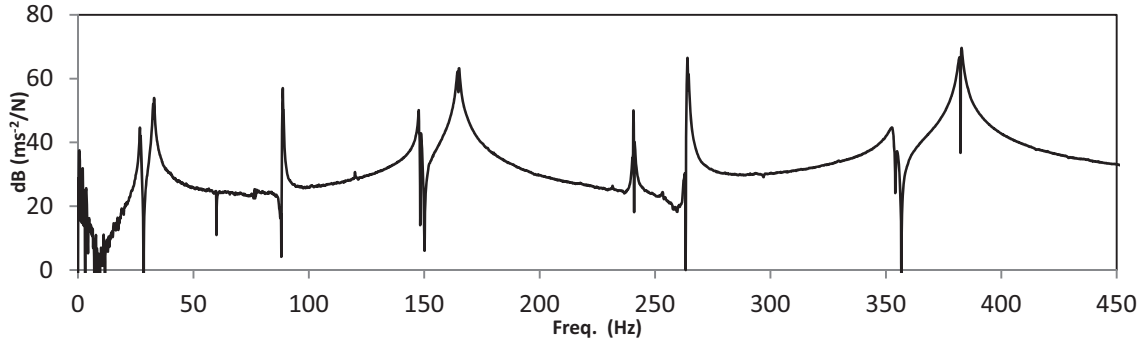

Figure 5.8: Magnitude of FRF corresponding to H21 for cone # 1

FRFs related to the modal test of the cone number 2 are shown for H11 (excitation and response both at point 1) in Figure 5.9 and for H21 (excitation at point 1, response at point 2) in Figure 5.10.

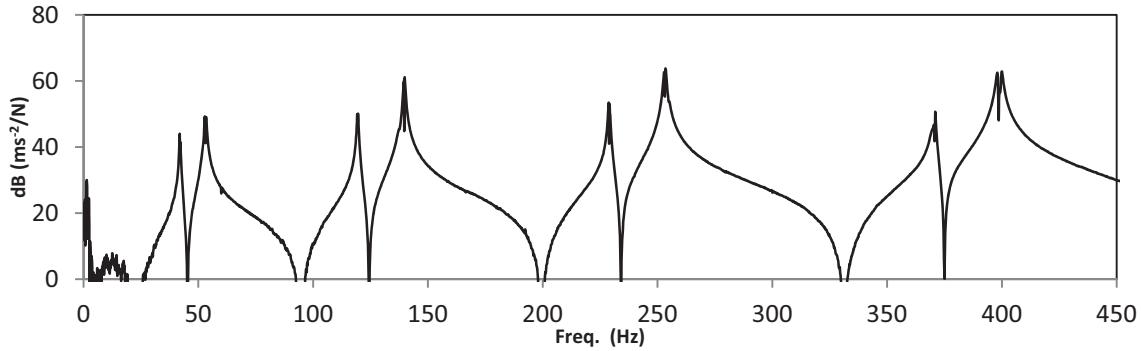

Figure 5.9: Magnitude of FRF corresponding to H11 for cone # 2

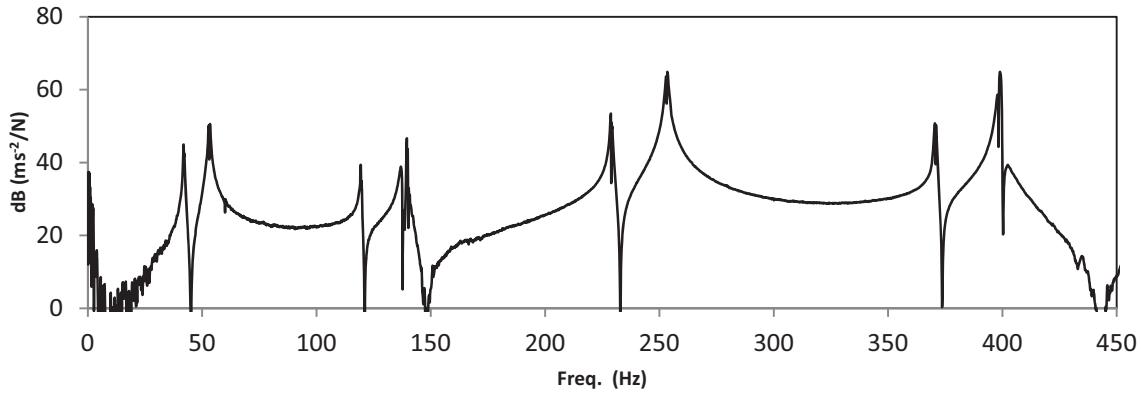

Figure 5.10: Magnitude of FRF corresponding to H21 for cone # 2

Natural frequencies are the peaks of FRF graphs and are extracted from Figure 5.7-Figure 5.10. Natural frequencies are listed for the cone number 1 along with theoretical results obtained from finite element analysis in Table 5.7. Similar results for the cone number 2 are shown in Table 5.8.

Table 5.7: Comparison between natural frequencies of cone #1 (experiment and theory before autoclave treatment)

Mode No.	Experimental Natural Freq. (Hz)	Theoretical Natural Freq. (Hz)	Difference (%)
$f_1=f_2$	26.9	27.7	+2.7
$f_3=f_4$	33	33.9	+2.5
$f_5=f_6$	76.6	78.8	+2.7
$f_7=f_8$	88.9	91.2	+2.5
$f_9=f_{10}$	147.6	151.3	+2.4
$f_{11}=f_{12}$	165.1	169.5	+2.6
$f_{13}=f_{14}$	241.1	244.8	+1.5
$f_{15}=f_{16}$	264.5	269	+1.7

Table 5.8: Comparison between natural frequencies of cone # 2 (experiment and theory before autoclave treatment)

Mode No.	Experimental Natural Freq. (Hz)	Theoretical Natural Freq. (Hz)	Difference (%)
$f_1=f_2$	41.9	40.7	-3
$f_3=f_4$	52.8	51.5	-2.6
$f_5=f_6$	119.5	114.9	-4
$f_7=f_8$	139.8	135	-3.6
$f_9=f_{10}$	228.7	219.8	-4
$f_{11}=f_{12}$	253.4	245.8	-3.1
$f_{13}=f_{14}$	370.9	354.6	-4.6
$f_{15}=f_{16}$	400	385.8	-3.7

As can be seen from Table 5.7 and Table 5.8, the difference between experimental and theoretical natural frequencies is about 2.3 % for cone number 1 and about -3.6 % for cone number 2.

5.2.6.3 Experimental modal analysis results after autoclave treatment

In order to see the effect of autoclave treatment on the natural frequencies of the cones, experimental modal analysis was repeated on the autoclave-treated cones using the method mentioned in section 5.2.6.1. The magnitude of FRFs for cone number 1 and cone number 2 in which the excitation is performed at point 1 and the responses were collected from the point 1 (H11) are shown in Figure 5.11 and Figure 5.12 respectively. FRF graphs before the autoclave treatment is also shown for comparison purpose. As can be seen, the peaks of the FRF graphs were shifted to the left after autoclave treatment. This means that the natural frequencies were decreased for both cones after autoclave treatment.

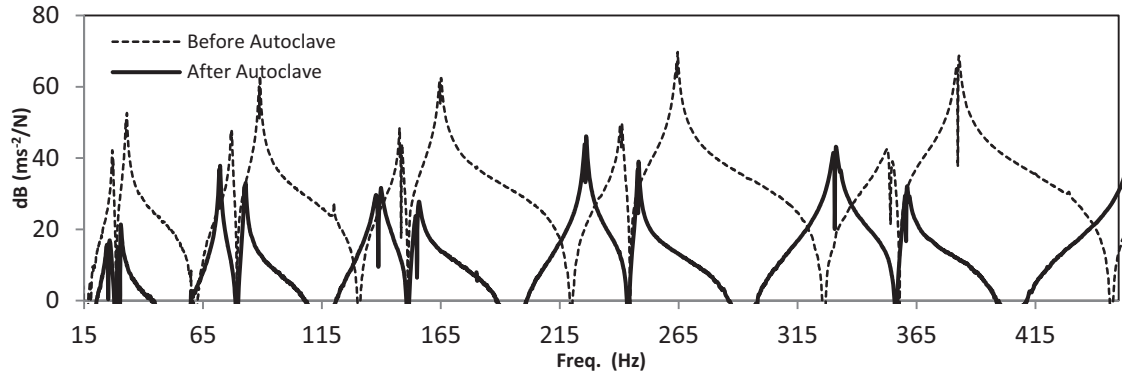

Figure 5.11: Comparison between FRF graphs for cone # 1 before and after autoclave treatment

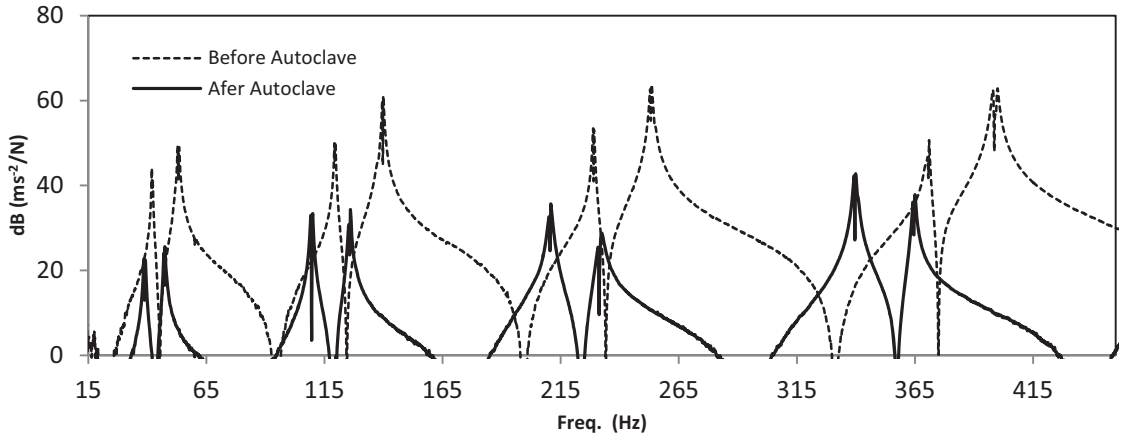

Figure 5.12: Comparison between FRF graphs for cone # 2 before and after autoclave treatment

The natural frequencies of cone number 1 and cone number 2 before and after autoclave treatment were listed in Table 5.9 and Table 5.10, respectively. As can be seen from these two tables, the first eight natural frequencies of cone number 1 decreased by an average of 6.6% and of cone number 2 by an average of 8.8%. Regarding this reduction in natural frequencies, the question arises that whether this reduction is due to change in stiffness properties or because of the change in geometry (thickness reduction) or both. In order to answer this question, the FEM

model was updated based on the new geometry. The results are presented in the following section.

Table 5.9: Comparison between experimental natural frequencies of cone # 1 (before and after autoclave)

Mode No.	Before Autoclave Freq. (Hz)	After autoclave Freq. (Hz)	Difference (%)
$f_1=f_2$	26.9	25.3	+5.9
$f_3=f_4$	33	30	+9.1
$f_5=f_6$	76.6	72.2	+5.8
$f_7=f_8$	88.9	82.3	+7.4
$f_9=f_{10}$	147.6	138.4	+6.2
$f_{11}=f_{12}$	165.1	155.2	+6.0
$f_{13}=f_{14}$	241.1	225.8	+6.3
$f_{15}=f_{16}$	264.5	248	+6.2

Table 5.10: Comparison between experimental natural frequencies of cone # 2 (before and after autoclave)

Mode No.	Before Autoclave Freq. (Hz)	After autoclave Freq. (Hz)	Difference (%)
$f_1=f_2$	41.9	38.91	+7.1
$f_3=f_4$	52.8	47.19	+10.6
$f_5=f_6$	119.5	109.4	+8.5
$f_7=f_8$	139.8	125.6	+10.2
$f_9=f_{10}$	228.7	210.5	+8
$f_{11}=f_{12}$	253.4	230.6	+9
$f_{13}=f_{14}$	370.9	339.5	+8.5
$f_{15}=f_{16}$	400	364.5	+8.9

5.2.6.4 Finite element modal analysis results after autoclave

The finite element model was updated to take into account the reduction in thickness of the cones after autoclave treatment. The theoretical natural frequencies obtained from updated FEM model

along with experimental ones are listed for cone number 1 and cone number 2 in Table 5.11 and Table 5.12, respectively. One can see from these two tables that the updated theoretical natural frequencies are in very good agreement with experimental ones within a difference of less than 2.6%. So it can be concluded that the change in the natural frequencies after the autoclave treatment is mainly due to change in the thickness of the cones and no significant changes in stiffness properties occurred after autoclave treatment.

Table 5.11: Comparison between natural frequencies of cone # 1 (experiment and theory after autoclave treatment)

Mode No.	Experimental Natural Freq. (Hz)	Theoretical Natural Freq. (Hz)	Difference (%)
$f_1=f_2$	25.3	25	-1.1
$f_3=f_4$	30	30.6	+2.1
$f_5=f_6$	72.2	71.3	-1.2
$f_7=f_8$	82.3	82.6	+0.3
$f_9=f_{10}$	138.4	137	-1
$f_{11}=f_{12}$	155.2	153.4	-1.1
$f_{13}=f_{14}$	225.8	221.6	-1.9
$f_{15}=f_{16}$	248	243.7	-1.8

Table 5.12: Comparison between natural frequencies of cone # 2 (experiment and theory after autoclave treatment)

Mode No.	Experimental Natural Freq. (Hz)	Theoretical Natural Freq. (Hz)	Difference (%)
$f_1=f_2$	38.9	38.3	-1.6
$f_3=f_4$	47.2	48.5	+2.6
$f_5=f_6$	109.4	108.2	-1.1
$f_7=f_8$	125.6	127.1	+1.2
$f_9=f_{10}$	210.5	207.1	-1.7

$f_{11}=f_{12}$	230.6	231.5	+0.4
$f_{13}=f_{14}$	339.5	334	-1.6
$f_{15}=f_{16}$	364.5	363.4	-0.3

5.2.7 Conclusions

Natural frequencies of two cones made by fiber placement technique out of thermoplastic composite material (AS4/PEEK) were experimentally obtained through modal analysis. Stiffness properties of AS4/PEEK material were experimentally attained using test coupons manufactured by autoclave process. It was assumed that resin system is fully consolidated in autoclave process and as a result, full stiffness properties are attained. These properties were entered to a finite element model as input and using normal mode analysis, theoretical natural frequencies were obtained.

It is observed that the theoretical natural frequencies agree well with the experimental ones. This implies that the overall stiffness properties of the cones made by AFP are the same as those of cones undergone autoclave treatment.

In order the see the effect of autoclave treatment on the thickness of the cones, the two cones were treated in the autoclave and the experimental modal analysis was repeated. It was observed that after autoclave treatment the thickness of both cones were reduced and furthermore the natural frequencies decreased. After updating the theoretical calculation considering the thickness reduction, it was revealed that theoretical and experimental natural frequencies were in a very good agreement (less than 2.6% difference). This implies that the decrease in natural frequencies was due to the change in the geometry alone, not the stiffness properties.

However, it should be mentioned that one cannot conclude that the quality of the cones made by fiber placement technique is high based on natural frequencies agreement alone. Strength properties should also be taken into account.

5.3 Determination of optimum process parameters for automated fiber placement technique from stiffness point of view[5]

5.3.1 Introduction

Optimal process parameters for the in-situ consolidation of thermoplastic composites were determined through manufacturing (under different manufacturing parameters) and modal testing of nine thermoplastic composite (AS4/PEEK) rings. Taguchi's method was utilized to analyze the experimental data to suggest the optimum condition for manufacturing those rings.

The quality of a composite structure, i.e. degree of cure, solidification, and void content, affected the natural frequencies of the part. Therefore, a trustable tool to indicate the quality of the part from stiffness point of view is experimental modal analysis in which one could find natural frequencies and compare these frequencies for different manufacturing parameters.

5.3.2 Design of experiment – Taguchi's method

An earlier study shows that the resulting laminate quality of in-situ thermoplastic composites strongly depends on heat flux, lay-down speed, and consolidation pressure [80-84]. In this study, nozzle temperature, nozzle location (that is defined as the distance between the tip of the nozzle of the hot gas torch and the nip point of the compaction roller), process rate, and compaction

[5] The content of section 5.3 has been published in [99].

force were selected to study the quality of the composite rings (Table 5.13). The nitrogen flow rate was ruled out here since lowering the nitrogen flow rate may significantly shorten the lifetime of hot gas torch. Other uncontrollable process parameters such as substrate temperature and roller temperature were excluded from the study as well.

Table 5.13: Description of factors and levels

Factor	Level 1	Level 2	Level 3
Nozzle Temperature (°C)	900	925	950
Process Rate (mm/sec)	25.4	50.8	76.2
Compaction Force (kgf)	30	40	50
Nozzle Location (mm)	11.38	17.77	21.62

Each parameter was assigned three levels to reflect the nonlinearity of factor influence. If all the possible combinations were to be tested, the number of tests would be $3^4 = 81$ which was impractical in terms of time and cost. In contrast, the use of Taguchi's method could effectively reduce the number of tests and estimate the interaction between the variables [92]. The method was developed based on the concept the orthogonal array which was introduced in 1940's and has been widely used in designing experiments. Experiments were laid out using an L-9 array (Table 5.14) and one sample was tested of the nine trial conditions (Table 5.15). Specifically, the array contained four factors with three levels. The first factor was assigned to the nozzle temperature, the second to the process rate, the third to the compaction force, and the fourth to the nozzle location. The response studied was the normalized fundamental natural frequency of thermoplastic rings fabricated on the AFP machine. The influence of each factor and interaction was assessed by the main effects and the analysis of variance (ANOVA). Qualiteck-4 software by Nutek was used for analyzing the data from the experiments.

Table 5.14: L-9 orthogonal array

Trial	Nozzle Temperature (Deg C)	Process Rate (mm/sec)	Compaction Force (kgf)	Nozzle Location (mm)
1	1	1	1	1
2	1	2	2	2
3	1	3	3	3
4	2	1	2	3
5	2	2	3	1
6	2	3	1	2
7	3	1	3	2
8	3	2	1	3
9	3	3	2	1

Table 5.15: Description of trial conditions

Trial	Nozzle Temperature (Deg C)	Process Rate (mm/sec)	Compaction Force (kgf)	Nozzle Location (mm)
1	900	25.4	30	11.38
2	900	50.8	40	17.77
3	900	76.2	50	21.62
4	925	25.4	40	21.62
5	925	50.8	50	11.38
6	925	76.2	30	17.77
7	950	25.4	50	17.77
8	950	50.8	30	21.62
9	950	76.2	40	11.38

5.3.3 Specimen fabrication

Based on pre-defined processing parameters, the thermoplastic composite rings were manufactured individually on the 6-axis gantry-type AFP machine equipped with the thermoplastic fiber placing head (Figure 5.13) by laying thermoplastic slit tape onto a cylindrical aluminum mold with the diameter of 146.05 mm. The working envelope of the machine is 4 m long by 2 m wide by 1 m diameter. A hot gas torch with the maximum capacity of 1000 °C is the primary heating system of the equipment.

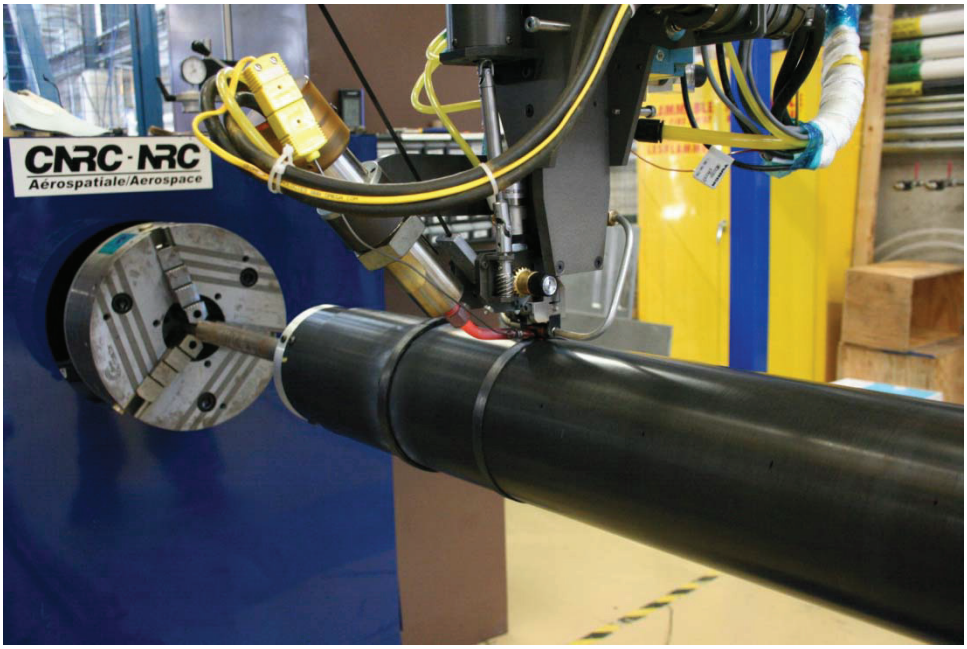

Figure 5.13: 6-axis gantry-type AFP machine equipped with the thermoplastic fiber placing head (Coutesy of National Research Council Canada)

The layup sequence of the rings was $[90]_{50}$ in order to meet the recommended specimen configurations specified in the standard test method for short-beam strength of polymer matrix composite materials (ASTM standard D2344M-00) and their laminates [93]. The selected material was AS4 (12k unsized fiber)/APC-2 (PEEK) unidirectional slit tape supplied by Cytec Engineered Materials (Cytec). The nominal width and thickness of the slit tape are 12.446mm and 0.125mm. The slit tape consists of a 68:32 wt% mixture of carbon fiber (AS4) and PEEK (APC-2) [85]. The melting temperature (Tm) determined by DSC analysis was at 346.1°C. The rings were removed from the mold and machined on a conventional lathe to facilitate the measurements performed on a coordinate-measuring machine (CMM). The CMM measurements are tabulated in Table 5.16. The inner diameter of the ring and its deviation were computed based on six evenly

divided points along the measuring circle. Deviation was equivalent to circularity in the language of geometric dimension and tolerance.

Table 5.16: CMM measurements of composite rings

Trial	Inner Diameter (mm)	Deviation (mm)	Thickness (mm)	Height (mm)
1	143.916	0.022	4.691	8.50
2	145.059	0.006	4.633	8.45
3	146.413	0.011	5.636	7.38
4	144.663	0.012	3.952	8.52
5	143.680	0.011	4.039	8.49
6	145.385	0.010	5.296	8.43
7	144.211	0.011	3.239	8.50
8	144.823	0.010	5.024	8.45
9	144.140	0.013	4.394	8.52

5.3.4 Test setup

Nine rings with geometric specifications listed in Table 5.16 were tested. In order to get the natural frequencies under free-free boundary condition, the composite rings were hung by a flexible rubber band. Since the rubber band has a very low spring constant, it will simulate free-free boundary condition as ring support. The impact hammer was used to excite the composite rings (as input) and output signals were captured using two small accelerometers attached to the top and side of the rings at a 90 ° circumferential space. A 4-channel data acquisition Bruel & Kjaer system was employed and frequency response functions (FRFs) and natural frequencies were obtained using PULSE 13 software provided by Bruel & Kjaer. The experimental setup is shown in Figure 5.14.

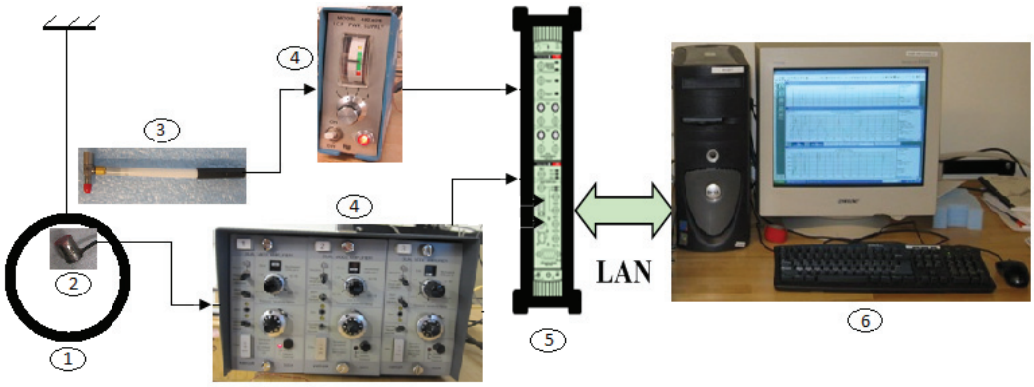

Figure 5.14: Experimental setup: 1- composite ring, 2- accelerometer, 3- hammer, 4- amplifier, 5- B&K data acquisition system, 6- computer system (PC)

5.3.5 Natural frequency results

The average of ten hits per sample was used to obtain fundamental natural frequency for nine composite rings. Results are shown in Table 5.17. All the rings were machined after manufacturing to the same height (except ring number 3 which was narrower) in order to make the comparison of the stiffness more meaningful. However, because of different manufacturing parameters used during the making of the rings, their thicknesses were different. These differences were mainly because of the different compaction forces used in manufacturing process. In order to eliminate the effect of the thickness of the ring in stiffness comparison, the fundamental natural frequencies of the rings were normalized to the thickness of the rings and listed in Table 5.17.

Table 5.17: Fundamental natural frequency

Trial	Fundamental Natural freq. (Hz)	Normalized Fundamental Natural freq. (Hz)
1	862	183.74
2	854	184.33
3	988	175.29
4	722	182.68
5	744	184.22
6	948	179.01
7	594	183.42
8	904	179.93
9	802	182.51

As can be seen from Table 5.17, ring number 2 is ranked first from stiffness point of view, offering that the associated manufacturing parameters were the best among the other eight rings. Ring number 3 has the minimum normalized fundamental natural frequency.

5.3.6 Statistical analysis

The main effect of the nozzle temperature is shown in Figure 5.15. The normalized first natural frequency seems to be independent of the nozzle temperature. This implies that the heat loss occurs between the nozzle of the hot gas torch and the nip point of the compaction roller. As a result, the substrate temperature might increase by 3 to 5°C while the nozzle temperature increases by 25°C. Figure 5.15 shows that the normalized first natural frequency decreases with the process rate. The process rate has the biggest impact on the normalized natural frequency. It is due to the fact that the incoming slit tape and the substrate could be heated and pressed much longer by slowing the process rate. However, it is desirable to have a high process rate in production because the operating costs can be significantly reduced. The main effect of the compaction force is presented in Figure 5.15. The compaction force improves the normalized first

natural frequency in the range of 30kgf to 40kgf, and then a decrease in the response is observed from 40kgf to 50kgf. The decrease in the normalized first natural frequency might be explained by the fact that the fiber distribution is completely altered under the compaction force of 50kgf. It can be concluded that the laminate quality is not always proportional to the compaction force exerted on the tool during the in-situ consolidation of thermoplastic composites. The main effect of nozzle distance to the nip point of the compaction roller is given in Figure 5.15. The result is not surprising since the normalized first natural frequency decreases linearly with the nozzle location. When the torch is pulled away from the compaction roller, the heat energy loss in the surroundings increases. Thus, the temperatures of the slit tape and substrate decrease with the input energy.

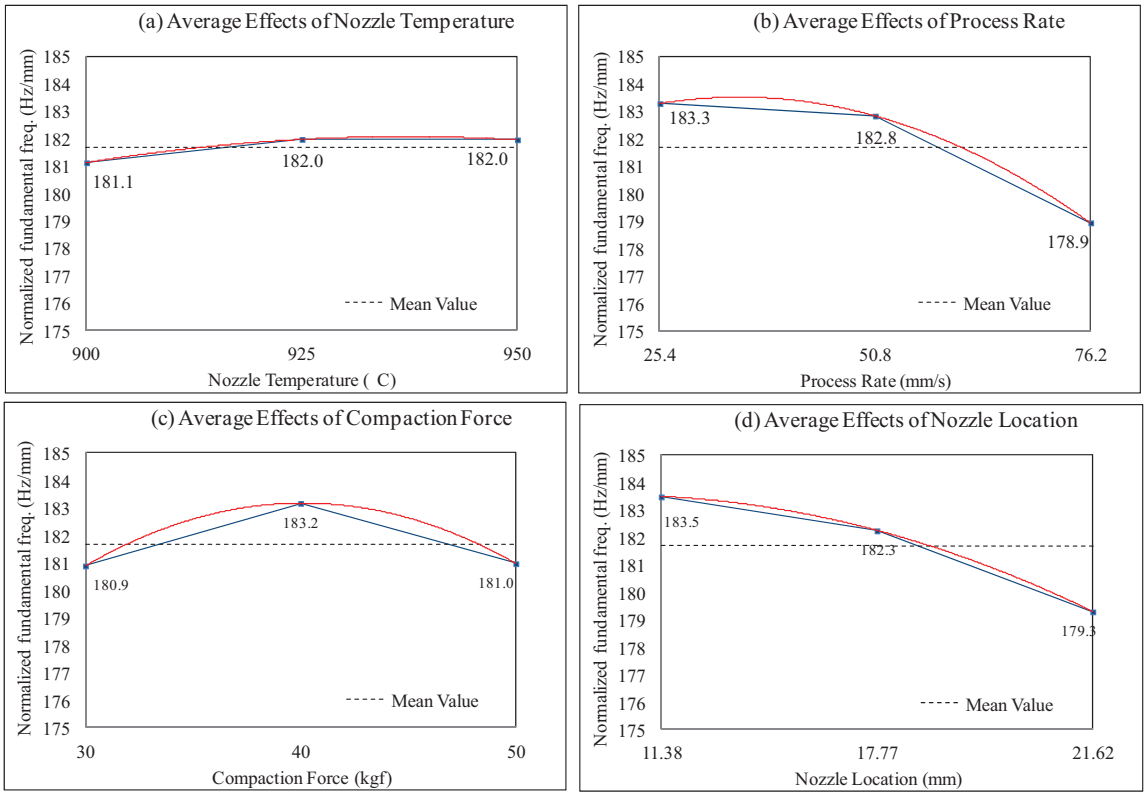

Figure 5.15: Plots of average effects of (a) nozzle temperature, (b) process rate, (c) compaction force, and (d) nozzle location at three levels

The analysis of variance (ANOVA) of the experimental results shows the relative importance of all the factors (Table 5.18). The main factor influencing the normalized first natural frequency are the process rate (46.5%), the nozzle location (37.9%), and the compaction force (13.7%). This suggests that the process rate has the most significant influence on the normalized first natural frequency. Surprisingly, the nozzle temperature seems to be insignificant to the normalized first natural frequency. With the information from both the experimental and statistical results, the optimum combination of processing parameters of fabricating AS4/PEEK rings is recommended in Table 5.19.

Table 5.18: Analysis of variance of experimental results

Factors	Percent (%)
Nozzle Temperature	1.9
Process Rate	46.5
Compaction Force	13.7
Nozzle Location	37.9

Table 5.19: Optimum process parameters by Taguchi's method

Factors	Level Description	Level	Contribution
Nozzle Temperature	925	2	0.29
Process Rate	25.4	1	1.60
Compaction Force	40	2	1.49
Nozzle Location	11.38	1	1.81
Total Contribution from All Factors			5.19
Current Grand Average of Performance			181.68
Expected Result at Optimum Condition			186.87

5.3.7 Conclusions

To achieve the optimum process parameters in the in-situ consolidation of thermoplastic rings, nine thermoplastic composite rings were manufactured using the automated fiber placement technique with different combinations of process parameters such as compaction force, nozzle temperature etc. The comparison between these rings from stiffness point of view was performed by the means of experimental modal analysis and determination of fundamental natural frequency. Taguchi's method was applied on the data obtained from modal analysis to achieve the optimum manufacturing parameters. As a result, the following optimum manufacturing parameters were obtained: nozzle temperature = 925 (˚C), process rate = 25.4 (mm/sec), compaction force = 40 (kgf), and nozzle location = 11.38 (mm).

5.4 Determination of optimum process parameters for automated fiber placement technique from strength point of view[6]

5.4.1 Introduction

A recent research work on the development of optimum conditions for processing AS4/PEKK confirms that the process parameters affect the interlaminar shear strength of fiber placed composite rings in many ways [94]. The study shows that the process rate has the most significant influence on the interlaminar strength, and the nitrogen flow rate has a nonlinear effect on the interlaminar strength. However, it is preferred that the nitrogen flow rate is maintained at 70 ~75 SLPM (Standard Liters Per Minute) to protect the heating elements from overheating or oxidation. In addition to those parameters, the relative nozzle location with respect to the impaction roller has a strong influence on the strength properties of fiber placed laminates.

Thus, since there are many processing parameters that may directly or indirectly influence the quality of fiber placed laminates, it is a great challenge to find optimum conditions for processing AS4/PEEK on an automatic fiber placement (AFP) system without assistance of a post-consolidation process in a high-temperature autoclave. An experimental investigation would be necessary to discover the interrelations of controllable processing parameters and strength properties of fiber placed laminates in the manufacturing of thermoplastic composite structures.

[6] The content of section 5.4 has been published in [97].

In order to determine optimum process parameters for AFP from the strength point of view, short-beam shear tests were performed on the samples cut from the nine thermoplastic rings (see section 5.3.3 for manufacturing of the rings) to determine the interlaminar shear strength. Based on the short-beam strength results, Taguchi's method was employed to identify the significance of each process parameters and to obtain the optimum process conditions. Furthermore, to compare the quality of the rings under different process conditions, Digital Image Correlation (DIC) technique was also used to measure ultimate through-the-thickness strain during the short-beam shear tests. Microscopic photos were used to determine the failure mode. Also, differential scanning calorimetry (DSC) test was conducted to investigate the crystallinity level in the samples.

5.4.2 Specimen preparation and short-beam strength test

The specimen configuration for the short-beam test is shown in Figure 5.16. The curved specimens were machined from the composite rings using a Guhring diamond impregnated end mill on a Computer Numerical Control machine so that the dimensional requirements were satisfied. Prior to testing, specimens were moisture conditioned by continuous exposure to 23 ± 3 °C and 50 ± 10 % relative humidity until the change of weight was negligible.

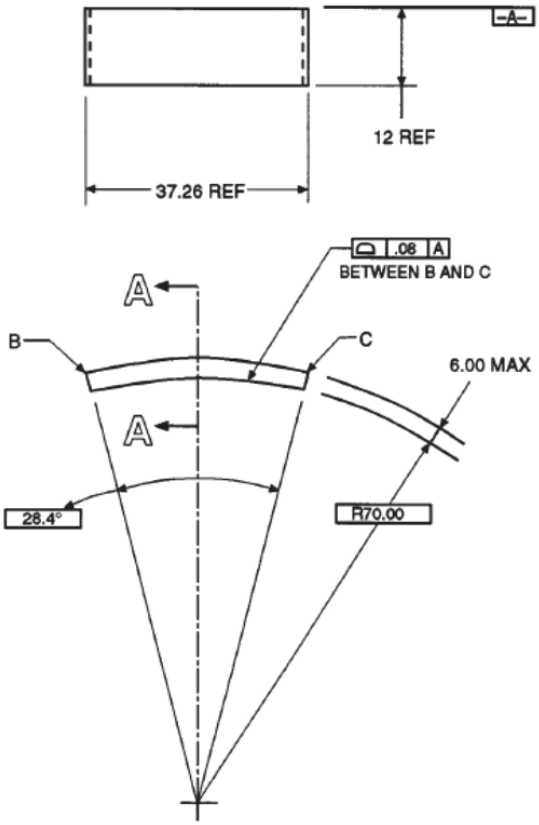

Figure 5.16: Curved specimen configuration (all dimensions are in mm) [93]

The short-beam strength test was performed using a MTS hydraulic testing system with the capacity of 100 kN. A test fixture in accordance with the ASTM standard D2344M-00 was used to align and center the specimen such that its longitudinal axis was perpendicular to the loading nose and side supports. The loading nose was located equidistant between the side supports to within ± 0.03 mm. Both the loading nose and side supports overhung the specimen width by at least ± 2 mm at each side. Specimens were tested until a load drop-off of 30% was observed. Static loads were applied at a rate of cross head movement of 1 mm/min, and load versus displacement graphs were recorded for all tests.

5.4.3 Experimental Results

Nominal short-beam strength (or interlaminar shear strength) of the specimens was calculated as follows [93]:

$$F^{sbs} = 0.75 \times \frac{P_m}{b \times h}$$

where:

F^{sbs} = short-beam strength, MPa;
P_m = maximum load observed during the test, N;
b = measured specimen width, mm; and
h = measured speciment thickness, mm.

Five specimens per test condition were tested, and the average value and standard deviation were calculated for each series of tests. A summary of the short-beam strength, interlaminar shear strain obtained at failure is presented in Table 5.20.

The digital image correlation (DIC) technique was used to obtain the distribution of interlaminar shear strains. The specimens were painted in black and random speckle pattern was applied by spray technique prior to the short-beam strength test. Two 28 mm lenses were equipped on the stereo-system to record the sample deformation during the test. A typical distribution of through-thickness shear strain of the short-beam specimen prior to the point of failure is shown in Figure 5.17. As one can expect, shear strain distribution from the middle to the right side of the sample has positive sign and from the middle to the left side of the sample has negative sign. The shear strain distribution is quite symmetric to the mid-plane and the effect of stress concentration is clearly visible under the loading point (Figure 5.17).

Figure 5.18 shows that the failure mode that can be identified as intralaminar shear, which means that the crack starts and propagates in the middle of plies instead of at the interface of plies. Dark black dots shown in Figure 5.18 represent the voids in the laminate, and it is obvious that the void content is less than 1 %. From Table 5.20, it can be observed that the short-beam strength varies from 31.330 MPa to 47.514 MPa by changing the process parameters. Among nine trials, the fourth ring offers the best mechanical performance, and the third one exhibits the lowest short-beam strength. It is inferred that the process parameters have a direct impact on the strength properties of composite structures made by AFP.

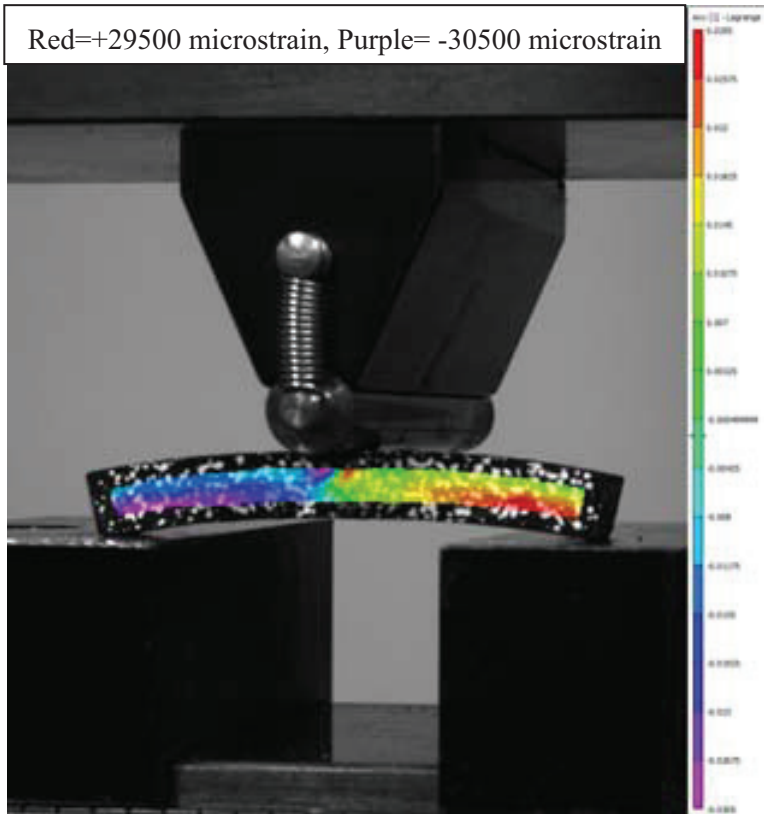

Figure 5.17: Through-thickness shear strain distribution by DIC

Table 5.20: Short-beam strength of composite rings made by AFP

Trial	Short-beam Strength (MPa)		Interlaminar Shear Strain (%)	
	$\bar{x}$	s_{n-1}	$\bar{x}$	s_{n-1}
1	43.891	4.274	1.100	0.071
2	44.991	0.675	0.957	0.009
3	31.330	0.976	0.597	0.068
4	47.514	1.638	1.227	0.083
5	42.779	1.779	0.723	0.017
6	39.910	0.962	1.300	0.143
7	34.755	1.823	1.223	0.113
8	41.436	0.999	1.172	0.155
9	41.934	1.984	0.990	0.016

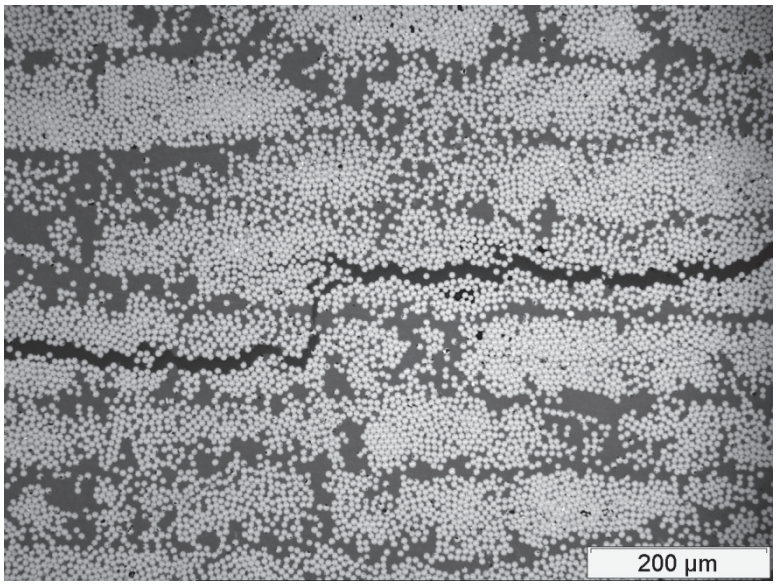

Figure 5.18: Photomicrograph of crack propagation of short-beam specimens

To determine the crystallinity of each ring, the heat flow versus temperature curve was acquired by DSC and analyzed by the Universal Analysis software. The test sample was heated to 400 °C at 10 °C/min and cooled at the maximum cooling rate to the room temperature. The degree of

crystallinity is computed by dividing the ultimate heat of crystallinity (which is a theoretically-derived number) by the experimental one. The ultimate heat of crystallization of APC-2 was considered to be 130 J/g, and the weight ratio of PEEK was taken to be 32 % [95]. Table 5.21 summarizes the average value of the degree of crystallinity of three samples for each ring. It can be concluded that process parameters has insignificant influence on the crystallinity of fiber placed composites.

Table 5.21: Degree of crystallinity of fiber placed composite rings

Trial	Degree of Crystallinity (%)	Average Value (%)	Percent Variation (%)
1	28.45	29.74	-4.36
2	29.50		-0.83
3	32.32		8.65
4	29.46		-0.96
5	29.53		-0.72
6	29.88		0.45
7	27.70		-6.87
8	29.97		0.75
9	30.90		3.89

5.4.4 Statistical Analysis

The average effects of four influencing factors are plotted in Figure 5.19. Figure 5.19.a shows that the interlaminar shear strength increases with increasing the nozzle temperature in the range of 900 °C to 925 °C, and then a decrease in the response is observed from 925 °C to 950 °C. Figure 5.19.b suggests that the interlaminar shear strength increases slightly with increasing the process rate up to 50.8 mm/sec, and then starts to decrease with increasing the process rate. It was obvious that the incoming slit tape and the substrate could be heated and pressed longer at a slow

process rate. However, a faster process rate would be preferred because the operating costs could be reduced. Figure 5.19.c demonstrates that the compaction force has the most significant influence on the interlaminar shear strength among all influencing factors. The interlaminar shear strength increases with increasing the compaction force in the range of 30 kgf to 40 kgf, and then a drop in the response is observed from 40 kgf to 50 kgf since the fiber distribution is altered under the compaction force of 50 kgf. It implies that the compaction force exerted on the mold during the in-situ consolidation of thermoplastic composites should be uniform and well-controlled at a constant level. Figure 5.19.d shows that the interlaminar shear strength drops slightly with increasing the nozzle location. When the torch pulls away from the compaction roller, the heat loss in the surroundings goes up rapidly. Thus, the temperatures of the slit tape and substrate decrease accordingly.

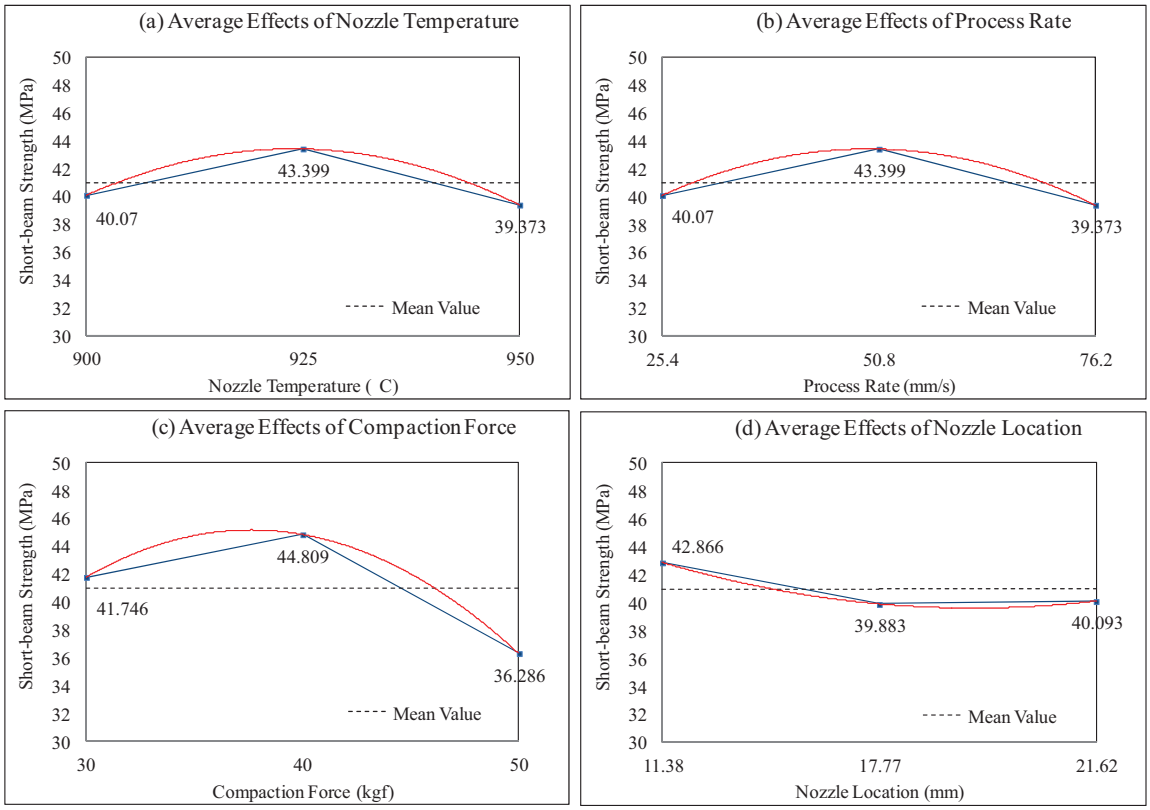

Figure 5.19: 6 Plots of average effects of (a) nozzle temperature, (b) process rate, (c) compaction force, and (d) nozzle location at three levels

In Table 5.22, the analysis of variance of the experimental results reveals the relative influence of factors and interactions to the variability of results. The main factors influencing the interlaminar shear strength are the nozzle temperature (13.58 %), the process rate (23.63 %), the compaction force (54.66 %), and the nozzle location (8.13 %). This suggests that the compaction force has the most significant influence on the interlaminar shear strength. Surprisingly, the nozzle temperature has less influence on the interlaminar shear strength compared to the others. Table 5.23 represents the predictive equation for performance at the optimum condition. The optimum condition is determined based on the quality characteristics selected for the analysis. The expected

interlaminar shear strength should be 51.301 MPa in comparison to the mean value of 40.947 MPa.

Table 5.22: Analysis of variance of experimental results

Factors	Percent (%)
Nozzle Temperature	13.580
Process Rate	23.628
Compaction Force	54.659
Nozzle Location	8.130

Table 5.23: Optimum process parameters by Taguchi's method

Factors	Level Description	Level	Contribution
Nozzle Temperature	925	2	13.894
Process Rate	50.8	2	24.173
Compaction Force	40	2	55.921
Nozzle Location	11.38	1	8.318
Total Contribution from All Factors			10.353
Current Grand Average of Performance			40.947
Expected Result at Optimum Condition			51.301

5.4.5 Conclusions

To achieve the optimum process conditions for the in-situ consolidation of AS4/PEEK rings, nine trial samples were manufactured using the automated fiber placement technique with different combinations of process parameters. A comparison of the interlaminar shear strength of the fiber placed rings was performed by the means of short-beam strength test. The Taguchi's method was implemented in designing experiments, analyzing experimental data, and interpolating test results. The optimum condition for processing AS4/PEEK was obtained as follows: nozzle

temperature = 925 (˚C), process rate = 50.8 (mm/sec), compaction force = 40 (kgf), and nozzle location = 11.38 (mm).

It can be concluded that the quality of fiber-placed laminates varies with the process parameters set to the fiber placement machine. Moreover, compaction force is the most significant factor that affects the strength properties of the laminates. Under the horizontal shear stress, a crack in a fiber-placed laminate initiates and propagates within the ply of a laminate. This implies that the strength properties at the interface of two plies are superior to the strength properties within the plies. The presence of micro-scale voids in between the fibers may be responsible for the degradation of short-beam strength, which can be confirmed by the scanning electron microscope technique.

5.5 Manufacturing and preparation of thermoplastic composite cone for test

5.5.1 Manufacturing of the thermoplastic composite cone

The test specimen is a section of a helicopter tailboom (cone shape) and is a replacement part for the aluminum counterpart. It was made out of advanced thermoplastic composite material which has carbon fiber as reinforcement and Polyether ether ketone (PEEK) as matrix. The commercial name of the material is AS4/APC-2 from Cytec Engineered Materials (Cytec) and it was supplied as a slit tape with 0.25in width. The specimen was made at the Aerospace Manufacturing Technology Centre (AMTC) in Montreal using a 6-axis gantry-type Automated Fiber Placement machine (AFP) supplied by ADC Company (Figure 5.20). It is equipped with a thermoplastic head which accepts one tow at the time and has nitrogen Hot Gas Torch (HGT) as heating system.

The mandrel used for manufacturing was a steel tool (Figure 5.20) with internal heating system, and a temperature controller was used to maintain the tool temperature around 120^0C.

In order to achieve good in-situ consolidation, optimum process parameters were selected based on the results of modal analysis and interlaminar shear strength test obtained in section 5.3 and 5.4. The process parameters used in manufacturing of the thermoplastic composite cone are listed in Table 5.24. The layup sequence and dimensionless parameters of the specimen is tabulated in Table 5.25. Figure 5.20 shows the AFP machine laying down 45^0 layer.

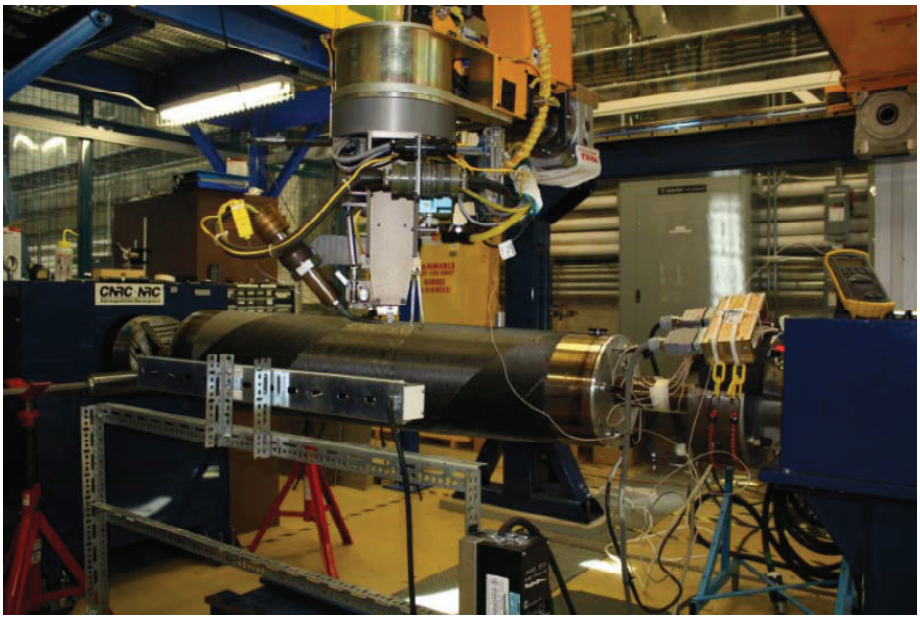

Figure 5.20: 6-axis AFP machine with steel mandrel (Courtesy of National Research Council Canada)

Table 5.24: AFP process parameters used in manufacturing of the thermoplastic composite cone

Parameter	Value
Torch temperature	925°C
Compaction force	40 Kg
Nitrogen flow rate	75 SLPM
Processing speed	50.8 mm/s
HGT location	11.38 mm

Table 5.25: Layup and dimensionless parameters of the thermoplastic composite cone*

Parameter	Value
Layup sequence	[90/±45/0/±45/0/±45/0]s
Length/Large radius (L/R_b)	6.4
Large radius/Total thickness (R_b/H)	93.75
Semi-cone angle range (α)	1°-3°

***Real dimensions and the specific cone angle are not provided for the sake of confidentiality.**

5.5.2 Preparation of the thermoplastic composite cone for bending-buckling test

In order to prepare the thermoplastic composite cone for bending-buckling test, the following steps were taken:

5.5.2.1 Manufacturing end tabs

In bending-buckling test, the bending moment is applied to both ends of the test specimen. Two ends of the specimen are located inside the inner and outer rings and the load is transferred to the circumference of the specimen. In order to prevent the failure from happening inside the rings where it cannot be detected and be seen by cameras, extra layers of composite were added to the end of the thermoplastic composite cone. These layers were built in a stepwise manner, i.e., more layers were added at the end of the specimen and as it moved toward the center of the specimen,

some layers were dropped until there was no extra layer. This would ensure smooth transition of the load to the specimen skin. The design and layup of the tabs are shown in Appendix D.

Furthermore, three composite rings were also manufactured at each end of the thermoplastic composite cone (Figure 5.21). The idea of adding these rings came from the experiment done on LMPA and composite plate (see section 4.2.8) and the purpose of having these rings is to create a self-locking mechanism that prevent the specimen from sliding out of the ring during the test. Basically, the LMPA is entrapped between these rings and the steps made on the inner and outer rings (see Figure 5.22) and stop the tension side of the specimen from slippage during the test.

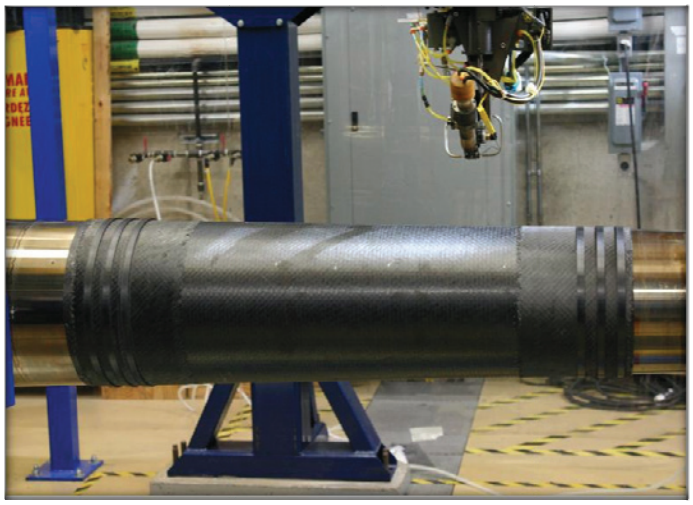

Figure 5.21: Tabs and rings manufactured by AFP on the thermoplastic composite cone

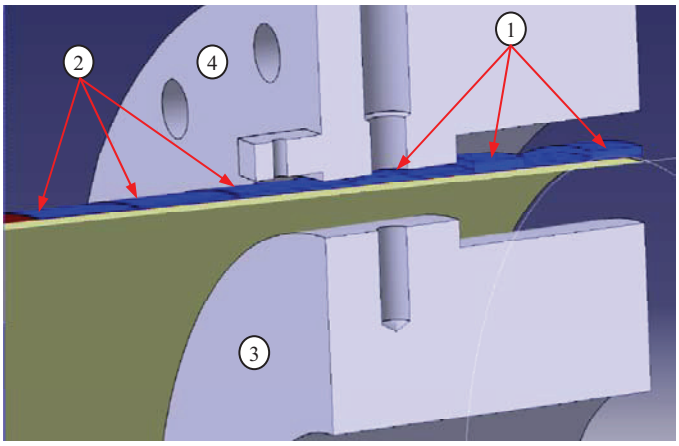

Figure 5.22: Section view of the specimen and rings: 1- tabs, 2- rings, 3- inner ring, 4- outer ring

5.5.2.2 Applying random pattern

Since the Digital Image Correlation (DIC) system was to be used for deformation and strain measurement, the surface of the specimen should have enough texture to be recognizable by cameras. The surface of the thermoplastic composite cone was fairly black after manufacturing and did not have enough texture. So, to have maximum contrast, a white random pattern was applied on the surface of the thermoplastic composite cone using permanent markers. The pattern applied by hand is shown in Figure 5.23.

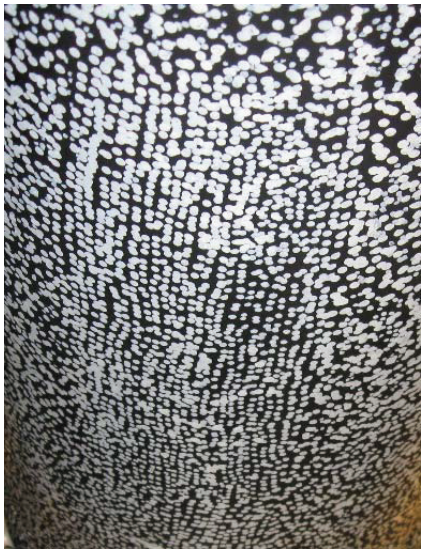

Figure 5.23: Random pattern applied on the surface of the specimen

5.5.2.3 Drilling radial holes

As it was mentioned in section 4.2.5, a series of radial cross bolts was designed to pass through the outer ring, test specimen and the inner ring. This would help the LMPA to prevent the test specimen from sliding out the rings during the test in tension side. In order to install these bolts, both ends of the thermoplastic composite cone were drilled by radial holes while it was fixed between the rings. These holes were drilled only on the tension side of the specimen as there was no concern of sliding on the compression side. The radial holes are shown in Figure 5.24.

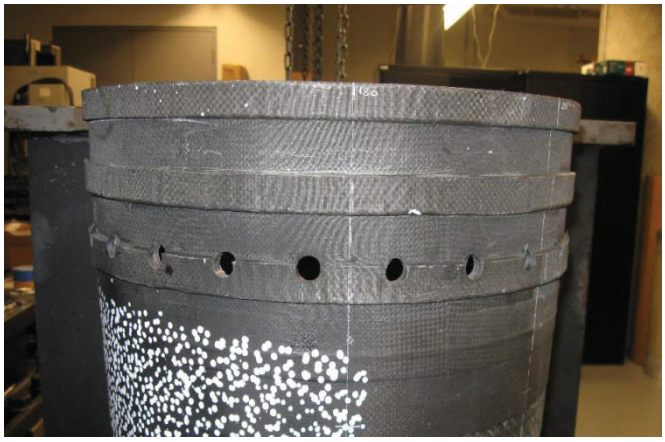

Figure 5.24: Radial holes at the tension side of the specimen

5.5.2.4 Applying strain gages

Twenty two strain gages were attached to the surface of the thermoplastic composite cone in 13 locations. The strain gage pattern, shown in Figure 5.25, was designed in such a way to have minimum interference with Digital Image Correlation system (four cameras). As can be seen from strain gage pattern, the majority of strain gages were oriented axially (11 gages) while 8 strain gages were placed circumferentially and three gages were oriented at 45^{o}. At three locations (i.e., mid-length and close to small end on tension side and close to small end on the compression side) three-arm rosette strain gages were placed which made it possible to read axial, circumferential and shear strain at these locations. No strain gage was placed on the tab area and all of them were attached to the skin of the thermoplastic composite cone.

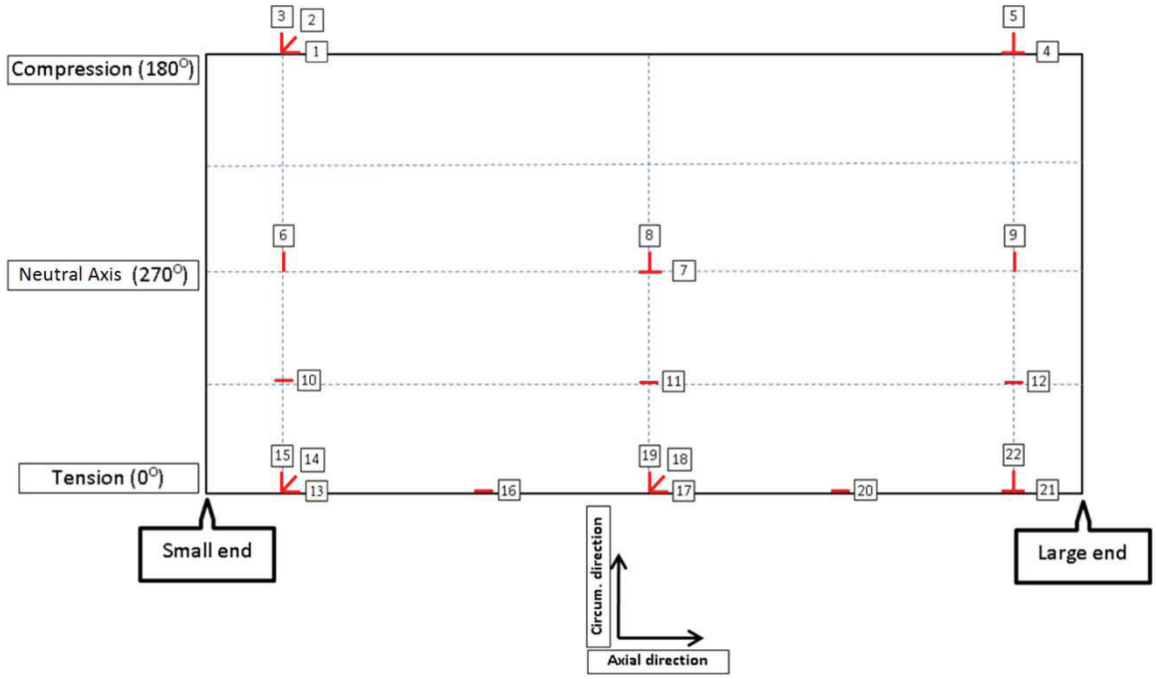

Figure 5.25: Strain gage pattern applied on the thermoplastic composite cone

Digital Image Correlation system (DIC) also was used to measure in-plane strains and out-of-plane deformation using two pairs of cameras (total four cameras). This measurement covered top surface (which was in compression) and side surface of the specimen.

5.5.2.5 Potting with LMPA and making the assembly

In order to pot the thermoplastic composite cone end into the space between the inner and outer ring using a Low Melting Point Alloy (LMPA), first the rings were mounted to the Adaptor Plate and then the assembly was put on a hot plate for several hours to reach about 100°C. The specimen was centered between the rings and while some LMPA was melting on the Adapter Plate (which was on the hot plate), some other amount of LMPA was melted in a separate pot and then poured around the circumference of the specimen in between the two rings (Figure 5.26).

Once the one side of the specimen was potted, Installation Spacer Beams (see section) were installed and the assembly was rotated 180^{o} on the hot plate and the same procedure was taken for the other end of the specimen.

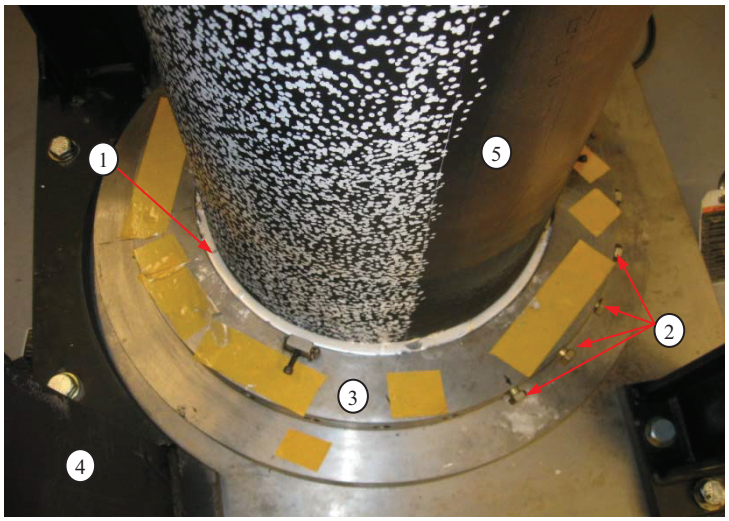

Figure 5.26: Potting the specimen between the ring using LMPA: 1- LMPA, 2- radial cross bolts, 3- outer ring, 4- Installation Spacer Beam, 5- specimen

The assembly after potting procedure and installing the Installation Spacer Beams was brought to the setup using a gantry crane and mounted to Back-plates (Figure 5.27). The last step was to remove the Installation Spacer Beams from the bending test setup.

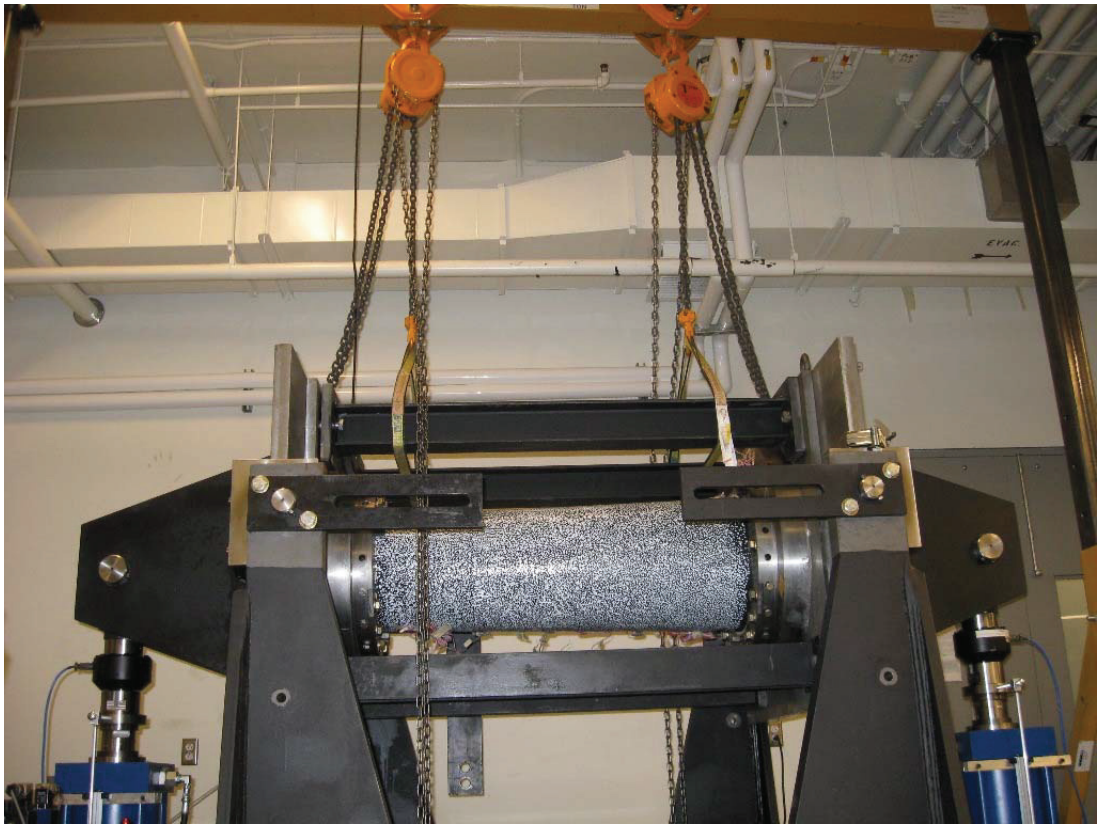

Figure 5.27: Installing the specimen assembly on the bending test setup

5.6 Bending-buckling experimental results for thermoplastic composite cone

5.6.1 Test plan

Two pairs of cameras were set; one pair was looking from the side (side view) while the other pair was looking from the top to the specimen (top view). After calibrating the cameras and connecting all the gages to the data acquisition system, the test was started and the load kept increasing until a loud sound was heard and the load dropped drastically. The buckling due to bending occurred and led to final failure. A visible crack was observed on the top surface and

near the small end of the thermoplastic composite cone (after tabs) as expected. The crack extended around the circumference of the cone. Looking at the failure section, one could clearly see the fiber and matrix breakage (see Figure 5.28). It was seen, also, that no slippage occurred between the specimen and the rings on the tension side, suggesting that the LMPA and cross bolts perfectly fulfilled their roles. The deformation, strain, and load results obtained are presented and discussed in the following sections.

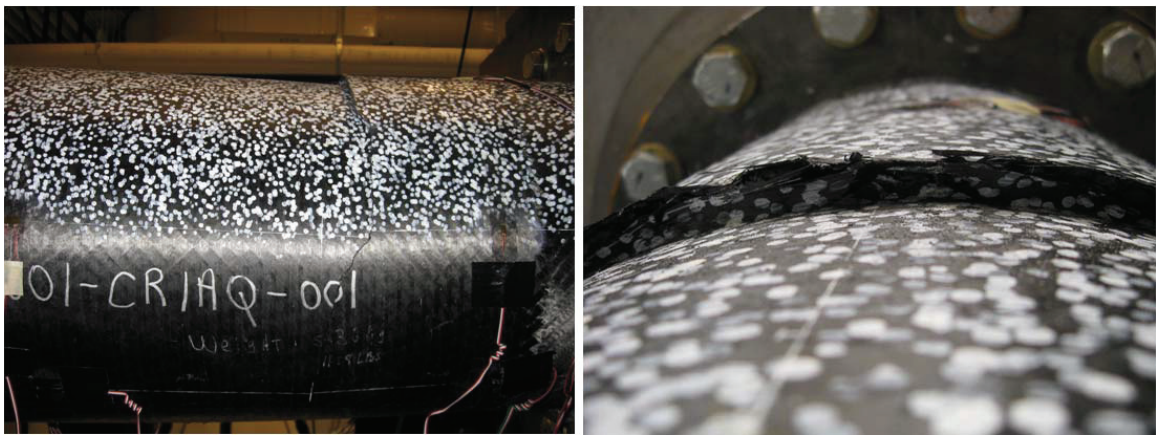

Figure 5.28: Failure section of the thermoplastic composite cone

5.6.2 Deformation and strain results obtained from the DIC system

5.6.2.1 Deformation results

The contour plot of axial deformation (U) of the thermoplastic composite cone (top view) just prior to buckling is shown in Figure 5.29. As it can be expected, the small end and the large end of the specimen (right side) moved toward one another during the bending test and the top surface was contracted. As a result, the axial deformation of the small end (right side in Figure 5.29) was negative while the axial deformation of the large end (left side in Figure 5.29) was positive and

the axial deformation was zero somewhere in between. The axial deformation pattern looks quite symmetric about the mid-plane and has a maximum magnitude of about 1.6 millimeter in the gage area, near the big end.

The contour plot of circumferential deformation (V) of the thermoplastic composite cone (top view) just prior to buckling is shown in Figure 5.30. It can be seen form Figure 5.30 that since the top surface of the specimen was under compression and consequently contracted in axial direction, it was expanded in the circumferential direction (Poisson effect). Figure 5.30 shows more deformation concentration close to the small end of the specimen where the failure happened.

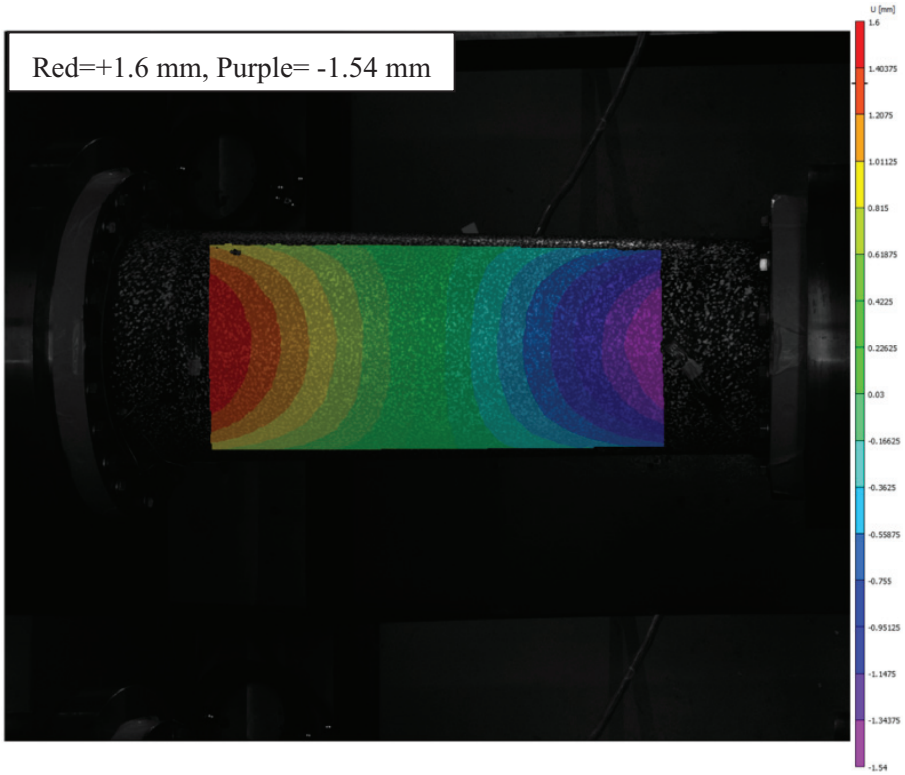

Figure 5.29: Axial deformation (U) contour plot obtained by DIC system (top view)

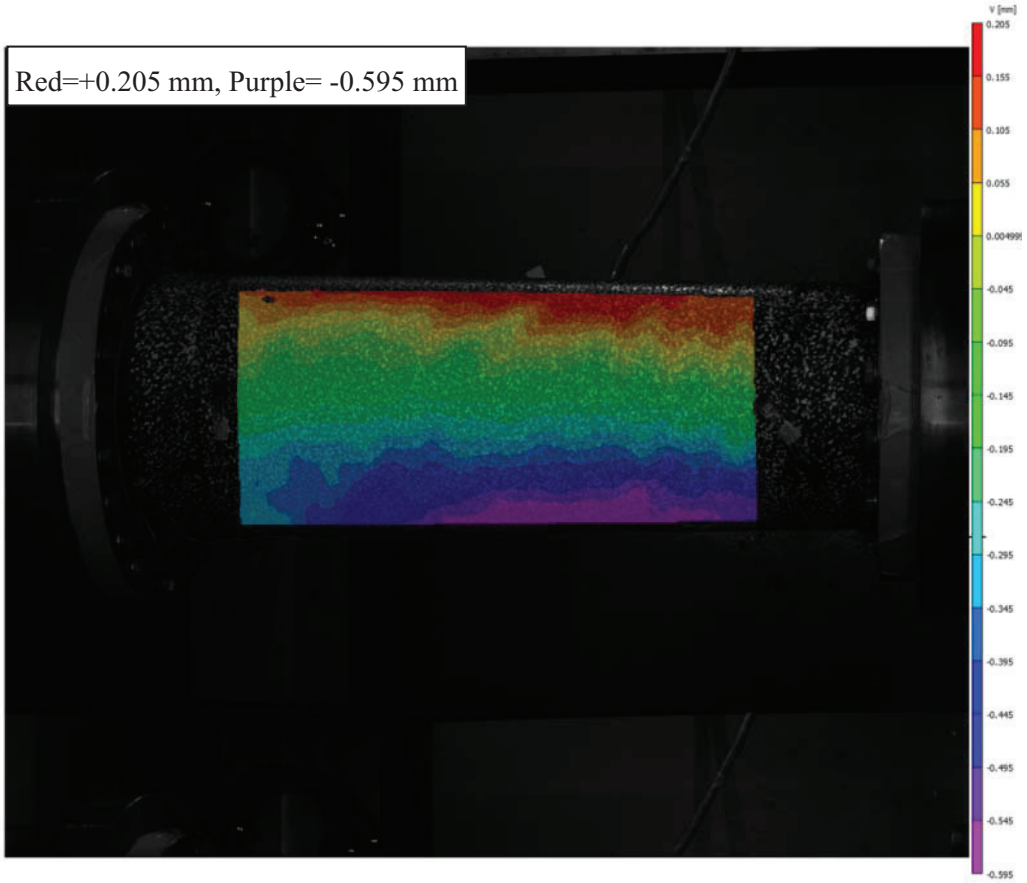

Figure 5.30: Circumferential deformation (V) contour plot obtained by DIC system (top view)

The out-of-plane deformation of the specimen (top view) is shown in Figure 5.31 just prior to failure. As one can expect, the maximum deflection happened near the middle of the specimen (toward the small end) while the deflection decreased toward both ends. The maximum top surface deflection was recorded to be about 5 millimeters.

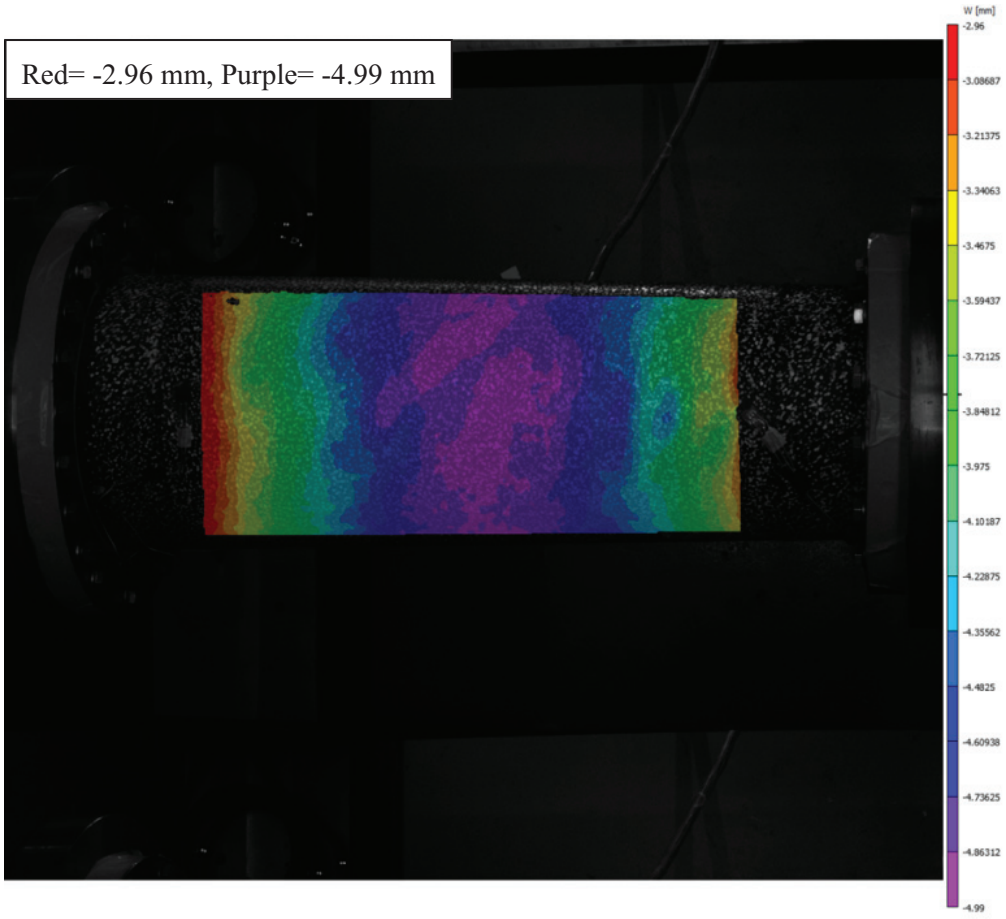

Figure 5.31: Out-of-plane deformation (W) contour plot obtained by DIC system (top view)

The contour plot of circumferential deformation (V) of the thermoplastic composite cone (side view) prior and after failure is shown in Figure 5.32. The maximum side surface deflection of 4.68 millimeter occurred at the middle of the specimen. Figure 5.32 also shows quite a symmetric deflection pattern prior to the failure. After failure, the location of the maximum deflection moved from the middle to the location of the failure where the crack separated the top surface of the specimen. Although the specimen was ruptured at the top (where the failure happened) under

compression load, the bottom surface of the specimen which was under tension was not ruptured completely and showed some resistance even after the failure.

5.6.2.2 Strain results

The axial strain obtained by two cameras looking at the top surface of the thermoplastic composite cone is shown in Figure 5.33. As can be seen from this figure, prior to failure, the whole top surface was under compression (negative strain) with the maximum strain of 7100 microstrain near the small end of the cone. The axial strain was not uniformly distributed on both ends of the specimen and more strain concentration could be seen at the small end. This was expected since the small end had less stiffness in comparison with the large end of the thermoplastic composite cone. From the axial strain distribution prior to buckling, one can predict the possible location of failure based on axial strain accumulation near the small end (see after failure image, Figure 5.33).

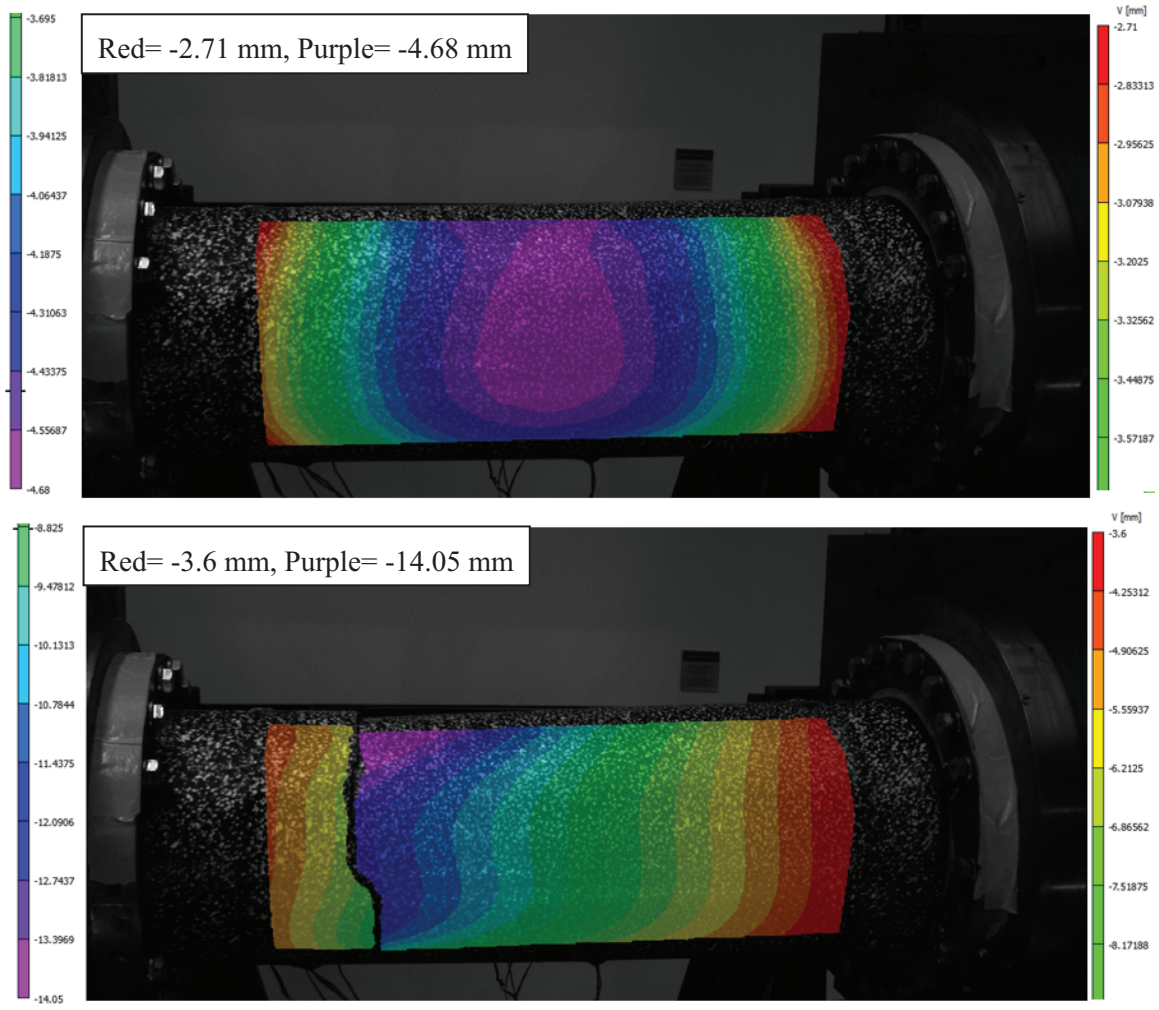

Figure 5.32: Prior and after failure circumferential deformation (V) contour plot obtained by DIC system (side view)

Using two cameras looking from the side to the specimen, the axial strain distribution is shown in Figure 5.34 prior to buckling. The purple and blue colors represent negative strain (compression) at the top, and the red and yellow colors represent positive strain (tension) at the bottom of the specimen. Neutral axis where the axial strain is zero falls almost at the middle of the cone and is

represented by green. Again, more axial strain concentration can be seen from Figure 5.34 near the small end (left side of Figure 5.34) where the failure occurred.

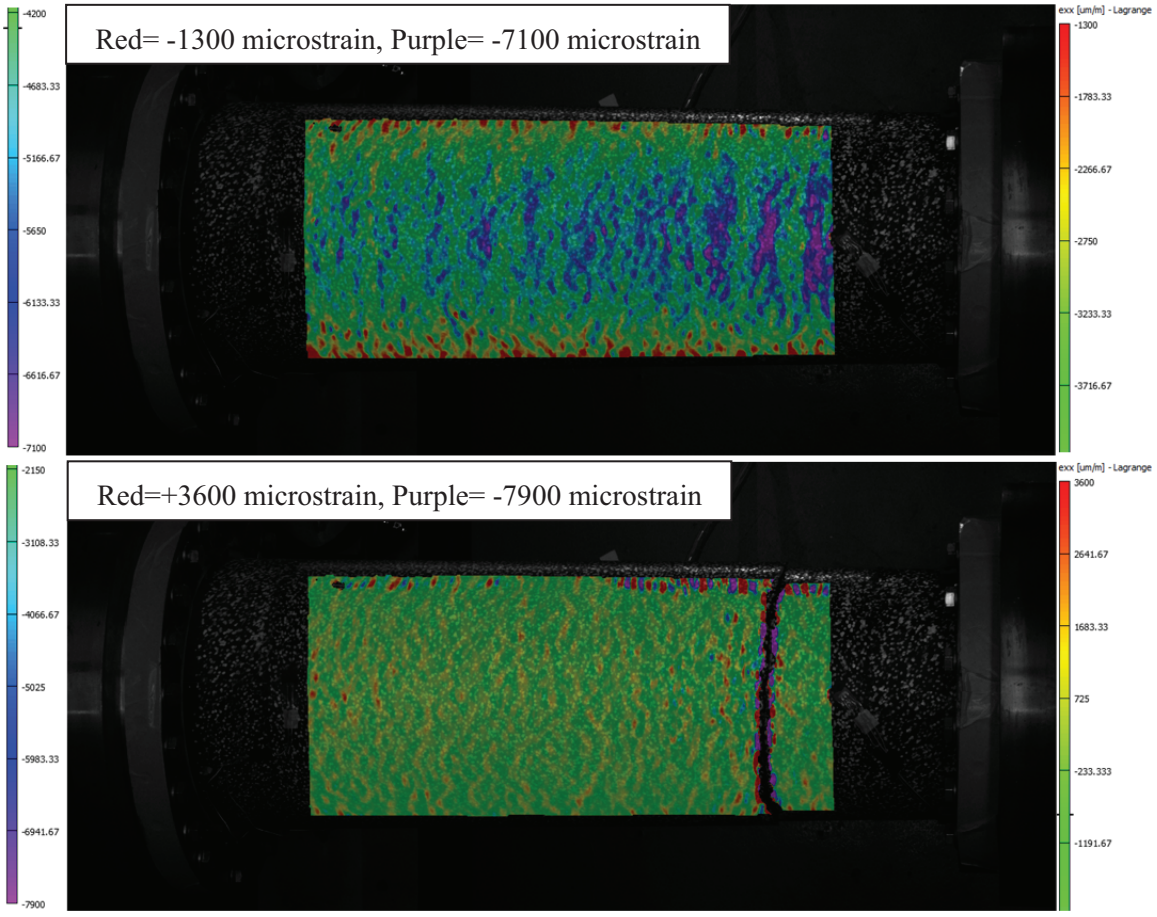

Figure 5.33: Prior and after failure axial strain (ε_{xx}) contour plot obtained by DIC system (top view)

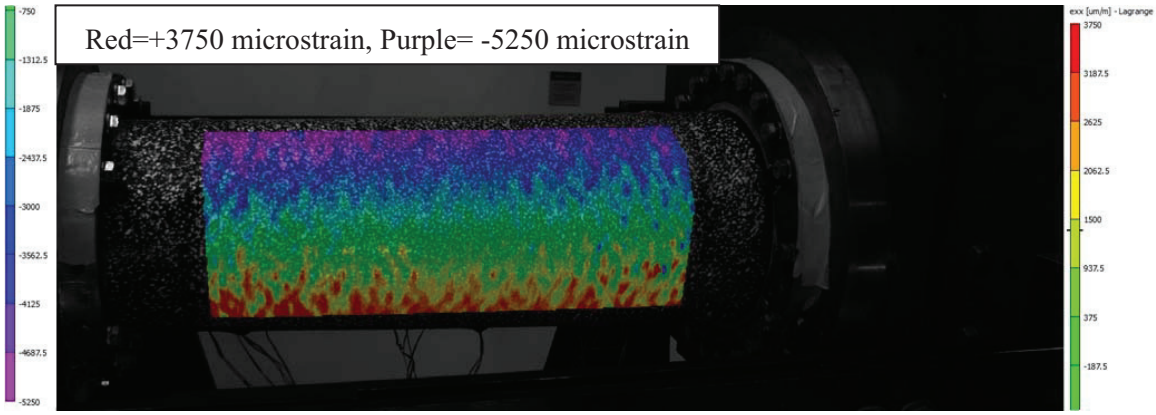

Figure 5.34: Prior to failure axial strain (ε_{xx}) contour plot obtained by DIC system (side view)

5.6.3 Strain results obtained from strain gages

Twenty two strain gages (numbered from 1 to 22) were installed according to pattern shown in Figure 5.25. The axial strains recorded by gage 1 on the compression side and gage 13 on the tension side are shown in Figure 5.35. Both gages were located at the same section near the small end (see Figure 5.25). As can be seen from Figure 5.35, both axial strain graphs are symmetric about horizontal axis prior to the buckling. This behavior is well-known from classical beam bending theory in which the axial strain is proportional to the distance of the point from the neutral axis. Close to the point that buckling occurred, gage 1, which was located near the failure point, exhibited nonlinear strain behavior which could be interpreted as the start of the failure. After buckling occured and the specimen failed, the strain at the compression side (gage 1) dropped almost to zero while gage 13 which was located at the tension side dropped first to about 2300 microstrain and then increased again to about 4000 microstrain. This could be attributed to the fact that while the compression side fell apart due the severe crack, the tension side still was bearing some load.

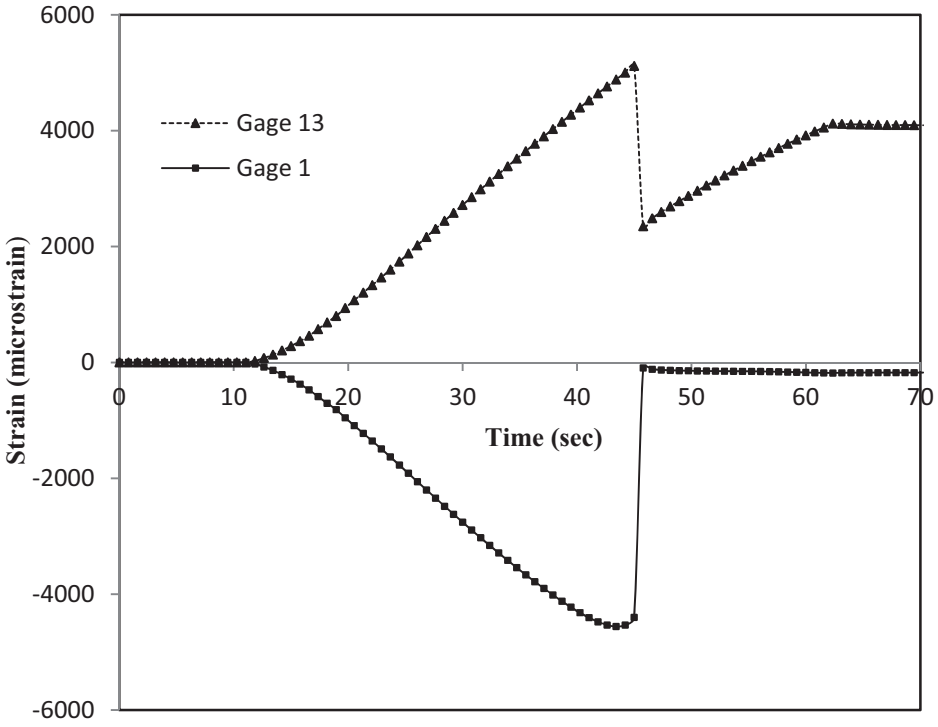

Figure 5.35: Axial strain at gage 1 and gage 13

Figure 5.36 shows the axial strain graphs for gage 7, gage 11, and gage 17. These three strain gages were placed (see Figure 5.25) at the mid-length of the cone in axial direction at tension side (gage 17), neutral axis (gage 7) and in between them (gage 11). Since gage 17 located at the bottom side of the specimen and had greatest distance from neutral axis, it recorded greater axial strain than gage 11 recorded. Gage 7 located at neutral axis showed about maximum 150 microstrain, which could be because of alignment error of the strain gage and /or due to restriction of the neutral axis in axial direction (boundary conditions). This suggests that the axial load on the specimen was small (as can be expected) during the test.

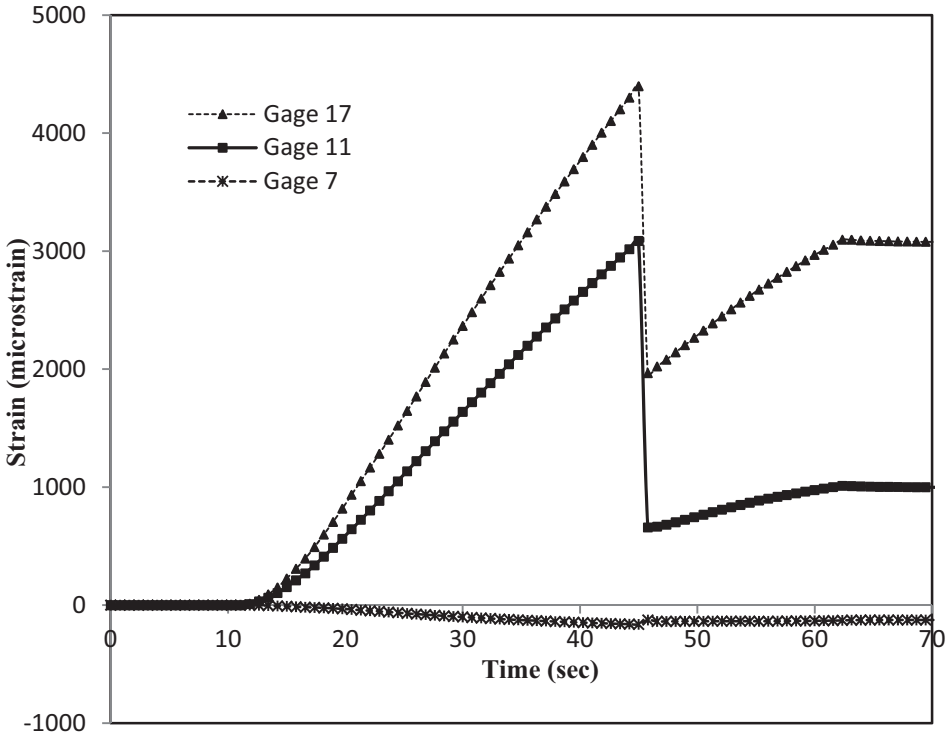

Figure 5.36: Axial strain at gages 7, 11 and 17

Figure 5.37 shows the axial strain graphs for gage 10, gage 11, and gage 12 which were located at small end, mid-length, and large end, respectively. Although these three strain gages had the same distance from the neutral axis, but they were placed at different length location (see Figure 5.25) so that one can see the axial strain distribution over the length of the specimen. As one can see from Figure 5.37, prior to buckling, gage 10 (which is place at small end) had the highest value at all time. Gage 11 (which was located at the mid-length of the cone) showed about 23% decrease in axial strain with respect to gage 10. Gage 12, which was placed at the large end, measured the axial strain by about 18% less than gage 11. This trend is logical since as one moves to larger section, stiffness increases and consequently, axial strain decreases. After failure occurred, the mentioned trend reversed; that is gage 12 recorded highest axial strain, gage 11 was at the second

high value, and finally gage 10 showed lowest axial strains. This inverse trend could be explained by the fact that failure occurred at the small end and as a result, the drastic drop was associated with gage 10 (88% of value) while gage 12 which had the most distance from the failure location showed the least drop in strain value (70%).

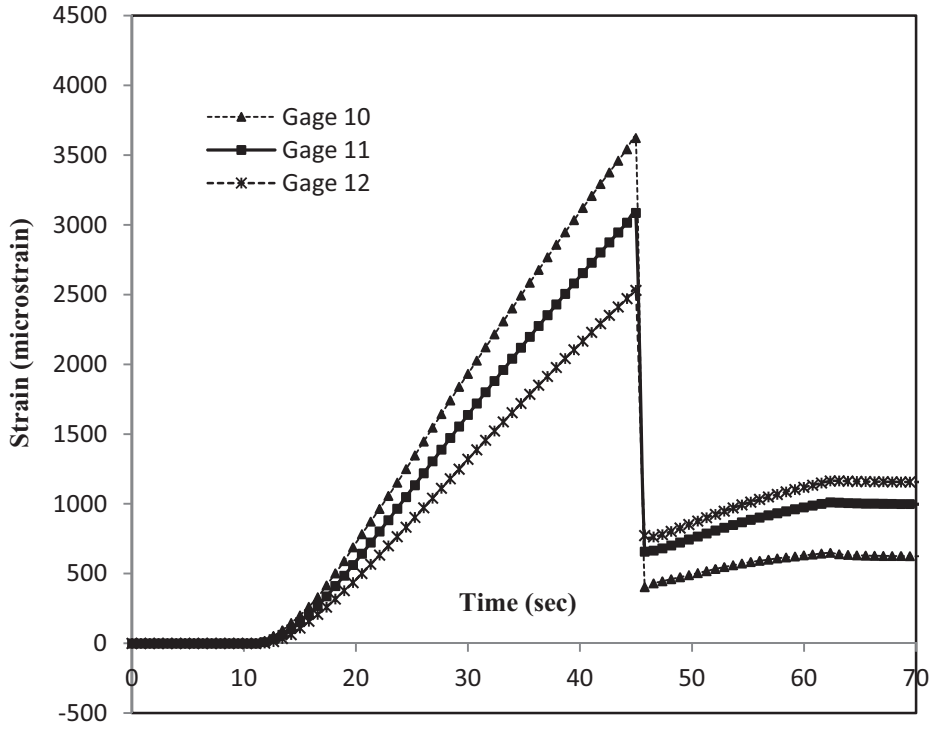

Figure 5.37: Axial strain at gages 10, 11 and 12

Circumferential strains measured at small end of the specimen are shown in Figure 5.38. Strain gage 3, 6, and 15 were oriented in circumferential direction on the top surface (compression side), mid-plane (neutral axis), and bottom surface (tension side) of the cone, respectively (see Figure 5.25). Circumferential strain was almost zero at the neutral axis (gage 6), suggesting that no significant strain (and therefore stress) occurred at neutral axis as expected. Gage 3 located on the compression side of the specimen showed positive circumferential strain; that means although the

top surface of the cone was under compression in axial direction, in the circumferential direction it was under tension all test time. On the other hand, gage 15, which was placed on the tension side of the cone, showed negative circumferential strain over test time, indicating that the bottom surface was under compression in circumferential direction (while was under tension in axial direction). As can be seen from Figure 5.38, strain graphs for gage 3 and 15 are symmetric about the horizontal axis and have quite linear trend except near the buckling point for gage 3 and after buckling occurred.

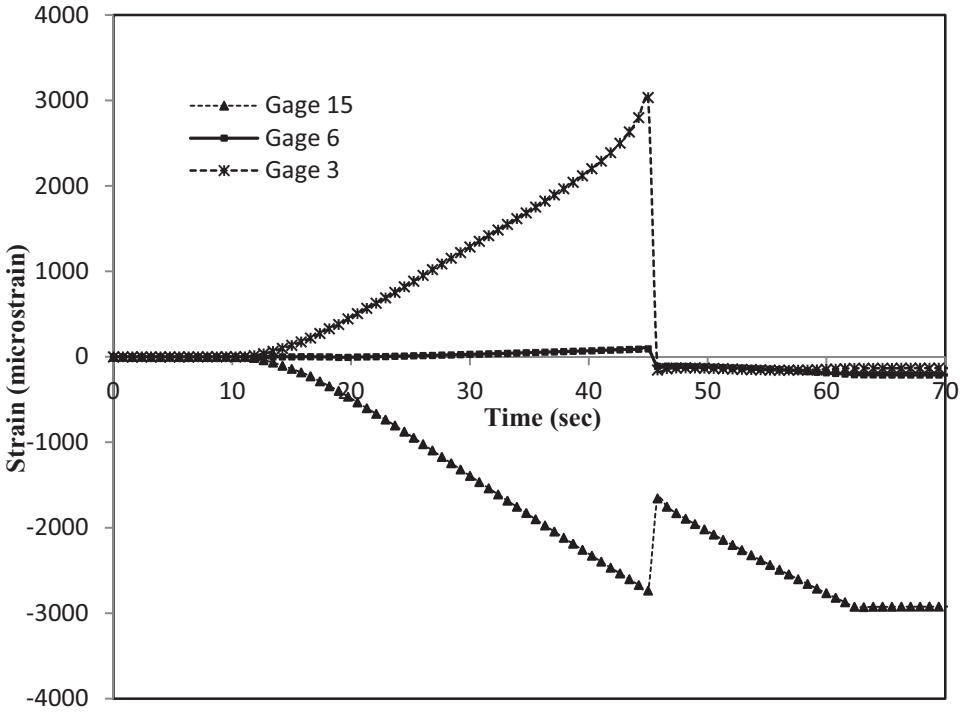

Figure 5.38: Circumferential strain at gages 3, 6 and 15

Figure 5.39 shows the circumferential strain graphs versus time for gages 5, 8, 9, 15, and 19 (see Figure 5.25 for gage locations). Comparing gage 15 and gage 19, one can see that the circumferential strain decreased along the length of the cone as one moves toward the small end.

This is due to decease of stiffness at smaller cross sections. Gages 8 and 9 were placed at neutral axis and showed small circumferential strains. Gage 9 was oriented at large end of the specimen on top surface (compression side) and recorded positive strain in tension in circumferential direction.

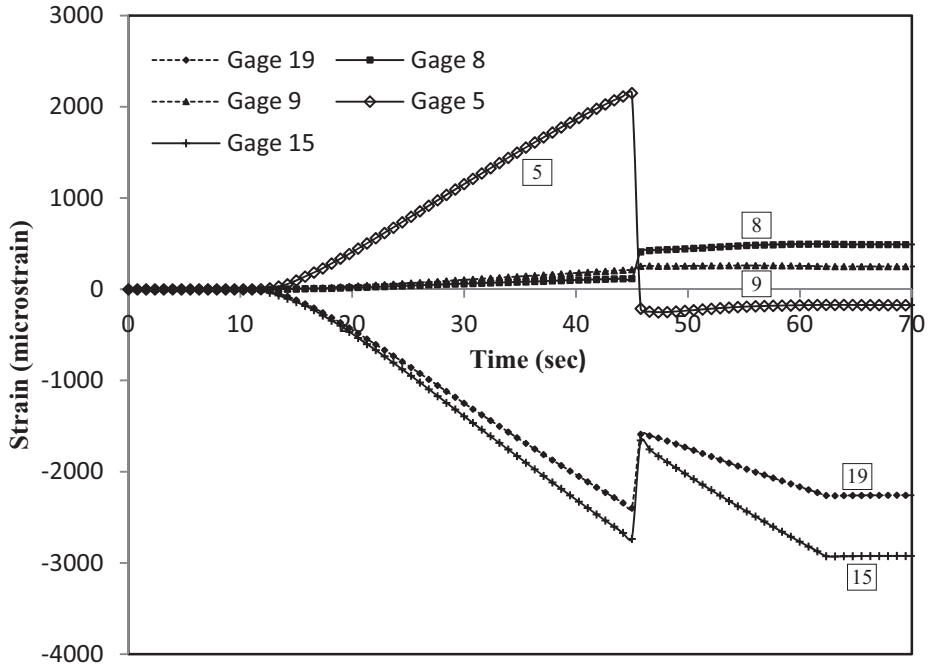

Figure 5.39: Circumferential strain at gages 5, 8, 9, 15, and 19

At three locations three-arm rosette strain gages were installed which enables one to obtain shear strains (see Figure 5.25). Figure 5.40 shows both shear strain and maximum shear strain at location of gages 1, 2 and 3 (small end top surface). As it can be seen, shear strain reached maximum of about 1000 microstrain while maximum shear strain at this point reached to about 7500 microstrain prior to the buckling. Drawing the Mohr's circle for strain at this point (using Figure 5.35, Figure 5.38 and Figure 5.40), one can comment that the axial and circumferential

directions on the cone were very close to principal directions as tonsorial shear strain was small in comparison with axial and circumferential strains.

Figure 5.41 shows the maximum shear strain at all three locations where three-arm rosette strain gages were installed (see Figure 5.25). All three locations had similar maximum shear strain up to the point of buckling. After buckling, the maximum shear strain at the location of gages 1, 2, and 3 dropped more drastically than other two locations. This was because of the fact that gages 1, 2, and 3 were located on the top surface (under compression) near the failure section.

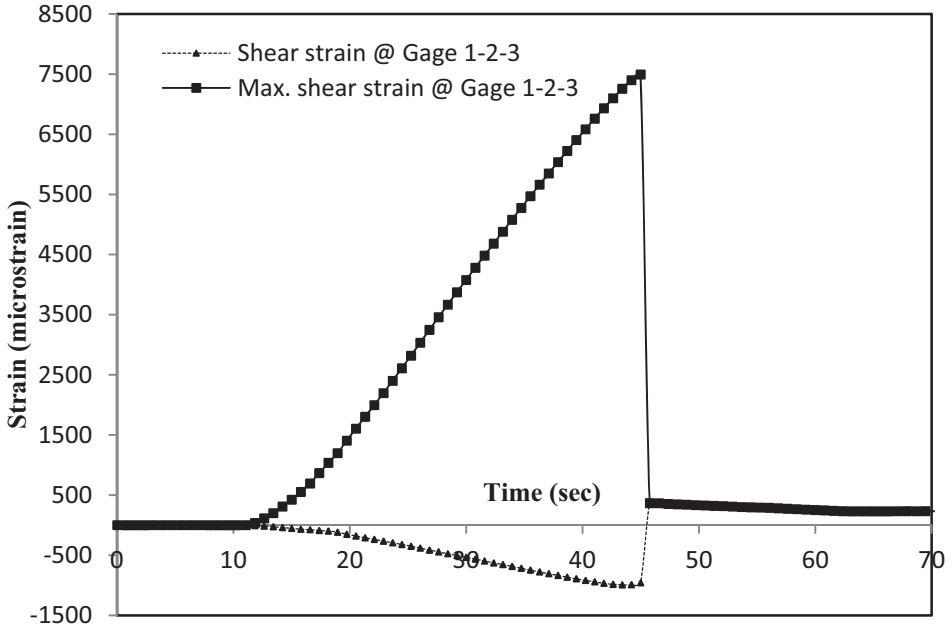

Figure 5.40: Shear and maximum shear strain at the location of gages 1, 2 and 3

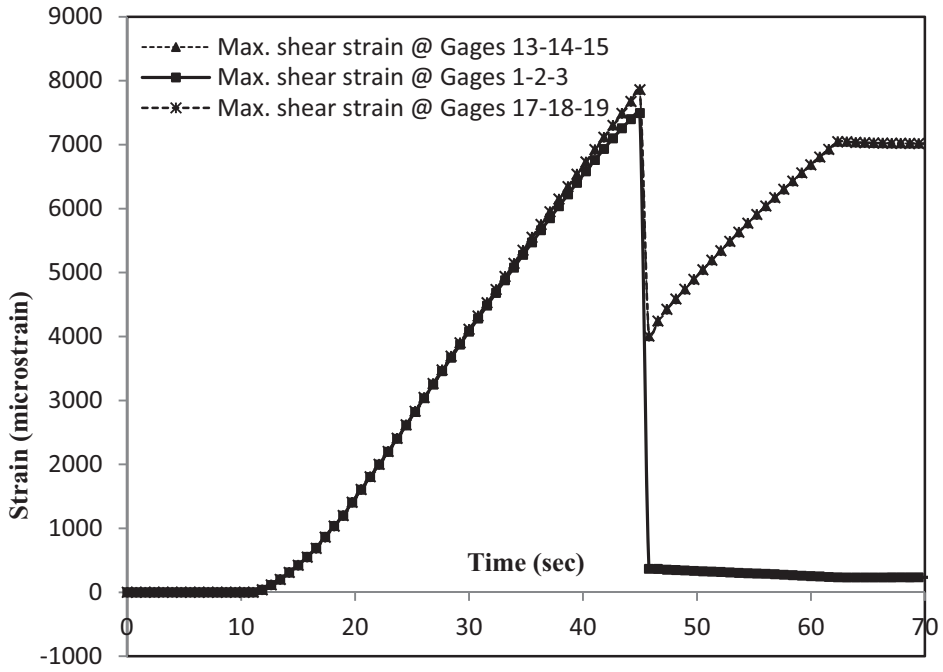

Figure 5.41: Maximum shear strain at the three locations

5.6.4 Force results obtained from the load cells

The graph of force versus time measured by two independent load cells is shown in Figure 5.42. Both load cells (right and left) recorded almost the same value for the force during the test that means the same moment was applied to both ends of the specimen. This was one the requirements in the design of the loading unit (see section 4.3.1) which was perfectly met. As can be seen from Figure 5.42, the load increases (in negative value) rapidly until 45 seconds passed from the test and reached to about 17500 lbf (critical load). After buckling occurred, the force measured by the left load cell, which was located at the small end of the specimen (close to

failure section), decreased by 84% and the force measured by the right load cell decreased by 80%.

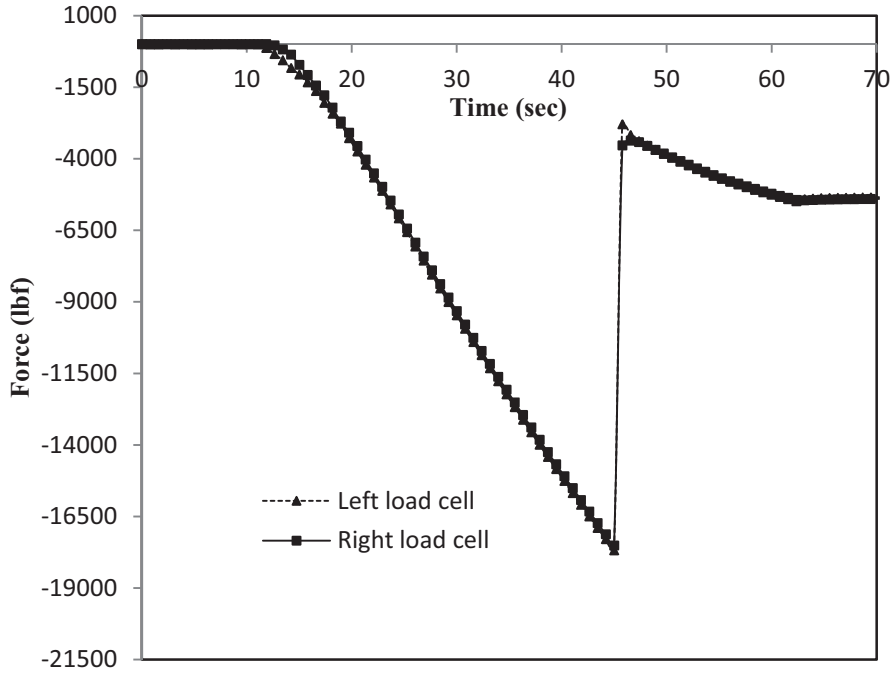

Figure 5.42: Load versus time graphs for bending-buckling test

5.7 Theory and experiment comparison

5.7.1 Buckling moment; theory and experiment

The applied moments on two ends of the specimen can be calculated from the force graphs (Figure 5.42) multiplied by the moment arm length. The results shown in Figure 5.43 indicate a maximum moment of 402,052 lbf-in applied to the left side of the specimen and a maximum moment of 418,657 lbf-in applied to the right side of the thermoplastic composite cone prior to

the buckling. So the experimental critical buckling moment of the thermoplastic composite cone would be the minimum of the above mentioned moment values which is 402,052 lbf-in.

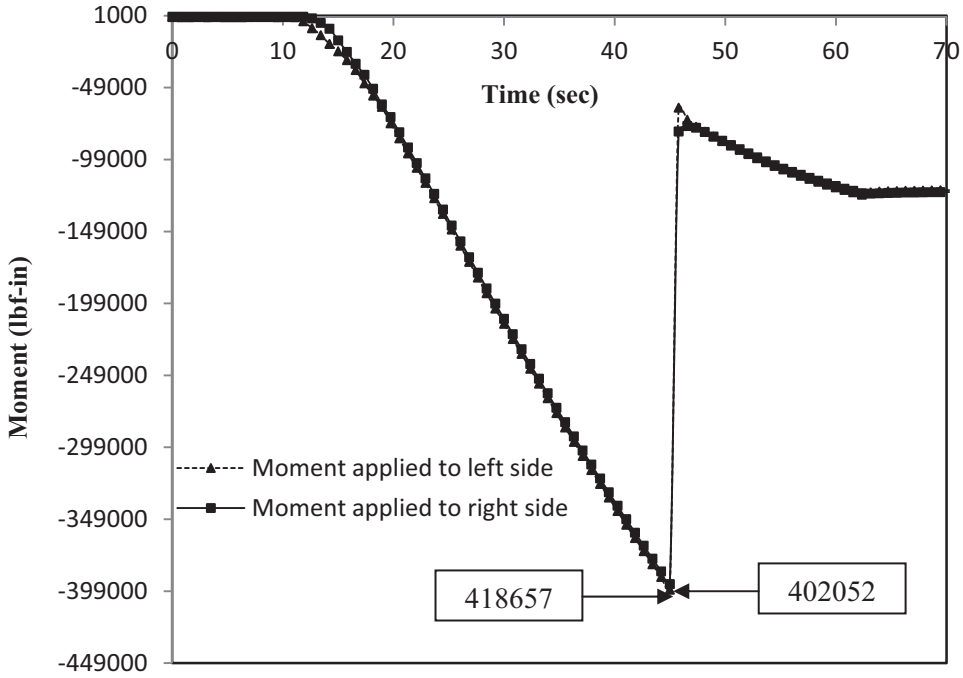

Figure 5.43: Moment versus time graphs for bending-buckling test

Theoretical buckling moment can be calculated from the formulation developed in section 2.3. Regarding the geometry, the tabs added to both ends of the specimen (see section 5.5.2.1) were not included in the analysis and consequently the gage area of the specimen was considered (which was the length between the end tabs). The dimensionless parameters and layup sequence used in theoretical analysis is shown in Table 5.26. The semi-cone angle is provided in a range as oppose to a specific value for the sake of confidentiality. Material properties of AS4/PEEK used in the theoretical analysis is the same as the ones used in sizing the thermoplastics cone and is listed in Table 5.27. These properties were obtained from supplier's handbook (Cytec Engineered

Materials) by applying a knock down factor. The knock down factor was determined by comparing the material properties of IM6/PEEK (the closest material that could be found to AS4/PEEK) from supplier handbook (Cytec Engineered Materials) and military handbook (MIL). Regarding the boundary condition, it was assumed that both ends of the thermoplastic composite cone were simply supported with axial degree of freedom allowed (S3-type).

Table 5.26: Dimensionless parameters and layup sequence of the specimen used in theoretical analysis*

Layup sequence	[90/±45/0/±45/0/±45/0]s
Length/Large radius (L/R_b)	4.13
Large radius/Total thickness (R_b/H)	90.87
Semi-cone angle range (α)	1°- 3°

***Real dimensions and the specific cone angle are not provided for the sake of confidentiality.**

Table 5.27: Material properties of AS4/PEEK used in buckling under bending analysis

E_{11}, psi (MPa)	15.34×10^6 (105.765)
E_{22}, psi (MPa)	1.31×10^6 (9.032)
$G_{12} = G_{13}$, psi (MPa)	0.44×10^6 (3.033)
G_{23}, psi (MPa)	0.32×10^6 (2.206)
$\nu_{12}= \nu_{13}$	0.248
ρ, lb/in^3 (kg/m^3)	0.0596 (1649.7)

The result of theoretical analysis and experimental approach in term of dimensionless critical buckling moment (defined in equation (2.45)) are tabulated in Table 5.28 for comparison purposes. The theoretical dimensionless buckling moment is provided for a range of semi-cone angle varying from 1^o to 3^o.Comparing the experimental dimensionless buckling moment with the theoretical one for the specific semi-cone angle of the thermoplastic composite tailboom, the difference less than 1% is achieved.

Table 5.28: Theoretical and experimental dimensionless bucking moment of the thermoplastic composite (AS4/PEEK) cone

	Experiment	**Theory (for $\alpha = 1° - 3°$)**
$\overline{\mathrm{M}}cr$	3263.2	3380.1 - 2985.2

Chapter 6

Conclusions, contributions and future works

6.1 Conclusions

Buckling analysis of laminated conical shells under axial compression load and under pure bending load was performed through a shear deformation shell theory in Chapter 2. For buckling under axial load, both non-axisymmetric and axisymmetric formulations were considered. From parametric studies it was concluded that for thin and short conical shells the critical buckling load decreases with increasing semi-cone angle. Likewise, the critical buckling load decreases with increasing fiber orientation of angle-ply thin and short conical shells.

For buckling under bending load, the Ritz method was used to obtain the semi-analytical solution for simply supported composite conical shells. It was observed from parametric studies that for thin and short conical shells considered in this study, the critical buckling moment decreases as the semi-cone angle increases. It was shown that the semi-cone angle, layup sequence, and the length-to-radius ratio have significant effect on the dimension less buckling moment. For angle-ply cones, it was seen from the numerical results that the dimensionless critical buckling moment depends significantly on the fiber angle in two intervals, namely $0^{o} < \theta < 15^{o}$ and $75^{o} < \theta < 90^{o}$ while it changes moderately when $15^{o} < \theta < 75^{o}$.

The effects of semi-cone angle, radius-to-thickness ratio, length-to-thickness ratio, layup sequence, and boundary conditions on the bending response of cross-ply conical shells were studied in Chapter 2 as well and it was shown that the dependency of the cone deflection on semi-cone angle is very different for different boundary conditions.

Bending, buckling and fundamental frequency of cross-ply circular cylindrical shells was presented in Chapter 3. The effect of assumed displacement field on both formulation and results was determined and it was shown that assumed displacement field has a significant effect on numerical results in some cases. Consequently, one can conclude that it is of substantial importance to choose an appropriate displacement field.

Regarding the manufacturing of the thermoplastic composite cone, Chapter 5, the study performed on the effect of autoclave process on the stiffness properties of two automated fiber placed thermoplastic composite cones suggested that the overall stiffness properties of the cones made by AFP (Automated Fiber Placement) are as good as those of cones undergone autoclave treatment. Furthermore, it was observed that after treating the two thermoplastic composite cones inside the autoclave, the thickness of both cones were reduced (by average of 7.7%) and consequently the natural frequencies were decreased. However, it should be mentioned that the quality of the thermoplastic composite cones does not only depend on the stiffness properties. Strength properties that depend vastly on the microstructure of the laminate can be different for AFP-made and autoclave treated cones which in turn can affect fatigue and dynamic behavior of these structures.

The optimum process parameters in the in-situ consolidation of thermoplastic composite rings using AFP technique were determined from both stiffness and strength point of view. The stiffness criterion was checked through fundamental natural frequency obtained by experimental modal analysis and stiffness criterion was measured by short-beam strength test. Nine thermoplastic composite rings were manufactured with different combinations of process parameters using Taguchi method of design of experiment. It was concluded that the quality of

fiber placed laminates varies with the process parameters set to the fiber placement machine. Moreover, it was observed that the process rate has the most significant effect on the stiffness properties of the laminate, while the compaction force is the most significant factor that affects the strength properties of the laminates. Based on this study, the following optimum conditions were used for manufacturing of thermoplastic composite (AS4/PEEK) cone: nozzle temperature = 925 (˚C), process rate = 50.8 (mm/sec), compaction force = 40 (kgf), and nozzle location = 11.38 (mm).

Regarding the experimental result of buckling under bending of the thermoplastic composite cone, a very good agreement (less than 1% difference) was achieved between the theory developed in Chapter 2 and the experimental critical buckling moment.

6.2 Contributions

1. A first order shear deformation shell theory to study buckling and bending behavior of composite conical shells has been proposed. A semi-analytical approach (Ritz method) has been applied to study buckling under axial load and buckling under bending of composite conical shells. The parametric studies have been performed based on the proposed formulation.
2. An analytical solution (Levy type solution) to study the bending response of cross-ply conical shells under sinusoidal bending load has been applied.
3. A new formulation has been proposed to study bending, buckling, and vibration of cross-ply cylindrical shells using an analytical solution (Levy type solution). A different displacement field from what was assumed in the literature ([17] and [18]) has been proposed and consequently a new formulation has been obtained for the problem. It has

been shown that it is essential to consider proper displacement field as it affects the numerical results significantly in some cases.

4. An experimental setup has been designed and developed to study bending, and buckling under bending load, behavior of composite shells. The setup has been designed to apply equal bending moments at the both ends of the structure, simulating pure bending test conditions. This setup is capable of performing bending test on samples with arbitrary cross-section shape (in the range of 1 inch, 25.4 mm, to 33 inches, 838 mm) with appropriate end fixture set. It can also accommodate samples with different lengths (from 30 inches (762 mm) to 48 inches (1219 mm)).
5. Experimental result has been obtained for buckling under pure bending of composite conical shells. To the best of the author's knowledge, this is the first time such experimental result is published. A digital Image Correlation technique has been employed to measure the full field strain and deformation of the sample during the test. The experimental result (critical buckling moment) agreed well with the theoretical one.
6. The effect of autoclave treatment on the stiffness quality of the thermoplastic composite cones made by Automated Fiber Placement (AFP) has been studied.
7. The d etermination of optimum process parameters for AFP in manufacturing of thermoplastic composite (AS4/PEEK) has been performed from both stiffness and strength point of view.

6.3 Future works

As an extension to this research, the following suggestions can be considered:

1. In order to improve the quality of the automated fiber placed laminate, further study can be made on the effect of different processing parameters in manufacturing of thermoplastic composites using AFP. For example, different heating system (e.g., laser heating head) can be considered instead of hot gas torch.
2. The effect of axial and circumferential stiffeners (stingers and ribs) on the buckling and bending behavior of composite conical shells can be studied both theoretically and experimentally. Samples can be made by Automated Fiber Placement (AFP) and can be tested under bending using the composite tube bending setup developed in this research.
3. The effect of autoclave treatment on the strength, fatigue, and dynamic response of composite conical shells and plates made by AFP is very important and needs to be addressed comprehensively. Comparison between the samples treated inside the autoclave and those made by AFP alone at the micro level would be helpful for quality check purposes.
4. An optimization technique can be employed to maximize the critical buckling moment of composite conical shells considering ply angles, thickness of layers, etc. as design variables.
5. The effect of combined loading (axial compression and bending) on the buckling behavior of composite conical shells can be considered.
6. Post-buckling response of composite conical shells can be studied using nonlinear formulation and progressive failure of the laminate can be considered.
7. More experimental study can be performed to verify theoretical parametric studied on the bucking under bending of composite conical shells.

Appendix A

Second variation of total potential energy, definition of matrices presented in section 2.1.3 and 2.3

The total potential energy of the conical shell can be written as

$$V = U + W$$
$$U = \frac{1}{2}\iint_{x\theta}(N_{xx}\varepsilon_x^0 + N_{\theta\theta}\varepsilon_\theta^0 + N_{x\theta}\gamma_{x\theta}^0 + M_{xx}\acute{\varepsilon_x} + M_{\theta\theta}\acute{\varepsilon_\theta} + M_{x\theta}\acute{\gamma_{x\theta}} + Q_\theta\gamma_{xz}^0 + Q_x\delta\gamma_{\theta z}^0)rd\theta dx$$
$$W = \int_\theta (\bar{N}_{xx}u + \bar{N}_{x\theta}v + \bar{M}_{xx}\beta_x + \bar{Q}_x w)rd\theta \tag{A-1}$$

where U is the strain energy and W is the potential energy of external forces. The first variation of V can be obtained by applying variation operator to the above equation as

$$\delta V = \delta U + \delta W$$
$$\delta U = \frac{1}{2}\iint_{x\theta}\{(\delta N_{xx}\varepsilon_x^0 + \delta N_{\theta\theta}\varepsilon_\theta^0 + \delta N_{x\theta}\gamma_{x\theta}^0 + \delta M_{xx}\acute{\varepsilon_x} + \delta M_{\theta\theta}\acute{\varepsilon_\theta} + \delta M_{x\theta}\acute{\gamma_{x\theta}} + \delta Q_\theta\gamma_{xz}^0 + \delta Q_x\gamma_{\theta z}^0) + (N_{xx}\delta\varepsilon_x^0 + N_{\theta\theta}\delta\varepsilon_\theta^0 + N_{x\theta}\delta\gamma_{x\theta}^0 + M_{xx}\delta\acute{\varepsilon}_x + M_{\theta\theta}\delta\acute{\varepsilon}_\theta + M_{x\theta}\delta\acute{\gamma}_{x\theta} + Q_\theta\delta\gamma_{xz}^0 + Q_x\delta\gamma_{\theta z}^0)\}rd\theta dx$$
$$\delta W = \int (\bar{N}_{xx}\delta u + \bar{N}_{x\theta}\delta v + \bar{M}_{xx}\delta\beta_x + \bar{Q}_x\delta w)rd\theta \tag{A-2}$$

And similarly the second variation can be obtained as

$$\delta^2 V = \delta^2 U + \delta^2 W$$
$$\delta^2 U = \frac{1}{2}\iint_{x\theta}\{(\delta^2 N_{xx}\varepsilon_x^0 + \delta^2 N_{\theta\theta}\varepsilon_\theta^0 + \delta^2 N_{x\theta}\gamma_{x\theta}^0 + \delta^2 M_{xx}\acute{\varepsilon_x} + \delta^2 M_{\theta\theta}\acute{\varepsilon_\theta} + \delta^2 M_{x\theta}\acute{\gamma_{x\theta}} + \delta^2 Q_\theta\gamma_{xz}^0 + \delta^2 Q_x\gamma_{\theta z}^0) + 2(\delta N_{xx}\delta\varepsilon_x^0 + \delta N_{\theta\theta}\delta\varepsilon_\theta^0 + \delta N_{x\theta}\delta\gamma_{x\theta}^0 + \delta M_{xx}\delta\acute{\varepsilon}_x + \delta M_{\theta\theta}\delta\acute{\varepsilon}_\theta + \delta M_{x\theta}\delta\acute{\gamma}_{x\theta} + \delta Q_\theta\delta\gamma_{xz}^0 + \delta Q_x\delta\gamma_{\theta z}^0) + (N_{xx}\delta^2\varepsilon_x^0 + N_{\theta\theta}\delta^2\varepsilon_\theta^0 + N_{x\theta}\delta^2\gamma_{x\theta}^0 + M_{xx}\delta^2\acute{\varepsilon}_x + M_{\theta\theta}\delta^2\acute{\varepsilon}_\theta + M_{x\theta}\delta^2\acute{\gamma}_{x\theta} + Q_\theta\delta^2\gamma_{xz}^0 + Q_x\delta^2\gamma_{\theta z}^0)\}rd\theta dx$$
$$\delta^2 W = 0 \tag{A-3}$$

Note that the second variation of the potential energy of external forces is zero and has no contribution to $\delta^2 V$.

In order to obtain buckling equation, nonlinear strain-displacement relations which include moderately large-deflection terms need to be considered. Analogous of Von Karman large-deflection plate theory, the strain-displacement relations for conical shell middle surface are

$$\begin{gathered}\varepsilon_x = \varepsilon_x^0 + z\acute{\varepsilon_x} \\ \varepsilon_\theta = \varepsilon_\theta^0 + z\acute{\varepsilon_\theta} \\ \gamma_{x\theta} = \gamma_{x\theta}^0 + z\acute{\gamma_{x\theta}} \\ \gamma_{xz} = \gamma_{xz}^0 \\ \gamma_{\theta z} = \gamma_{\theta z}^0\end{gathered}$$

where

$$\begin{aligned}&\varepsilon_x^0 = \frac{\partial u}{\partial x} + \frac{1}{2}\left(\frac{\partial w}{\partial x}\right)^2 \qquad \varepsilon_\theta^0 = \frac{1}{\mathrm{r}}\left(\frac{\partial v}{\partial \theta} + usin(\alpha) + wcos(\alpha) + \frac{1}{2}\left(\frac{1}{r}\frac{\partial w}{\partial \theta}\right)^2\right) \\ &\acute{\varepsilon_x} = \frac{\partial \beta_x}{\partial x} \qquad \acute{\varepsilon_\theta} = \frac{1}{\mathrm{r}}\left(\frac{\partial \beta_\theta}{\partial \theta} + \beta_x sin(\alpha)\right) \\ &\gamma_{x\theta}^0 = \frac{\partial v}{\partial x} - \frac{1}{\mathrm{r}}\left(vsin(\alpha) - \frac{\partial u}{\partial \theta} + \frac{1}{r}\frac{\partial w}{\partial \theta}\frac{\partial w}{\partial x}\right) \\ &\gamma_{xz}^0 = \frac{\partial w}{\partial x} + \beta_x \qquad \acute{\gamma_{x\theta}} = \frac{\partial \beta_\theta}{\partial x} + \frac{1}{\mathrm{r}}\frac{\partial \beta_x}{\partial \theta} - \frac{\beta_\theta}{x} \\ &\gamma_{\theta z}^0 = \frac{1}{\mathrm{r}}\frac{\partial w}{\partial \theta} - \frac{v}{\mathrm{r}}\cos(\alpha) + \beta_\theta\end{aligned} \tag{A-4}$$

The first variation of the strain-displacement relations can be obtained as

$$\begin{aligned}&\delta\varepsilon_x^0 = \delta\left(\frac{\partial u}{\partial x}\right) + \frac{\partial w}{\partial x}\delta\left(\frac{\partial w}{\partial x}\right) \qquad \delta\varepsilon_\theta^0 = \frac{1}{\mathrm{r}}\left(\delta\left(\frac{\partial v}{\partial \theta}\right) + \delta usin(\alpha) + \delta wcos(\alpha) + \frac{1}{r}\frac{\partial w}{\partial \theta}\delta\left(\frac{\partial w}{\partial \theta}\right)\right) \\ &\delta\acute{\varepsilon_x} = \delta\left(\frac{\partial \beta_x}{\partial x}\right) \qquad \delta\acute{\varepsilon_\theta} = \frac{1}{\mathrm{r}}\left(\delta\left(\frac{\partial \beta_\theta}{\partial \theta}\right) + \delta\beta_x sin(\alpha)\right) \\ &\delta\gamma_{x\theta}^0 = \delta\left(\frac{\partial v}{\partial x}\right) - \frac{1}{\mathrm{r}}\left(\delta vsin(\alpha) - \delta\left(\frac{\partial u}{\partial \theta}\right) + \frac{1}{r}\delta\left(\frac{\partial w}{\partial \theta}\right)\frac{\partial w}{\partial x} + \frac{1}{r}\frac{\partial w}{\partial \theta}\delta\left(\frac{\partial w}{\partial x}\right)\right) \\ &\delta\gamma_{xz}^0 = \delta\left(\frac{\partial w}{\partial x}\right) + \delta\beta_x \qquad \delta\acute{\gamma_{x\theta}} = \delta\left(\frac{\partial \beta_\theta}{\partial x}\right) + \frac{1}{\mathrm{r}}\delta\left(\frac{\partial \beta_x}{\partial \theta}\right) - \frac{\delta\beta_\theta}{x} \\ &\delta\gamma_{\theta z}^0 = \frac{1}{\mathrm{r}}\delta\left(\frac{\partial w}{\partial \theta}\right) - \frac{1}{\mathrm{r}}\delta v\cos(\alpha) + \delta\beta_\theta\end{aligned} \tag{A-5}$$

The second variation of the strain-displacement relations can be calculated by apply one more time the variation operator to the first variation relations as

$$\delta^2\varepsilon_x^0 = \left(\delta\frac{\partial w}{\partial x}\right)^2 \qquad \delta^2\varepsilon_\theta^0 = \left(\frac{1}{\mathrm{r}}\delta\frac{\partial w}{\partial \theta}\right)^2 \quad \delta\gamma_{x\theta}^0 = \frac{2}{r}\delta\left(\frac{\partial w}{\partial \theta}\right)\delta\left(\frac{\partial w}{\partial x}\right)$$
$$\delta^2\acute{\varepsilon}_x = \delta^2\acute{\varepsilon}_\theta = \delta^2\gamma_{xz}^0 = \delta^2\acute{\gamma}_{x\theta} = \delta^2\gamma_{\theta z}^0 = 0 \tag{A-6}$$

The force and moment resultants and their first and second variation are related to strains and variation of strains as follows

$$\begin{Bmatrix} N_{xx} \\ N_{\theta\theta} \\ N_{x\theta} \\ M_{xx} \\ M_{\theta\theta} \\ M_{x\theta} \end{Bmatrix} = \begin{bmatrix} A_{11} & A_{12} & A_{16} & B_{11} & B_{12} & B_{16} \\ A_{12} & A_{22} & A_{26} & B_{12} & B_{22} & B_{26} \\ A_{16} & A_{26} & A_{66} & B_{16} & B_{26} & B_{66} \\ B_{11} & B_{12} & B_{16} & D_{11} & D_{12} & D_{16} \\ B_{12} & B_{22} & B_{26} & D_{12} & D_{22} & D_{26} \\ B_{16} & B_{26} & B_{66} & D_{16} & D_{26} & D_{66} \end{bmatrix} \begin{Bmatrix} \varepsilon_x^0 \\ \varepsilon_\theta^0 \\ \gamma_{x\theta}^0 \\ \acute{\varepsilon}_x \\ \acute{\varepsilon}_\theta \\ \acute{\gamma}_{x\theta} \end{Bmatrix}$$

$$\begin{Bmatrix} Q_\theta \\ Q_x \end{Bmatrix} = K_s \begin{bmatrix} A_{44} & A_{45} \\ A_{45} & A_{55} \end{bmatrix} \begin{Bmatrix} \gamma_{\theta z}^0 \\ \gamma_{xz}^0 \end{Bmatrix}$$

$$\begin{Bmatrix} \delta N_{xx} \\ \delta N_{\theta\theta} \\ \delta N_{x\theta} \\ \delta M_{xx} \\ \delta M_{\theta\theta} \\ \delta M_{x\theta} \end{Bmatrix} = \begin{bmatrix} A_{11} & A_{12} & A_{16} & B_{11} & B_{12} & B_{16} \\ A_{12} & A_{22} & A_{26} & B_{12} & B_{22} & B_{26} \\ A_{16} & A_{26} & A_{66} & B_{16} & B_{26} & B_{66} \\ B_{11} & B_{12} & B_{16} & D_{11} & D_{12} & D_{16} \\ B_{12} & B_{22} & B_{26} & D_{12} & D_{22} & D_{26} \\ B_{16} & B_{26} & B_{66} & D_{16} & D_{26} & D_{66} \end{bmatrix} \begin{Bmatrix} \delta\varepsilon_x^0 \\ \delta\varepsilon_\theta^0 \\ \delta\gamma_{x\theta}^0 \\ \delta\acute{\varepsilon}_x \\ \delta\acute{\varepsilon}_\theta \\ \delta\acute{\gamma}_{x\theta} \end{Bmatrix}$$

$$\begin{Bmatrix} \delta Q_\theta \\ \delta Q_x \end{Bmatrix} = K_s \begin{bmatrix} A_{44} & A_{45} \\ A_{45} & A_{55} \end{bmatrix} \begin{Bmatrix} \delta\gamma_{\theta z}^0 \\ \delta\gamma_{xz}^0 \end{Bmatrix}$$

$$\begin{Bmatrix} \delta^2 N_{xx} \\ \delta^2 N_{\theta\theta} \\ \delta^2 N_{x\theta} \\ \delta^2 M_{xx} \\ \delta^2 M_{\theta\theta} \\ \delta^2 M_{x\theta} \end{Bmatrix} = \begin{bmatrix} A_{11} & A_{12} & A_{16} & B_{11} & B_{12} & B_{16} \\ A_{12} & A_{22} & A_{26} & B_{12} & B_{22} & B_{26} \\ A_{16} & A_{26} & A_{66} & B_{16} & B_{26} & B_{66} \\ B_{11} & B_{12} & B_{16} & D_{11} & D_{12} & D_{16} \\ B_{12} & B_{22} & B_{26} & D_{12} & D_{22} & D_{26} \\ B_{16} & B_{26} & B_{66} & D_{16} & D_{26} & D_{66} \end{bmatrix} \begin{Bmatrix} \delta^2 \varepsilon_x^0 \\ \delta^2 \varepsilon_\theta^0 \\ \delta^2 \gamma_{x\theta}^0 \\ \delta^2 \acute{\varepsilon}_x \\ \delta^2 \acute{\varepsilon}_\theta \\ \delta^2 \acute{\gamma}_{x\theta} \end{Bmatrix}$$

$$\begin{Bmatrix} \delta^2 Q_\theta \\ \delta^2 Q_x \end{Bmatrix} = K_s \begin{bmatrix} A_{44} & A_{45} \\ A_{45} & A_{55} \end{bmatrix} \begin{Bmatrix} \delta^2 \gamma_{\theta z}^0 \\ \delta^2 \gamma_{xz}^0 \end{Bmatrix}$$

(A-7)

In the present study, a membrane prebuckling equilibrium state is assumed. That is, the prebuckling rotations are neglected ($\frac{\partial w}{\partial x} = \frac{\partial w}{\partial \theta} = \beta_x = \frac{\partial \beta_x}{\partial x} = \frac{\partial \beta_x}{\partial \theta} = \beta_\theta = \frac{\partial \beta_\theta}{\partial x} = \frac{\partial \beta_\theta}{\partial \theta} = 0$). Considering this simplifications and substituting equations (A-4)-(A-7) into (A-3), one can get the second variation of the total potential energy of the conical shell as

$$\delta^2 V = \delta^2 U_1 + \delta^2 U_2$$

$$\delta^2 U_1 = \iint_{x\theta} (\delta N_{xx} \delta \varepsilon_x^0 + \delta N_{\theta\theta} \delta \varepsilon_\theta^0 + \delta N_{x\theta} \delta \gamma_{x\theta}^0 + \delta M_{xx} \delta \acute{\varepsilon}_x + \delta M_{\theta\theta} \delta \acute{\varepsilon}_\theta + \delta M_{x\theta} \delta \acute{\gamma}_{x\theta} + \delta Q_\theta \delta \gamma_{xz}^0 + \delta Q_x \delta \gamma_{\theta z}^0) r d\theta dx$$

$$\delta^2 U_2 = \iint_{x\theta} \left[N_{xx} \left(\delta \frac{\partial w}{\partial x} \right)^2 + N_{\theta\theta} \left(\frac{1}{\mathrm{r}} \delta \frac{\partial w}{\partial \theta} \right)^2 + N_{x\theta} \left(\frac{2}{r} \delta \left(\frac{\partial w}{\partial \theta} \right) \delta \left(\frac{\partial w}{\partial x} \right) \right) \right] r d\theta dx$$

By defining $\widehat{N}_{xx} = -N_{xx}$, $\widehat{N}_{\theta\theta} = -N_{\theta\theta}$ and $\widehat{N}_{x\theta} = -N_{x\theta}$, the buckling loads are defined as positive in compression (for the sake of convenience) and $\delta^2 U_2$ can be rewrite as

$$\delta^2 U_2 = -\iint_{x\theta}\left[\widehat{N}_{xx}\left(\delta\frac{\partial w}{\partial x}\right)^2 + \widehat{N}_{\theta\theta}\left(\frac{1}{\mathrm{r}}\delta\frac{\partial w}{\partial \theta}\right)^2 + \widehat{N}_{x\theta}\left(\frac{2}{r}\delta\left(\frac{\partial w}{\partial \theta}\right)\delta\left(\frac{\partial w}{\partial x}\right)\right)\right] r d\theta dx$$

The matrices appearing in equation (2.27) are:

$$[U]^T = [\delta u\ \delta v\ \delta w\ \delta\beta_x \delta\beta_\theta] = [\Phi][\mathrm{C}]$$

$$[C]^T = [c_{11}^u\ c_{11}^v\ c_{11}^w\ c_{11}^{\beta_x}\ c_{11}^{\beta_\theta}\ \ldots\ c_{mn}^u\ c_{mn}^v\ c_{mn}^w\ c_{mn}^{\beta_x}\ c_{mn}^{\beta_\theta}]$$

$$[\Phi] = \begin{vmatrix} \Phi_{11}^u & 0 & 0 & 0 & 0 & \ldots & \Phi_{21}^u & \ldots & \Phi_{mn}^u & 0 & 0 & 0 & 0 \\ 0 & \Phi_{11}^v & 0 & 0 & 0 & \ldots & \Phi_{21}^v & \ldots & 0 & \Phi_{mn}^v & 0 & 0 & 0 \\ 0 & 0 & \Phi_{11}^w & 0 & 0 & \ldots & \Phi_{21}^w & \ldots & 0 & 0 & \Phi_{mn}^w & 0 & 0 \\ 0 & 0 & 0 & \Phi_{11}^{\beta_x} & 0 & \ldots & \Phi_{21}^{\beta_x} & \ldots & 0 & 0 & 0 & \Phi_{mn}^{\beta_x} & 0 \\ 0 & 0 & 0 & 0 & \Phi_{11}^{\beta_\theta} & \ldots & \Phi_{21}^{\beta_\theta} & \ldots & 0 & 0 & 0 & 0 & \Phi_{mn}^{\beta_\theta} \end{vmatrix}$$

$$[B] = \begin{vmatrix} \frac{\partial}{\partial x} & 0 & 0 & 0 & 0 \\ \frac{1}{r}\sin(\alpha) & \frac{1}{r}\frac{\partial}{\partial\theta} & \frac{1}{r}cos(\alpha) & 0 & 0 \\ \frac{1}{r}\frac{\partial}{\partial\theta} & \frac{\partial}{\partial x} - \frac{1}{r}\sin(\alpha) & 0 & 0 & 0 \\ 0 & 0 & 0 & \frac{\partial}{\partial x} & 0 \\ 0 & 0 & 0 & \frac{1}{r}\sin(\alpha) & \frac{1}{r}\frac{\partial}{\partial\theta} \\ 0 & 0 & 0 & \frac{1}{r}\frac{\partial}{\partial\theta} & \frac{\partial}{\partial x} - \frac{1}{x} \\ 0 & -\frac{1}{r}cos(\alpha) & \frac{1}{r}\frac{\partial}{\partial\theta} & 0 & 1 \\ 0 & 0 & \frac{\partial}{\partial x} & 1 & 0 \end{vmatrix}$$

$$[F] = \begin{vmatrix} A_{11} & A_{12} & A_{16} & B_{11} & A_{12} & B_{16} & 0 & 0 \\ A_{12} & A_{22} & A_{26} & B_{12} & A_{22} & B_{26} & 0 & 0 \\ A_{16} & A_{26} & A_{66} & B_{16} & B_{26} & B_{66} & 0 & 0 \\ B_{11} & A_{12} & B_{16} & D_{11} & D_{12} & D_{16} & 0 & 0 \\ B_{12} & A_{22} & B_{26} & D_{12} & D_{22} & D_{26} & 0 & 0 \\ B_{16} & B_{26} & B_{66} & D_{16} & D_{26} & D_{66} & 0 & 0 \\ 0 & 0 & 0 & 0 & 0 & 0 & A_{45} & A_{45} \\ 0 & 0 & 0 & 0 & 0 & 0 & A_{45} & A_{55} \end{vmatrix}$$

$$[\hat{B}] = \begin{vmatrix} 0 & 0 & 0 & 0 & 0 \\ 0 & 0 & 0 & 0 & 0 \\ 0 & 0 & \frac{P_{cr}}{2\pi \cos(\alpha)\, r}\left(\frac{\partial^2}{\partial x^2}\right) & 0 & 0 \\ 0 & 0 & 0 & 0 & 0 \\ 0 & 0 & 0 & 0 & 0 \end{vmatrix}$$

The matrices related to axisymmetric problem are:

$$[C]^T = [c_1^u \; c_1^w \; c_1^{\beta_x} \; \ldots \; c_m^u \; c_m^w \; c_m^{\beta_x}]$$

$$[\Phi] = \begin{vmatrix} \Phi_1^u & 0 & 0 & \ldots & \Phi_m^u & 0 & 0 \\ 0 & \Phi_1^w & 0 & \ldots & 0 & \Phi_m^w & 0 \\ 0 & 0 & \Phi_1^{\beta_x} & \ldots & 0 & 0 & \Phi_m^{\beta_x} \end{vmatrix}$$

$$[B] = \begin{vmatrix} \frac{\partial}{\partial x} & 0 & 0 \\ \frac{1}{r}\sin(\alpha) & \frac{1}{r}cos(\alpha) & 0 \\ 0 & 0 & \frac{\partial}{\partial x} \\ 0 & 0 & \frac{1}{r}\sin(\alpha) \\ 0 & \frac{\partial}{\partial x} & 1 \end{vmatrix}$$

$$[F] = \begin{vmatrix} A_{11} & A_{12} & B_{11} & B_{12} & 0 \\ A_{12} & A_{22} & B_{12} & B_{22} & 0 \\ B_{11} & B_{12} & D_{11} & D_{12} & 0 \\ B_{12} & B_{22} & D_{12} & D_{22} & 0 \\ 0 & 0 & 0 & 0 & A_{55} \end{vmatrix}$$

$$\left[\hat{B}\right] = \begin{vmatrix} 0 & 0 & 0 \\ 0 & \dfrac{P_{cr}}{2\pi\cos(\alpha)\, r}\left(\dfrac{\partial^2}{\partial x^2}\right) & 0 \\ 0 & 0 & 0 \end{vmatrix}$$

The matrix $\left[\hat{B}_{bend}\right]$ in equation (2.43) is:

$$\left[\hat{B}_{bend}\right] = \begin{vmatrix} 0 & 0 & 0 & 0 & 0 \\ 0 & 0 & 0 & 0 & 0 \\ 0 & 0 & \dfrac{\mathrm{M_{cr}}}{\pi\cos(\alpha)\, r^2}\left(\dfrac{\partial^2}{\partial x^2} - \dfrac{1}{x}\dfrac{\partial}{\partial x}\right) & 0 & 0 \\ 0 & 0 & 0 & 0 & 0 \\ 0 & 0 & 0 & 0 & 0 \end{vmatrix}$$

Appendix B

Definition of matrices and C_i coefficients presented in section 2.4

The coefficients C_i in equation (2.58), matrix [C] and matrix $\{l\}$ in equation (2.60) are:

$$[C]=\begin{bmatrix} 0 & 1 & 0 & 0 & 0 & 0 & 0 & 0 & 0 & 0 \\ C_1 & C_2 & C_3 & C_4 & C_5 & C_6 & C_7 & C_8 & C_9 & C_{10} \\ 0 & 0 & 0 & 1 & 0 & 0 & 0 & 0 & 0 & 0 \\ C_{11} & C_{12} & C_{13} & C_{14} & C_{15} & C_{16} & C_{17} & C_{18} & C_{19} & C_{20} \\ 0 & 0 & 0 & 0 & 0 & 1 & 0 & 0 & 0 & 0 \\ C_{21} & C_{22} & C_{23} & C_{24} & C_{25} & C_{26} & C_{27} & C_{28} & C_{29} & C_{30} \\ 0 & 0 & 0 & 0 & 0 & 0 & 0 & 1 & 0 & 0 \\ C_{31} & C_{32} & C_{33} & C_{34} & C_{35} & C_{36} & C_{37} & C_{38} & C_{39} & C_{40} \\ 0 & 0 & 0 & 0 & 0 & 0 & 0 & 0 & 0 & 1 \\ C_{41} & C_{42} & C_{43} & C_{44} & C_{45} & C_{46} & C_{47} & C_{48} & C_{49} & C_{50} \end{bmatrix}$$

$$\{l\}=\left\{0,0,0,0,0,\frac{q_0\sin\left(\frac{\pi\left(x-\frac{x_b+x_t}{2}\right)}{x_b-x_t}+\frac{\pi}{2}\right)}{K_sA_{55}},0,0,0,0\right\}^T,\ F=\frac{1}{K_sA_{55}}q_0\sin\left(\frac{\pi\left(x-\frac{x_b+x_t}{2}\right)}{x_b-x_t}+\frac{\pi}{2}\right)$$

$$C_1=\frac{-A_{22}D_{11}\sin(\alpha)^2+B_{11}B_{22}\sin(\alpha)^2+B_{11}B_{66}-A_{66}D_{11}}{r^2(B_{11}^2-A_{11}D_{11})} \qquad C_2=\frac{\sin(\alpha)\,(D_{11}A_{11}-B_{11}^2)}{r(B_{11}^2-A_{11}D_{11})}$$

$$C_3=\frac{\sin(\alpha)\,(B_{11}B_{22}+B_{11}B_{66}-A_{66}D_{11}-A_{22}D_{11})}{r^2(B_{11}^2-A_{11}D_{11})} \qquad C_4=\frac{A_{22}D_{11}-B_{11}B_{12}-B_{11}B_{66}+A_{12}D_{11}}{r(B_{11}^2-A_{11}D_{11})}$$

$$C_5=\frac{\sin(\alpha)^2\,(-B_{22}D_{11}+B_{11}D_{22})+(B_{11}D_{66}-B_{66}D_{11})+K_sA_{55}B_{11}r^2}{r^2(B_{11}^2-A_{11}D_{11})} \qquad C_6=0$$

$$C_7=\frac{\sin(\alpha)\,(-B_{22}D_{11}-D_{11}B_{66}+B_{11}D_{22}+B_{11}D_{66})}{r^2(B_{11}^2-A_{11}D_{11})} \qquad C_8=\frac{B_{11}D_{12}-B_{11}D_{66}+B_{12}D_{11}+B_{66}D_{11}}{r(B_{11}^2-A_{11}D_{11})}$$

$$C_9=\frac{\sin(\alpha)\cos(\alpha)\,(B_{11}B_{22}-A_{22}D_{11})}{r^2(B_{11}^2-A_{11}D_{11})} \qquad C_{10}=\frac{K_sA_{55}B_{11}r+A_{12}D_{11}\cos(\alpha)-B_{12}B_{11}\cos(\alpha)}{r(B_{11}^2-A_{11}D_{11})}$$

$$C_{11}=\frac{\sin(\alpha)\,(B_{66}^2-A_{22}D_{66}+B_{22}B_{66}-A_{66}D_{66})}{r^2(B_{66}^2-A_{66}D_{66})} \qquad C_{12}=\frac{B_{66}^2-A_{12}D_{66}+B_{12}B_{66}-A_{66}D_{66}}{r(B_{66}^2-A_{66}D_{66})}$$

$$C_{13}=\frac{\sin(\alpha)^2\,(B_{66}^2+K_sA_{44}D_{66}-A_{66}D_{66})-K_sA_{44}D_{66}-A_{22}D_{66}+B_{22}B_{66}-K_sA_{44}B_{66}r\cos(\alpha)}{r^2(B_{66}^2-A_{66}D_{66})} \qquad C_{14}=\frac{\sin(\alpha)\,(-B_{66}^2+A_{66}D_{66})}{r(B_{66}^2-A_{66}D_{66})}$$

$$C_{15}=\frac{\sin(\alpha)\,(B_{66}D_{22}-B_{22}D_{66})}{r^2(B_{66}^2-A_{66}D_{66})} \qquad C_{16}=\frac{-D_{66}B_{12}+B_{66}D_{12}}{r(B_{66}^2-A_{66}D_{66})}$$

$$C_{17} = \frac{-B_{22}D_{66} + K_sA_{44}B_{66}r^2 + D_{22}B_{66} + K_sA_{44}D_{66}rcos(\alpha)}{r^2(B_{66}^2 - A_{66}D_{66})} \qquad C_{18} = 0$$

$$C_{19} = \frac{-K_sA_{44}B_{66}r - A_{22}D_{66}\cos(\alpha) + B_{22}B_{66}\cos(\alpha) - K_sA_{44}D_{66}\cos(\alpha)}{r^2(B_{66}^2 - A_{66}D_{66})} \qquad C_{20} = 0$$

$$C_{21} = \frac{A_{22}\sin(\alpha)\cos(\alpha)}{r^2(K_sA_{55})} \qquad C_{22} = \frac{A_{12}\cos(\alpha)}{r(K_sA_{55})}$$

$$C_{23} = \frac{\cos(\alpha)\,(A_{22} + K_sA_{44})}{r^2(K_sA_{55})} \qquad C_{24} = 0$$

$$C_{25} = \frac{B_{22}\sin(\alpha)\cos(\alpha)}{r^2(K_sA_{55})} \qquad C_{26} = \frac{-K_sA_{55}r + B_{12}\cos(\alpha)}{r(K_sA_{55})}$$

$$C_{27} = \frac{K_sA_{44}r + B_{22}\cos(\alpha)}{r^2(K_sA_{55})} \qquad C_{28} = 0$$

$$C_{29} = \frac{A_{22}\cos(\alpha)^2 + K_sA_{44}}{r^2(K_sA_{55})} \qquad C_{30} = 0$$

$$C_{31} = \frac{\sin(\alpha)^2\,(-A_{11}B_{22} + A_{22}B_{11}) + (-A_{11}B_{66} + A_{66}B_{11})}{r^2(B_{11}^2 - A_{11}D_{11})} \qquad C_{32} = 0$$

$$C_{33} = \frac{\sin(\alpha)\,(-A_{11}B_{66} + A_{22}B_{11} + A_{66}B_{11} - A_{11}B_{22})}{r^2(B_{11}^2 - A_{11}D_{11})} \qquad C_{34} = \frac{A_{11}B_{66} + A_{12}B_{11} - A_{66}B_{11} + A_{11}B_{12}}{r(B_{11}^2 - A_{11}D_{11})}$$

$$C_{35} = \frac{\sin(\alpha)^2\,(-A_{11}D_{22} + B_{22}B_{11}) - A_{11}D_{66} + B_{66}B_{11} - K_sA_{55}A_{11}r^2}{r^2(B_{11}^2 - A_{11}D_{11})} \qquad C_{36} = \frac{\sin(\alpha)\,(A_{11}D_{11} - B_{11}^2)}{r(B_{11}^2 - A_{11}D_{11})}$$

$$C_{37} = \frac{\sin(\alpha)\,(-A_{11}D_{22} - A_{11}D_{66} + B_{11}B_{22} + B_{11}B_{66})}{r^2(B_{11}^2 - A_{11}D_{11})} \qquad C_{38} = \frac{(A_{11}D_{12} + A_{11}D_{66} - B_{11}B_{12} - B_{11}B_{66})}{r(B_{11}^2 - A_{11}D_{11})}$$

$$C_{39} = \frac{\sin(\alpha)\cos(\alpha)\,(-A_{11}B_{22} + A_{22}B_{11})}{r^2(B_{11}^2 - A_{11}D_{11})} \qquad C_{40} = \frac{-K_sA_{55}A_{11}r + A_{11}B_{12}\cos(\alpha) - A_{12}B_{11}\cos(\alpha)}{r(B_{11}^2 - A_{11}D_{11})}$$

$$C_{41} = \frac{\sin(\alpha)\,(A_{66}B_{22} - A_{22}B_{66})}{r^2(A_{66}D_{66} - B_{66}^2)} \qquad C_{42} = \frac{A_{66}B_{12} - A_{12}B_{66}}{r(A_{66}D_{66} - B_{66}^2)}$$

$$C_{43} = \frac{-K_sA_{44}B_{66} - K_sA_{44}A_{66}r\cos(\alpha) - A_{22}B_{66} + K_sA_{44}B_{66}\sin(\alpha)^2 + A_{66}B_{22}}{r^2(A_{66}D_{66} - B_{66}^2)} \qquad C_{44} = 0$$

$$C_{45} = \frac{-K_sA_{44}A_{66}r + A_{66}B_{22}\cos(\alpha) - A_{22}B_{66}\cos(\alpha) - K_sA_{44}B_{66}\cos(\alpha)}{r(A_{66}D_{66} - B_{66}^2)} \qquad C_{46} = \frac{A_{66}D_{12} + A_{66}D_{66} - B_{12}B_{66} - B_{66}^2}{r(A_{66}D_{66} - B_{66}^2)}$$

$$C_{47} = \frac{\sin(\alpha)\,(-B_{66}^2 + A_{66}D_{22} + A_{66}D_{66} - B_{22}B_{66})}{r^2(A_{66}D_{66} - B_{66}^2)} \qquad C_{48} = \frac{\sin(\alpha)\,(A_{66}D_{66} + B_{66}^2)}{r(A_{66}D_{66} - B_{66}^2)}$$

$$C_{49} = \frac{\sin(\alpha)^2\,(-B_{66}^2 + A_{66}D_{66}) - B_{22}B_{66} + A_{66}D_{22} + K_sA_{44}r(A_{66}r + B_{66}\cos(\alpha))}{r^2(A_{66}D_{66} - B_{66}^2)} \qquad C_{50} = 0$$

where

$$\left(A_{ij}, B_{ij}, D_{ij}\right) = \sum_{k=1}^{N} \int_{\zeta_{k-1}}^{\zeta_k} \bar{Q}_{ij}^{(k)}(1, \zeta, \zeta^2) d\zeta \qquad K_s = 5/6$$

Appendix C

Definition of matrices and C_i coefficients presented in Chapter 3

The coefficients C_i in equation (3.17), matrix [C] and matrix $\{l\}$ in equation (3.22) are:

$$[C] = \begin{bmatrix} 0 & 1 & 0 & 0 & 0 & 0 & 0 & 0 & 0 & 0 \\ C_1 & 0 & 0 & C_2 & 0 & C_3 & C_4 & 0 & 0 & C_5 \\ 0 & 0 & 0 & 1 & 0 & 0 & 0 & 0 & 0 & 0 \\ 0 & C_6 & C_7 & 0 & C_8 & 0 & 0 & C_9 & C_{10} & 0 \\ 0 & 0 & 0 & 0 & 0 & 1 & 0 & 0 & 0 & 0 \\ 0 & C_{11} & C_{12} & 0 & C_{13} & 0 & 0 & C_{14} & C_{15} & 0 \\ 0 & 0 & 0 & 0 & 0 & 0 & 0 & 1 & 0 & 0 \\ C_{16} & 0 & 0 & C_{17} & 0 & C_{18} & C_{19} & 0 & 0 & C_{20} \\ 0 & 0 & 0 & 0 & 0 & 0 & 0 & 0 & 0 & 1 \\ 0 & C_{21} & C_{22} & 0 & C_{23} & 0 & 0 & C_{24} & C_{25} & 0 \end{bmatrix}$$

$$C_1 = \frac{B_{11}(-\beta_m^2 B_{66} + I_2\omega_m^2) + (\beta_m^2 A_{66} - I_1\omega_m^2)D_{11}}{A_{11}D_{11} - B_{11}^2}$$

$$C_2 = \frac{\beta_m B_{11}(B_{12} + B_{66}) - \beta_m D_{11}(A_{12} + A_{66})}{A_{11}D_{11} - B_{11}^2}$$

$$C_3 = \frac{B_{11}\left(\frac{B_{12}}{R} - K_s A_{55}\right) - \frac{D_{11}A_{12}}{R}}{A_{11}D_{11} - B_{11}^2}$$

$$C_4 = \frac{B_{11}(-\beta_m^2 D_{66} - K_s A_{55} + I_3\omega_m^2) + D_{11}(\beta_m^2 B_{66} - I_2\omega_m^2)}{A_{11}D_{11} - B_{11}^2}$$

$$C_5 = \frac{\beta_m B_{11}(D_{12} + D_{66}) - \beta_m D_{11}(B_{12} + B_{66})}{A_{11}D_{11} - B_{11}^2}$$

$$C_6 = \frac{-\beta_m D_{66}(A_{12} + A_{66}) + \beta_m B_{66}(B_{12} + B_{66})}{B_{66}^2 - A_{66}D_{66}}$$

$$C_7 = \frac{(-\beta_m^2 A_{22} + I_1\omega_m^2)D_{66} - B_{66}(-\beta_m^2 B_{22} + I_2\omega_m^2) - K_s A_{44}(D_{66}/R^2 + B_{66}/R)}{B_{66}^2 - A_{66}D_{66}}$$

$$C_8 = \frac{\frac{-D_{66}A_{22}\beta}{R} - B_{66}\beta\left(K_s A_{44} - \frac{B_{22}}{R}\right) - (K_s\, A_{44}D_{66}\,\beta)/R}{B_{66}^2 - A_{66}D_{66}}$$

$$C_9 = \frac{-\beta_m D_{66}B_{12} + \beta_m B_{66}D_{12}}{B_{66}^2 - A_{66}D_{66}}$$

$$C_{10} = \frac{(-B_{22}\beta_m^2 + I_2\omega_m^2)D_{66} - B_{66}(-D_{22}\beta_m^2 - K_s A_{44} + I_3\omega_m^2) + (K_s A_{44}D_{66})/R}{B_{66}^2 - A_{66}D_{66}}$$

$$C_{11} = \frac{\frac{A_{12}}{R}}{K_s A_{55} - N}$$

$$C_{12} = \frac{\frac{\beta_m A_{22}}{R} + (K_s\, A_{44}\, \beta)/R}{K_s A_{55} - N}$$

$$C_{13} = \frac{\beta_m^2 K_s A_{44} - I_2 \omega_m^2 + A_{22}/R^2}{K_s A_{55} - N}$$

$$C_{14} = \frac{-K_s A_{55} + \frac{B_{12}}{R}}{K_s A_{55} - N}$$

$$C_{15} = \frac{\beta_m (-K_s A_{44} + \frac{B_{22}}{R})}{K_s A_{55} - N}$$

$$C_{16} = \frac{B_{11}(-\beta_m^2 A_{66} + I_1 \omega_m^2) - A_{11}(-\beta_m^2 B_{66} + I_2 \omega_m^2)}{A_{11} D_{11} - B_{11}^2}$$

$$C_{17} = \frac{\beta_m B_{11}(A_{12} + A_{66}) - \beta_m A_{11}(B_{12} + B_{66})}{A_{11} D_{11} - B_{11}^2}$$

$$C_{18} = \frac{\frac{B_{11} A_{12}}{R} + A_{11}(K_s A_{55} - \frac{B_{12}}{R})}{A_{11} D_{11} - B_{11}^2}$$

$$C_{19} = \frac{B_{11}(-\beta_m^2 B_{66} + I_2 \omega_m^2) - A_{11}(-\beta_m^2 D_{66} - K_s A_{55} + I_3 \omega_m^2)}{A_{11} D_{11} - B_{11}^2}$$

$$C_{20} = \frac{\beta_m B_{11}(B_{12} + B_{66}) - \beta_m A_{11}(D_{12} + D_{66})}{A_{11} D_{11} - B_{11}^2}$$

$$C_{21} = \frac{-\beta_m A_{66} B_{12} + \beta_m B_{66} A_{12}}{B_{66}^2 - A_{66} D_{66}}$$

$$C_{22} = \frac{A_{66}(-B_{22}\beta_m^2 + I_2 \omega_m^2) - (-A_{22}\beta_m^2 + I_1 \omega_m^2) B_{66} + K_s A_{44}(A_{66}/R + B_{66}/R^2)}{B_{66}^2 - A_{66} D_{66}}$$

$$C_{23} = \frac{A_{66}\beta_m (K_s A_{44} - B_{22}/R) + \frac{B_{66}(A_{22}\, \beta_m)}{R} + (B_{66}\, K_s A_{44} \beta_m)/R}{B_{66}^2 - A_{66} D_{66}}$$

$$C_{24} = \frac{-\beta_m A_{66}(D_{12} + D_{66}) + \beta_m B_{66}(B_{12} + B_{66})}{B_{66}^2 - A_{66} D_{66}}$$

$$C_{25} = \frac{A_{66}(-D_{22}\beta_m^2 - K_s A_{44} + I_3 \omega_m^2) - (I_2 \omega_m^2 - B_{22}\beta_m^2) B_{66} - (K_s A_{44}\, B_{66})/R}{B_{66}^2 - A_{66} D_{66}}$$

$$\{l\} = \left\{0,0,0,0,0,\frac{q_0 \sin(\frac{\pi x}{l} + \frac{\pi}{2})}{K_s A_{55}}, 0,0,0,0\right\}^T$$

Appendix D

Tab dimensions and layup

All dimensions are in inches.

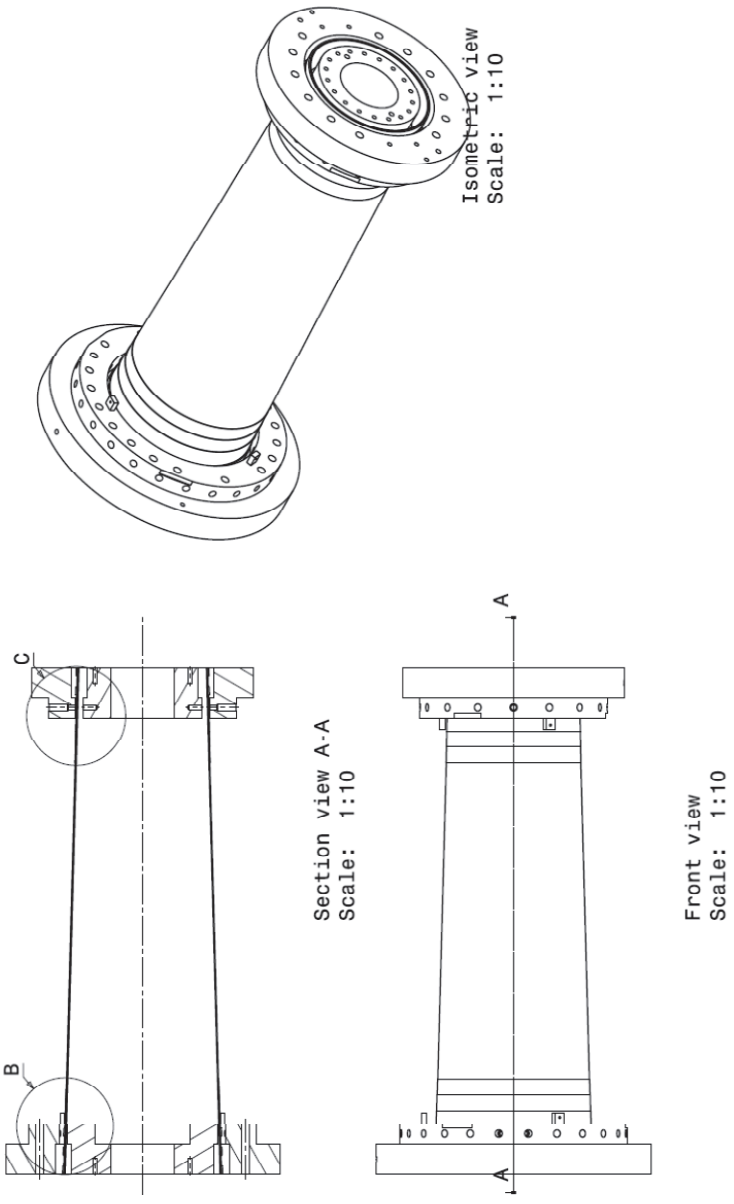

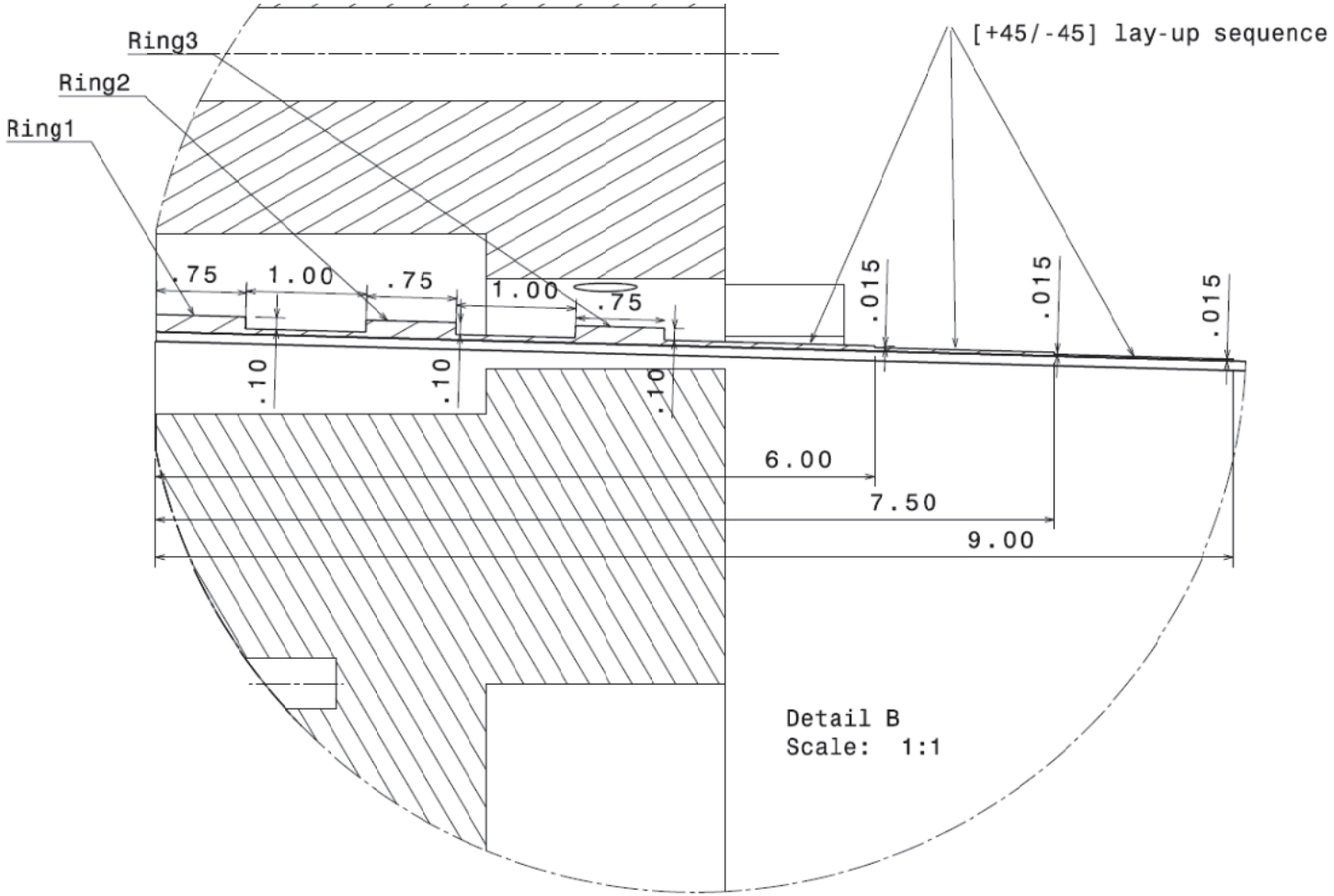

All three rings (1,2 and 3) have [90] lay-up sequence

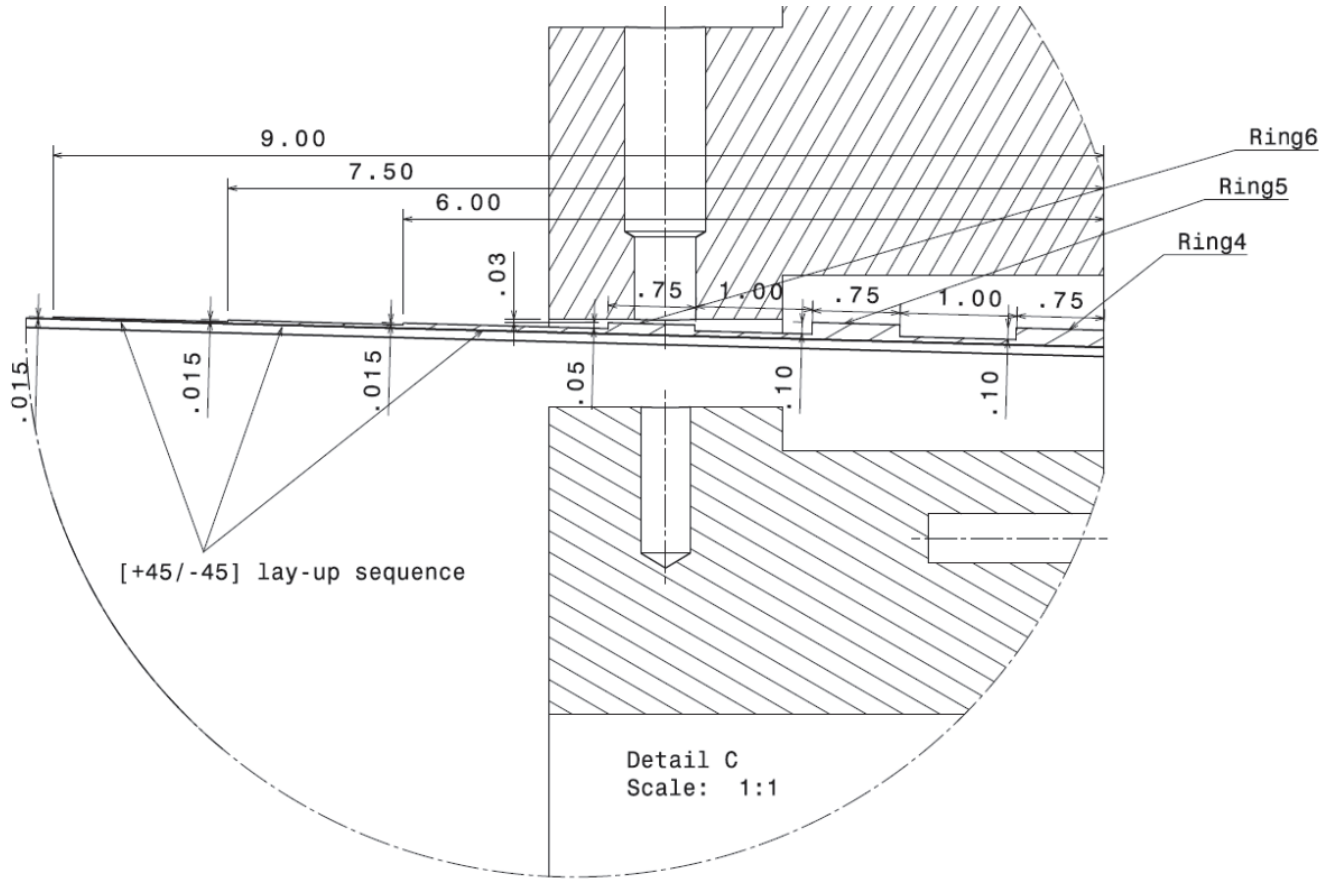

All three rings (4,5 and 6) have [90] lay-up sequence

Bibliography

[1] S. Beland, High Performance of Thermoplastic Resins and Their Composites, Noyes Data Corporation, 1990.

[2] K. P. Soldatos, "Review of three dimensional dynamic analyses of circular cylinders and cylindrical shells," *Appl. Mech. Rev,* vol. 47, no. 10, pp. 501-516, 1994.

[3] G. A. Kardomateas, "Buckling of thick orthotropic cylindrical shells under external pressure," *ASME Transactions Series E Journal of Applied Mechanics,* vol. 60, pp. 195-202, 1993.

[4] G. A. Kardomateas, "Benchmark three-dimensional elasticity solutions for the buckling of thick orthotropic cylindrical shells," *Composites Part B,* vol. 27, no. 6, pp. 569-580, 1996.

[5] Y. Kim, G. Kardomateas and A. Zureick, "Buckling of thick orthotropic cylindrical shells under torsion," *ASME Journal of Applied Mechanics,* vol. 66, no. 3, pp. 41-50, 1999.

[6] T. K. Varadan and K. Bhaskar, "Bending of laminated orthotropic cylindrical shells--An elasticity approach," *Compos. Struct.,* vol. 17, no. 2, pp. 141-156, 1991.

[7] J. Ye and K. P. Soldatos, "Three-dimensional buckling analysis of laminated composite hollow cylinders and cylindrical panels," *International Journal of Solids and Structures,* vol. 32, no. 13, pp. 1949-1962, 1995.

[8] J. Ye and K. P. Soldatos, "Three-dimensional vibration of laminated cylinders and cylindrical panels with symmetric or antisymmetric cross-ply lay-up," *Compos. Eng.,* vol. 4, no. 4, pp. 429-444, 1994.

[9] A. Bhimaraddi and K. Chandrashekhara, "Three-dimensional elasticity solution for static response of simply supported orthotropic cylindrical shells," *Compos. Struct.,* vol. 20, no. 4, pp. 227-235, 1992.

[10] N. N. Huang, "Exact analysis for three-dimensional free vibrations of cross-ply cylindrical and doubly-curved laminates," *Acta mechanica,* vol. 108, no. 1, pp. 23-34, 1995.

[11] T. D. Hawkes and K. P. Soldatos, "Three-dimensional axisymmetric vibrations of orthotropic and cross-ply laminated hollow cylinders," *AIAA journal,* vol. 30, no. 4, pp. 1089-1098, 1992.

[12] K. P. Soldatos and J. Q. Ye, "Three-dimensional static, dynamic, thermoelastic and buckling analysis of homogeneous and laminated composite cylinders," *Compos. Struct.,* vol. 29, no. 2, pp. 131-143, 1994.

[13] A. Noor and W. Burton, "Assessment of computational models for multilayered composite shells," *ASME Applied Mechanics Reviews,* vol. 43, no. 4, pp. 67-97, 1990.

[14] R. M. Jones, "Buckling of circular cylindrical shells with multiple orthotropic layers and eccentric stiffeners," *AIAA Journal,* vol. 6, no. 12, pp. 2301-2305, 1968.

[15] A. Messina and K. P. Soldatos, "Ritz-type dynamic analysis of cross-ply laminated circular cylinders subjected to different boundary conditions," *Journal of sound and vibration,* vol. 227, no. 4, pp. 749-768, 1999.

[16] H. Matsunaga, "Vibration and buckling of cross-ply laminated composite circular cylindrical shells according to a global higher-order theory," *International journal of mechanical sciences,* vol. 49, no. 9, pp. 1060-1075, 2007.

[17] A. A. Khdeir, J. N. Reddy and D. Frederick, "A study of bending, vibration and buckling of cross-ply circular cylindrical shells with various shell theories," *International Journal of Engineering Science,* vol. 27, no. 11, pp. 1337-51, 1989.

[18] A. Nosier and J. N. Reddy, "Vibration and stability analyses of cross-ply laminated circular cylindrical shells," *Journal of Sound and Vibration,* vol. 157, no. 1, pp. 139-159, 1992.

[19] K. Soldatos and T. Timarci, "A unified formulation of laminated composite, shear deformable, five-degree-of-freedom cylindrical shell theories," *Compos. Struct.,* vol. 25, no. 1 - 4, pp. 165-171, 1993.

[20] T. Timarci and K. P. Soldatos, "Comparative dynamic studies for symmetric cross-ply circular cylindrical shells on the basis of a unified shear deformable shell theory," *Journal of sound and vibration,* vol. 187, no. 4, pp. 609-624, 1995.

[21] K. P. Soldatos and A. Messina, "Vibration studies of cross-ply laminated shear deformable

circular cylinders on the basis of orthogonal polynomials," *Journal of sound and vibration,* vol. 218, no. 2, pp. 219-243, 1998.

[22] A. Kayran and G. Anlas, "Effect of stacking sequence on free vibration frequencies of laminated composite circular cylindrical shells," *Journal of Vibration and Control,* vol. 5, no. 3, pp. 355-372, 1999.

[23] D. O. Brush and B. O. Almroth, Buckling of bars, plates, and shells, New York: McGraw-Hill, 1975, p. 379.

[24] P. Seide, "Axisymmetrical buckling of circular cones under axial compression," *Journal of Applied Mechanics,* vol. 23, p. 626, 1956.

[25] M. Baruch, O. Harari and J. Singer, "Low Buckling Loads of Axially Compressed Conical Shells," *Journal of Applied Mechanics,* vol. 37, no. 2, pp. 384-392, 1970.

[26] L. Lackman and J. Penzien, "Buckling of circular cones under axial compression," *Journal of Applied Mechanics,* vol. 27, p. 458, 1960.

[27] P. Seide, "Buckling of circular cones under axial compression," *Journal of Applied Mechanics,* vol. 28, p. 315, 1961.

[28] V. I. Weingarten, E. J. Morgan and P. Seide, "Elastic stability of thin-walled cylindrical and conical shells under axial compression," *AIAA Journal,* vol. 3, no. 3, p. 500, 1965.

[29] J. Singer, "Buckling of circular conical shells under uniform axial compression," *AIAA Journal,* vol. 3, no. 5, p. 985, 1965.

[30] J. Tani and N. Yamaki, "Buckling of truncated conical shells under axial compression," *AIAA Journal,* vol. 8, pp. 568-571, 1970.

[31] L. Tong and T. K. Wang, "Buckling analysis of laminated composite conical shells," *Composites Science and Technology,* vol. 47, no. 1, pp. 57-63, 1993.

[32] L. Tong and T. K. Wang, "Simple solutions for buckling of laminated conical shells," *International Journal of Mechanical Sciences,* vol. 34, no. 2, pp. 93-111, 02 1992.

[33] L. Li, "The stability of composite material stiffened conical shells under axial compression," *Composite Structures,* vol. 38, no. 1-4, pp. 169-177, 8 1997.

[34] A. H. Sofiyev, "The buckling of an orthotropic composite truncated conical shell with continuously varying thickness subject to a time dependent external pressure," *Composites Part B: Engineering,* vol. 34, no. 3, pp. 227-233, 4 2003.

[35] I. F. Pinto, C. M. Mota, C. A. Mota and J. Herskovits, "Analysis of laminated conical shell structures using higher order models," *Composite Structures,* vol. 62, no. 3-4, pp. 383-390, 2003.

[36] Y. Goldfeld and J. Arbocz, "Buckling of laminated conical shells given the variations of the

stiffness coefficients," *AIAA Journal,* vol. 42, no. 3, pp. 642-9, 03 2004.

[37] B. P. Patel, Y. Nath and K. K. Shukla, "Nonlinear thermo-elastic buckling characteristics of cross-ply laminated joined conical-cylindrical shells," *International Journal of Solids and Structures,* vol. 43, no. 16, pp. 4810-4829, 2006.

[38] B. P. Patel, K. K. Shukla and Y. Nath, "Nonlinear thermoelastic stability characteristics of cross-ply laminated oval cylindrical/conical shells," *Finite Elements in Analysis and Design,* vol. 42, no. 12, pp. 1061-70, 08 2006.

[39] B. P. Patel, K. K. Shukla and Y. Nath, "Thermal postbuckling analysis of laminated cross-ply truncated circular conical shells," *Composite Structures,* vol. 71, no. 1, pp. 101-14, 10 2005.

[40] B. P. Patel, K. R. Shukla and Y. Nath, "Thermal postbuckling characteristics of laminated conical shells with temperature-dependent material properties," *AIAA Journal,* vol. 43, no. 6, pp. 1380-1388, 2005.

[41] B. P. Patel, S. Singh and Y. Nath, "Postbuckling characteristics of angle-ply laminated truncated circular conical shells," *Communications in Nonlinear Science and Numerical Simulation,* vol. 13, no. 7, pp. 1411-30, 2008.

[42] S. Singh, B. P. Patel and Y. Nath, "Postbuckling behavior of cross-ply laminated conical and joined conical-cylindrical shells subjected to thermo-mechanical loads," *International*

Journal of Structural Stability and Dynamics, vol. 7, no. 3, pp. 543-553, 2007.

[43] S. Singh, B. P. Patel and Y. Nath, "Postbuckling behavior of angle-ply laminated joined circular conical - Cylindrical shells," *AIAA Journal,* vol. 45, no. 4, pp. 942-949, 2007.

[44] R. C. Tennyson, "Buckling of laminated composite cylinders: a review," *Composites,* vol. 6, no. 1, pp. 17-24, 1975.

[45] G. J. Simitses, "Buckling and postbuckling of imperfect cylindrical shells: a review," *Applied Mechanics Review,* vol. 39, pp. 1517-1524, 1986.

[46] M. F. Card and J. P. Peterson, "On the instability of orthotropic cylinders," NASA TN D-1510, pp. 297-308, 1962.

[47] M. F. Card, "Experiments to determine the strength of filament-wound cylinders loaded in axial compression," NASA TN D-3522, 1966.

[48] J. Tsai, A. Feldman and D. A. Stang, "The buckling strength of filament wound cylinders under axial compression," NASA CR-266, 1965.

[49] D. W. Jensen and P. A. Hipp, "Compressive Testing of Filament-Wound Cylinders," in *Composites, Proc. of the 8th Intern. Conf. on Composite Materials (ICCM8)* , Honolulu, Hawaii, July 15-19, 1991.

[50] H. T. Hahn, D. W. Jensen, S. J. Claus, S. P. Pai and P. A. Hipp, "Structural design criteria

for filament-wound composite shells," Annual Report, NASA Contract: NAG- 1-982, 1994.

[51] J. Singer, J. Arbocz and T. Weller, Buckling experiments;experimental methods in buckling of thin-walled sructures, John Wiley & Sons Ltd, 1998.

[52] R. C. Tennyson and D. B. Muggeridge, "Buckling of laminated anisotropic imperfect circular cylinders under axial compression," *Journal of Spacecraft and Rockets,* vol. 10, no. 2, pp. 143-8, 02 1973.

[53] G. Sun, "Optimization of laminated cylinders for buckling," Institute for Aerospace Studies, University of Toronto (UTIAS Rept 317), 1987.

[54] R. C. Tennyson, D. B. Muggeridge and R. D. Caswell, "Buckling of circular cylindrical shells having axisymmetric imperfection distributions," *AIAA Journal,* vol. 9, no. 5, pp. 924-930, 1971.

[55] V. Giavotto, C. Poggi, G. C. D. and M. Fezzani, "Buckling behavior of composite shells under combined loading," in *Proceedings of 17th European Rotorcraft Forum, pp. 84-1-84-13*, Berin, 1991.

[56] C. Poggi, A. Taliercio and A. Capsoni, "Fiber orientation effects on the buckling behavior of imperfect composite cylinders," in *International Colloquium on Buckling of Shells Structures on Land, in Sea and in the Air*, 1991, pp. 114-123.

[57] D. L. Block, "Buckling of eccentrically stiffened orthotropic cylinders under pure

bending.," NASA TN D3351, 1966.

[58] A. Holston, "Buckling of inhomogeneous anisotropic cylindrical shells by bending.," *AIAA Journal,* vol. 6, pp. 1837-1841, 1968.

[59] S. Cheng and A. Ugural, "Buckling of composite cylindrical shells under pure bending, solving Flugge differential equations of equilibrium," *AIAA JOURNAL,* vol. 6, pp. 349-354, 1968.

[60] K. A. Lou and G. Yaniv, "Buckling of circular cylindrical composite shells under axial compression and bending loads," *J. Compos. Mater.,* vol. 25, no. 2, pp. 162-187, 1991.

[61] H. P. Fuchs and M. W. Hyer, "Bending response of thin-walled laminated composite cylinders," *Composite Structures,* vol. 22, pp. 87-107, 1992.

[62] H. P. Fuchs and M. W. Hyer, "The nonlinear prebuckling response of short thin-walled laminated composite cylinders in bending," *Composite Structures,* vol. 34, no. 3, pp. 309-24, 03 1996.

[63] J. P. Fuchs, M. W. Hyer and J. H. Starnes, "Numerical and experimental investigation of the bending response of thin-walled composite cylinders," NASA-CR-195730, NAS 1.26:195730, CCMS-93-19, VPI-E-93-11 , Sep. 1993.

[64] A. W. Blom, B. P. Stickler, M. Rassaian and Z. Gurdal, "Bending test of a fiber reinforced composite," *American Society for Composite, 24th Technical Conference,* Sep. 2009.

[65] E. J. Barbero, J. N. Reddy and J. L. Teply, "General two-dimensional theory of laminated cylindrical shells," *AIAA journal,* vol. 28, no. 3, pp. 544-552, 1990.

[66] H. Kraus, Thin elastic shells: an introduction to the theoretical foundations and the analysis of their static and dynamic behavior, New York: Wiley, 1967.

[67] R. M. Jones, Buckling of bars, plates, and shells, Bull Ridge Publishing, 2006.

[68] J. N. Reddy, Mechanics of laminated composite plates and shells: theory and analysis, CRC Press, 2004.

[69] S. P. Timoshenko and G. J. M., Theory of elastic stability, McGraw-Hill Book Company , 1961.

[70] J. N. Reddy, Energy principles and variational methods in applied mechanics, John Wiley & Sons Inc, 2002.

[71] F. Shadmehri, S. V. Hoa and M. Hojjati, "The effect of displacement field on bending, buckling and vibration of cross-ply circular cylindrical shells," *Mechanics of Advanced Materials and Structures,* vol. InPress., 2012.

[72] D. J. Tenerelli and W. H. Horton, "An experimental study of the local buckling of ring-stiffened cylinders subject to axial compression," *Israel J. Technol.,* vol. 7, pp. 181-194, 1969.

[73] J. Singer, "The influence of stiffener geometry and spacing on the buckling of axially compressed cylindrical and conical shells," in *Proc. of 2nd IUTAM Symp. Theory of Thin Shells, Copenhagen, Springer-Verlag, Berlin (1969), pp. 234–263*, 1969.

[74] N. Yamaki, K. Otomo and K. Matsuda, "Experiments on the postbuckling behavior of circular cylindrical shells under compression," *Experimental Mechanics,* vol. 15, no. 1, pp. 23-28, 1975.

[75] Y. S. Kim, Biaxial buckling of laminated composite plates, Thesis (Ph.D.)-Dept. of Mechanical Engineering, Concordia University, 1995, p. 216.

[76] R. V. Southwell, "On the Analysis of Experimental Observations in Problems of Elastic Stability," *Proceedings of the Royal Society of London.Series A, Containing Papers of a Mathematical and Physical Character,* vol. 135, no. 828, pp. 601-616, Apr. 1 1932.

[77] L. H. Donnell, "On the Application of Southwell's Method for the Analysis of Buckling Tests," New York, McGraw-Hill, 1938, pp. 27-38.

[78] C. Herbst and K. Splitthof, "Basics of 3D digital image correlation," http://www.dantecdynamics.com/Default.aspx?ID=855. [Online].

[79] "Deformation Measurment," Correlated Solutions, I., "http://www.correlatedsolutions.com/data/vic2d-vic3d-flyer.pdf,". [Online].

[80] S. V. Hoa, Principles of the manufacturing of composite materials, DEStech Publications, Inc, 2009.

[81] A. Yousefpour and M. N. Ghasemi Nejhad., "Experimental and Computational Study of APC-2/AS4 Thermoplastic Composite C-Rings," *J. Thermoplast. Compos. Mater.,* vol. 14, no. 2, pp. 129-145, 2001.

[82] M. N. Ghasemi Nejhad, R. D. Cope and S. I. Güçeri, "Thermal analysis of in-situ thermoplastic composite tape laying," *J. Thermoplast. Compos. Mater.,* vol. 4, no. 1, pp. 20-45, 1991.

[83] M. N. Ghasemi Nejhad, "Issues related to processability during the manufacture of thermoplastic composites using on-line consolidation techniques," *J. Thermoplast. Compos. Mater.,* vol. 6, no. 2, pp. 130-146, 1993.

[84] M. Hojjati, G. Chouinard and A. Yousefpour, "Crystallization Behavior of PEKK Thermoplastic Polymer," in *Proceedings of SAMPE 2006*, Long Beach, California, 2006.

[85] Cytec Fiberite, Thermoplastic Composite Material Handbook, Cytec Engineered Materials, 1999.

[86] ASTMD3039/D3039M, "Standard Test method for Tensile Properties of Polymer Matrix Composite Materials," American Society for Testing and Materials, Philadelphia, 2009.

[87] ASTM D3410/D3410M, "Standard Test method for Compressive Properties of Polymer Matrix Composite Materials with Unsupported Gage Section by Shear Loading," American Society for Testing and Materials, Philadelphia, 2009.

[88] ASTM D5379/D5379M, "StandarTest method for Shear Properties of Composite Materials by the V-Notched Beam Method," American Society for Testing and Materials, Philadelphia, 2009.

[89] D. L. Brown, R. J. Allemang and W. G. Halvorsen, "Impulse technique for structural frequency response testing," *The Journal of the Acoustical Society of America,* vol. 63, no. S1, pp. S81 - S81, 1978.

[90] M. Maia. and M. Silva, "Modal analysis identification techniques," *Philosophical Transactions of the Royal Society of London. Series A: Mathematical, Physical and Engineering Sciences,* vol. 359, no. 1778, pp. 29-40, 2001.

[91] D. J. Ewins, Modal testing: Theory, practice and application, Research Studies Press, Ltd., 2000.

[92] R. K. Roy, Design of experiments using the Taguchi approach: 16 Steps to product and process improvement, Wiley-Interscience, 2001.

[93] ASTM D2344/D2344M00, "Standard Test method for Short-Beam Strength of Polymer Matrix Composite Materials and Their Laminates," American Society for Testing and

Materials, Philadelphia, 2009.

[94] M. Hojjati, J. Chen, M. Tanguary and A. Yousefpour, "Process optimization for fiber placement of Carbon/PEKK thermoplastic composites," in *Proceedings of 38th SAMPE Fall Technical Conference*, Dallas, Texas, 2006.

[95] W. I. Lee and G. S. Springer, "A model of the manufacturing process of thermoplastic matrix composites," *J. Compos. Mater.,* vol. 21, no. 11, pp. 1017-1055, 1987.

[96] F. Shadmehri, S. V. Hoa and M. Hojjati, "Buckling of conical composite shells," *Compos. Struct.,* vol. 94, no. 2, pp. 787-792, 2012.

[97] X. Cai, F. Shadmehri, M. Hojjati, J. Chen and S. V. Hoa, "Determination of Optimum Process Conditions for Processing AS4/APC-2 Thermoplastic Composites by Automated Fiber Placement," in *The Society for the Advancement of Material and Process Engineering (SAMPE) conference*, Baltimore, MD, May 2012.

[98] F. Shadmehri, S. V. Hoa and M. Hojjati, "Buckling of conical composite shells," in *16th International Conference on Composite Structures (ICCS16)*, FEUP Proto, June 2011.

[99] F. Shadmehri, X. Cai, M. Hojjati, J. Chen and S. V. Hoa, "Determination of Optimal Process Parameters for Manufacturing Thermoplastic Composite Rings by Automated Fiber Placement," in *26 American Society for Composites (ASC) annual technical conference (Second Joint US-Canada Conference on Composites)*, Montreal, Canada,

September 2011.

[100] F. Shadmehri, X. Cai, M. Hojjati, J. Chen and S. V. Hoa, "Effect of autoclave process on the quality of thermoplastic cones manufactured using automated fiber placement technique," in *The Society for the Advancement of Material and Process Engineering (SAMPE) conference*, Long Beach, CA, May 2011.

[101] F. Shadmehri, S. V. Hoa and M. Hojjati, "Bending analysis of cross-ply laminated conical shells," in *24 American Society for Composites (ASC) annual technical conference (First Joint US-Canada Conference on Composites)*, University of Delaware, September 2009.

[102] F. Shadmehri, S. V. Hoa and M. Hojjati, "Effect of displacement field on vibration of cross-ply circular cylindrical shells," in *The Canadian Society of Mechanical Engineering (CSME) Conference*, University of Victoria, British Columbia, June 2010.